Application of Optical Coherence Tomography in Investigating Cell Migration

Sara Rey

School of Biosciences, Cardiff University

PhD Thesis

June 2012

DECLARATION

This work has not been submitted in substance for any other degree or award at this or any other university or place of learning, nor is being submitted concurrently in candidature for any degree or other award.

Signed …… (candidate) Date ……

STATEMENT 1

This thesis is being submitted in partial fulfillment of the requirements for the degree of ……(insert MCh, MD, MPhil, PhD etc, as appropriate)

Signed …… (candidate) Date ……

STATEMENT 2

This thesis is the result of my own independent work/investigation, except where otherwise stated.
Other sources are acknowledged by explicit references. The views expressed are my own.

Signed …… (candidate) Date ……

STATEMENT 3

I hereby give consent for my thesis, if accepted, to be available for photocopying and for inter-library loan, and for the title and summary to be made available to outside organisations.

Signed …… (candidate) Date ……

STATEMENT 4: PREVIOUSLY APPROVED BAR ON ACCESS

I hereby give consent for my thesis, if accepted, to be available for photocopying and for inter-library loans **after expiry of a bar on access previously approved by the Academic Standards & Quality Committee.**

Signed …… (candidate) Date ……

Thesis Summary

Student ID Number:	**010074396**

Summary of Thesis:

Chemotaxis and cell migration are important processes for life, involved in organism development and homeostasis and implicated in a number of disease states. *Dictyostelium discoideum*, an amoeba, is a useful model for investigation of chemotaxis and development, due to its ability to undergo chemotactic aggregation and development upon starvation. Although cell migration has been well described on planar transparent surfaces, it is uncertain how well these conditions replicate the natural environment of a cell. However, attempts to better replicate these environments generally make use of opaque substrates and 3D matrices, in which it is more challenging to image cell migration.

Protocols were developed to enable optical coherence tomography, a 3D structural imaging technique which requires no sample processing or staining, to be successfully employed in imaging *Dictyostelium* cell migration in time-lapse on non-transparent substrata and within an agarose gel. I compared the effects of two substrates, a nitrocellulose filter and a polystyrene Petri dish on aggregating cells and found differences in speed but not persistence. Extension of this to include cells within agarose revealed that these cells exhibited less directed migration, but their velocity was unaffected. I showed that cells lacking myosin II failed to complete development within an agarose gel and had significantly reduced velocity and directional migration when compared to their parent strain. Furthermore, the velocities of cells migrating within agarose gel were bimodally distributed, potentially indicating two distinct cell populations, fast and slow, and fast movement was shown to be largely myosin II dependent. Great potential therefore exists for cell-substrate and cell-matrix interactions to affect the migration character of cells, even those, such as *Dictyostelium*, which do not form strong focal adhesions. Moreover a properly ordered cytoskeleton is implicated in enabling cells to effectively utilise different modes of cell motility.

Acknowledgements

The completion of a project is a journey of exploration, and fortunately it is not made alone. First I would like to thank my supervisors, Professors Adrian Harwood and Wolfgang Drexler and the members of both of their labs (and the members of the other labs in Third Floor East, BIOSI) for help, suggestions and support. I was welcomed kindly into both groups and greatly benefited from the opportunity to work with and take part in discussions with both cell and molecular biologists, and biomedical physicists and software engineers. Bernd Hofer and Alexandre Tumlinson deserve a special mention as without their software tools this work could not have been completed. I would also like to thank Boris Považay for design and manufacture of the OCT microscope. A number of people have contributed to ImageJ (NIH, USA) and its plugins, which I made use of. I am grateful to them for making their work freely available for use by others. Dictybase has been an extremely valuable resource and the efforts of members of the Dicty community to set it up and keep it running are most appreciated.

My friends and family were always there with love and support, and tea/coffee! John Donne said that no man is an island and without the peninsulas connecting me to others there is little doubt I would have been swept away. I have been extremely fortunate to know all of the people that I have met during this journey. Thank you.

Finally, I would like to thank the BBSRC for their funding for this PhD programme, without which I could not have undertaken the project.

Table of Contents

List of Tables and Figures

Chapter 1

Chapter 2

Chapter 3

Chapter 4

Chapter 5

Chapter 6

List of Abbreviations

2D→ two-dimensional

3D→ three-dimensional

4D→ four-dimensional

ABP→ actin binding protein

ACA→ adenylyl cyclase

ADF→ actin depolymerizing factor

AFM→ atomic force microscopy

Akt→ Ak thymoma

Arp2/3→ actin related protein 2/3

Ax2 & **Ax3**→ strains of *Dictyostelium* which can grow in axenic medium (i.e. independent of bacteria)

cAMP→ cyclic adenosine 3',5' monophosphate

cAR→ cAMP receptor

CARS→ coherent anti-Stokes

cdc42→ cell division control protein 42

cGMP→ cyclic guanosine 3',5' monophosphate

CRAC→ cytosolic regulator of adenylyl cyclase

CT→ computed tomography

DIC→ differential interference contrast

Dictyostelium→ *Dictyostelium discoideum*

DIF-1→ differentiation inducing factor

F-actin→ filamentous/fibrillar-actin

FRET→ Förster/fluorescence resonance energy transfer

GbpC→ cGMP binding protein

GC→ guanylyl cyclase

GCA→ guanylyl cyclase A

GFP→ green fluorescent protein

GTPase→ guanosine triphosphate-ase

IP_3→ inositol triphosphate

IQ motif→ isoleucine (commonly) and glutamine (always) calmodulin-binding motif

IQGAPs→ IQ motif containing GTPase activating protein

JH10→ an auxotrophic axenic strain of *Dictyostelium* requiring thymidine supplementation

MHC→ myosin heavy chain

mhcA-→ myosin II heavy chain null *Dictyostelium* mutant

MHCK→ myosin heavy chain kinase

MLC→ myosin regulatory light chain

MLCK→ myosin regulatory light chain kinase

MRI→ magnetic resonance imaging

NA→ numerical aperture

OCM→ optical coherence microscopy

OCT→ optical coherence tomography

PakA→ p21-activated kinase A

Par1/MARK→ partitioning defective/MAP or microtubule affinity regulating kinase

PET→ positron emission tomography

PH domain→ pleckstrin homology domain

PhdA→ pleckstrin homology domain A

PI3K→ phosphatidylinositol-3-kinase

PI5K→ phosphatidylinositol-5-kinase

PIP2→ phosphatidylinositol-4,5-biphosphate

PIP3→ phosphatidylinositol-3,4,5-triphosphate

PKA→ protein kinase A

PKB→ protein kinase B

PKBR1→ protein kinase B-related kinase

PLA2→ phospholipase A2

PLC→ phospholipase C

PP2a→ protein phosphatase 2A

PTEN→ phosphate and tensin homologue deleted on chromosome ten

Rac→ Ras-related C3 botulinum toxin substrate

Ras→ rat sarcoma (origin of gene isolation)

RasGEF→ Ras guanine nucleotide exchange factor

SadA→ substrate adhesion deficient A

SCAR→ suppressor of cAR

Sib→ similar to integrin beta

STED→ stimulated emission depletion

TIRF→ total internal reflection fluorescence

TM9/Phg1→ transmembrane segment 9/phagocytosis

TorC2→ target of rapamycin complex 2

UV→ ultraviolet

VCA domain→ verprolin-cofilin-acidic domain

WASP→ Wiskott-Aldrich syndrome protein

WAVE→ WASP family verprolin-homologous protein

WD-repeat→ tryptophan-aspartic acid repeat

Abstract

Chemotaxis and cell migration are important processes for life, involved in organism development and homeostasis and implicated in a number of disease states. *Dictyostelium discoideum*, an amoeba, is a useful model for investigation of chemotaxis and development, due to its ability to undergo chemotactic aggregation and development upon starvation. Although cell migration has been well described on planar transparent surfaces, it is uncertain how well these conditions replicate the natural environment of a cell. However, attempts to better replicate these environments generally make use of opaque substrates and 3D matrices, in which it is more challenging to image cell migration.

Protocols were developed to enable optical coherence tomography, a 3D structural imaging technique which requires no sample processing or staining, to be successfully employed in imaging *Dictyostelium* cell migration in time-lapse on non-transparent substrata and within an agarose gel. I compared the effects of two substrates, a nitrocellulose filter and a polystyrene Petri dish on aggregating cells and found differences in speed but not persistence. Extension of this to include cells within agarose revealed that these cells exhibited less directed migration, but their velocity was unaffected. I showed that cells lacking myosin II failed to complete development within an agarose gel and had significantly reduced velocity and directional migration when compared to their parent strain. Furthermore, the velocities of cells migrating within agarose gel were bimodally distributed, potentially indicating two distinct cell populations, fast and slow, and fast movement was shown to be largely myosin II dependent. Great potential therefore exists for cell-substrate and cell-matrix interactions to affect the migration character of cells, even those, such as *Dictyostelium*, which do not form strong focal adhesions. Moreover a properly ordered cytoskeleton is implicated in enabling cells to effectively utilise different modes of cell motility.

Chapter 1: Introduction

1.1 Why explore chemotaxis on non-transparent surfaces and in 4D (3D with time)

Tissues, formed during development, grow and are remodelled throughout life[40,56,172,201,461,517]. These processes, which are crucial for the creation of multicellular organisms and their continued existence, arise from the organization of cells by physical, mechanical and chemical cues[40,56,172,201,461,517]. One of the key ways in which cells are guided to their required location, for example during oocyte fertilization, gastrulation, immune response, inflammation and wound healing, is by chemotaxis, directed migration in response to a chemokine or chemoattractant[98,141,171,242,289,517,532,551,558,634]. Chemokines have also been implicated in apoptosis, the process of programmed cell death, which is critical for proper regulation of cell proliferation[163,671]. In addition to normal physiological roles, chemotaxis is also involved in disease states, ranging from arthritis and allergies to tumour metastasis in cancer[8,232,246,295,342,527,532,537,653,677]. Hence, due to this widespread involvement in diverse biological processes, understanding of the mechanisms of actions of chemokines and chemoattractants and the process of chemotaxis is of great interest to the scientific community[98,141,161,171,242,289,295,517,532,558,634,642].

A great deal of research has focused on unravelling the processes and mechanisms of eukaryotic chemotaxis[161,257]. However, the majority of these studies have relied on the use of cells, grown and experimented on in 2D monolayer cultures on planar surfaces of glass or plastic for ease of visualisation and good levels of cell viability, which is a very different environment from that which cells experience in nature[40,119,164,172,257,299,478]. This may result in oversimplified or incorrect models of cell migration[195,513,677]. For example, it has been shown that PI3Kγ is required for the migration of neutrophils on surfaces coated with fibrinogen, but is not required for their migration on glass[184]. Experimentation solely on glass surfaces may have led the authors to conclude that PI3Kγ (phosphatidylinositol-3-kinase) plays no role in cell migration. Cells have also been shown to preferentially adhere to certain materials, which can have effects on morphology and cytoskeletal organisation[94,433]. The effects of substrata on cell behaviour have been studied since the early 20th century, with recent advances in technology leading to much wider application of this research, for example investigation of the effects of biomaterials, as well as studies into cell behaviour within three-dimensional matrices[18,103,130,172,248,305,368].

1.1.1 The effects of the substratum on cells

The natural environment of mammalian cells is tissue, an intricate structure composed of both other cells and non-cellular material, such as collagen[118,164,478]. These structures expose the cell to a complex topography on both the macroscopic and microscopic scale[118,478,688]. The same can be said for *Dictyostelium*, where the natural environment is soil[55,299]. One might expect that, living in a complex environment, cells are able to detect and respond to these topological environmental cues as they also respond to chemical and photonic cues; and indeed, the first studies of the effect of surface morphology on cells led to the discovery of 'contact guidance'[106,118,152,660]. This is a process where, when placed on an etched surface, cells align themselves along the grooves, remaining in contact with both the upper and lower surfaces simultaneously[106,118] More recently, controlled studies with manufactured topographies of known size and shape have indicated that cells can detect and react to steps in a surface of between 50 nm and 100 nm depending on the cell type[107,118,491,678,688]. Atomic force microscopy images show that new tissue culture dishes, which are made with the plastic polystyrene, have nanometre-scale ridges, as do freshly-cleaned glass surfaces possibly as a result of the manufacturing process, and aspiration and pipetting of cells can lead to surface scratches on a larger scale[107,506,548]. Therefore, it can be seen that at all times, whether in the body, in the soil or in culture, cells are constantly being exposed to small or larger variations in topology, which can have significant effects on their behaviour, even when the temperature, chemical environment and amount and quality of light remains the same[118].

In addition to guiding cell migration, the topography of the environment has been shown to have a number of effects on cells, such as affecting gene expression, increasing proliferation, directing differentiation, modifying adhesion, increasing or decreasing motility and modulating cellular morphology[14,24,95,118,300,361,477,491,577]. In addition, charge, pH, surface chemistry and biomechanical properties of the environment, such as shear force, stretching, and elasticity can play a role, potentially through altering adhesion of the cell to the substratum[258,300,606,661,684]. However, even though these more complex environments can help to further unravel the mechanics of cell-substrate interactions and context-dependent cell behaviour, and can potentially approximate the natural cellular environment better than planar glass or plastic substrata, they still lack the third-dimension found in nature[18,184,237,329,433,461,477].

1.1.2 The effects of a three-dimensional environment on cells

Although, for convenience, cells are frequently cultured and studied on 2D transparent surfaces, as the cells have high levels of viability and are easy to visualise, it is widely recognised that 3D matrices offer a closer approximation to the natural environment[40,130,195,479,483,698]. Cells have been found to exhibit different phenotypes and genotypes when cultured in 3D as opposed to on 2D substrates[40,461,477]. There are many examples of this in a range of different cell types. Migratory fibroblasts grown in 2D have different morphology and adhesion foci patterns, than those cultured in 3D environments[116]. Breast cancer cells have been shown to differ from non-cancerous cells, by the manner in which they respond to a 3D environment[224]. Epithelial cells grown in 3D form more natural hollow tubular structures when grown in 3D as opposed to the flat monolayers formed when grown in 2D[699]. Hepatic cells show increased survival in 3D culture when compared to 2D[228]. Hepatic and epithelial cells retain their differentiation better in 3D[228,699]. Gene expression is also affected by growing cells in 3D, as has been shown in melanoma cells and in endothelial cells, possibly by epigenetic modulation of chromatin by the matrix[36,46,221,661]. Thus, it can be seen that the environment of a cell has great potential to affect its behaviour[482].

The rapidly emerging field of mechanobiology attempts to unravel the mystery of how cell behaviour is affected by environment by focusing on the forces a cell exerts on its environment, for example through focal adhesions[43,133,195,258,482]. The motility of cells in 2D has been shown to be affected by the both the adhesivity and the elastic properties of the substrate, and while this has been shown to also play a role in 3D cell migration within a matrix, research thus far has shown this to be a complex area and the features of this migration remain to be fully elicidated[248,258,482,513]. Cell projections differ within 3D matrices when compared to on 2D surfaces[195]. Cells have been shown to create multiple matrix protrusions and use them all to generate traction rather than having one and stabilising it, as on 2D substrata[195]. Focal adhesions, features of cell-substrate interactions in 2D cell migration, are not seen in cells in 3D matrices or on soft substrates[195,514]. In cells embedded in a 3D matrix, the proteins involved in formation of focal adhesions are found distributed throughout the cytoplasm, whereas in 2D migration they are found tightly localised to the cytoplasm[117,195]. Conversely, a recent study has suggested that these can form in 3D, but may often be masked by background fluorescence[324]

Nonetheless, while some of the differences in cell behaviour between 3D and 2D environments may in fact be attributable to differences in composition and therefore

physiochemical properties between the commonly used solid glass or plastic substrata and the deformable elastic 3D matrices, a study comparing 2D and 3D cell migration in fibrocarcinoma cells utilising the same material for both conditions, showed that it was the added dimensionality which resulted in the different features of cell migration between the two conditions, rather than differences in the composition of the matrix and substrata[195]. This indicates that, although physiochemical properties of a surface may certainly play a role in modulating cell behaviour, the addition of an extra dimension can also exert effects on cells independent of this. These effects may be mediated by the fact that the cell is in contact with matrix on both the dorsal and ventral sides, as fibroblasts in this configuration have been shown to change from the flattened morphology seen on 2D surfaces, to the more in vivo-like morphology[38,116].

Different modes of movement of tumour cells have been found to exist, owing to the use of 3D environments, and the mode of migration can additionally be controlled by the dimensionality of the environment[203,479,533,537,677,679]. Not only does this have important implications for understanding the process of tumour metastasis, but also in cell migration in general, as two distinct patterns of migration have also been shown in fibroblasts and switching between them seems to solely depend on the elasticity of their matrix[479]. While some modes of cell migration in 3D appear to rely on degradation of the matrix by matrix metalloproteinases, lymphocytes have been shown to migrate in 3D independent of this, and it is therefore likely that degradation of the matrix is a side effect of 3D migration, but not requirement, or that it is only important under certain conditions[680,698].

In general, migration depends on stiffness of the matrix, adhesion of the cells to the matrix and the ability of cells to degrade the matrix, particularly when the pore size is small[479,483,698]. Despite this, leucocytes move independently of integrins within a 3D matrix, illustrating that there are other modes of migration in 3D in which the role of cell adhesion may be less significant[43,248,332]. However, although there is general consensus that the above factors play a role in 3D cell migration, and that the effects and mechanisms appear to differ from those seen with 2D planar substrates, the complex mechanics of cell-matrix interactions within three-dimensional environments currently remain unelucidated[129,248,483,639,698].

1.2 Dictyostelium discoideum

Dictyostelium discoideum are eukaryotic social amoebae, which in the wild live in soil[55]. In the absence of a signal, *Dictyostelium* extends pseudopods at locations all around the cell, and cells move around randomly, often changing direction[197,230,295,478,583,646]. In this case, the cell has to enable and properly regulate cell motility machinery, in order for the cell to be mobile. This non-directional cell movement, called chemokinesis, can be increased, in intrinsically motile cells, or stimulated, in intrinsically non-motile cells, by a chemical factors[295,478]. In their natural environment they are chemotactic to pterins released by their food source, bacteria, a process mediated through G-protein-coupled receptors regulated by the GTPases Rac and cdc42[72,161,350,682]. Once food supply is exhausted, they enter a developmental program where the expression of many genes is rapidly altered. One of the results of these changes in gene expression is that the cells begin to secrete the chemoattractant cyclic adenosine 3', 5' monophosphate (cAMP) in a coordinated manner. Propagation of these waves of cAMP creates a gradient, which the cells orient with respect to and migrate up, a process known as chemotaxis[55,72,390,463]. The cells therefore migrate together and aggregate, forming multicellular structures comprising up to $2x10^5$ cells. They then begin to differentiate into different cell types with defined roles[55,134,676]. This process, which takes approximately 24 hours to complete, culminates in the formation of a fruiting body, consisting of a stalk which holds up a sorus (comprised of multiple spores), and subsequent sporulation, allowing the *Dictyostelium* to move to a new location and try to locate additional food (Figure 1.1)[13,55,72].

Figure 1.1: Life cycle of Dictyostelium discoideum

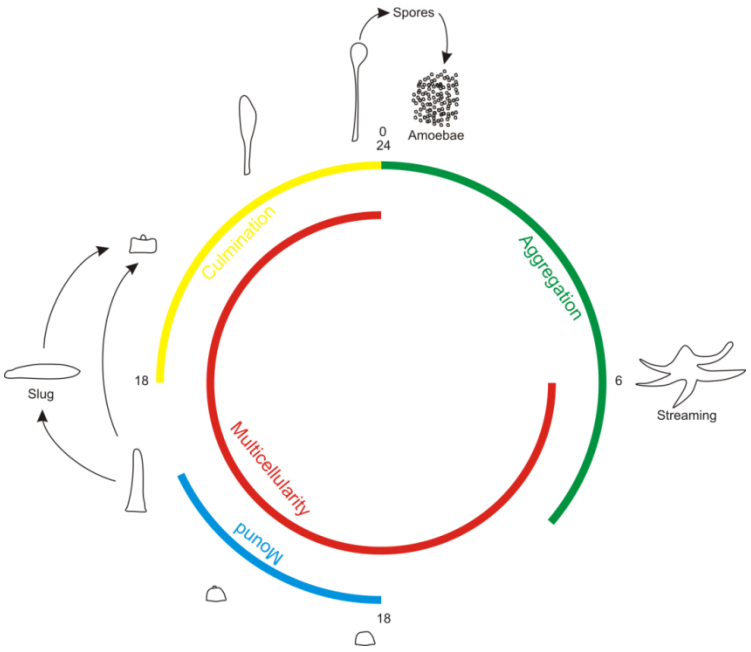

Figure 1.1: The developmental life cycle of *Dictyostelium discoideum*. Under starvation conditions, single cells aggregate to form multicellular aggregates, culminating in the formation of a fruiting body. The cells then sporulate allowing them to move to a new location and seek food. Adapted from a figure in Coates et al, Journal of Cell Science, 2001[109].

1.2.1 Dictyostelium discoideum as a model system

Current phylogenetic trees place *Dictyostelium* as having diverged from the metazoan branch after the split between plants and metazoa occurred[29,160,271]. As a eukaryote which is easy to culture and easily accessible to genetic manipulation and also capable of robust differentiation, chemotaxis, and development; *Dictyostelium* is a useful model system, possessing a cytoskeleton and number of cellular transduction mechanisms which bear many similarities to those of other eukaryotes including mammalian cells[160,466,544,599,704]. Therefore, *Dictyostelium* has been used as a model organism to study diverse biological processes including virulence, altruism, parasitology, lipid metabolism, bipolar disorder and autophagy [72,74,82,134,207,251,308,309,424,543]. Nonetheless, it is still best known and has been widely and rigorously studied as a model system for the investigation of chemotaxis[202,309,390,444,544,583,599].

1.3 Overview of chemotaxis in Dictyostelium discoideum

Chemotaxis is a key component of cell behaviour and is found in eukaryotes from single celled amoebae to humans[161,202]. Budding yeasts such as *Saccharomyces cerevisiae*, often used as models to investigate eukaryotic cell signalling, do not undergo chemotaxis[573]. However, *Dictyostelium* cells do, and are able to respond to even the smallest gradients of chemoattractant, down to a 2% difference between the front and rear of the cell[191,402]. As such, *Dictyostelium* has been extensively used in studies of chemotaxis, guided cell movement to a chemoattractant gradient, and the basic mechanisms and processes by which this occurs have been reasonably well described; although the exact mechanism remains to be fully elucidated, and competing models have been proposed[134,197,295,444,544,599,642].

The amoeboid movement of *Dictyostelium* towards the chemoattractant cAMP can be considered as composed of three phases, namely directional sensing, pseudopod extension and polarization[135,269,539,642,644]. Directional sensing is the ability of the cell to detect a chemoattractant spatial gradient, pseudopod extension is the creation and extension of pseudopodia by the cell, and polarization is the establishment of polarity in the cell, with the anterior end (the leading edge) having different properties to the posterior end. *Dictyostelium* cells are able to respond when the direction of the source of chemoattractant is moved[295,601]. If the gradient is strong, then the cell reorients by creating a new pseudopod towards the direction of chemoattractant and begins moving in this direction[295,601]. However, in a weak chemoattractant gradient, the cell will instead retain the same pseudopod and leading edge when the chemoattractant source is moved, and will make a 'U-turn' to reorient towards the chemoattractant[295]. This 'U-turn' behaviour is also seen in neutrophils[710].

1.4 Cell motility in Dictyostelium discoideum

While chemotaxis deals with directed cell migration in the presence of a chemoattractant gradient, many cells, including *Dictyostelium*, are motile, either intrinsically or in the presence of chemokines[18,43,410,541]. There are two common modes of migration exhibited by mammalian cells, that of 'mesenchymal' migration, and 'amoeboid' migration[43,537]. *Dictyostelium*, in common with leucocytes and neutrophils as well as some types of cancer cell, exhibits amoeboid migration, which is characterised by the extension of actin rich protrusions from the front of the cell, and the retraction of the rear of the cell mediated by myosin-driven contraction[279,295,537].

1.4.1 Actin driven cell motility

Cells move by the process of actin polymerization at the leading edge of the cell[275]. During cell migration, pseudopodia are extended at the leading edge of the cell, creating an anchor towards which the rest of the cell can move. Pseudopods are either generated by splitting of an existing pseudopod, or by formation of an entirely new pseudopod from a different part of the cell[12,646]. Pseudopod extension is governed by remodelling of the actin cytoskeleton, thought to be driven by small GTPases, through activation of the WASP and SCAR/WAVE protein complexes (members of the WASP, Wiskott-Aldrich syndrome protein, family) and the Arp2/3 (actin-related protein-2/3) seven-subunit complex[161,225,275,304,384,450,469,487,495,599,631,673]. The Arp2/3 complex is not intrinsically active and therefore relies on interaction with SCAR/WAVE to become activated[275,487,631]. The VCA domains of this regulatory complex are sufficient to promote actin polymerization, but as the SCAR/WAVE complex is intrinsically active, the other subunits are necessary for proper regulation of this process, mediated through signalling molecules such as small GTPases, phosophoinositides and dephosphorylation by protein kinases[275,316,420,486,631]. Clearly, actin polymerization at the leading edge must be balanced by depolymerization, in order to replenish the stores of actin monomers. This is thought to be mediated through ADF/cofilins (actin-depolymerizing factor) binding ADP bound actin filaments and promoting their depolymerisation, and enhancing actin remodelling into thick bundles by severing actin filaments[6,385,450,486,632]. Cofilin is inactivated by phosphorylation with protein kinases or by binding PIP2 (phosphatidylinositol-4,5-biphosphate)[266,317,536]. PIP2 is a phosphoinositide molecule implicated in directional sensing a chemoattractant gradient, offering a potential explanation for how actin polymerization is restricted to the leading edge of the cell during chemotaxis[317].

During chemotaxis, the Arp2/3 complex is translocated to the cytoskeleton, where it binds actin monomers to begin filament nucleation[272,275,336,486]. The complex has two actin-like motifs, which bind actin monomers and result in the formation of this new filament. In the presence of the actin polymerization inhibitor latrunculin, recruitment of the Arp2/3 complex to the membrane has been shown to be inhibited, suggesting that Arp2/3 is bound to actin filaments already present, rather than to a signalling complex[336]. The result is that the new filament is generated on the side of the pre-existing filament, causing a bifurcated structure[275,486]. Therefore, this actin polymerization directly under the membrane at the 'front' of the cell, leads to the formation of a network of branching filaments which results in the extension of pseudopodia[161,350,469]. The organisation of the network of the

(fibrillar/filamentous) F-actin filaments within these membrane-bound protrusions is responsible for the shape and form of the extensions formed[304,350,644]. Importantly, pseudopod extension does not occur at the back and sides of the cell so that resources are not wasted on formation of unnecessary extensions[642,646]. Pseudopod suppression on the back and side of the cell may also play a role in cell polarization, as one mechanism by which the cell defines its polarity[197,350,644]. The cell could also retain its polarity by positive feedback loops dependent on the actin cytoskeleton, as cells treated with actin polymerization inhibitors such as latrunculin A are able to alter their polarity more rapidly when there is a change in chemoattractant gradient direction[197,284,539,644].

Dictyostelium cells also extend other actin rich protrusions termed filopodia[587]. These have previously been postulated to have a sensory role in addition to involvement in cell motility[363,406,582]. This extension is not mediated through Arp2/3, but instead by processive multidomain proteins called Formins, which stimulate profilin mediated actin monomer addition to the barbed end of the actin filament, preventing capping, which results in the elongation of actin filaments[472,486,524,587]. Formins, which are intrinsically active are thought to be regulated by autoinhibition, mediated by small GTPases and have been postulated to have a role in blebbing-driven cell motility[173,229,524,561].

1.4.2 Blebbing driven cell motility

Blebs are extensions of the cell membrane, which occur as a result of increased hydrostatic pressure within the cell[335,693]. They form as a result of the extrusion of hemispherical protrusions at points of weakness between the cell cortex and membrane which either ruptures the actin cortex or causes the membrane to detach from the cell cortex[92,335,693]. Thus they are devoid of cortical components, until expansion of the membrane and cytosol slows and cytoskeletal remodelling begins[92,335,693]. Blebs have been seen to occur in *Dictyostelium* cells exposed to a high uniform concentration of cAMP, which led the authors to postulate a role for blebbing in chemotaxis[335]. Since then, blebbing has been shown to play a role in cell migration and to be found at the leading edges of migrating cells[47,693]. Although the molecular mechanisms behind this process are currently unknown, calcium influx occurs prior to blebbing, and Rho GTPase signalling has also been implicated, as RacB Dictyostelium mutants show increased blebbing[173,346]. SCAR/WAVE may also be involved as it has been shown that SCAR null cells move largely by blebbing[631]. Accumulation of ezrin at the rear of

the cell may play a role in defining the direction of bleb-driven cell motility[377]. Additionally myosin is known to be critical for blebbing to occur, as cells lacking myosin, either through mutation or pharmacological treatments such as blebbistatin, are unable to move by blebbing[47,568,693]. This may be because they are unable to retract the bleb, the final stage in blebbing cell motility[92,173].

Tumour cells and white blood cells have been shown to use blebbing to migrate within 3D environments, and it is postulated that blebbing may play a role in cell migration in 3D matrices, by aiding cells to squeeze through small pores in matrices[92,204,377,520,586]. It has been suggested that cells may move through a combination of blebbing and pseudopod extension, switching between the two dependent on circumstances, and this type of cell motility could play a role in tumour cells metastasis and inflammation in vivo[92,204,586].

1.5 Myosin II in Dictyostelium discoideum

Myosin II is a conventional non-muscle myosin which has been shown to be involved in many processes ranging from cell division to cell motility[278,310,668]. Unlike mammalian systems where there are three isoforms, *Dictyostelium* has a single myosin II which is comprised of two heavy chains, two essential light chains and two regulatory light chains[60,73,99]. It is found distributed throughout the cytoplasm of the cell and is translocated to the cell cortex on stimulation with cAMP, where it is thought to play a role in strengthening the actin cytoskeleton[39,209,438]. This idea is supported by the fact that a constitutively unphosphorylated myosin II mutant overassembles cortical myosin II and has increased cortical tension[158,378]. It also has roles in maintenance of a single frontal pseudopod, as it is transiently found in retracting pseudopods, and is crucial in proper retraction of the rear of the cell, a necessary step for the cell to move forwards[39,209,255,279,328,350,428,438,668]. In addition to a role in cell motility, it is involved in formation of the cleavage furrow during cytokinesis, although *Dictyostelium* myosin II null cells are still able to divide on a solid substratum through a myosin II independent mechanism[60,278,310].

1.5.1 Regulation of myosin II in Dictyostelium discoideum

Despite its similar roles within the cell, myosin II appears to be differentially regulated in *Dictyostelium* and mammalian cells[89]. For proper full function, myosin II must be assembled

into long contractile bipolar filaments (ATPase function alone is insufficient). This filament formation, from a soluble pool of myosin II is regulated by the phosphorylation state of the myosin heavy chain (MHC) at three threonines present on the tail of this molecule, with dephosphorylation promoting filament formation[60,115,255,509,593,628]. This is supported by the fact that mutants which express a constitutively unphosphorylatable form of the myosin heavy chain, achieved by conversion of the threonines to alanines (3XALA), overassemble myosin II in the cortex[157,255,593]. Recruitment of myosin II to the cytoskeleton of the cell, on stimulation with cAMP requires phosphorylated MHC, and cGMP (cyclic guanosine, 3',5' monophosphate) may also play a role[58,197,582]. This recruitment is additionally thought to be actin-mediated, as fluorescence labelling imaging experiments revealed that cells treated with the actin polymerization inhibitor latrunculin A, did not localise myosin filaments to the cortex, although the filaments were continuously formed[356]. Furthermore cells with deletion of the myosin head domain, which is known to interact with actin filaments, showed the same defect[356].

MHC phosphorylation is regulated by the protein kinases, MHCK A-C (myosin heavy chain kinase), which are all thought to act by the same mechanism, phosphorylation of the threonines on the tail of the MHC, as 3XALA mutants do not disassemble myosin filaments on overexpression of any of these MHCKs[197,696]. There is also an MHCKD, with similar sequence homology, but its role, if any, is as of yet unclear[696]. MHCKs A-C are all differentially localised within the cell and therefore may perform different regulatory functions[696]. MHCKA undergoes autophosphorylation, interacts with and is activated by F-actin, and may play a role in supressing formation of myosin filaments at the leading edge during pseudopod formation and in regulation of actin by cross-linking of filaments[115,156,531,588]. MHCKC, myosin II dependent and localised to the rear of the cell where it may act to depolymerise myosin at the uropod, may also undergo autophosphorylation, due to similarities in sequence[60,115,439]. Both MHCKA and MHCKC require their WD (tryptophan-aspartic acid)-repeat section for targeting and subsequent phosphorylation of MHC[628]. However, MHCKB, has been shown to have an additional independent mechanism for targeting MHC, indicating that it may be regulated independently of the other MHCKs, and could therefore be involved in maintaining a basal level of MHC phosphorylation[60,519,628]. Upstream regulation of these kinases is currently not fully established, however, cGMP may play a role[57,58,350]. Furthermore, it has been suggested that PakA (p21-activated kinase) is required for the activation of myosin II, although this may be mediated through alteration of the F-actin cytoskeleton, rather than through one of the MHCKs[60,350].

MHC dephosphorylation is mediated by a PP2A (protein phosphatase 2A) cytosolic holoenzyme[435,509,653,696]. This process may occur continuously in an unregulated manner as PP2A activity has not been shown to change on cAMP stimulation of cells[60,347]. However, a Ras signalling complex including PP2A has been shown to be involved in regulation of F-actin at the leading edge of a chemotaxing cell, indicating a potential role for PP2A to be regulated by cAMP stimulation[91]. Furthermore, a recent study showed a role for *Dictyostelium* huntingtin in assembly of myosin II filaments and regulation of the phosphorylation state of myosin II through PP2A, indicating that this protein may play a role in controlling PP2A mediated MHC dephosphorylation[653]. Additionally, Par-1/MARK (Partitioning defective-1, MAP/Microtubule Affinity Regulating Kinase), a serine-threonine kinase involved in cell polarity, from a family of small GTPases has been shown to control myosin phosphatase in *Drosophila*, although there is no current evidence of a role for this kinase in *Dictyostelium*[409,457].

The motor activity of myosin II plays a role in cytokinesis, completion of development and proper localisation and disassembly of myosin filaments[97]. It is regulated by the phosphorylation state of the regulatory light chain (RLC) at a serine residue[233,702]. This phosphorylation is enhanced by cAMP stimulation, resulting in increased actin-activated ATPase activity and motor function[209,702]. Although this phosphorylation is not required for myosin II function, as the phenotype of cells lacking the RLC can be rescued by constitutively unphosphorylated alanine replacing the serine, it is required for the appropriate response to a temporal cAMP gradient, cellular depolarization and proper pseudopodial regulation in basic cell motility[454,702]. cGMP is an important regulator of MLC (myosin regulatory light chain), through enhancing the activity of an autophosphorylated myosin light chain kinase, MLCKA (myosin regulatory light chain kinase A) [197,575,605]. This is potentially mediated through the activity of GbpC (cGMP binding protein), as cells lacking GbpC show similarly reduced RLC phosphorylation to cells lacking cGMP[57,58].

1.6 Directional sensing in Dictyostelium discoideum

Although *Dictyostelium* cells are intrinsically motile, in the presence of a chemoattractant gradient they migrate persistently up the gradient towards the source[55]. The method by which they detect this gradient is known as directional sensing. Directional sensing in *Dictyostelium* is a complex process, which is not yet fully understood.

1.6.1 cAMP binding and signal propagation

The process of directional sensing is initiated by binding of a molecule of cAMP to a cAMP receptor on the cell surface membrane[140]. *Dictyostelium* has four different G-protein coupled cAMP receptors (cARs), each of which are expressed at different points in development[140]. The first receptor to be expressed is the cAR1 receptor[140]. Its expression levels rise after initiation of starvation, peaking at around 4 hours[542]. It is the receptor thought to be primarily responsible for aggregation, as cAR1 null cells are unable to aggregate, although as they have been shown to respond to high levels of cAMP[140]. This is thought to occur through cAR3 as a mutant lacking both of these receptors has been shown to be unable to respond to cAMP[276,580]. Furthermore, both cAR1 and cAR 3 have been shown to activate the same G-protein subunit, Gα2, although the folate receptor is Gα2 independent and possibly activates Gα4[239,276]. This signal cascade is eventually thought to result in the release of Ca^{2+} from intracellular stores, possibly through the second messenger IP_3 (inositol triphosphate), created by PLC mediated hydrolysis of PIP2 (phosphatidylinositol-4,5-biphosphate), binding IP_3 receptors (iplA in *Dictyostelium*, by sequence homology)[382,489,545]. This release of calcium ions can ultimately affect motility and differentiation of *Dictyostelium* cells, potentially via PLC (phospholipase C), tyrosine phosphatases, calmodulin, IQGAPS (scaffolding proteins involved in cytoskeletal regulation) and membrane-associated G-proteins[16,350,489,545,562].

On stimulation with cAMP, *Dictyostelium* cells propagate the signal by release of additional cAMP[323,570]. The relay of this extracellular cAMP signal occurs in a wave-like manner, with periods of approximately 6 minutes between releases[121,140]. This periodicity is caused by the receptor becoming insensitive to cAMP for a period of 30-120 seconds after binding a molecule by C-terminal phosphorylation[121,140]. The pattern of response to cAMP changes dependent on the developmental stage, and this is thought to be due to changes in the activation profiles of downstream effectors of cAMP signalling, resulting in reduced sensitivity to cAMP[121]. The process of relaying the signal is mediated by ACA (adenylyl cyclase) localising to the uropod (rear of the cell) and synthesising cAMP[28,323,570]. Activation of ACA is thought to be dependent on PI3K (phosphatidylinositol 3-kinase) activation of CRAC (cytosolic regulator of adenylyl cyclase), which has been shown to localise to the front of chemotaxing cells, and Pianissimo (Pia), a subunit of TorC2 (target of rapamycin complex 2)[80,90,112,121]. Much of the intracellular cAMP is released extracellularly, but some is retained within the cell and activates protein kinase A (PKA) and its downstream effectors, resulting in changes in gene expression which cause cell development[28,392]

Interestingly, cAMP receptor expression and signalling has been shown to require the actin cross-linking proteins cortexillin I and II, and ACA translocation to the rear of the cell has been shown to be inhibited by an aberrantly organised cytoskeleton, indicating the complex interplay of intracellular signalling in response to a chemoattractant requires a properly ordered cytoskeleton[323,569,570].

1.6.2 Sensing the gradient

Although directional sensing could be most easily explained by differential expression of cAMP receptors between the front and rear of chemotaxing cells, this is not the case, as these are always found to be uniformly distributed[682]. Several competing models have been suggested to attempt to explain the cellular processes behind directional sensing in *Dictyostelium*[269,415,430,465]. Of these, one of the most well-known is that of local excitation-global inhibition (LEGI), and several models built on this basic principle have been proposed[354,358,465,599,682]. In this model, chemotaxis is regulated by two signals, a local fast response, which affects the front of the cell, promoting the formation and extension of pseudopodia, and a global inhibitory response, which affects the rest of the cell, suppressing pseudopod formation[354,358,465].

The LEGI model in its simplest form, i.e. that of receptor occupancy, with receptors closest to the chemoattractant having more chemoattractant bound than those at the rear, is unable to explain the extreme polarity seen in a chemotaxing cell which has an extremely well-defined front and back, with certain subcellular components bound to the membrane at the front and not at the rear of the cell[284,464,539]. If a simple amplification of the gradient of cAMP sensed by the cell were solely responsible for this polarization, then a more gradual cell polarization would be expected. Levine et al modified the model to also include a balanced inactivation in order to attempt to account for this discrepancy, by addition to the model of a membrane bound inactivator, activated by the global inhibitory pathway, which antagonises and is antagonised by the response mediated through the local excitation pathway[358]. However, this balanced-inactivation model is unable to account for the fact that chemotaxis is remarkably robust despite the presence of 'background noise' from conflicting signals, such as those generated from additional chemoattractant sources or from the random nature of biochemical pathways, as in this case it predicts inaccuracy of pseudopod generation[273,594].

Therefore, an alternative hypothesis is that, rather than chemoattractant signalling directly causing pseudopod formation, pseudopods are instead continuously formed by the cell, largely splitting off from existing pseudopodia, and the chemoattractant acts only to bias the direction of pseudopod formation[59,273,444,657]. In support of this, vegetative (unstimulated) *Dictyostelium* cells are motile and this motility is characterised by extension of pseudopodia, and cells in shallow gradients of chemoattractant do not generate new pseudopodia of different size or at a faster rate than unstimulated cells[12,18,59]. Furthermore, cells lacking the G-protein coupled receptor subunit Gβ, display no chemotactic response, but exhibit random motility of the same speed as wild-type cells, which indicates that pseudopod generation occurs independently of chemotaxis[474]. A computational model generated of this view of cell chemotaxis, characterised by biasing of pseudopodial dynamics, agrees well with experimental observations, further lending support for this idea[444].

It was originally thought that gradient sensing was mediated through coordination of PIP3 (phosphatidylinositol-3,4,5-triphosphate) by PI3K and PTEN (phosphatase and tensin homologue deleted on chromosome ten) as it was one of the first molecules discovered to be non-uniformly distributed in a chemotaxing cell[135,214,215,469,644]. PI3K catalyses a reaction that phosphorylates PIP2 and produces PIP3, and PTEN conversely converts PIP3 to PIP2[214,215,350,469,642]. In general, PI3K is found to be bound to the plasma membrane at the 'front' of a chemotaxing cell, and PTEN to the 'rear'[214,215,599]. This pattern has been seen in *Dictyostelium*, neutrophils and fibroblasts and results in the accumulation of PIP3 at the front of the cell[252,464,560]. This localised expression of PIP3 at the leading edge of a chemotaxing cell, the direction of the chemoattractant source, recruits proteins, such as CRAC and PhdA (pleckstrin homology domain A) to the membrane at this leading edge and coincides with pseudopod formation[214,317,350,469,642,646].

PIP signalling cannot, however, be the only mechanism by which the cell maintains polarity or senses the chemoattractant gradient as it has been previously shown that when all five PI3K genes and PTEN were knocked out in a *Dictyostelium* cell, so that all of the currently known signalling pathways which are able to create a PIP3 gradient at the cell membrane of the cell were eliminated, the cells were able to chemotax effectively, although their speed was reduced[5,259]. As the speed of random movement was reduced more than the speed during chemotaxis, a role was postulated for PIP3 in cell motility, rather than chemotaxis, possibly in creation or maintenance of pseudopodia[12,96,259]. Subsequently, two independent studies discovered that a second lipid signalling pathway, PLA2 (Phospholipase A2), appeared to

mediate chemotaxis in PI3K null cells, likely through a PIP3 independent mechanism[5,96,643]. In another study it was observed that after 7 hours starvation, cells with both PI3K and PLA2 genetically deleted, or pharmacologically inhibited, chemotaxed well. [646]. A third PI3K/PLA2-independent chemotaxis pathway mediated by a soluble GC (guanylyl cyclase) (activated by cAMP) was postulated, active in polarized cells, in order to account for this[525,643,646]. This pathway is thought to be able to effect two separate signals[646]. The first is through the localisation of the protein product of this gene to the leading edge of a cell, where it can interact with the actin cytoskeleton, which occurs when the cell is within a gradient of cAMP[646]. This indicates a potential role for this protein in signalling at the front of a chemotaxing cell, or in splitting of pseudopods from existing pseudopodia. The second is through the cGMP product of the enzyme, which appears to play a role in pseudopod suppression at the back and sides of the cell, likely through induction of myosin filament formation by its target protein GbpC[12,60,259,637,646]. Of these two signalling pathways controlled by sGC, the first results in cells which chemotax but do not polarize, while the second yields cells which are polarized but do not chemotax[646]. This supports the hypothesis that the first pathway is involved in sensing of the chemoattractant gradient, and indicates that pseudopod suppression at the sides and rear of the cell is insufficient for directed cell migration, but is involved in cell polarization[646].

TorC2, a highly evolutionarily conserved serine-threonine protein kinase, has also been proposed as a strong candidate for involvement in gradient sensing[91,349,369,370]. It forms a complex with the scaffolding protein Sca1, RasGEF (Ras guanine nucleotide exchange factors), RasGEFH (Aimless) and PP2A, which translocates to the leading edge of cells exposed to a chemoattractant gradient where the RasGTPase is subsequently activated[91,540]. This TorC2 protein complex is tightly regulated by RasC activation which has been shown to occur downstream of G-protein activation as cells lacking G-proteins show abnormal Ras mediated signalling[91,274,349,540]. The complex is involved in the regulation of the two *Dictyostelium* homologs of Akt/PKB, PKBa (protein kinase B alpha) and PKBR1 (protein kinase B-related kinase), which in turn negatively regulate association of the Ras complex to the membrane by phosphorylation[91,349,540]. As, *Dictyostelium* cells lacking RacC show impaired directional motility, this negative regulation is important for directional sensing[80]. Interestingly, myosin II null cells show similarly extended Ras activation, indicating that myosin plays a role in regulating this Ras-mediated signalling process[350]. The role of the PP2A protein in the TorC protein complex is currently unknown; however, as PP2A is also involved in dephosphorylation of the myosin

II heavy chain, involvement of the cytoskeleton in regulation of this process is potentially further indicated[435,509,653,696].

PKB and PKBR1 are activated downstream of both the PI3K and TorC2 pathways[292,293,370]. Signalling through these protein kinases is emerging as an important step in cAMP mediated chemotaxis[370]. PKB is thought to be localised to the membrane by binding of its PH domain (pleckstrin homology domain) by PIP3, a step required for its full activation, although it shows some residual activity independent of this[292,293]. PKBR1 has no PH domain and is constitutively membrane bound[292]. Although it is not known how these signalling events act to direct cell migration in chemotaxis, they may be mediated through downstream effectors of the PKBs. The PKB kinases have many phosphorylation substrates in *Dictyostelium*, including TalinB, a protein involved in cell adhesion, Ras GTPases, PakA (p21-activated kinase A) which is involved in myosin II filament assembly, and a PI5K (phosphatidylinositol-5-kinase), some or all of which may be involved in the regulation of *Dictyostelium* chemotaxis[105,448,599,622]

To summarise, four pathways have been proposed to be involved in the regulation of chemotaxis in *Dictyostelium*. Due to the intricate nature of cell signalling and requirement for proper regulation of complex processes, involving different parts of the cell acting in concert, these pathways cannot truly considered to be independent and are likely controlled and triggered by common signalling molecules, and involve a great deal of crosstalk and cross-regulation between pathways[5,539,646,651].

1) PI3K and PTEN mediated phospholipid signalling (PIP3 and PIP2), with PI3K activated by Ras GTPases[96,215,259,464,643,646].
2) A PLA2 mediated parallel pathway[259,643,646].
3) Soluble GC signalling, involved in regulating the front and rear of a cell[58,60,646,651].
4) Activation of TorC2 by Ras GTPases, a signalling pathway which shares regulatory proteins with the PI3K/PTEN pathway and could regulate and be regulated by this pathway via feedback and feedforward loops[91,369,370,651].

1.7 Optical Coherence Tomography

Much of the information currently known about the molecular mechanisms and signalling pathways involved in cell migration and chemotaxis comes from imaging studies[165,231,295,611]. Many types of microscopy have been used to image cells and, depending on the intended

application, each has its strengths and limitations[142,432,461]. Optical Coherence Tomography (OCT), pioneered in 1991, is now a well-established imaging technique for acquiring images of the eye, particularly retina[147,180,265,353,535]. The first images of in vivo tissue were acquired in 1993[181,600]. In terms of resolution and depth penetration, OCT lies somewhere between confocal fluorescence microscopy and ultrasound, with a deeper penetration and axial range than confocal fluorescence microscopy and a higher resolution than ultrasound imaging[208]. The performance of the technologies obviously varies between instruments and is constantly being improved and developed, however, in the original publication in 1991, the retinal images produced had an axial resolution of ~15 μm, approximately 10 times the resolving power of ultrasound, and a depth-penetration of ~2 mm, which was, at the time, approximately 6 times the penetration of confocal microscopy[265]. More recently, technological developments have led to increases in resolution of up to 1 μm axially with state-of-the art light sources and 1-2 μm transversally with high NA objectives[148]. New instruments and detection techniques have led to the potential for data acquisition rates of up to 5 million samples per second, increasing to 20 million samples per second when 4 beams are used (multi-spot imaging)[10,499,672]. Consequently, in recent years the technique has expanded into other areas, for example, skin imaging, aiding in cancer diagnosis, cardiac imaging, endomicroscopy and developmental biology[4,7,101,110,208,243,353,559,602,609]. Modified forms of OCT allow attainment of different kinds of information, for example Doppler OCT which allows acquisition of flow and structural information concurrently and therefore has applications in haemodynamics; and Polarization-sensitive OCT, which brings out contrast in certain structures, e.g. collagen, allowing them to be much more easily seen and identified than with conventional OCT[326,352]. New advances in technology leading to faster acquisition times and better resolutions have enabled cellular-level resolution volumetric images of tissue to be acquired with conventional OCT[56,315,499,620,687]. With increasing interest in growing, developing and exploring the behaviour of cells in 3D, OCT is emerging as a promising technique for use in the field of tissue engineering, as it enables label-free imaging of cells within three-dimensional scaffolds[56,208,353,461,504,513,606,687].

1.7.1 Principles of Optical Coherence Tomography

In Optical Coherence Tomography (OCT), low temporally coherent broadband light, usually from a laser or super luminescent diode is used in conjunction with a standard Michelson-Morley interferometer to generate structural images of tissues and other specimens based on

refractive index variations within the sample.[71,147,148,265]. The technique requires no staining or sample processing, therefore artefacts are reduced and cell viability is increased, particularly when imaging over long periods of time[56,148,208]. Samples can be probed to depths of between 1 mm and 2 mm, due to the wavelength of light used and the interferometric detection technique, which results in suppression of photons which have been multiply scattered[148,208].

The light source is raster scanned across the surface of the sample to be imaged and the magnitude and echo time delay of the backscattered light is measured at each sampling point[180,208]. This is achieved by splitting the illuminating light with a beam splitter so that some of the light is passed to the sample arm of the system and the rest is passed to the reference arm[180,208]. When the two beams are in phase (the path lengths of the light are the same), and the back reflected light from the sample is interfered with the light from the reference arm, constructive interference occurs between the beams and creates maximum signal[180,549]. This point is called the 'zero delay' point as there is no delay between the light from the sample and the light from the reference arms. If the beams are not exactly in phase, a reduced signal is created. This signal weakens the further the sample is from the zero delay point, until eventually no signal can be detected above the noise floor[180,265,549].

The size of the raster scan and number of sampling points can be set to an appropriate value for the type of sample being measured. At each sampling point, the light backscattered from each axial position in depth is collected and comprises a single A-scan[208]. By scanning the light source across the surface of the sample transversally, a B-scan, made up from a series of A-scans, is acquired. Finally a volume, comprising a series of B-scans, can be acquired by raster scanning the light[180,208,549].

As the light is scanned when it passes through the objective, in general OCT systems use scan lens objectives, which are designed to be telecentric[208,615]. Such lenses are usually more expensive and heavier than the more common entocentric lenses as they are usually more complex and contain more optical elements, however, they have a number of advantages[155]. These include eliminating magnification changes caused by object displacement from the lens objective (parallax) by ensuring that all the chief rays in the lens system are parallel to the optical axis of the system, and thereby reducing distortions in the image by creating a flat imaging plane[155,264,615]. A flat imaging plane is particularly important when a beam is scanned across a lens, as the image is formed from beams of light which go through the edges of the lens as well as beams which go through the centre. If an endocentric lens was used, the centre of the image would remain undistorted, however, the edges of the image would be subject to

more severe lens aberrations and, due to being viewed from a different angle to the centre, the shape of an object at the edge of the lens would appear distorted[155,253,264,427,615]. Furthermore, telecentric lenses also keep the magnification the image constant across the field of view, which is of particular importance when imaging a sample at different depths[155,253,264,427,615].

1.7.2 Theory of Optical Coherence Tomography

In OCT the spectral interferogram is generated by mathematical description of the incoming light, of wavelength λ, in terms of its wavenumber $k = \frac{2\pi}{\lambda}$ (the spatial frequency), its angular frequency $\omega = 2\pi\nu$ (the temporal frequency), the electric field amplitude as a function of the wavenumber and angular frequency, $s(k, \omega)$, and the wavefunction $e^{i(kz-\omega t)}$ where z= distance t= time and i= square root of negative 1[180,265,281]. Figure 1.2 illustrates this, showing the electric fields of the beam path of a simple OCT system using a Michelson interferometer.

$$Incident\ power = E_i = s(k, \omega)\, e^{i(kz-\omega t)} \quad \text{(i)}$$

The incident power E_i is divided into two beams at the beam splitter. Each of these beams has an electric field amplitude of $\frac{E_i}{\sqrt{2}}$, a reflection constant r, and wavefunction e^{i2k}. The z_R and z_S also seen in the power on the diagram (Figure 1.2) are the distances between the beamsplitter and the reference reflector and the beam splitter and the sample reflectivities respectively. Usually, the reference reflector is a perfect mirror, having an r_R (reference path reflection constant) as close to 1 as possible[281]. This is the ideal case as it simplifies the reflectivity function. The sample arm reflectivity function is significantly more complex, due to the multiple reflectivities from the sample, at different values of z_s. Therefore, the reflectivity profile is depth-dependent and, although it is in actuality a continuous function due to the fact that the sample always has a continuously varying refractive index, and can be complex encoding the phase in addition to the sample, it can be written as a series of N discrete real delta functions where reflectivity r_s is a function of sample depth z_s[180,182,265,281].

$$r_s(z_s) = \sum_{n=1}^{N} r_{Sn}\delta(z_S - z_{Sn}) \quad \text{(ii)}$$

The primary objective of the low coherence interferometry in OCT is to approximate the value of $r_s(z_s)$ as closely as possible, as this variable encodes all of the depth information

about the sample. As power reflectivity of each reflector is given by the modulus of the electric field reflectivity squared, the function we want to reconstruct can also be written as $\sqrt{R_S(z_S)}$, where R_S is the power reflectivity[281,549].

Figure 1.2: Beam path of a simple OCT system

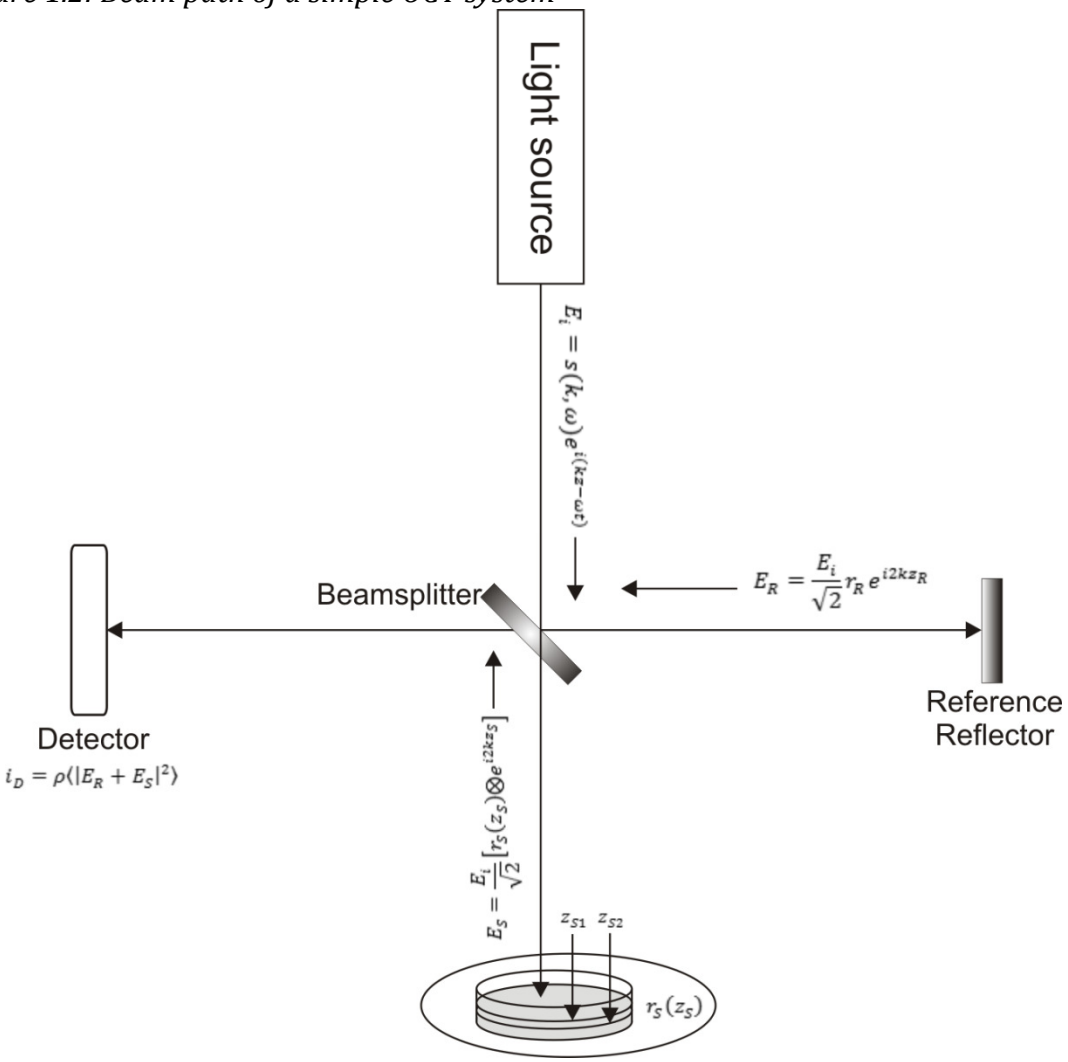

Figure 1.2: The beam path of a simple OCT system utilising a Michelson interferometer. The electric fields are shown on the diagram indicating that the information we wish to obtain to reconstruct a tomogram of the sample is $r_s(z_s)$, the depth dependent reflections in the sample, which will need to be extracted from the electric field returning from the sample, $E_s = \frac{E_i}{\sqrt{2}}\left[r_s(z_s) * e^{i2kz_s}\right]$. Figure adapted from a figure from Optical Coherence Tomography, Eds W. Drexler and J.G. Fujimoto[281].

In order to obtain this reflectivity profile, we assume discrete reflectors in the sample arm and perform the phase convolution $r_S(z_S) * e^{i2kz_S}$, essentially multiplying the wavefunction by each of the reflections in the sample and giving the resultant returning electric field $E_S = \frac{E_i}{2}\sum_{n=1}^{N} r_{Sn}\, e^{i2kz_{Sn}}$. In the case of biological tissues and samples, the reference reflectivity generally dominates the sample reflectivity, as the reflections from the sample are much weaker than those from the reference reflector, which is usually a mirror. The returning electric fields E_R and E_S pass though the beam splitter once more and are therefore halved in power (in the case of a 50/50 beam splitter). They then interfere at the detector where the detected photocurrent is proportional to the square modulus of the sum of the incident electric fields. This can be expressed by the multiplication of the complex conjugate by itself, where ρ is the response of the detector based on its quantum efficiency and the angled brackets represent time averaging performed by the detector, related to its exposure time, which usually can be manually set[180,281,549].

$$I_{D(k,\omega)} = \frac{\rho}{2}\langle |E_R + E_S|^2 \rangle = \frac{\rho}{2}\langle (E_R + E_S)(E_R + E_S)^* \rangle \ldots\ldots\ldots\ldots\ldots\ldots\ldots\ldots \text{(iii)}$$

Setting the spatial origin z=0 at the surface of the beamsplitter and inserting the expressions for E_R and E_S into the above equation gives an equation for the detector current. As the wavelengths at which OCT operate, typically between 800 nm and 1300 nm, oscillate faster than the response time of the detector; when the modulus function is expanded, the terms which are dependent on angular frequency, ω are eliminated, leaving only temporally invariant terms remaining. Simplification then results in the terms below[147,281,549].

The spectral interferogram consists of three main separate components,

A. The DC terms

$$I_{D(k)} = \frac{\rho}{4}[S(k)[R_R + R_{S1} + R_{S2} + \cdots]]$$

B. The cross-correlation terms

$$+\frac{\rho}{2}[S(k)\textstyle\sum_{n=1}^{N}\sqrt{R_R R_{Sn}}\,(\cos[2k(z_R - z_{Sn})])]$$

C. The auto-correlation terms

$$+\frac{\rho}{4}[S(k)\textstyle\sum_{n\neq m=1}^{N}\sqrt{R_{Sn} R_R}\,(\cos[2k(z_{Sn} - z_{Sm})]] \ldots\ldots\ldots\ldots\ldots\ldots\ldots\ldots \text{(iv)}$$

A. This term is made up of a constant current offset proportional to the reflectivity of the reference mirror added to the sum of the reflectivities in the sample. It is independent of the path length of either the reference or the sample arm[281,549].

B. A cross-correlation component that describes the position of the sample reflectivities with respect to the path length of the reference mirror, which is known $(z_R - z_{Sn})$. This is the component which is of interest for OCT imaging. It is often dominated by the DC term as the cross-correlation terms are proportional to the square root of the sample reflectivities, however this method of detection is still considered superior to direct detection due to the increased gain[281,549].

C. The autocorrelation terms describe the interference between different reflectors within the sample, $(z_{Sn} - z_{Sm})$ and create artefacts within the image, which can be reduced by correct selection of the reference reflectivity rendering this term significantly smaller than the other terms[25,123,281,549].

If the spectral interferogram $I_{D(k)}$ is plotted for a single sample reflector (R_{S1}) $\frac{[R_R+R_{S1}]}{2}$ against wavenumber (k), an impression of the type of results seen with OCT can be gained[147]. The oscillations in this wavenumber spectrum reveal the position of the reflecting surface, defined by the cross-correlation terms which are present on top of the DC term. How easily the spectral fringes are seen, i.e. the amplitude of the spectral modulations is dependent on the reflectivity of that particular reflection within the sample. In the case of multiple sample reflectivities, as is usually the case with a biological sample, a superposition of multiple cosinusoidal waves is seen, each with different frequencies (positions on the spectral interferogram) and amplitudes, depending on the position and reflectivity of that reflection. Auto-correlation components also appear, but these usually have a frequency higher than the cross-correlation terms due to the fact that the reflectors in the sample $(z_{Sn} - z_{Sm})$ generally have a much smaller distance between them than the distance between the sample and the reference retro-reflector $(z_R - z_{Sn})$[180,281,549].

1.7.3 Resolution of Optical Coherence Tomography

In OCT, axial resolution is entirely decoupled from lateral resolution and is dependent on the bandwidth of the light source rather than, as in conventional microscopy, the NA (numerical aperture) of the objective[147,549].

Lateral resolution, as in other forms of microscopy, is related to the NA of the objective and is the diffraction limited spot size on the sample, which is determined by the optics in the system that focus the light on to the sample. The equation governing this resolution is given below

$$\Delta x = \frac{4\lambda_0}{\pi} \cdot \frac{f_{obj}}{d} \quad \text{.....(v)}$$

where λ_0 is the central wavelength of the light source, f_{obj} is the focal length of the objective lens and d is the diameter of the spot on the backplane of the objective lens[208,253]. The depth which can be penetrated into the sample is also related to the lateral resolution, so there is a trade-off between lateral resolution and depth into the sample which can be probed[208,281].

The equation linking axial resolution (δz) to the coherence length (l_c) of the light source has been defined as

$$\delta z = l_c = \frac{2\ln(2)}{\pi} \cdot \frac{\lambda_0^2}{\Delta\lambda} \quad \text{.....(vi)}$$

where $\Delta\lambda$ is the Gaussian shaped spectral bandwidth of the light source[147,208,281].

1.7.4 Frequency domain Optical Coherence Tomography

The original incarnation of OCT, time domain OCT (TD-OCT), requires the reference mirror to be scanned, in order to have a zero-delay at all points of the sample and therefore ensure that signal is acquired from the entire depth range of the sample[180,208,549]. This places a physical limitation on the speed at which volumes can be acquired due to the mechanical nature of the lateral and axial scanning aspects of the system, making three-dimensional imaging of in vivo tissues difficult and of moving objects impossible[182,208,549]. Frequency or spectral domain OCT (FD-OCT) was first described by Fercher et al in 1995[182]. As the depth information is encoded in frequency rather than time, the reference reflector is stationary and the acquisition process is speeded up considerably[182,549]. The principle is similar to time domain OCT in that the maximum signal from the interferometer is achieved when the path lengths of the reference and sample arm are equal. In this case, however, the entire spectrum is recorded at once on a detector array placed at the output of a spectrometer[50,549].

The recorded output on the spectrometer is an oscillating frequency spectrum encoding the detector current as a function of wavenumber (k), which is called a spectral interferogram[281].

This sample reflectivity profile and hence depth information is approximated from an inversely Fourier transforming the spectrally resolved interference fringes in the sample arm of the interferometer[281,549]. After inverse Fourier transform, the sample reflectivity profile is embedded in the cross-correlation terms as described above, however, it is surrounded by several other terms, which must be appropriately dealt with in order to reconstruct an accurate image[50,281].

Important considerations in FD-OCT when interpreting the data to reconstruct the image are that the distance both to and from the sample reflector and the beamsplitter is measured by the interferometer, doubling the apparent position of each sample reflection from the reference mirror[281,549]. Additionally, the apparent depth dependent sample reflectivities, ($\sqrt{|R_S(z_S)}$), are amplified by the reference reflectivity (a strong signal) and the zero position must be considered as the position of the reference reflector rather than the beamsplitter. Furthermore, each one of these is convolved with the point spread function (PSF)[281]. The axial PSF of an OCT system (employing an objective with relatively low NA) is dominated by the inverse Fourier transform of the spectral term $S(k)$ from equation (iv), known as the real space coherence function, ($\gamma(z)$), with the full width half maximum (FWHM) of this coherence function being equal to the coherence length of the light source l_c[71,281]. Each cross-correlation term in the inversely Fourier transformed spectral interferogram (the calculated spatial domain) is therefore broadened by the coherence length of the light source and the direct relationship between axial resolution of the system and the broad bandwidth of the illuminating light source can be seen[147,281]. More serious artefacts in the spectral interferogram are caused by the DC and auto-correlation terms[549]. The DC terms result in a large artificial signal being detected at the point where there is no difference between the sample and reference path lengths. As this is convolved by the PSF of the system, it is Gaussian shaped and the edges of its spectrum can drown out desired signals[281,549]. The easiest way to overcome this is to measure the background signal from the reference arm with the sample arm blocked and then subtract this amplitude value from each spectral interferogram acquired. The auto-correlation terms give rise to artefacts at and near to the zero delay position. As mentioned above they can usually be reduced by correct selection of reference reflectivity[281,553]. Finally, because the detected interferogram is real, the resultant inversely transformed signal contains two mirror images, one each side of the zero delay (the point of zero path length difference). These are complex conjugates of one another and so this is termed the complex conjugate artefact[261,262,281]. This artefact can either be overcome by simply

displaying only the positive or negative distances, which is acceptable when the images do not overlap, or can be reduced or removed by signal processing at the same time as the Fourier transform is performed, by a number of different approaches[123,261,262,281,549].

As with other forms of optical microscopy, FD-OCT suffers from the problem of chromatic dispersion[50,179,261,262]. Introduced by the optics in the system, this is tolerable when dispersion is equal in both arms of the interferometer, however, it becomes a particular problem when the dispersion is mismatched and broad bandwidth light sources are used because when there is dispersion, each frequency in the spectrum experiences a slightly different phase velocity, resulting in the inversely Fourier transformed data being warped[183,253]. This manifests mainly in loss of sensitivity, and axial blurring and therefore loss of resolution in the OCT image. It usually arises due to the refractive index difference between the sample and reference arms introduced when a sample is placed in the sample arm[179]. It can be compensated for by achromatic lenses and mirrors, however at broad bandwidths it is not possible to completely eliminate and can be a major problem[179,208,365]. Various approaches have been taken to the problem, including compensation by introduction of defined phase shifts, and iterative computation of quadratic dispersion terms. It has also been shown to be possible to utilise dispersion mismatch to deal with the problem of the complex conjugate mentioned above[50,183,261,262,366,624].

As previously mentioned, the output from an FD-OCT system is recorded using a spectrometer. The speed of acquisition is partially controlled by the exposure time of the camera, which can be manually set. Higher exposure times result in the collection of more pixels and therefore a stronger signal (until saturation), however, they also increase the acquisition time of a tomogram. The best compromise between signal and acquisition time varies depending on the sample type and individual requirements of each experiment. In addition high power laser light sources are also commonly used in order to increase the signal to noise ratio (SNR). The spectral resolution of the spectrometer and the spacing of the pixels on the CCD array mean that there is a finite limit to the maximum spectral resolution physically achievable[147,281]. Due to a decrease in the visibility of the higher fringe frequencies, this results in a significant reduction in sensitivity with depth into the sample, as these fringe frequencies correspond to lower depths[262,281,624]. Therefore it is practical, when measuring, to locate samples as close to the zero delay as possible in order to maximise the signal from the sample's various reflection interfaces[50,624].

Finally, it is relevant to note that, while a 2D TD-OCT image (B-scan) can be reconstructed by alignment of A-Scans, FD-OCT data first requires Fourier transformation. Fourier transforms are an extremely processor-intensive task and therefore time taken between tomogram acquisition and viewing the final image is significantly increased. FD-OCT has greatly benefitted from rapid increases in the performance of central processing units, graphical processing units, RAM and the availability of multicore processors in standard desktop computers[362,367,655,703].

1.7.5 Light Sources for Optical Coherence Tomography

The light source is one of the most important components of an OCT system because, as touched on in the previous section, it is responsible for both the signal power, related to signal to noise ratio, for the penetration depth into the sample, and for the axial resolution of the system[147,208,281]. OCT requires a source with high intensity, Gaussian spectral shape and broad bandwidth[630]. Sources commonly used include femtosecond pulsed lasers, superluminescent diodes (SLDs), Amplified spontaneous emission light sources (ASEs) and incandescent white light sources (halogen lamps)[147,208]. Although white light lamps have extremely broad bandwidths, they do not have very high power density levels and therefore are not able to achieve as high brightness levels as focused sources. SLDs and ASEs also do not achieve as high power levels as lasers, nor as broad bandwidth levels, however they are usually cheaper and more reliable sources. Lasers are commonly used as the light source as they have a high power output which can be focused to a small point. One of the major properties of lasers, which is undesirable in OCT, is that of their long coherence length, a measure of how long a light source maintains an unbroken modulation without phase changes. As mentioned above, OCT relies on the phase of reference and sample beams being equal in order to create an image[147,208]. If the coherence length is longer than a single wavelength, as is the case with lasers, the two beams are completely in phase at multiple points and will therefore interfere at those points as well making the exact location of the reflective surface in the sample unknowable[208]. The longer the coherence length of the light source, the greater the number of the in phase positions resulting in rapid deterioration in the resolution of the system. In order to overcome this, lasers with extremely broad bandwidths are used, proportionately reducing the coherence length, the distance the unbroken wave travels, l_c as seen in equation (vii)[147,208]

$$l_c = \frac{c}{n\Delta\lambda} \quad \text{(vii)}$$

Where c is the speed of light in a vacuum, n is the refractive index of the medium through which it travels, and Δλ is the bandwidth of the light source[208].

One of the common ways of achieving a broad bandwidth high power laser is mode-locking[208]. Mode-locking involves generation of concentrated power ultrashort (usually femtosecond) optical pulses, which are obtained by selection of a desired frequency mode or a small number of modes which are then forced to oscillate in a phase related manner. When the phase difference between the modes approaches zero, pulses of femtosecond duration and high intensity can be generated[630]. There have been many methods for generating mode-locking in solid state lasers developed. The current most commonly used method is referred to as Kerr lens mode-locking, which relies on the self-focussing of Gaussian beams which occurs when strong nonlinear refraction occurs at high peak intensities[630]. This usually has to be initiated by a change in the laser cavity which is enough to remove the other longitudinal modes of the laser and allow mode-locking to occur[630]. Spectral shaping can be implemented, by both physical and signal processing methods, to compensate for the fact that the spectrum generated by a laser is not an exact Gaussian shape, as a non-Gaussian source spectrum results in side lobes in the point spread function, which causes a reduction in axial resolution and sensitivity in the OCT image generated[84,281,398,652].

Another important property of the light source in OCT is that of the central wavelength[147]. This is because the shorter the central wavelength, the higher the resolution of the system (as seen in equations v and vi)[7,170,630]. A further important consideration when imaging cells and tissues is the absorption of light by water (a major cell and tissue component). This is low for light in the visible range and near infrared range, below a peak which occurs at ~970 nm[241,500]. The most commonly used wavelength in OCT for imaging of tissue and other biological samples is ~800 nm, which lies within this range and has good availability of broad-bandwidth sources[146,208,500]. A second narrow bandwidth dip in the absorption spectrum of water of approximately 100 nm around 1000 nm wavelength is also seen[500]. This wavelength is considered to be of particular use for imaging the choroid and ocular vasculature[170,500,501]. OCT is also frequently performed using sources with central wavelength of 1300 nm, particularly when imaging the skin, because of the increased penetration into tissue seen at this longer wavelength due to decreased light scatter, at the cost of reduced resolution[7,630].

1.7.6 Noise in Optical Coherence Tomography

With OCT, as with other imaging techniques, it is desirable to obtain the highest SNR possible in order to obtain the images with the best appearance and resolution. There are many potential sources of noise in an OCT system, which can adversely affect the SNR. Some of these originate because the spectrometer detects light by use of a charge-coupled device (CCD) camera. This noise is contributed to by read out noise, dark noise, shot noise and relative intensity noise and can be reduced by diverting optimum light source power to the reference arm, careful choice of camera parameters, such as integration time, and use of post-processing filters after image acquisition[50,218,399]. As the image in OCT is reconstructed from modulations in the recorded spectrum, artefacts in OCT images are caused by any effects which also cause modulations in this spectrum[208,399]. Many of these effects are constant and so are present in any spectra acquired. This fixed pattern noise is usually eliminated by averaging of many images, or by blocking of the sample arm and recording a reference spectrum which is then subtracted from the final image. This last approach is sometimes used in combination with a low-pass filter, which assists in removing some of the stronger signals generated by fixed pattern noise[50,399].

In OCT images, one of the major noise issues seen in the final postprocessed images is that of speckle noise, reducing sample probing depth and SNR[218,408,550]. Resulting from the interference of mutually coherent wavelets of random phases and amplitudes generated by scattering within the sample, speckle in OCT is of slightly reduced contrast when compared to laser speckle, but is caused by the same factors[179,408,550]. One of the main ways suggested for speckle reduction in OCT is the taking of two separate images and averaging the results, or indeed averaging any two (or more) images where the laser speckle is uncorrelated[179,494]. This is not always practical, therefore many speckle suppression techniques have been proposed to combat the problem[179,399,550]. The main issue with removal of speckle is that speckle which is noise must be removed or reduced, while speckle which originates in the sample and therefore contains information about the sample structure should be retained. The most commonly used methods attempt to determine the probability that particular speckles are noise or genuine signal and to remove those classified as noise[399,408,550]. Wavelet filters are commonly used and give reasonable results, although there is always some loss of signal where noise frequencies and signal frequencies overlap[179,399,408,550].

1.8 Comparison of Optical Coherence Tomography and other microscopic techniques used in cell biology

Many imaging systems currently available, particularly those involved in clinical imaging, are based on the interaction of electromagnetic radiation with biological tissue, through physical processes such as reflection, scattering, absorption and attenuation[175]. Although many of the available imaging technologies give only structural information, it is also possible in some cases to obtain functional information reflecting the physiological processes of the imaged structure[22,234,352,484]. Molecular imaging allows access to this functional information through labelling with biomarkers, which alter contrast in images through chemical interaction with molecular processes[175,556]. For example, in PET (positron emission tomography), a radiolabelled glucose analogue is injected, which is then taken up into tissues and concentrates in areas of high metabolic activity[175,556]. Fluorescence can also be used to provide molecular information. Fluorochromes can be introduced which have an affinity for a particular ligand. They bind this ligand and then provide an indirect readout of the location of this protein[452,458]. Additionally, introduction of a reporter gene encoding a fluorescent protein into a cell or organisms results in an indirect readout of the expression of this gene. This can be used to explore gene expression patterns and changes[452]. FRET (Förster/Fluorescence resonance energy transfer) can be used to detect and quantify interactions between labelled molecules[458]. Furthermore, it is possible to image with molecular resolution, through TIRF (total internal reflection fluorescence) microscopy, STED (stimulation emission depletion) microscopy and AFM (atomic force microscopy)[144,405,534]. Nonetheless, for tracking living cells in time-lapse, the major requirements of an imaging technique are that it has suitable spatial resolution and contrast to resolve single cells and that it be suitable for use in cells which are alive, and not cause disruption to cellular processes or cell death during the course of the experiment.

Differential Interference Contrast (DIC), also known as Nomarski Interference Contrast (NIC), and Phase contrast microscopy are commonly used to image cells on transparent backgrounds, particularly in time-lapse[611,669]. No sample manipulation is required because intrinsic optical properties of the imaged samples, usually cells or small organisms, are used to generate contrast[253]. As the illumination is not very powerful, there is also minimal risk of phototoxicity over long periods of acquisition. These imaging techniques cause a few artefacts to appear in images (discussed later) largely due to the methods by which contrast is generated. In addition, they are only capable of imaging relatively thin samples on transparent

surfaces and are not generally suitable for 3D imaging, although some 3D DIC microscopy techniques have been proposed[19,277,502,598].

Probably the current most widely used three-dimensional live cellular and sub-cellular imaging technique in the biological sciences is confocal fluorescence microscopy[473,552]. Two-photon-microscopy, a form of non-linear optical microscopy is also widely used particularly when a deeper sample penetration is required[256,473]. CARS (coherent anti-Stokes raman spectroscopy) microscopy, also a nonlinear microscopy technique, that enables molecular information about a sample at cellular resolution to be acquired, is gaining popularity[64,421,484]. Other techniques, for example ultrasound, magnetic resonance imaging (MRI) and computed tomography (CT) are useful for live imaging but lack the spatial resolution to resolve cellular structures[81,288,429]. Conversely, electron microscopy gives excellent subcellular resolutions, due to the much smaller wavelength of electrons than photons, but requires the samples to be heavily processed and is therefore not suitable for live imaging[193].

1.8.1 Phase Contrast and Differential Interference Contrast microscopy

The original and simplest form of microscopy is bright field microscopy. In this configuration, a sample is illuminated from below and a magnified image is viewed from the top[253,417]. Contrast is introduced by dense structures in the sample, which absorb the light, so the final image appears as a dark sample on a light background[417,434]. The sample is often seen with low contrast as the contrast in the image arises due to changes in the amplitude of the incoming light and as many biological structures are transparent, they do not cause many amplitude variations[253]. One way in which this has been overcome is to decrease the amplitude of transmitted light by the use of sample stains, e.g. haematoxylin and eosin (H and E). Unfortunately many of these stains require sample fixation prior to staining, which can introduce artefacts into the sample and importantly renders the technique unusable in live cell imaging[417].

Due to the low contrast seen in samples with this technique, in 1934, Fritz Zernike pioneered the use of changes in the phase of light passing through a sample to enhance contrast[77,434]. Transparent objects, for example cells, while they do not create many changes in the amplitude of incoming light, do alter the phase of this light. This is due to the refractive index of the sample differing from that of the surrounding medium and creating proportional

changes in the velocity of the light[417,434]. The human eye is not sensitive to phase variations in light, only to the energy of light reaching the retina, and therefore these objects appear almost invisible[253].

Zernike discovered that interference between a probe beam and a reference beam could be used to translate these phase changes into amplitude changes visible to the eye[434]. This was achieved by the introduction of two additional optical elements into the microscope design[417]. A phase ring is introduced into the rear focal plane of the objective. The phase plate is usually designed to adjust the phase by ¼λ, sometimes achieved by etching rings on the lens. It can also be coated to reduce the amplitude of light[77,434]. A condenser annulus, of the same diameter as the phase plate, is placed into the front focal aperture of the condenser, a conjugate plane to the back focal plane of the objective[434]. The light, emerging from this annulus as a divergent beam, is focused to infinity by the condenser. Some of the light passes through the sample and is scattered, diffracted and retarded in phase according to the refractive index of the sample, whereas other light does not and continues straight onward unchanged[417]. These are focused differently by the objective with the rays diffracted by the sample (probing beam) being focused on to the imaging plane while the light which does not pass through the sample (reference beam) forms a bright ring in the back focal plane of the objective, which is superimposed on the phase plate[77]. The phase plate therefore affects probing light while leaving most of the sample beam unaffected[417]. Because the surrounding and probing beams of light are spatially separated in the back focal plane of the objective, altering the phase of one does not affect the phase of the other. The phase (and usually also amplitude) of the probing beam is changed by the plate, resulting in amplitude changes seen in the image plane due to constructive or destructive interference (dependent on the phase changes introduced by the phase plate) between the probe and sample beams[77,434].

Phase contrast images suffer from a haloing artefact seen around the edges of specimens and from shading off, where a pattern of light and dark patches are seen in the specimen[434,690]. These have two causes, the phase ring affecting a small proportion of the diffracted light from the sample (sample beam) and some of the reference beam not passing through the phase plate. Phase contrast microscopy is also unsuitable for imaging thick structures as the multiple phase altering structures at different layers in the sample produce a confusing superimposed image[417,434,690].

DIC is an improvement on phase contrast microscopy as it does not suffer from the artefact of the bright halo which surrounds phase contrast microscopy images and therefore gives a

better idea of the 3D structure of the sample (albeit in two dimensions)[19,417]. Other artefacts are reduced as well due to the fact that the reference and signal beams have the same resolution. The resolution of the system is also slightly increased over phase microscopy, as in phase contrast microscopy a part of the objective is occupied by the phase ring reducing the effective NA of the objective. DIC works on a similar principle to phase contrast microscopy, but uses a different method to achieve contrast, namely polarization[277,434]. A polarized (at 45º) light source is split into two beams orthogonal to one another (by use of a Wollaston prism) and these are focused by the condenser to take different routes through the sample, less than a μm apart (usually approximately the resolution of the microscope)[434]. The difference in polarization means that they cannot interfere until they are recombined, using a second Wollaston prism[253]. As they have different optical path lengths, when they are recombined they interfere to produce an image with the phase differences in the sample observable as intensity and colour differences[19,277,434].

The image is generated due to the fact that the two rays generate two bright-field images which are slightly out of phase, caused by the fact that they have taken slightly differing paths through the sample[434]. These rays interfere, but because the illumination of the paths is slightly offset they interfere with rays that did not go through the same point but went through an adjacent point[417,434]. The changes in optical path length (phase) are converted to changes in amplitude, by interference. The interference pattern reflects the optical path length difference between the beams[19]. The apparent illumination of the object, i.e. whether it appears to go into or out of the sample plane, is dependent on the direction of the slope of the phase difference. Where it is positive, the object appears to go into the plane and where it is negative the object appears to come out of the plane[277,417,434].

DIC, like phase contrast microscopy, has the advantage of being able to be performed in unstained samples. However, it cannot be achieved with thick samples or pigmented cells[434]. Due to the properties of the Wollaston prism, parallel features to the apparent illumination direction cannot be observed until the sample is rotated, and orientation dependent artifacts are sometimes observed[417,434]. Unlike phase contrast microscopy, DIC is sensitive to polarization and birefringence effects and so artefacts can be caused by use of plastic tissue culture dishes when imaging. It is therefore also unsuitable for imaging samples which are polarizing[19,417].

1.8.2 Fluorescent confocal microscopy

Prior to imaging with a fluorescence microscope, fluorophores must be introduced into the sample to create contrast in the image. Many fluorophores are currently available to target many different cellular structures and molecules and at many different excitation and emission wavelengths allowing different molecules to be simultaneously visualised[473,697]. Originally immunofluorescence (labelling a secondary antibody with a fluorescent dye and coupling it to a primary antibody which has been raised to the molecule of interest) was used although due to localisation problems and interference with cellular functions it has largely been superseded by fluorescent tagging. A current commonly used fluorophore is green fluorescent protein (GFP), which is derived from a species of jellyfish *Aequorea victoria*[86,87,407,697]. Other fluorescent proteins have been developed in different colours to allow more than one molecule to be stained simultaneously and easily visualised[697]. These include yellow fluorescent protein (YFP) and red fluorescent protein (RFP), also derived from *Aequorea victoria*, which have different excitation and emission spectral characteristics to GFP, and synthetic fluorophores, which are of small size and readily chemically modifiable and available with a wide variety of emission spectra[407,635].

As mentioned above GFP can be used to label molecules of interest within a cell or organism[86,473]. GFP tagged molecules are made by tagging GFP DNA to the 5' or 3' end of the DNA of the gene of interest (the GFP is rarely also placed in the middle of the gene but this is more likely to interfere with function), to create a fusion protein[86,151,473]. The GFP thereby acts as a reporter for gene expression of this protein of interest, being driven by the same promoter and regulatory elements[85,87]. Upon exposure to light of appropriate wavelength to excite the GFP (usually UV light), fluorescence appears at the locations where the protein of interest is expressed[473]. Use of a reporter gene in time-lapse fluorescent microscopy can thereby allow visualisation of the temporal dynamics of the expression and localisation of the protein of interest[436,473]. GFP can also be tagged to a constitutively active promoter, in which case it is always transcribed and the cell or organism fluoresces independent of gene expression, or to a promoter which is inducible under certain circumstances, which allows fluorescence to be triggered when certain experimental conditions are met[268,345,473]. The activity of a particular promoter can also be assessed by quantification of the fluorescence intensity of a promoter tagged with GFP in comparison to a tagged promoter of known activity[334,473]. Using two (or more) different fluorescent proteins to tag different genes of interest, enables two (or more) proteins to be simultaneously labelled

and visualised in the same image, within the same cell or organism. This is of particular interest in enabling visualisation of the expression patterns of two proteins simultaneously, for example to determine if two potentially interacting proteins are localised within the same subcellular compartment of a cell[153,473].

The fluorescent microscope is a primarily 2D imaging technique and so is not useful for imaging structures at an imaging plane which lies at great depth into scattering samples or for imaging volumes[473]. Fluorescent molecules are detected by shining UV (ultraviolet) light onto the sample (this cannot be visible light as it does not contain enough energy to excite the fluorophores). A wavelength of light corresponding to the excitation wavelength of the fluorophores is used to excite a target fluorescent molecule. The energy from the photons is absorbed by the fluorescent molecule and transferred to electronic excitation causing an electron to jump to a more excited state. The energy is party dissipated and then re-emitted as a photon of a different energy, namely the emission wavelength[473]. The entire process takes a fraction of a second[697]. An excitation filter is used to filter out certain wavelengths ensuring that the light is as monochromatic as possible close to the excitation wavelength of the light. Detection filters are also used to filter out light emitted of wavelengths other than the emission wavelength of the fluorophores[473]. Where more than one dye is used, the different channels can be detected by different photodetectors, allowing filters for the appropriate emission wavelengths to be placed in front of each one[697].

Fluorescence microscopy allows in vivo imaging of cells, however, a dye must first be introduced into the organ to be imaged[231,380]. Unfortunately, fluorescence microscopy suffers from the problem of photobleaching. Another problem is that the UV light does not only excite the fluorophores but excites other molecules in the sample[473,508]. These then emit some out of phase fluorescence which causes interference and results in a blurred image[473]. This can be overcome by the use of confocal fluorescence microscopy which limits the light source to a tightly focused laser beam of a single wavelength[508].

Fluorescence microscopy can also be phototoxic to living cells and organisms. UV light, commonly used to excite the fluorophores, has been shown to have detrimental effects on cells, resulting in the formation if free radical oxygen species and causing single nucleotide polymorphisms and changes to protein structure and function[471,473]. Furthermore, fluorophores can themselves be toxic when in an excited state both through production of radical oxygen species, and through affecting enzyme activity within the cell[102,138,473]. This is a

particular problem when viewing cells in time-lapse as cellular damage accumulates over time and can result in the death of the cell[138,473].

Confocal fluorescence microscopy uses many of the same principles as fluorescence microscopy. Light of the appropriate excitation wavelength passes through a beamsplitter and on to the sample. It then passes back through the beamsplitter, separating the emitted light from the sample fluorophores from the excitation light[508]. Light of the emission wavelength is passed to the detection arm where a pinhole is place in front of the detector. This excludes out of focus light, an important factor in improving image quality, and results in increased resolution over conventional fluorescence microscopy, although photobleaching can still be a problem[473,508]. Confocal microscopy, like conventional widefield microscopy, is limited in resolution by diffraction (determined by the diameter of the Airy disk) and can be approximated as the FWHM of the PDF[473]. The improvement in resolution seen with confocal microscopy is by a factor of $\sqrt{2}$ when the pinhole diameter is of less than the diameter of the Airy disk[9,473]. This is due to a reduction in the spread of the PSF, caused by the fact that due to the pinhole illumination and detection fluorescence is only detected where the PSF of the illumination and detection overlap, so the resultant PSF is the product of these two independent PSFs[473,508]. Interestingly, recent advances in technology have allowed the diffraction limit to be overcome by various methods[217,547]. These microscopic techniques are known collectively as super-resolution microscopy and enable visualisation of subdiffraction sized structures and intracellular motions in live cells[217,547].

Volumetric 3D confocal fluorescence microscopy images can be obtained by raster scanning a laser over the surface of the sample (x-y) and taking many images from a confocal microscope at different horizontal levels, by z-scanning the sample stage and stopping at set points to acquire a 2D image (x-z) for each sampling point in x-y. Images are taken at all required sampling points, each axial sampling point at a different focal plane, and amalgamated by a computer to make a 3D image[473,508]. The requirement for the physical movement of the sample stage is time consuming, resulting in increased acquisition time, particularly when imaging over a large depth volume with many sampling points[508]. Penetration depth is limited by absorption of incident photons all along the beam path and sample scattering of the excitation and emission photons. The pinhole detection results in a reduction in the number of detected photons and so a decrease in image contrast[473]. In order to overcome this, higher excitation powers can be used, but this increases the risk of photobleaching and phototoxicity to the cell[473].

These problems have been partially overcome, in recent years, by the use of a Nipkow scanning disk, a series of pinholes on a disk, two of which are spun in tandem during image acquisition, allowing for simultaneous acquisition from all of the pinholes (parallel acquisition) as opposed to scanning a laser across the surface of the sample (serial acquisition), and can therefore speed up imaging, as well as increase effective pixel dwell time so that a lower excitation intensity is required thereby reducing phototoxicity and photobleaching[159,697]. However, this technique does bring its own set of problems. These include slightly reduced axial resolution due to out of focus light reaching the detector from adjacent pinholes (pinhole crosstalk), and low contrast due partially to low light transmission through the Nipkow disk and partially to increased background from reflected light from the disk[159,473]. Although this technique significantly reduces the acquisition time by speeding up acquisition of the sample in the x-y plane, it should be noted that acquisition of a 3D image requires z-scanning of the sample stage[159,473].

Many time domain OCT systems use also confocal gating to improve resolution, involving the placement of a pinhole in front of the detector, reducing background noise by preventing some of the out-of-focus light from reaching the camera[208,549]. In fiber optic based FD-OCT, the sample arm of an OCT microscope can be considered as a scanning reflection confocal microscope, as the single mode fiber optic cable is a pinhole in both the illumination and detection paths of the microscope[208,281].

1.8.3 Two-photon microscopy

Two-photon microscopy is an improved alternative to confocal microscopy. Rapid focused infrared laser pulses, separated by at least one pulse to eliminate interference, are fired at the sample[159,529]. The use of infrared photons increases sample penetration and reduces photobleaching as the photons are lower energy[697]. Two coincident photons are required to cause nonlinear excitation of the fluorescent molecule tagged to the sample and result in the emission of a photon. In the case of multiphoton microscopy, three-photon excited fluorescence, second- and third-harmonic generation can also be used for excitation[473]. This technique does not require the pinhole used in confocal microscopy, as excitation occurs only at the focus of the excitation beam[473,529]. The advantages of two-photon microscopy are that phototoxicity is reduced and there is deeper tissue penetration. It can be performed in vivo and be used to penetrate the tissue to up to a depth of one millimetre. The use of an infrared

laser with a longer wavelength reduces the scattering of the beam as it passes through the sample making the image higher resolution[159,529]. A disadvantage is that the chance of two photons being simultaneously absorbed is very low so many exciting photons need to be put in to the system and a special microscope is required to withstand the intense laser pulses required to generate good image contrast. Image acquisition time is also quite long and therefore is a problem for tracking moving living structures[307,529].

1.8.4 Comparison Summary

In summary, while phase contrast, DIC, confocal and two-photon microscopy have vastly better resolution than OCT, for tracking whole cells such high resolutions are not required, and the ~5 μm lateral and ~4.5 μm (in air) axial resolutions of our OCT microscope are sufficient for this application. DIC and phase contrast are not suitable, in general, for acquisition of 3D datasets nor for imaging on opaque samples. Confocal and multiphoton microscopy can be used for 3D and 4D imaging, however, it is important to note that very high lateral resolutions are achievable only when a very high NA objective is used and this severely limits depth of field. In any case effective penetration depth with fluorescent confocal microscopy is limited to about 300 μm into scattering samples, due to the wavelength of the light required to excite the fluorophores, and dependent on the choice of objective (and its working distance)[473,529]. Two-photon microscopy is able to penetrate deeper, to about twice this, which can be a problem with thicker specimens[529]. These techniques are also able to achieve high axial resolutions, but again this comes at a cost, increased acquisition time and reduced depth acquired. Acquisition time is also reduced by the mechanical movement of z-scanning the sample stage in order to acquire 3D volumetric data. In fast moving cells such as *Dictyostelium*, this could result in blurring of the sample due to it moving while being imaged. Finally both confocal and two-photon microscopy require the use of endogenous fluorophores, which may interfere with the biological processes taking place within the cell[508]. OCT does not require cells to be stained or prepared in any way for visualisation and is completely non-invasive resulting in a very low chance of cellular damage. Furthermore, axial information is acquired by low-coherence interferometry so the sample stage is not moved during image acquisition. OCT can penetrate up to 2 mm into scattering tissue, dependent on the objective used[148,208].

1.9 Objectives of the project

The objectives of this thesis are to investigate the utility of Optical Coherence Tomography for probing cell chemotaxis under environments that are not readily accessible to commonly used conventional microscopy techniques, such as within 3D environments and on opaque 2D substrates, in time. Throughout the project existing experimental protocols were modified and new methods developed in order to facilitate this aim. The methods and protocols developed were then used to investigate the effects of different substrata on *Dictyostelium* cell motility in 2D with time; how *Dictyostelium* aggregates and chemotaxes within a 3D environment; and the chemotaxis of *Dictyostelium* cells lacking the gene encoding the myosin heavy chain, an important cytoskeletal component, within this 3D environment[209]. The approaches taken and results are discussed within the thesis, wherein I explore how *Dictyostelium* cell migration and behaviour differ between the commonly used experimental environments of on 2D plastic or glass transparent surfaces, and within a more natural and challenging 3D environment and what these differences may tell us about cell migration and chemotaxis.

Chapter 2: General Methods

2.1 Cell culture and experimental set-up

Ax2 cells were from lab stocks. JH10 (deposited by Jeffrey Hadwiger, Department of Microbiology and Molecular Genetics, Oklahoma State University, Oklahoma, USA) and myosin heavy chain null cells (mhcA-) (JH10 parent strain, deposited by Doug Robinson, John Hopkins University School of Medicine, Maryland, USA) were obtained from the dictyBase 'Dicty Stock Center'[1,185,238,530]. Cells were initially grown using standard methods on SM agar plates (10 g/L proteose peptone, 1 g/L yeast extract, 10 g/L glucose, 1.9 g/L KH_2PO_4, 1.3 g/L $K_2HPO_4.3H_2O$, 0.4 g/L $MgSO_4$, 17 g/L agar) on a bacterial lawn of *Klebsiella aerogenes*, then transferred, at least 24 hours prior to experimentation, and grown axenically in HL-5 growth media (ForMedium, UK) (14 g/L proteose peptone, 7 g/L yeast extract, 13.5 g/L glucose, 0.5 g/L Na_2HPO_4, 0.5 g/L KH_2PO_4, pH 6.4) on 10 cm diameter plastic Petri dishes and harvested at the log-growth phase, approximately $2x10^6$ cell/ml[186,670]. For the JH10 cells, the medium was supplemented with 200 μg/ml thymidine, as these cells are thymidine auxotrophs[393]. The mhcA- cells were grown in HL-5 medium supplemented with maltose instead of with glucose on advice from the Dicty Stock Center, following problems with cells becoming contaminated with yeast at the Center[565]. The recipe used was supplied by personal communication by Kerry Sheppard of dictyBase and is originally from Pierre Cosson's lab (Department of Cell Physiology and Metabolism- University of Geneva, Switzerland) (See Appendix 1 for recipe)[565].

For the 3D (2D+time) experiments, on the nitrocellulose filter, $1x10^7$ cells were taken, pelleted by centrifugation at 700 x g for 2 minutes and washed three times in KK2 buffer (16.5 mM KH_2PO_4, 3.8 mM K_2HPO_4, pH 6.2). They were then resuspended in 0.5 ml KK2 buffer and evenly dispersed over a 47mM diameter 0.45 μm pore nitrocellulose filter (Millipore, Merck KGaA, Germany), prewashed and pre-soaked in KK2 buffer and sitting on two saturated Millipore prefilters (Millipore, Merck KGaA, Germany). The same protocol was used to seed cells onto 1.8% non-nutrient agar, made with KK2 buffer, where an area of the same size as the nitrocellulose filters (47 mm diameter) was marked out and seeded with the cells. For the cells under buffer experiments, $3.24x10^7$ cells were taken and washed and pelleted as described above and resuspended in 3.2 ml KK2 buffer. The cell-buffer suspension was then transferred to a ~90 mm diameter plastic cell culture dish. In both cases, the cells were then left to develop for 6 hours and imaged for 4 hours at 30 second intervals.

For the 4D (3D+time) development experiments, a 1% agar (w/v) solution was made up, poured into a 10 cm diameter plastic cell culture dish (BD Biosciences, UK) and set at room

temperature. $1.9x10^7$ cells were taken, pelleted at 700 x g for 2 minutes and washed 3 times in KK2 buffer. They were then gently mixed with 3 ml of a 0.5% low gelling temperature agarose solution (w/v) (Sigma-Aldrich, UK), which had been equilibrated in a water bath to a temperature of approximately 25ºC. This was further mixed by pipetting to ensure even dispersal of the cells. The cell-agarose mixture was added to the top of the 1% agar (w/v) and immediately set at ~6ºC. Just prior to imaging, the dish was covered over with clingfilm to keep the sample from drying out. Ax2 cells were imaged 600 minutes (10 hours) after setting and JH10 and mhcA- cells were imaged 480 minutes (8 hours) after setting, at 2 minute intervals over 2 hours. Imaging was performed using a custom-built OCT microscopy system in a temperature controlled room kept at between 21 ºC and 22.5ºC, as *Dictyostelium* cells are sensitive to changes in temperature and chemotaxis will be affected by this[55]. Temperatures in excess of 27ºC risk cell death[222]. The lights were turned off for the duration of the imaging, as light has been shown to affect multicellular cell movement in *Dictyostelium*[55,423].

For the 4D (3D+time) chemotaxis experiments, $5x10^7$ cells were pelleted at 700 x g for 2 minutes and washed three times in KK2 buffer. These cells were made chemotactically competent by being resuspended in 10 ml KK2 buffer and subjected to 100nM cAMP pulses at intervals of 6 minutes for 5 hours[403]. At approximately 4 hours 30 minutes into pulsing, a 1 μm solution of cAMP agar was made up using 1% cell culture tested agar (w/v) (Sigma-Aldrich, UK), poured into 10 cm diameter Petri dishes and set at ~6ºC. This was equilibrated to room temperature after it was set. $1.9x10^7$ pulsed cells were taken and gently mixed with 3 ml of a 0.5% low gelling temperature agarose solution (w/v) (Sigma-Aldrich, UK), and set and imaged as described above for the 4D (3D+time) development experiments, after 30 minutes had elapsed, to allow for a cAMP gradient to establish through the agarose. Figure 2.1 shows photographs of the cells on a nitrocellulose filter and seeded within the 1% agarose gel. The cells give the agarose a coarse appearance when viewed by eye (Figure 2.1B).

Figure 2.1: Photographs of cells on a nitrocellulose membrane and cells within agarose

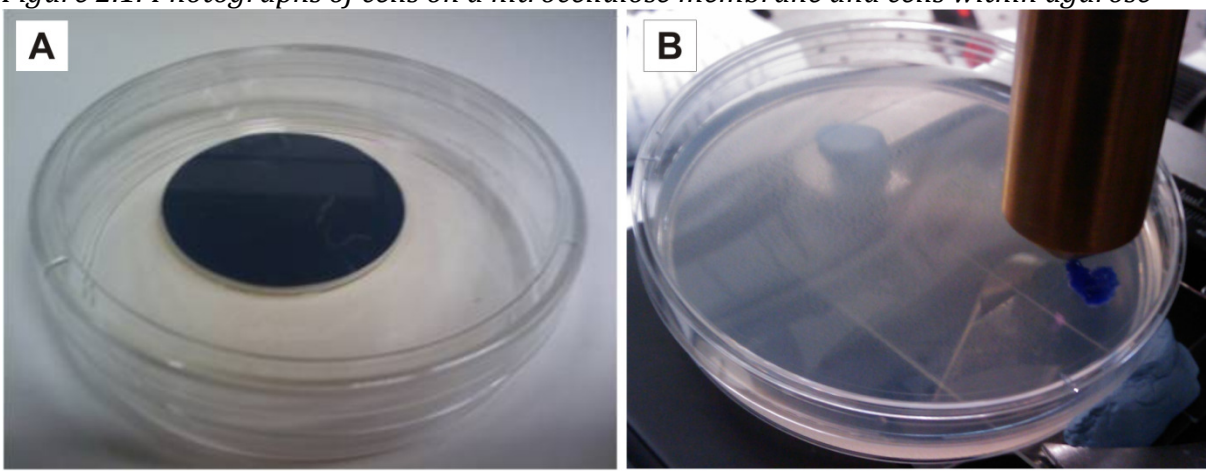

Figure 2.1: Photographs of (A) 107 cells on a 45 mm diameter 0.45 µm pore nitrocellulose filter (B) $1.9x10^7$ cells suspended in 0.5% agarose on a 1% agar base, for illustration of the experimental set up. The cells give the agarose a granular appearance to the naked eye.

2.2 Electron Microscopy

Samples were prepared for imaging by Dr Christopher Von Ruhland, Medical Microscopy Services, Central Biotechnology Services, Institute for Translation, Innovation, Methodology and Engagement, School of Medicine, Cardiff University[83]. The agar sample was dehydrated by use of increasing concentrations of ethanol with the sample placed for 3 hours in each concentration beginning with 50% and finishing with 3x3 hours in 100% ethanol. The ethanol was then removed by means of the critical point drying technique, using an Emitech K850 critical point dryer[11]. The HMDS (hexamethyldisiliazane) solvent evaporation technique was also trialled, but this caused excessive sample shrinkage (from 10x5 mm to 4x2 mm, compared to 10x5 mm to 7x3.5 mm with critical point drying)[17,65,67,440]. The samples were then attached to double-sided carbon tape and spin coated with gold in an EMscope chamber vacuum sputter coater. Imaging was subsequently performed by Dr Von Ruhland with a JEOL 840A scanning electron microscope using an accelerating voltage of ~5kV.

2.3 Optical Coherence Microscopy

The OCT system used was a frequency domain fiber-based OCT system utilising FiberCore SM750 single mode fibers with a cut off wavelength of 650 μm and a 90/10 beamsplitter (Ipitek Inc, USA). The light source was a Femtolasers Femtosource Integral OCT Titanium Sapphire laser (Femtolasers, GmbH, Austria) with a central wavelength of 820 nm and a bandwidth of between 130 and 150 nm. The power on the sample was kept between 1.1 and 1.5 mW, in order to minimise the chance of cellular damage[426,473]. The sample arm comprised galvanometric scanners built into a microscope with a Thorlabs LSM02-BB broadband telecentric scan lens (Thorlabs, Inc., USA) of 7.5 mm working distance and ~0.11NA and controlled by a Field Programmable Grid Array (FPGA) integrated with a CameraLink frame grabber. Some of the pilot data was taken using a telecentric objective which was custom-built and designed by Dr Boris Považay of the Biomedical Imaging group at OPTOM, Cardiff University with NA of ~0.1 and a working distance of approximately 15mm. A moveable stage with a gold-coated retro-reflector was built into the reference arm to allow adjustment of the reference delay. An attenuator in the reference arm allowed the signal to be manually adjusted to be kept close to but below the saturation level of the spectrometer, an ATMEL AViiVA M2 CL 2048 pixel CCD camera (ATMEL Corp, USA) operating at 20,000Hz. Polarization was manually adjusted to match between the reference and sample arms (by maximisation of fringe visibility) using paddles containing rolled fiber optic cable from both the reference and sample arms. Acquisition, real-time display, FPGA, galvanometers and data storage were controlled by software custom written by members of the Biomedical imaging group at OPTOM, Cardiff University, in LabVIEW (National Instruments, USA). The acquired images were saved on a striped RAID array (RAID0) to speed up saving time. The resolutions of the system were measured to be ~5 μm laterally and ~4.5μm axially in air and ~3.25 μm in agarose (approximately 4.5 μm/n when in a medium with a refractive index other than air, where n is refractive index)[253,654]. A simple schematic of the system is shown in Figure 2.2.

Figure 2.2: Schematic of the OCT microscope

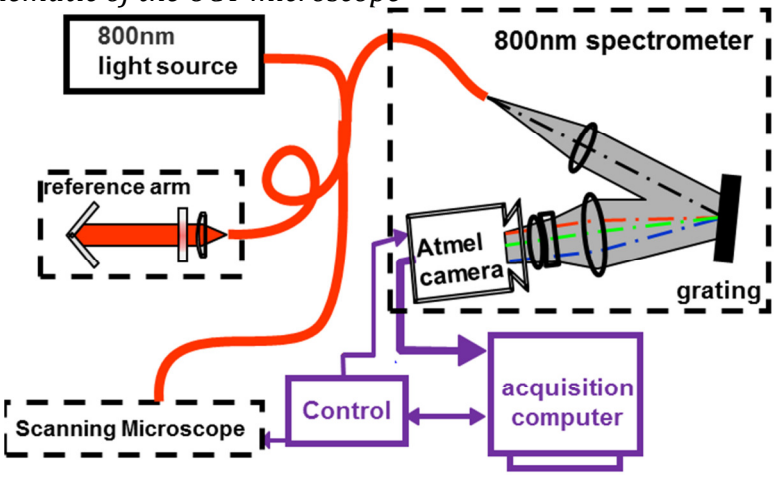

Figure 2.2: A simplified schematic of the OCT microscopy system employed showing the constituent parts which comprise the instrument. Adapted from an image created by Dr Boris Považay.

2.4 Data acquisition and processing

A sample holder was made to hold the sample in a plastic 10 cm diameter dish in place on the microscope and to keep the sample at a roughly constant slight tilt. This tilt enabled the reduction of the intensity of the specular reflections from the surface in the tomograms acquired. This was necessary in order that the intensity changes caused by the cells on the surface of the sample were not masked by the very strong signal from the surface. Figure 2.3 shows the difference in appearance of the same sample, cells on a nitrocellulose filter, in the enface plane, created by reslicing and summing over ~15 μm around the surface of the filter, untilted and after adding a slight tilt (between ~15° and ~25° from horizontal is optimum). When the tilt is added the cells are clearly seen on the surface (Figure 2.3B). Otherwise they are masked by background from the highly scattering surface of the nitrocellulose filter (Figure 2.3A).

Figure 2.3: Cells on a flat surface and cells on a tilted surface

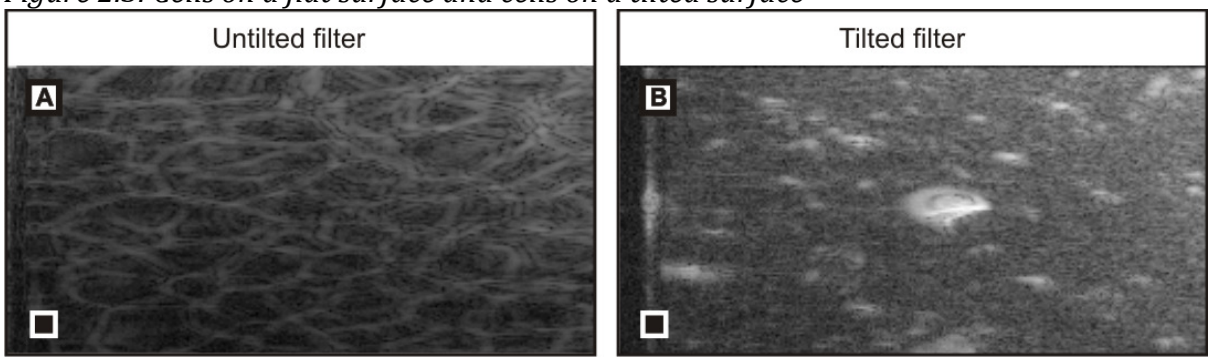

Figure 2.3: Ax2 cells seeded on a 45 mm diameter 0.45 μm pore nitrocellulose filters at 1 hour after seeding. Images cropped, resliced to enface and summed over ~15 μm. (A) Appearance if the filter is not tilted. (B) Appearance if the filter is tilted by about 15º from horizontal. Scale bars are 20 μm.

Volumes were collected in stacks of tomograms. The 3D (2D+time) data consisted of 576 x 576 pixels over 900 μm transversally (1.56 μm per pixel). The 4D (3D+time) data consisted of 800 x 800 pixels over 1000 μm transversally (1.25 μm per pixel). The depth always remains constant at 1024 pixels and 1433 μm in air (0.7 μm per pixel in air). Software custom written in Matlab (The MathWorks, Inc, USA) by members of the Biomedical imaging group at OPTOM, Cardiff University, was used to convert to the spatial domain, remove background and to correct for spectral shape, dispersion and camera nonlinearities[260-262,624]. Parallel processing code developed by Dr Alexandre Tumlinson, formerly of the Biomedical imaging group at OPTOM, Cardiff University was used to spread the processing task over several cores, utilising the Condor and Merlin computer clusters (ARCCA, Cardiff University, UK) to vastly speed up the time taken for the processing of large sets of 3D time-lapse images. With use of the clusters, processing a typical 3D time-lapse series took several hours. The code running serially on a single dual-core computer took between two and three days to process the same number of tomograms. Subsequently, ImageJ (NIH, USA) was used for further post-processing.

ImageJ macros were written to iterate though an entire time series of tomograms, unskew the images (all unskewing was performed using the TransformJ ImageJ plugin by Erik Meijering)[412,413], further remove the mean background intensity, suppress speckle, and crop the images. Rescaling was also performed so that the post-processed image was isotropic in the axial and transversal directions, as the initially captured tomograms were differently scaled in the axial and transversal directions due to different sampling rates. This was unavoidable as the axial sampling density is a property of the camera used for imaging and cannot be varied,

and choosing this sampling density for the transversal directions would have involved excessive oversampling and increased image acquisition time (discussed in chapter 3, section 3.3)[281]. The results of this post-processing are shown in Figure 2.4. Figure 2.4 shows single side-on images of a single slice taken from the image stack A) before batch post-processing and B) after batch post-processing. Where additional post-processing was required on a stack by stack basis, ImageJ was also used.

Figure 2.4: Post-processing with ImageJ

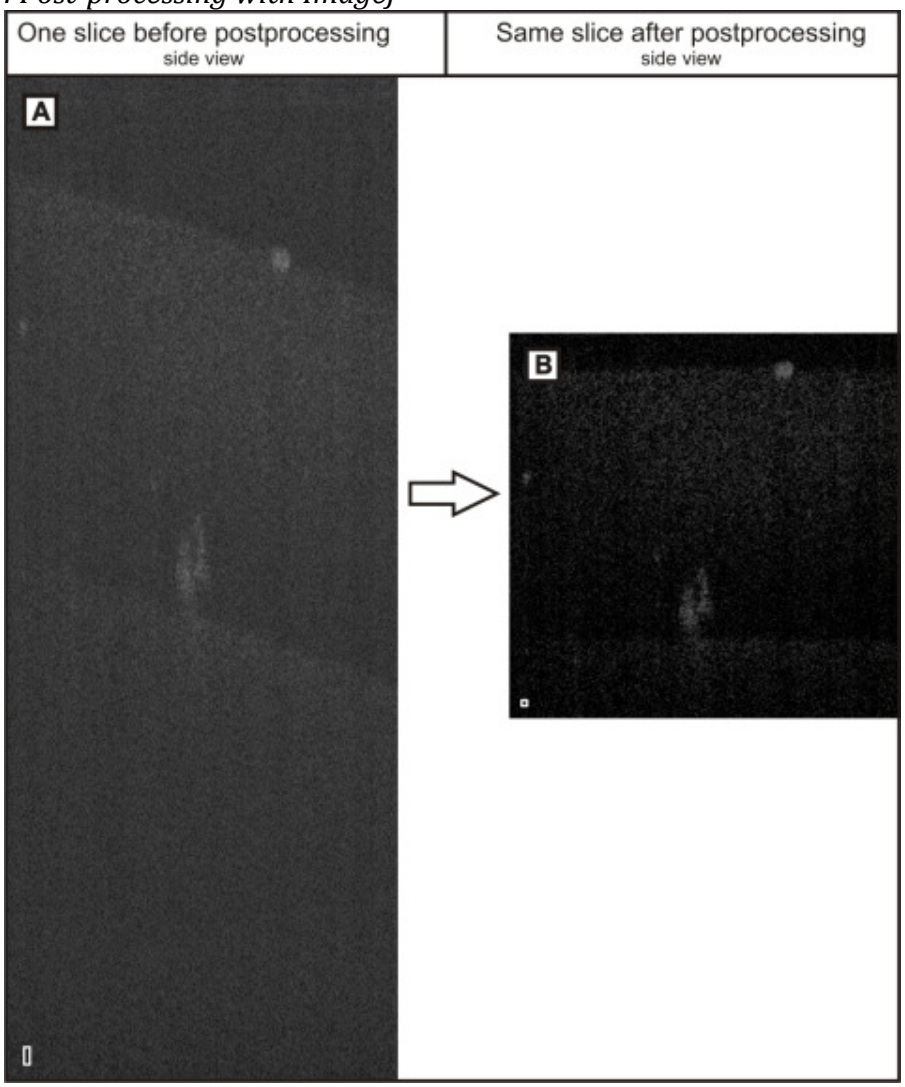

Figure 2.4: Example tomogram to illustrate post-processing showing the Ax2 cells and multicellular aggregates within 0.5% agarose on an agar base layer. (A) Single B-scan from the middle of the stack after conversion of the tomogram from the spectral to the spatial domain, note the anisotropic scale bar as the axial and transverse scaling were different prior to rescaling. (B) The same single B-scan after cropping, unskewing, rescaling and additional noise removal using ImageJ (NIH, USA). Image acquired 8 hours after seeding. Scale bars are 20 μm.

The stage of the microscope appeared to shift downwards throughout the period of acquisition of the time series, and this could not be prevented by fixing the microscope stage in place, (discussed in chapter 3, section 3.8). Therefore 4D (3D+time) tomograms were then registered across the time series by an ImageJ macro written to align all of the stacks to the central stack, or to align sequential stacks using the ImageJ plugins TurboReg (Thévenaz P., Swiss Federal Institute of Technology, Lausanne, Switzerland) and PoorMan3dReg (Liebling, M., California Institute of Technology USA), adjusting the minimum value in the TurboReg code, using a macro to align the stacks by a different method involving finding the interface between the agarose and agar base layer, detailed later in section 3.8, and finally manually aligning any stacks where necessary[364,613].

For easy visualisation of the cells on the substrata, and for compatibility with the tracking software used, the 3D data were collapsed into the enface plane at the surface of the substrate. Initially this was done manually with the use of an ImageJ macro written to unskew, remove noise and allow for manual selection of a region of interest around the surface, which was then resliced, summed using the 'sum slices' projection in ImageJ, and saved to give an enface view around the surface of the substrate (see Appendix 2 for macro). This was rather time consuming as it required manual input for every tomogram of the time series. In order to overcome this, a macro was written in ImageJ to automatically find the surface of an image which had been previously unskewed, denoised and cropped and crop a region of interest comprising 20 pixels (~25 μm) around the surface. This cropped area was then resliced, summed, using the 'sum slices' projection in ImageJ, and saved. The operation was repeated on all of the images from the time series to generate an enface view of the cells on the substratum for each time point over the entire time.

A summary of the horizontal and vertical movement of the cells in the 4D (3D+time) time-lapse images was obtained by collapsing the 3D volumetric data similarly into 2D images, collapsing regions of interest in the images into the enface and transversal (B-scan) views and then importing each of the collapsed 2D time points into ImageJ for visualisation as a 3D (2D+time) image sequence. The enface images over a region of interest were obtained as described above (giving horizontal motion) and the B-scan images (transversal view) were obtained by selecting an area of interest within a single 3D time point and summing the slices over that area, using the 'sum slices' projection in ImageJ, then applying the same operation to each image stack of the time series (giving vertical motion). In some cases these images

were given false colour in Corel Photo Paint (Corel Corporation, Canada), colour-coding selected time points for ease of visualisation.

In order to give a visual representation of the paths which the cells had travelled in a single image, the previously summed 2D collapsed image sequences (described above), were imported as a stack and then summed again, this time over all time-points, using either the 'sum slices' or 'standard deviation' projection in ImageJ (sometimes one gave better performance than the other). As the image is stored within ImageJ as an array of pixel intensity values, the 'sum slices' projection sums the values of each of the pixels stored at the same location in the array while the 'standard deviation' projection calculates the standard deviation of these values, for all of the images in the stack, and outputs the resulting intensity values into an array, i.e. a summed single image. This allows the positions of the cells and multicellular aggregates at each time-point to be superimposed on to the same image, thus giving a representation of the movement of the cell or multicellular aggregate over time.

Collapsing a 4D (3D+time) time series to a 3D (2D+time) time series results in loss of data, therefore, in order to visualise a volumetric 4D (3D+time) sequence, a trial version of Amira software (Visage Imaging, USA) was used. Within this software the volumetric data stack could be viewed from several angles and all of the time points imported as a series so that the motion of the cells within the agarose in time could be seen.

The time series of tomograms were imported into Amira as a series of stacks in the Tiff format with each stack representing a single time-point. The 'Volren' option was then selected. This module performs volume rendering; addition of texture, colour, lighting and shading to a model arranged with appropriate spatial orientation to give a realistic 2D approximation of 3D data[62,192,647]. Rendering can be performed using a number of different methods, some optimised for speed, for real-time rendering, and others for quality, when media is pre-rendered[62,192,485]. Nonetheless, all of these methods attempt to do the same thing, summarised in the rendering equation first published by Kajiya in 1986, model the path and interaction of photons within the scene (or object) to be rendered, based on knowledge of the behaviour of light[62,192,291,485]. Amira offers three user-selectable options for projecting the volume[647]. These methods are; texture-based direct volume rendering (VRT), where a transfer function is used to determine the colour and level of absorption (opacity) of each point in the volume; digitally reconstructed radiograph (DRR), a computed simulation of x-ray data (this can be computed using a number of volume rendering techniques, such as ray casting); and maximum intensity projection (MIP), which involves tracing a ray from the viewpoint of the

volume along the line-of-sight and projecting the voxels with maximum intensity[192,418,647,649]. The maximum intensity projection was used, as by iteration it gave the best view, by eye, of the cells within the volume. The depth perception of the volumes, which is not well represented using maximum intensity projection due to a lack of visual depth cues, was enhanced by manual outlining of the volumes with guidelines delineating the edges of the volumes, in CorelDraw (Corel Corporation, Canada)[62,649]. These guidelines were defined by manual rotation of the Amira-generated projections, allowing the edges of the volumes to be seen by eye due to the changes in perspective[62,649].

A viewpoint to best show the 4D motion of the cells within the 3D gel was selected and the Amira generated time-lapse images were exported as 3D (2D+time) MPEG files. These were then converted to AVI files using VirtualDub (Avery Lee, released under GNU General Public License) for further processing with ImageJ, as ImageJ cannot import MPEG files[344]. This method of presenting the data gave a more useful visualisation, in most cases, and more complete overview of the 4D data than the alternative method (collapsing into 2D vertical and horizontal images at a chosen plane), although it is also a 3D projection of 4D data and therefore involves some loss of data.

These Amira-generated projections were further processed using ImageJ. The images were converted to 8-bit greyscale; then objects were thresholded from the background using the 'Threshold' plugin in ImageJ and outlined using the 'Analyse Particles' plugin in ImageJ. This plugin outlined the objects found by the thresholding step, more clearly showing the borders of individual objects and making objects easier to see as individuals when a time series was summed together. The resulting image stack was projected using the 'standard deviation' projection in ImageJ (z-project) to show the paths which the cells had travelled, as described above.

Visualisation of optical density waves was enhanced by performing image subtraction in ImageJ. Enface images were obtained from the 3D volumetric image stacks, as described above Each image in the time series was subtracted from the subsequent image in the time series using the 'Image Calculator' built-in plugin, in order to achieve better visualisation of the wave fronts[143].

2.5 Quantitative Analysis

2.5.1 2D-DIAS software- quantitative analysis of 3D data

Quantitative analysis of 3D (2D+time) data was performed over 20 minutes after the cells had been developed for 6 hours. This time point was chosen as there were chemotactically competent single cells available for analysis. By later time points, single cells had joined together to form multicellular structures and could not therefore be identified as separate structures and tracked. In conventional chemotaxis assays, cells are generally tracked for between 10 and 15 minutes, therefore 20 minutes was thought to have good possibility of giving sufficient time to see any trends in the data[611,669]. The cell motion across the surface of the substrate was analysed using 2D-DIAS (Soll Technologies Inc, Iowa, USA) from enface images created as described above[669]. Motile cells were discriminated from the background by eye and manually outlined using a mouse at each time point, as the 'automatic outline' software algorithm built in to 2D-DIAS was unable to discriminate between the cells and the background for the OCT images. Subsequently the 2D-DIAS generated centroid-based tracks were saved and the persistence and speed were calculated for each cell and exported for additional analysis.

2.5.2 Volocity software- quantitative analysis of 4D data

Quantitative analysis of 4D (3D+time) data was performed using Volocity Quantitation software (PerkinElmer, USA). Due to memory limitations in computer hardware, stacks were downscaled prior to importing into Volocity, by a factor of 2, in order that analysis would complete successfully. The entire 2 hour time series, evenly temporally sampled every 2 minutes, was imported into the software. Objects were then selected from the background, within the volume, using intensity thresholding, restricted to a region of interest to exclude the camp agar at the bottom, and included and excluded on the basis of volume[476].

The number of slices and pixel spacing (1.25 μm/pixel) were entered into the software, along with the time between image stacks. A region of interest was drawn to exclude the cAMP agar at the bottom as otherwise the program found many objects within the agar due to its grainy appearance when imaged by OCT. The 'Measurements' tab was opened and the 'Find Objects' protocol was selected which automatically plotted a histogram of the intensities found within the current volume. The automatic setting for thresholding relies on Otsu's

method to automatically separate signal from background, which on a basic level involves reducing grayscale images to binary data[455,476].

Otsu's method requires a greyscale image with a bimodal histogram of greyscale intensities, i.e. that the background intensity be separated from the object intensity with few objects corresponding to intensities in between these two extremes. The algorithm regards the histogram of the intensity data as a normalised probability distribution and assumes two classes, separated by a threshold, where everything with an intensity value below the threshold is assigned to one class and everything above to the other[455,480]. In Volocity, the two classes defined by this threshold are objects and background[476]. The algorithm attempts to define the optimum threshold between these classes (k) by finding regions of high homogeneity. As highly homogenous regions have low variance this can be achieved by minimising the variance within each of the classes. Because the weighted within-class variance is calculated by addition of the variances of each of the classes weighted by their estimated probabilities, the greyscale value in the histogram at which this sum of variances minimises gives the optimum value of the threshold (k)[188,455,480]. It is possible to obtain this threshold value by iteratively testing each value until the minimum is found, but this is time consuming. Otsu's method exploits the fact that the sum of weighted variance is constant, independent of the threshold (k), and therefore for any given value of the threshold, the minimum between-class variance corresponds to the maximum inter-class variance[455,480]. Therefore the threshold (k) can be calculated by maximising the between-class variance rather than by minimising the within-class variances. This is useful because the between-class variance can be computed from the means of the two classes, rather than the variances, which simplifies the calculation. Furthermore, the values required to calculate this between-class variance (estimated probability and mean) can be recursively computed as the algorithm iterates through the greyscale values to find the maximum[455,480].

The 'automatic' setting in Volocity recalculates the classes for each time-point, therefore it is suggested to be the best method to use for time resolved data, where there might be differences, however minor, between stacks[476]. With the OCT data, however, this results in Volocity picking out features from the agarose gel as objects to be tracked and classifying the bright spots representing cells to a single large object with the agarose features (Figure 2.5). It is possible to enter a manual offset to alter the classification algorithm. An offset of between 60-80% was found to work well with the OCT data, exact value dependent on the particular set of image stacks, resulting in the agarose background being excluded and picking out many

of the cells (Figure 2.5). The cells within the agarose which were touching other cells or forming multicellular structures were excluded from the analysis of single cell behaviour by volume thresholding, approximated by assuming a perfect sphere and using $vol = \frac{4}{3}\pi r^3$, where r is the radius, and taking the diameter of a single cell to be between ~8 μm and ~17 μm. Settings in the software allowed volumes of objects of volumes outside of the range 350 μm^3 to 3000 μm^3 and outside of our selected region of interest to be excluded from analysis. This size of object was found to correspond well to the cells, observed and selected as cells qualitatively by eye, using this imaging method and this method and software for volume estimation. Objects were then measured for all time points and tracked using the 'Track Objects' protocol in the 'Measurements' tab. The 'Shortest Path' model was chosen, which attempts to match the centroids of the objects found between time points. New objects were excluded and the track start position was restricted to within the region of interest. The software can join broken tracks if an object is missing from one time point due to noise or changes in image contrast in certain parts of the image. It will only do this if the trajectory of the two tracks is consistent. This option was selected, as it had previously been noted in the 3D (2D+time) data that when cells became long and thin they became more difficult to see in the OCT images. Finally, the model was restricted by the maximum distance between objects, which was manually set to 35 μm, based on the maximum average speed of a wild type *Dictyostelium* cell at ~10±3 μm/min and refined by iteration[596,611,666]. The tracks were automatically plotted by the software and the parameters calculated and recorded were exported for further analysis.

Figure 2.5: Selecting objects from the background with Volocity®

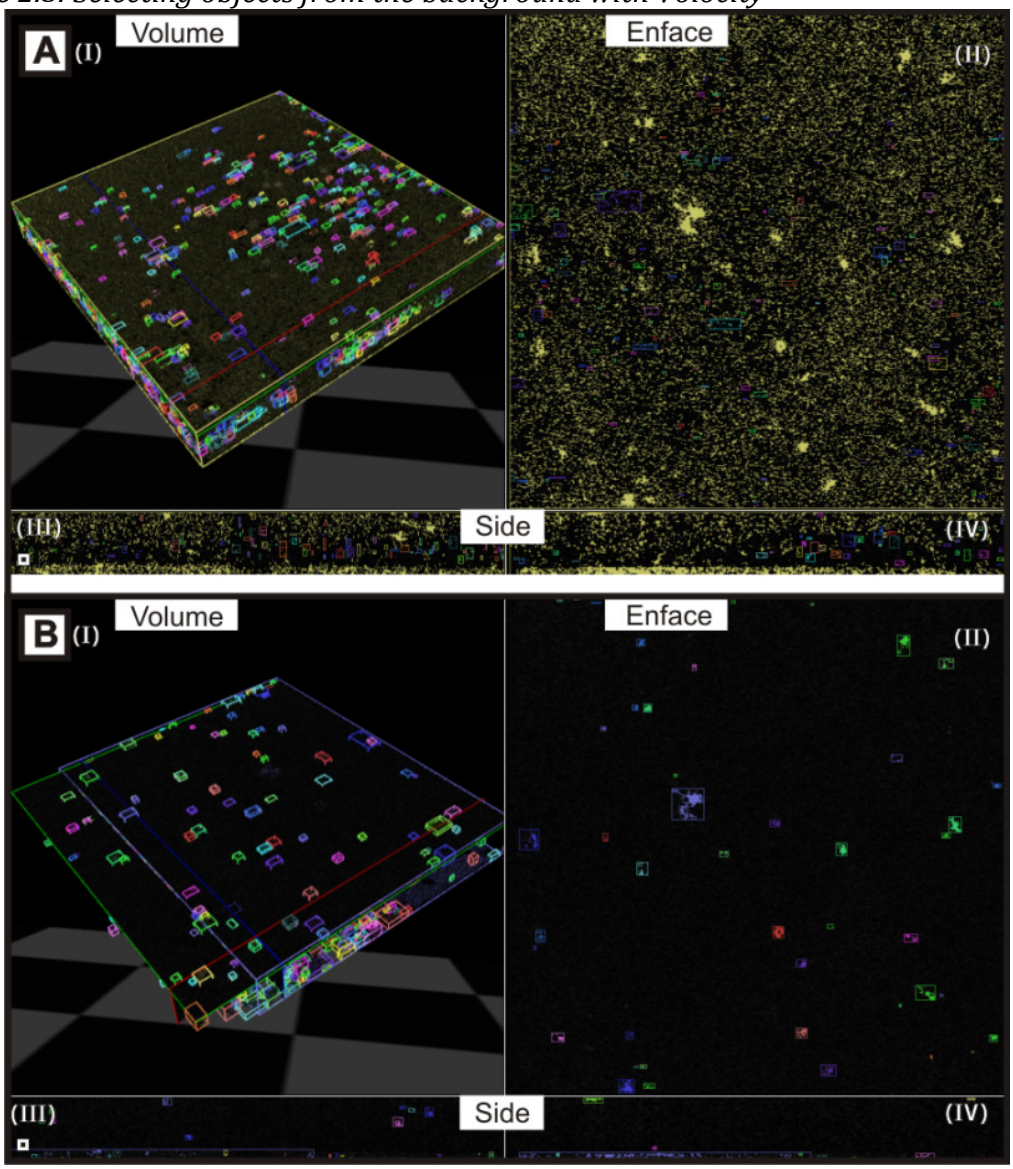

Figure 2.5: Images of one time point of JH10 cells seeded within a 0.5% agarose gel on a 1 µM cAMP agar base layer (I) entire cell volume in 3D, (II) enface view (x and y), (III) B-scan view (x and axial), (IV) transversal view in the other dimension (y and axial). (A) No offset in the intensity thresholding, many of the brightest objects, cells, are considered to be part of a large object including features in the agarose (yellow). (B) A thresholding offset of 70% applied; features in the agarose are now assigned to the background and the bright spots (cells) are picked out and highlighted, in false colour, as object of interest to be tracked. Scale bars are 20 µm.

2.5.3 Statistical Analysis

Box and whisker plots were generated of mean speed and persistence for the 3D (2D+time) data and for mean velocity and meandering index for the 4D (3D+time) data using Origin 8 (OriginLab, MA, USA). Probability density plots were generated by use of the R statistical package (released under the GNU General Public License)[387,505]. The observed data were tested for normality by both visual inspection of the plotted probability distribution and using the Anderson-Darling test in Minitab 14 (Minitab Inc., PA, USA), a goodness-of-fit test which compares the distribution of the observed data with a normal distribution of the same variance and mean, thereby providing a probability value of the degree of normality of the data[154,188,591]. Statistics were calculated using an unpaired two-tailed Student's T-test for comparison of normal data, a Mann-Whitney rank-sum test for comparison of non-normal data and a Kruskal-Wallis rank-sum test for comparison of more than two non-normal sets of data, using IBM SPSS Statistics 19 (IBM, USA)[188,391]. Hartigan's dip tests of unimodality, a test to discover whether there is more than one mode in a distribution, were performed using the R statistical package (released under the GNU General Public License). This test compares the distribution of the observed data (the empirical distribution) with a unimodal distribution chosen to be closest to this empirical distribution. The greatest difference between the empirical distribution and the chosen unimodal distribution is the dip test statistic. The significance of this test statistic is calculated by comparison of the statistic with a distribution generated by repeated sampling, using the same number of sampling points as number of observations, of the uniform distribution (argued by Hartigan and Hartigan to have the largest dip value of all of the unimodal distributions and therefore to be the best null unimodal distribution). If the test statistic is greater than the sampled values at the 95% confidence interval, then the empirical distribution is statistically non unimodal[247,387,505].

2.5.4 Quantitative chemotactic parameters

For the 3D (2D+time) data, speed and persistence were measured. These parameters, calculated using 2D-DIAS software, describe the 2D migration of the cells in time over the surface of the substrates[669]. Speed was calculated from the total path length in μm per minute. Persistence is a measure of how much a cell turns while migrating, i.e. how much the cell continues to move in the same direction. A higher persistence means that a cell is moving more directly. Persistence, measured in units of μm/min-degrees, was calculated by division

of the speed by the direction change of the cell at each time-point. Therefore if a cell is not turning the persistence will be equal to the speed[669].

For the 4D (3D+time) chemotaxis data, chemotactic parameters describing the 3D migration of the cells in time were calculated using the Volocity software. Velocity was calculated from the total path length in μm per second. Meandering index provides a measure of how much the track of the cell deviates from a straight line. The maximum possible meandering index value is 1 which indicates a perfect straight line. It was calculated from the displacement rate (displacement divided by time) divided by the velocity (total path length divided by time)[476]. Displacement differs from total path length as total path length describes the entire distance the cell has travelled while displacement is a measure of how far the cell has displaced from its original starting point in a straight line (Figure 2.6A)[476]. Hence meandering index provides a quantitative measure of how much the cell deviates from the shortest possible route between the start point of its track and the end point of its track.

Chemotactic index provides a quantitative measure of how much the track of the cell deviates from the source of the chemoattractant i.e. the accuracy of a cell's chemotaxis[213,295]. Chemotactic index was manually calculated by taking the cosine of the angle between the trajectory of the cell and a reference line which points from the cell directly towards the chemoattractant, i.e. the angle of deviation from the direction of the cAMP source (Figure 2.6B)[213,295]. A value of 1 indicates that the cell is moving directly towards the source, while a value of -1 indicates movement in the opposite direction. As the cAMP agar was directly underneath the agarose gel in which the cells were suspended, in this case the reference line points straight downwards.

The angle between the trajectory of the cell and the up axis of the stack is output by the Volocity software (as 'Angle') in degrees. Volocity calculates this angle from the inverse cosine of the dot product of the normalised vectors of the trajectory of the cell and the up axis, which is defined as the vector (0, -1, 0) in Volocity[475,476,557]. The vector of the cell trajectory is not made accessible to the end user, only the value 'Angle'. Therefore, the chemotactic index with respect to the bottom of the stack, the location of the cAMP agar chemoattractant source, was calculated by multiplying the cosine of the 'Angle' (the chemotactic index with respect to the top of the stack) by -1[476,557].

Figure 2.6: Illustration of chemotactic parameters

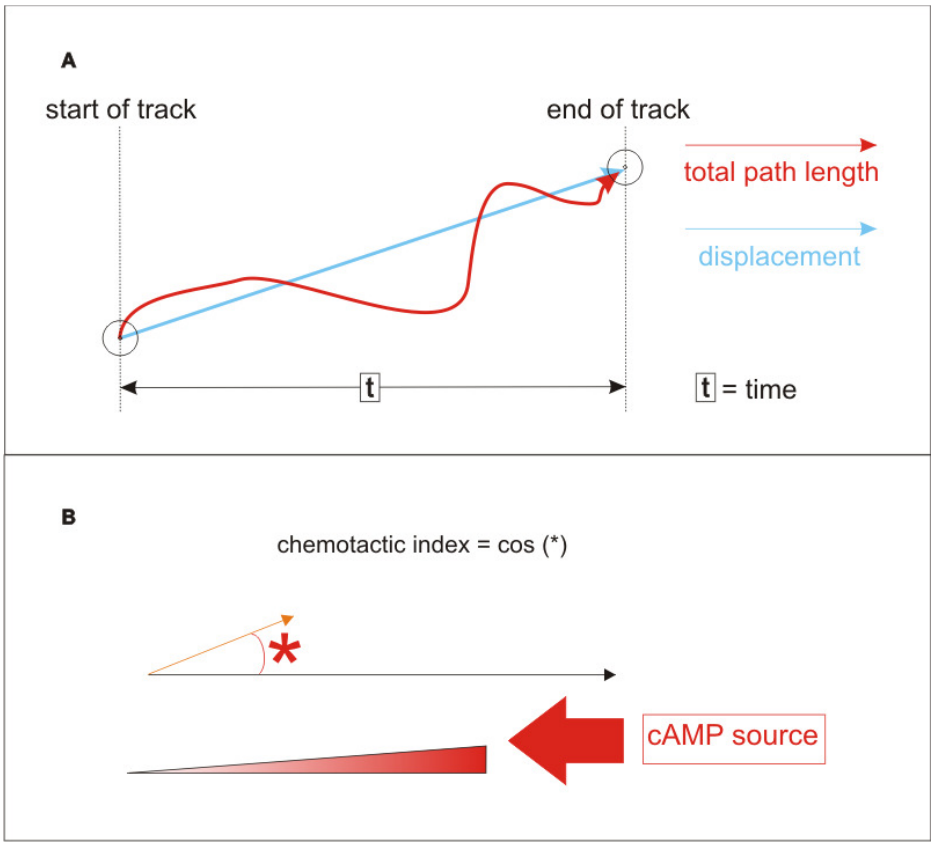

Figure 2.6: (A) Illustration of the difference between total path length, from which Velocity is calculated, and displacement, from which displacement rate is calculated. (B) The calculation of the chemotactic index from the cosine of the angle between the trajectory of the cells and the direction f the chemoattractant source (*).

Where plots were generated comparing the velocity and meandering index of Ax2 cells on a nitrocellulose filter, Ax2 cells under buffer on a Petri dish, and Ax2 cells in agarose, speed output from 2D-DIAS software (for the 3D (2D+time) data) was converted from μm per minute to μm per second. Meandering index was calculated manually for the 3D (2D+time) data by first calculating the displacement rate from displacement (called net path length by 2D-DIAS) by dividing the displacement by the time over which the experiment was performed in seconds and then dividing the displacement rate by the speed (in μm per second).

Chapter 3: Development of Methods and Protocols

3.1 Chapter 3 Aims

The aim of this chapter was to develop and refine methods for Optical Coherence Tomography imaging of cell movement on opaque surfaces in 3D (2D+time) and in 4D (3D+time). Optical Coherence microscopes vary in resolutions and performance depending on a number of factors including optical design and light source wavelength and bandwidth, therefore it was important to determine that the system was suitable for imaging of the relatively small (~10 μm diameter) and relatively fast moving *Dictyostelium* cells[208,611]. I needed to adapt some existing experimental protocols in order to suit this imaging method and develop new experimental protocols. Once I had acquired the initial test images and found resolution and signal-to-noise satisfactory for cell visualisation, I made refinements to the imaging protocols and equipment, to improve performance for this particular application.

3.2 Resolutions of the Optical Coherence Microscopy system

3.2.1 Transversal Resolutions

The crucial starting point for this project was determination of the suitability of OCT for tracking cells in 4D (3D+time) and in 3D (2D+time) on non-transparent surfaces. An important first step was to determine whether the two resolutions of the system (both axial and transversal) were sufficient for this purpose. Initially the OCT system had a custom-built objective designed and manufactured by Dr Boris Považay from the Biomedical Imaging group at OPTOM, Cardiff University. The numerical aperture (NA) of the objective was approximately 0.1NA, the maximum possible theoretically calculated resolution of the objective was ~3 μm and the measured resolution achieved with this objective was ~5 μm.

NA was approximated using

$$NA \sim \frac{Pupil\ Diameter}{Effective\ Focal\ Length} \quad \text{(viii)}$$

Theoretical resolution was approximated using

$$R = 0.37 \cdot \frac{\lambda}{NA} \quad \text{(ix)}$$

Where λ is the wavelength of the light and NA is the numerical aperture of the objective[253,281].

The resolution was measured by imaging a 1951 USAF Hi-Resolution target (Edmund Optics, Inc., USA), reslicing the images in the enface plane and manually selecting the smallest line pairs which could be distinguished.

3.2.1.1 Replacement of the Objective lens

It was noted that in some of the tomograms which were taken and processed that aberrations appeared towards the edges of the image. This was particularly noticeable in enface summed images of cells on a nitrocellulose surface (Figure 3.1A) and presents a problem for accurate tracking (potential variations in magnification across the image and inability to accurately determine the centroid of a cell)[389]. The aberrations resembled coma (comatic aberration), an optical aberration where point becomes blurred to a comet-like shape, illustrated in Figure 3.2[253,389]. Coma increases towards the edges of the lens (with increasing angle between the off-axis light ray and the optical axis) and therefore primarily affects the periphery. It is caused by off-axis rays of light, which pass through the lens at an angle, being refracted to focus at a different position when they pass through the centre of the lens compared to when they pass through the periphery, in accordance with Snell's law[253,389].

Figure 3.1: Cells on nitrocellulose before and after objective lens replacement

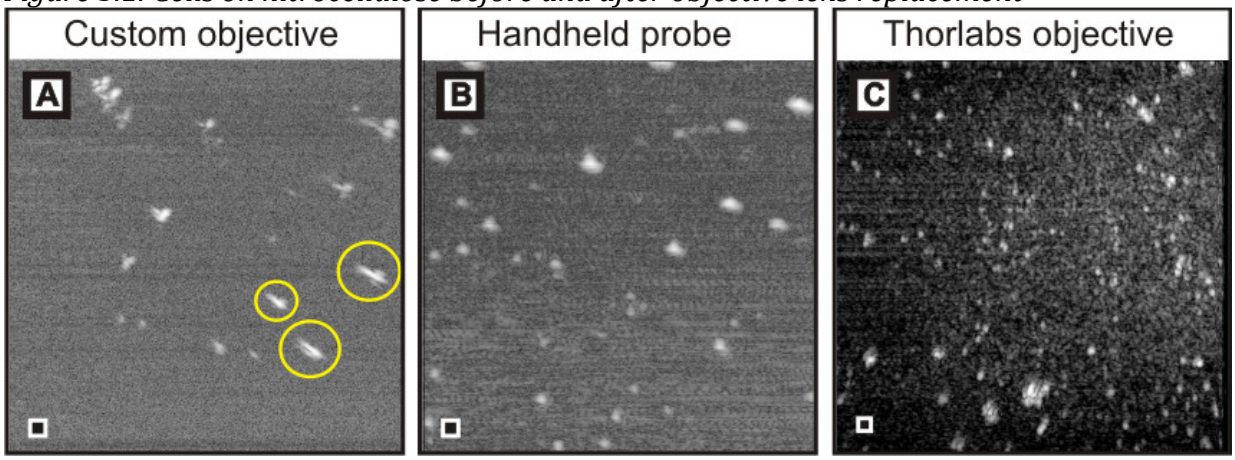

Figure 3.1: Enface (summed over ~15 µm) images of Ax2 cells on 45 mm diameter 0.45 µm pore nitrocellulose filters at 1 hour after seeding. (A) With the custom built objective, (B) With the handheld probe, (C) With the Thorlabs objective (LSM02-BB). Yellow circles denote cells which are spread out, due to optical aberrations. Scale bars are 20 µm.

Figure 3.2: Illustration of comatic aberration

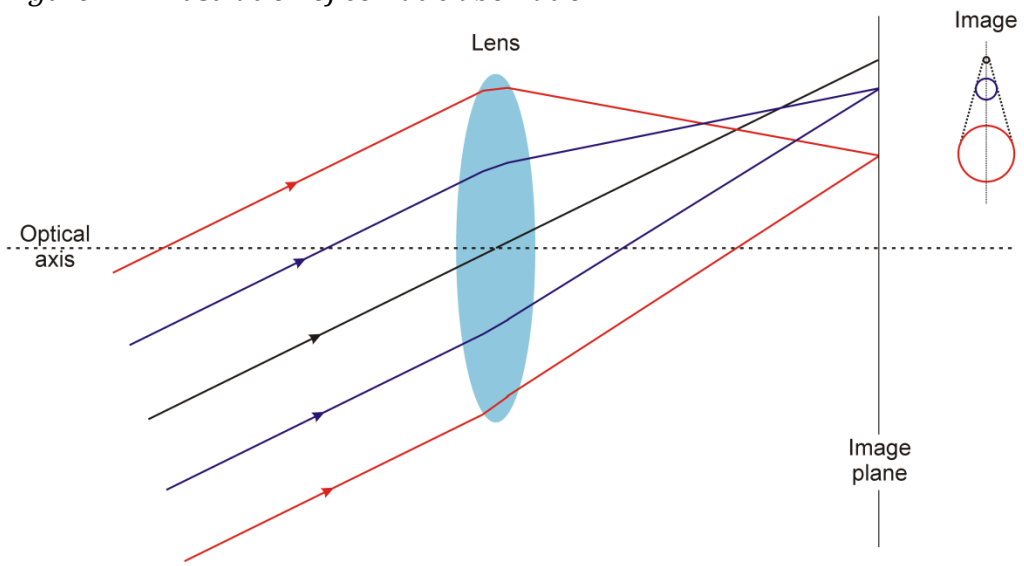

Figure 3.2: Illustration of coma showing off-axis light rays being refracted differently by the lens depending on the position at which they hit the lens. The rays which got through the edges of the lens are not focused correctly on the image plane. The 'comet-like' shape of the image generated in the image plane is shown to the right of the image.

This observation led to the idea that there was a possible problem with the optics of the OCT microscope. As at the time no alternative objectives were available in the lab which were suitable for use with this OCT system, this was experimentally tested by imaging cells on a nitrocellulose filter after replacing the microscope part with a handheld probe, usually used for dermal imaging. In this case these aberrations were not seen (Figure 3.1B) confirming that the problem was indeed with the microscope optics of the OCT system. If it were due to other factors, then the aberrations would still be seen, as the rest of the OCT system remained the same. The original objective was replaced by a broadband telecentric scan lens objective LSM02-BB (Thorlabs, Inc., USA) specifically designed for laser scanning applications[615]. With the new objective, the aberrations were significantly improved (Figure 3.1C).

Although the NA of this objective was calculated to be ~0.1NA, giving a theoretical resolution of ~2.75 μm, it is important to note that we cannot use the entire NA of the objective with frequency domain OCT, resulting in a slightly smaller NA for the entire system than for the objective used. This is because frequency domain OCT requires the beam to be raster scanned across the sample. If we were to scan a beam which was already filling the back plane of the objective, the edges of the scan would overlap the sides of the objective.

Therefore, the optics prior to the objective are designed to have a beam diameter which is smaller than the pupil size of the objective. This beam diameter was measured to be ~3.5 mm. Using the beam diameter instead of the pupil size in equation (i) above, the NA of the system can be found to be ~0.09NA and, using equation (ii), subsequently the approximate theoretical transversal resolution of the system can be calculated to be approximately 3.3 μm. Using a 1951 USAF Hi-Resolution target (Edmund Optics, Inc., USA), reslicing the images in the enface plane and manually selecting the smallest line pairs which could be distinguished, the resolution was measured to be ~5 μm.

3.2.2 Axial Resolution

The major difference between OCT and other forms of optical microscopy is that in OCT the axial image is formed by a ranged measurement with low coherence interferometry[281,549]. Axial resolution of an OCT system is decoupled from the lateral resolution and is a property of the light source[208]. It is therefore not dependent on the objective used.

Axial resolution for an OCT system is calculated using

$$l_c = \frac{2\ln(2)}{\pi} \cdot \frac{\lambda_0^2}{\Delta\lambda} \quad \text{.....(x)}$$

where l_c is the coherence length of the light source, λ_0 is the central wavelength of the light source and $\Delta\lambda$ is the bandwidth of the light source[281]. The theoretical axial resolution of our system was calculated to be ~2.3 μm in air.

Axial resolution was measured by imaging a mirror and plotting the intensity profile of the image for one slice of the stack, a roughly Gaussian curve. This Gaussian curve shows the step up to the signal from the mirror, the signal from the mirror, and the step down again. If the resolution were perfect both the step up and the step down would be straight lines, connected by a straight line at the maximum intensity, i.e. a rectangular shape. As the resolution is non-perfect, a roughly Gaussian shape is seen. The axial resolution can be therefore seen to be the difference between half of the Gaussian curve and a straight line (i.e. one surface reflex). Therefore, half of the full-width half-maximum is the measured axial resolution of the system[281].

The measured axial resolution of the OCT system in air was found to be ~4.5 μm. The optical path length is greater in agarose than in air, due to the larger refractive index of

agarose ($n_{agarose}$=1.34, n_{air}=1)[253,654]. This results in the retardation of the light which passes through the agarose. The frequency of the light is unchanged, and therefore we can see from

$$v = \lambda f \quad \text{(xi)}$$

where v=velocity of the light, λ=wavelength and f=frequency, that the wavelength of the light is also reduced[253]. This means that for any given physical distance, the light will experience a greater number of wavelengths in agarose (when the refractive index is higher) when compared to in air. As can be seen from equation (iii), axial resolution in OCT is related to wavelength. Therefore, the axial resolution in agarose is higher than the resolution in air. The achieved axial resolution of the OCT system is therefore ~3.25 μm in agarose and ~4.5 μm in air.

It can be seen from the above numbers that the OCT microscope has a suitable resolution for imaging whole cell structures such as the ~10 μm diameter *Dictyostelium* cells. However, chemotactic cells are not rounded but instead have an elongated shape (Figure 3.3)[669]. The diameter in one direction is therefore much smaller than the diameter in the perpendicular direction. Cells therefore have different equatorial (~5 μm) and polar (~20 μm) diameters when chemotaxing. Figure 3.3 shows a cropped enface image of starved and aggregating *Dictyostelium* cells seeded onto a carbon nanotube surface (provided by E. Brunner, University of Surrey, UK). A single elongated polarized cell is highlighted (Figure 3.3B) and, as shown, can be resolved with our OCT microscope.

Figure 3.3: Image of an elongated chemotaxing cell with OCT

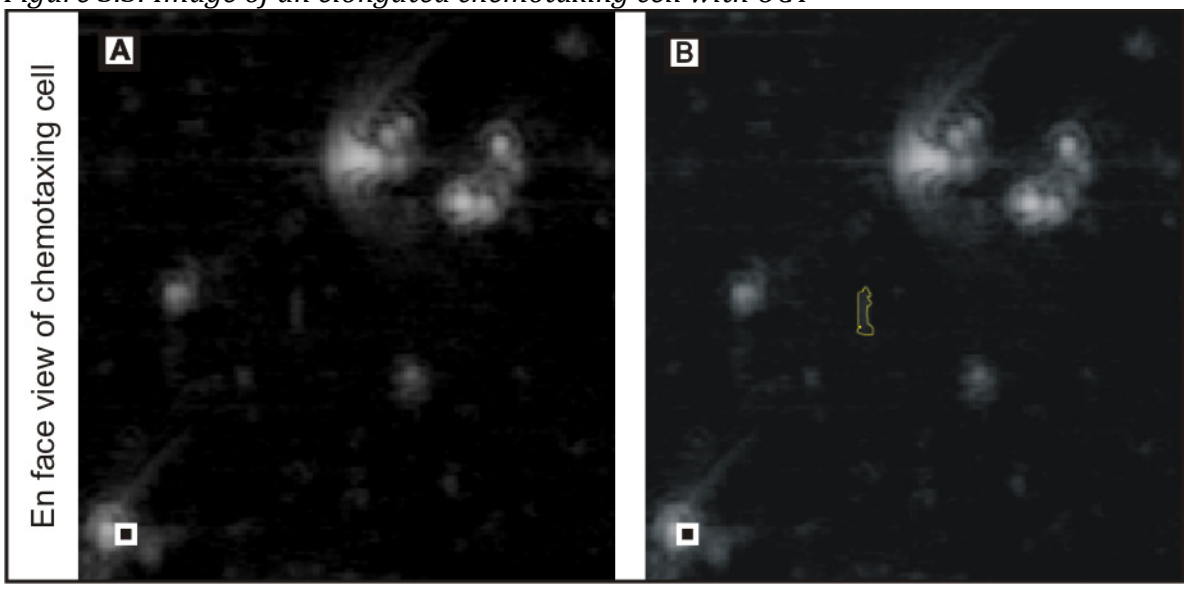

Figure 3.3: (A&B) En face images of a single time-point of a cell chemotaxing towards a multicellular aggregate. The cell has an elongated shape, so the diameter is smaller in one direction compared to the perpendicular direction. Cells of this shape can be resolved with the OCT microscope. (B) Cell outlined in yellow for visibility. Scale bars are 10 μm.

3.3 Size of scan area and sampling density

The next step was to decide on the size of the area to be imaged and the sampling density of the images. The axial size and sampling density are always the same, as they are a property of the camera used for imaging, however the lateral parameters can be varied[281]. In order to properly resolve structures at the resolution limit, the pixels must be at least two times smaller than the resolution[379,473]. This is known as critical or Nyquist sampling[379]. For our system, in order to avoid undersampling, sampling should take place at least once every 2.5 μm, as the measured lateral resolution is ~5 μm. As can be seen from this, larger scan areas require more sampling points, resulting in a limit being placed on the maximum size which can be acquired. Added to this is the consideration that larger scan areas and higher sampling densities produce larger tomograms, and larger tomograms take longer to acquire and save. Therefore there is a trade-off between total image size, at critical sampling rate or better, and image acquisition and saving time. Sampling more points than critical sampling is known as oversampling, which results in the acquisition of more data per resolution point and can therefore reduce background noise, particularly shot noise[473]. For the 3D (2D+time) experiments (Chapter 4), a sampling rate of 1.56 μm per pixel was chosen with a total image

size of 900 μm, as this enabled cells to be easily distinguished from the substrata on which they were seeded while still allowing an acquisition rate of 2 images per minute. The 4D (3D+time) experiments (Chapters 5 and 6) required a slightly larger area in order to be sure that the visual field was of sufficient size to include cell streams and multicellular aggregates when they formed. In this case, a sampling rate of 1.25 μm per pixel was chosen with a total image size of 1000 μm, which allowed cells to be seen as bright spots within the agarose background. 800 x 800 was the largest isometric number of sampling points possible to acquire, equating to a ~2.25GB file when the image size was 1000 μm and rising to ~3GB when the image size was ~1300 μm, as the acquisition software initially saved the image file to the virtual memory (a write buffer) before reading it out on to the RAID array. Although the acquisition computer had a 64-bit processor and a 64-bit operating system, LabVIEW (National Instruments, USA), the software used to write the acquisition software, was only available in a 32-bit version at that time (LabVIEW 8.5) and 32-bit versions of LabVIEW are limited to accessing 3GB of virtual memory[441,442]. Therefore images in excess of 3GB caused LabVIEW to crash on saving[442]. An acquisition rate of every 2 minutes per image was used for the 4D (3D+time) experiments because of the increased acquisition and saving time.

For the 3D data, acquisition of one time point, a ~1.26 GB file, took ~20 seconds and saving took ~4.5 seconds. For the 4D data, acquisition of one time point, a ~2.25 GB file, took ~40 seconds and saving ~8 seconds with the ATMEL AViiVA M2 CL 2048 pixel CCD camera operating at 20,000Hz. Bearing in mind costs in time and money for designing and aligning a new spectrometer, and some signal to noise problems which were occurring with the faster cameras when used for OCT imaging, it was decided to continue to use this camera although faster speed cameras were available at the time and would have enabled a slightly faster acquisition rate.

3.4 Optimisation of background subtraction

Originally our OCT cell images suffered from some troublesome background artefacts (Figure 3.4). Artefacts were more severe when a highly scattering, fairly opaque surface was present, such as nitrocellulose or agar (Figure 3.4A), but they were still a problem with the diffuse bright spots of cells within agarose, and reflective agarose surface when the cells were set within an agarose gel (Figure 3.4C). The main causes of these issues were camera fixed pattern noise and artefacts introduced by errors in the background subtraction. A method to

supress the time varying fixed pattern camera noise and to reduce these artefacts was proposed and implemented by Dr Bernd Hofer of the Biomedical imaging group at OPTOM, Cardiff University[260]. Briefly, the camera noise caused broad horizontal stripes to appear in the image because the camera noise is not constant across the pixel array. The horizontal stripes are broad because of the spectrometer resampling in wavenumber (k) space, which occurs as part of image transformation to the time domain, and is necessary because the spectrometer does not evenly sample in k space[50,624]. This noise was suppressed by use of a binary filter mask designed to block the worst of the noise. The filter mask was created and used prior to spectral resampling as at this point the stripes are un-broadened. The filtered tomogram was then converted to the spatial domain[260]. The background noise of the tomogram is usually calculated from the mean of the signal acquired when the sample arm is blocked and is then subtracted from the image. Horizontal lines appear in the image when this method is used with cells on a substrate because the surface is highly scattering, resulting in a skewed distribution of amplitudes. The result is that the mean is not a good estimate of the distribution's background[260]. Instead the median is used, obtained after spectrometer resampling for better effect, and applied to the tomograms in the frequency domain, as this excludes the outliers in the amplitude distribution created by the strongly scattering surface of the substrate. The result of using both of these methods is tomograms where artefacts are considerably reduced (Figure 3.4B&D)[260].

Figure 3.4: Difference between mean and median subtraction for cells on agar

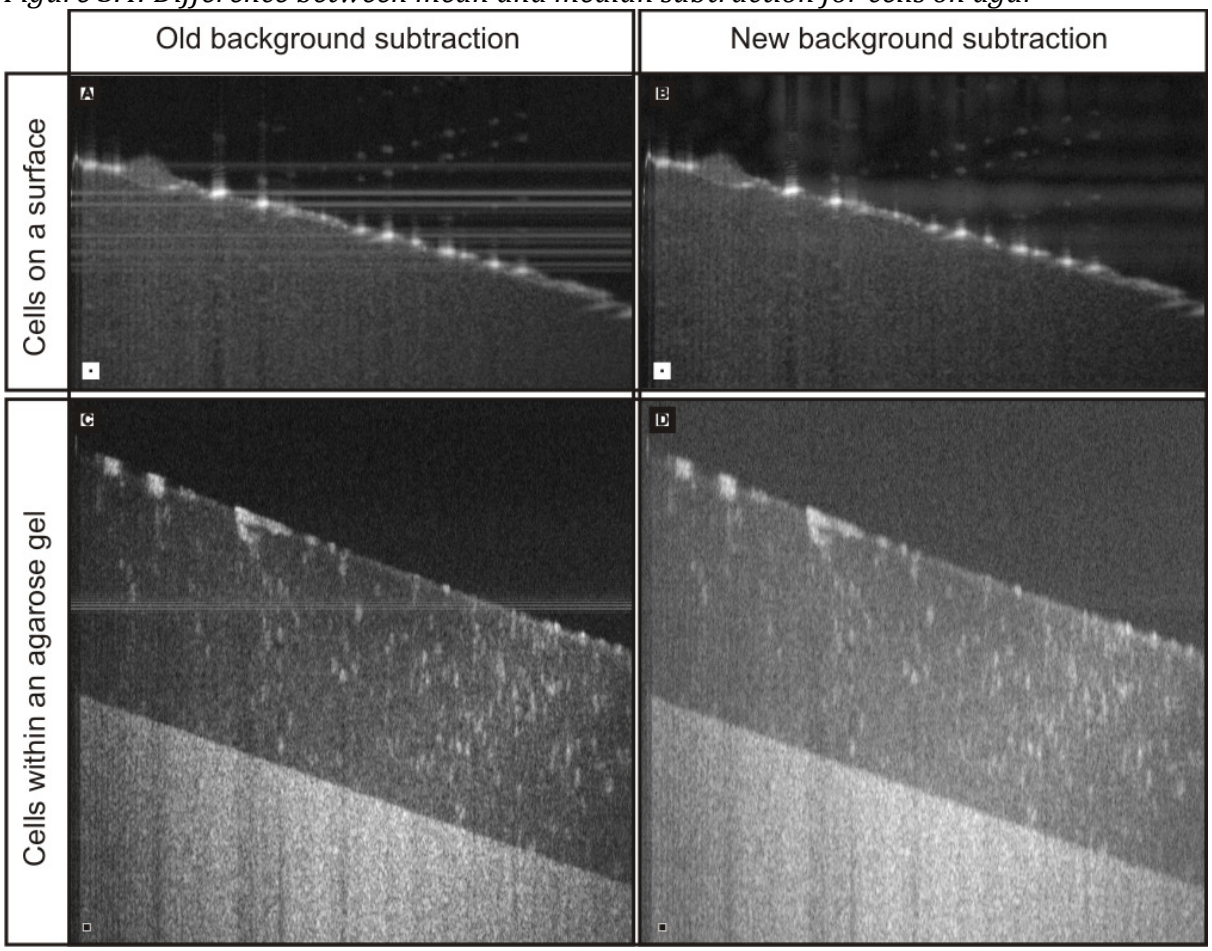

Figure 3.4: Ax2 cells (A-B) on a 45 mm diameter 0.45 µm pore nitrocellulose filters at 6 hours after seeding (C-D) within a 0.5% agarose gel. Images summed over ~25µm. (A&C) Processing with mean subtraction and no camera noise suppression. (B&D) Processing with median subtraction and camera noise suppression[260]. Scale bars are 20 µm.

The new methods of noise reduction add additional steps into the FD processing and so are more time consuming than the original method of transformation to the time domain. However, the artefacts were obscuring some of the cells, making them difficult to see and select by eye. Additionally, automated post-processing of images and selection of cells failed to function correctly[260]. The benefits of this additional processing, for cellular imaging, therefore outweigh the cost of increased image processing time.

3.5 Seeding densities of cells

In Chapter 4, the effects of two different conditions and substrata on the migration characteristics of *Dictyostelium* cells in 3D (2D+time) are explored. In these experiments, cells were seeded for development on a nitrocellulose filter and on a plastic petri dish under KK2 buffer. The cells were seeded at $1x10^7$ cells in 0.5 ml KK2 buffer on a nitrocellulose filter, a protocol commonly used for assessing cell development. The diameter of the Petri dish used for the development of the cells under buffer was ~90 mm compared to ~40 mm of the nitrocellulose filters. Using a ratio of the diameters of the filter and the petri dish respectively, the number of cells used when the cells were developed in a Petri dish under buffer was scaled up to $3.24x10^7$, under 3.2 ml KK2 buffer. This kept the density of cells fairly consistent between the two conditions. As cell density has been shown to affect cell behaviour and chemotaxis in *Dictyostelium*, it was necessary, for the 4D (3D+time) experiments, to select a reproducible density which allowed a sufficient number of single cells to be identified within the agarose for visualisation and any subsequent quantification[282,396,638]. There also needed to be enough cells for aggregation to occur, as previous work has shown that Dictyostelium cell development does not occur if cells are too widely spaced[250]. A standard chemotaxis assay in 3D (2D+time), on a glass Zigmond chamber and imaging with a DIC microscope, uses cells at $1.25x10^4$ cells/ml (Harwood lab protocol)[308,611]. By iteration, a similar dispersal of cells to that of the Zigmond chamber was obtained when a 40 mm diameter nitrocellulose filter was seeded with ~$5x10^6$ cells in 0.5 ml KK2 buffer.

In the 4D (3D+time) experiments (Chapters 5 and 6), the chemotaxis and development of *Dictyostelium* cells within a three-dimensional environment, agarose, are examined (section 3.7 covers this in more detail). As a cAMP agar base was used as chemoattractant (section 3.9), it was important to ensure that the depth of the agarose was approximately the same in all experiments, so that the gradient of chemoattractant would remain constant between experiments. By observation, I determined that the OCT microscope was able to image with good signal-to-noise and focus to a depth of approximately 700 μm with the type of sample I would be using, by imaging 6 μm glass beads seeded in agarose gel. In order to give a little leeway I aimed for a depth of approximately 500 μm in the agarose, By iteration, it was determined that 3 ml agarose, evenly distributed, resulted in a depth of approximately 500 μm in the middle of a 100 mm diameter Petri dish (data not shown). Based on the number of cells/ml used for the nitrocellulose filter and the volumetric ratio obtained between the filter and the agarose (1:6), $3x10^7$ cells were originally mixed into the agarose for the 4D

experiments (Figure 3.5). Due to the number of cells, it proved difficult to assess individual cell behaviour, partly because when there were a great number of cells the cells tended to clump together more. It is also important to not have too many cells, as a previous study has shown that *Dictyostelium* cell streams break apart when there are too many cells, which would disrupt cell aggregation[226]. Therefore the number of cells seeded within the agarose was dropped to $1.9x10^7$, which made individual cells easier to see and reduced the number of cells in contact with other cells.

Figure 3.5: A higher density of Ax2 cells within 0.5% agarose

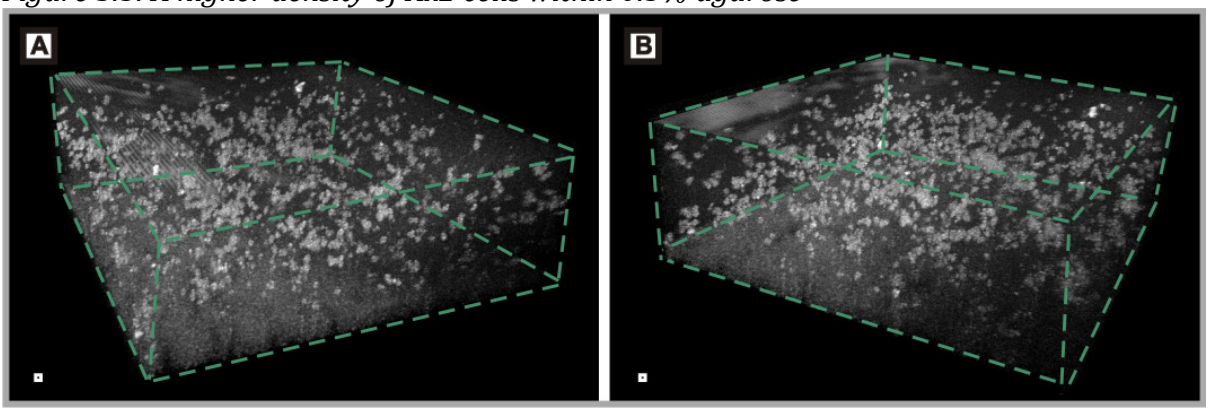

Figure 3.5: (A-B) Ax2 cells seeded at a higher density than usually used, at 3x107 cells in 3 ml 0.5% agarose viewing from different angles. Many cells can be seen, both as individual cells and as clumps of cells. The number of cells makes it difficult to examine the behaviour of individual cells. Green guidelines indicate the edges of the images for ease of visualisation. Scale bars are 20 μm.

3.6 Automatic selection of the area around the interface for 3D cell migration

In order to reduce the need for user input and speed up the process of attaining an enface representation of the 3D time series data for analysis, it was necessary to find a way to automatically locate the surface of the substratum on which the cells were seeded. For the cells to be clearly resolved against the substratum, it was necessary to crop the image close to the surface and to reslice only this small area and sum. If a larger area was resliced and summed, most of the detail in the image was lost and the cells became impossible to see, masked by background signal. Figure 3.6 illustrates this, showing an enface view from reslicing a B-scan image stack, (A) cropped and resliced at ~25 μm around the interface compared to (B) cropped and resliced at ~563 μm around the interface. The signal from the

cells is almost completely lost in Figure 3.6B. Initially a region was selected around the surface for the first time point, the indices of the positions on the image recorded and applied to the entire time series. However, due to the focus slippage seen with the microscope, the substratum surface shifted downwards with each successive time point, resulting in the enface image for later time points no longer being of the surface of the substratum, but rather of the air above the surface (see chapter 3, section 3.10 for elaboration on the focus slippage). This was overcome in the first instance by user input defining the surface manually. Unfortunately, this was time consuming, and so an approach to automate the process of selection of the surface was taken to speed up the process and remove the need for user input.

Figure 3.6: Enface summed images over a large area and small area around a region of interest

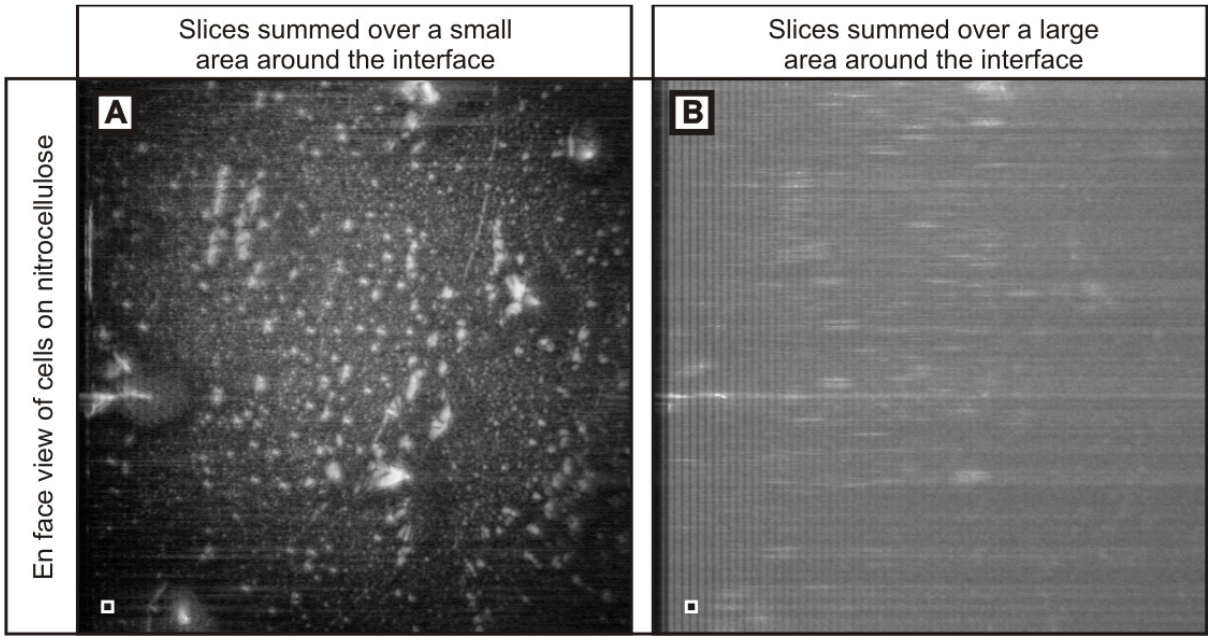

Figure 3.6: Enface images of Ax2 cells on a 45 mm diameter 0.45 µm pore nitrocellulose filter at 6 hours after seeding. Original B-scan images were identical. (A) Summing ~25 µm around the interface. (B) Summing over ~563 µm and including the surface; the background noise masks the signal from the cells. Scale bars are 20 µm.

Initially, the TurboReg plugin for ImageJ (Thévenaz P., Swiss Federal Institute of Technology, Lausanne, Switzerland) (discussed in section 3.10) was used to attempt to align the 3D (2D+time) stacks, however, this method was unable to reliably align these stacks successfully. A macro was written in ImageJ that located the surface of the substratum. A 3D

image, representing a single time point of the time series, which had already been unskewed, cropped and denoised using a previous macro, was loaded and collapsed into a 2D side-on view of the image (B-scan) by summation of the slices in a z-projection. The intensity profile of this resulting 2D image was plotted and the intensity value of each pixel in the 2D image was output in a matrix, where the indices of the matrix correspond to the x and y positions of the pixel within the 2D image. The differences between each value of the matrix were calculated and outputted in a second matrix. The maximum of this matrix was found and the index at which it is located was the surface of the sample. The indices of the surface were then recorded and output to the original 3D image. A region of interest comprising 18 pixels (~13 μm) around the surface of the 3D image was then selected, resliced, summed and saved. The macro then iterated through the entire time series and the resulting images were a time series of an enface view of the cells on the substratum (see Appendix 2 for macro).

3.7 Setting up cells for 4D cell migration

In the wild, *Dictyostelium* live in soil at the air-water interface[299]. Originally cultured in dung, developments since allowed them to be grown on bacterial lawn and finally mutants to be grown in liquid media[299,670]. Many previous time-lapse studies into cell behaviour and chemotaxis have taken place on 2D transparent surfaces, due to limitations of imaging techniques and the practice of culturing cells on glass and plastic surfaces [172,669]. There is great current interest in a comparison of the behaviour of cells on 2D surfaces and cells in 3D environments, such as the mammalian body or the soil of *Dictyostelium,* in order to determine the differences and similarities between cells in a more natural 3D environment and in a 2D environment such as is commonly found in the laboratory[195,236].

The extension of 2D assays to the third dimension has resulted in the need for scaffolds and matrices in which to set cells[237]. With mammalian cells there is the consideration of the effects of different cell types which would be found in vivo around the cultured cell type[40,237]. Fortunately this is not necessary in *Dictyostelium* as the vegetative cells spontaneously differentiate into different types of cell as a part of development[676]. Matrigel (BD Biosciences), a commonly used scaffold for mammalian cells which mimics the extracellular matrix (ECM), is not suitable for use with *Dictyostelium* as their natural environment is not ECM, although they do secrete an ECM at the slug stage, which shares some similarities with animal ECM[397,456,633,675]. Nonetheless, it sets between 22ºC and 35ºC, an ideal temperature for

mammalian cells, but slightly above the required range for our experiments with *Dictyostelium*[35,222].

In looking for a 3D cellular scaffold for the *Dictyostelium* cells, the major considerations were; that it be biocompatible, having no adverse effects on cell behaviour and proliferation and permeable to oxygen; that it be solid enough so that cells do not sink, but not so solid that they are unable to move through it, i.e. a gel; that it be set at between 21ºC and 23ºC, the maximum temperature variation experienced during the course of the experiments; that it be transparent to OCT, enabling the cells to be seen within; and that it be easily obtainable[320,592]. Ease of use was another important consideration, as performing multiple experiments in order to refine conditions and procedures is easier when protocols are kept simple. Cell-culture-tested high-purity agarose gel, commonly used in laboratories, meet all of the above requirements in addition to having been successfully previously used with *Dictyostelium* for growth and development and chemotaxis studies[312,320,329,592,616,656,682].

The cells needed to be mixed with the agarose while the agarose was still quite liquid, so that the cells would be evenly dispersed. In order to accomplish this without subjecting the cells to heat shock, low melting point high purity agarose (Sigma-Aldrich, UK) was used as *Dictyostelium* cells are quite temperature-sensitive[463]. This agarose was found to remain liquid at a temperature of 25ºC at concentrations less than and including 1% (w/v), unlike conventional agarose which was found to set quite rapidly at this temperature even at these low concentrations.

A strong signal is obtained in OCT from surface reflections of glass and plastic. In order to prevent the higher order images from the bottom of the Petri dish from appearing in the OCT image and creating noise or drowning out parts of the image, a separation layer of agar between the agarose and the plate was introduced. This may also act to help keep the agarose hydrated[312]. Agar, unlike agarose, did not appear transparent to OCT so the delineation between the agar and the agarose layer was able to be easily seen. Agar is also too thick for the *Dictyostelium* cells to penetrate so this surface provided a barrier to their movement in much the same way as the bottom of the dish would otherwise.

This experimental setup allows for the investigation of the movement of *Dictyostelium* cells within an agarose gel, at the agarose-air interface and at the agarose-agar interface. All of these are of potential interest in elucidating the behaviour of *Dictyostelium* in 4D (3D+time),

potentially giving insights into the differences between what is observed in the laboratory in 2D and 3D (2D+time) and the more natural 4D environment.

3.8 Concentration of agarose for 4D experiments

Having selected agarose as the 3D scaffold in which to set the cells to observe their behaviour in 4D (3D+time), the optimum concentration of this agarose needed to be determined. In order to set up an assay which would enable difference in behaviour between different strains of cells, including knockouts and drug-treated cells to be seen, the wild-type Ax2 cells must be able to move freely within the agarose. Initially cells were set in 0.2%, 0.3%, 0.4%, 0.5% and 0.6% low melting point agarose (w/v) and looked at through a conventional phase contrast microscope. Cells were seen to sink almost immediately at the lowest concentrations (0.2% and 0.3% (w/v)) and the gel at these concentrations was not well set and very liquid[604]. From 0.4% (w/v) on, the agarose was reasonably well set and the cells were not seen to immediately sink. To experimentally test the effects of varying the concentrations of agarose on the ability of *Dictyostelium* cells to migrate, in order to experimentally determine the optimum concentration of agarose to use for my experiments, concentrations of 0.4%, 0.5%, 0.7% and 1% (w/v) low melting point agarose were seeded with 1.9×10^7 Ax2 cells harvested at the log growth phase, which had been rendered chemotactically competent by exposure to 100nM cAMP pulses at intervals of 6 minutes over 5 hours (pulsed), and set on 1 μM 1% (w/v) cAMP agar.

Figure 3.7 shows the paths of the cells (cell tracks) through the agarose. To achieve this, all of the individual time points (already collapsed into either the enface or side-view) are summed together. As can be seen below in Figure 3.7, during the 2 hours of imaging time, at 1% (w/v), Figure 3.7A and D, the Ax2 cells are not able to move within the agarose, at 0.7% (w/v), Figure 3.7B and E, cells are able to move down but are relatively restricted in their transversal motion. However, at 0.4% (w/v), Figure 3.7C and F, cells are moving well in both the lateral and axial directions. A concentration of 0.5% (w/v) was chosen as the best compromise because the gel was well set and the cells were able to move freely in both the lateral and axial directions (Figure 3.8).

Figure 3.7: Cells set in different concentrations of agarose

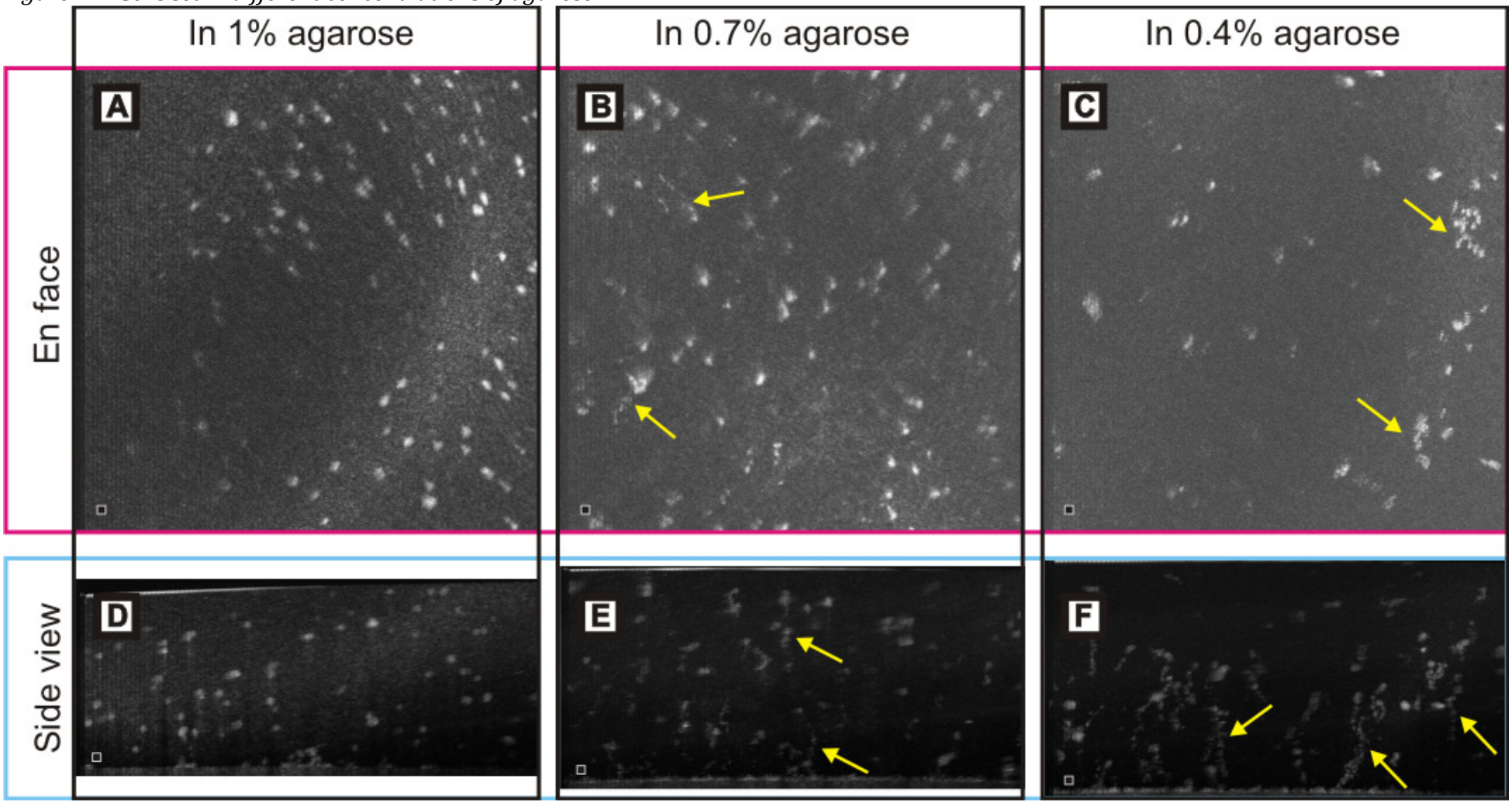

Figure 3.7: Ax2 cells pulsed for 5 hours and set in different concentrations of agarose on a 1 μM cAMP agar base layer, for experimental determination of the optimum concentration of agarose to use in future experiments, and imaged for 120 minutes, sampling every 2 minutes. (A-C) Enface images are summed over ~10 μm and then all of the time points are summed using the standard deviation projection allowing the tracks of the cells to be seen. (D-F) B-scan side view images are summed over ~50 μm and then all of the time points are summed using the standard deviation projection allowing the tracks of the cells to be seen. (A&D) in 1% agarose, the cells do not exhibit any significant migration. (B&E) in 0.7% agarose, the cells exhibit horizontal motion, but lateral motion appears restricted. (C&F) in 0.4% agarose, the cells appear to move freely in both the horizontal and lateral directions Yellow arrows point to some of the tracks seen in the images. Scale bars are 20 μm.

Figure 3.8: Tracks of Ax2 cells moving within a 0.5% agarose gel

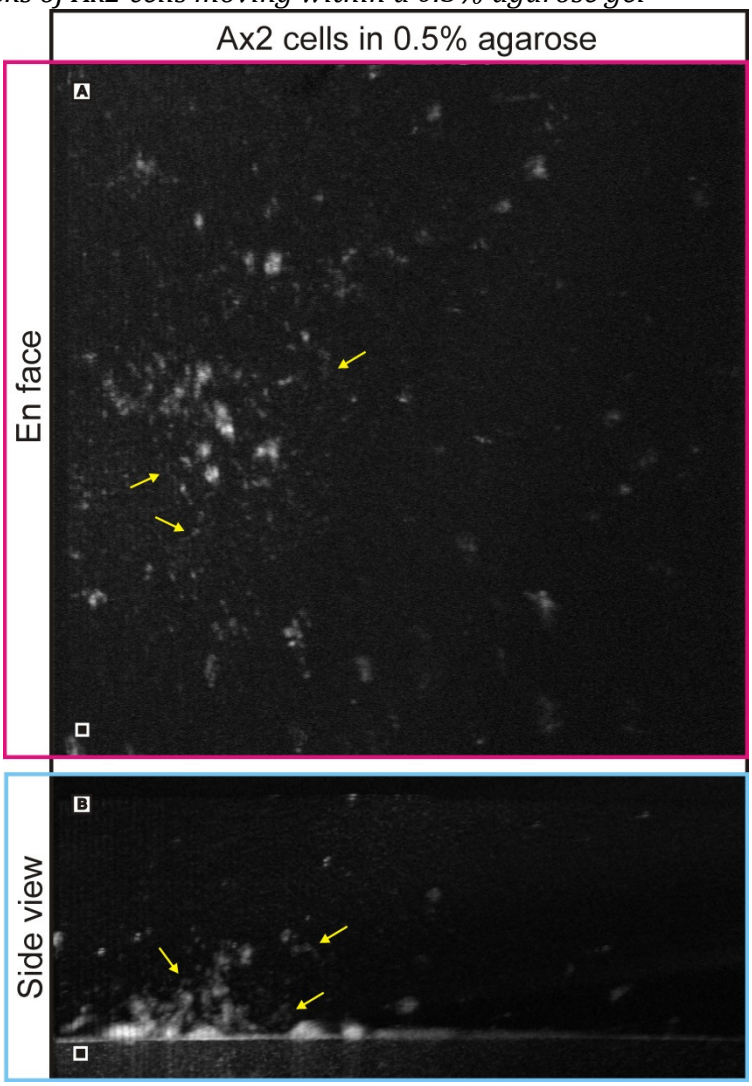

Figure 3.8: Ax2 cells pulsed for 6 hours, seeded within a 0.5% agarose gel on a 1 µM cAMP agar base. Imaged over 2 hours sampling every 2 minutes. All of the time points are superimposed by use of the standard deviation projection in ImageJ. This enables cell tracks to be seen within the agarose (yellow arrows show some examples). (A) En face view with slices summed over ~10 µm at ~75 µm above the cAMP layer. (B) B-scan (side-on) view at the middle of the stack, summed over 25 µm. Horizontal and lateral migration of the cells can be seen to occur. Scale bars are 20 µm.

3.9 4D chemotaxis- establishing a chemoattractant gradient

Cells were set in agarose as described above, and originally a spot of 1μM 1% cAMP agar, dyed blue with bromophenol blue for visibility and easy location, was placed at a point on the surface of the agarose in order to set up a cAMP gradient. A major difficulty with this experimental set-up was that the direction and extent of the cAMP gradient through the agarose was difficult to assess and problematic to accurately model in 4D[496,513]. Therefore cells within the agarose were exposed to different concentrations of cAMP in an unknown manner, making a quantitative assessment of their response to the signal difficult. In order to overcome these problems, the base layer of 1% agar (w/v) was replaced with a base layer of 1 μM 1% cAMP agar (w/v). Diffusion of the cAMP remains approximately constant throughout the agarose, therefore the cells as the bottom are initially exposed to a greater concentration of cAMP than the cells nearer the top of the agarose, however, the concentration should be roughly constant for all cells at a certain depth into the agarose[496,682]. Additionally a recent study indicated that the strength of the cAMP signal only weakly affects the ability of *Dictyostelium* cells to respond to the chemoattractant signal by moving towards it when the cells are capable of signalling to one another, such as would be expected from the cells used in my experiments[410]. Other frequently used chemotaxis assays also use this diffusion-based method to establish gradients, such as the micropipette assay, under-agarose assay and Zigmond, Dunn and Boyden chambers[41,63,449,708,710]. Additionally, mammalian cells in vivo and *Dictyostelium* cells in the wild also experience gradients generated by diffusion, for example during development or immune response, where a chemokine, or chemoattractant is released from a population of cells, which then diffuses and is detected and in some cases propagated by other cells[134,143,302,383,496]. Agarose has been shown to be a useful material in which to establish a gradient, as it is capable of stabilizing chemoattractant gradients, both spatially and in time[338,341].

In *Dictyostelium* cell chemotaxis assays using a Zigmond chamber, cells are usually left for 20 minutes after the cAMP gradient is set up, before imaging is begun, to allow the gradient to establish[611]. Additionally a mathematical model of the diffusion of cAMP within a Zigmond chamber indicated that a stable gradient takes between 10 and 20 minutes to establish[496]. As the volume of agarose used in my experiments was greater than the volume of buffer used in Zigmond chamber assays, but smaller than that used in under agarose chemotaxis assays (~3 ml (3000 μl) agarose in my experiments, ~135 μl buffer in a Zigmond chamber and ~4 ml (4000 μl) in under agarose folate assays), I waited 30 minutes for the

gradient to establish, before commencing imaging[329]. By iteration, this time was optimum, as it allowed a gradient to establish and cells to be imaged chemotaxing (see results section, chapter 5), without wasting time and hard drive space acquiring images of motionless or non-chemotactic cells, and was not too late to miss single cell movement, when chemotaxis would have already occurred and only multicellular aggregates, or cells sitting atop the cAMP agar would remain to image. Moreover this allowed ample time for the cells to be taken to the OCT microscope and the microscope to be set up for imaging.

In this experimental configuration of a base layer of cAMP agar, the expected perfect direction of cell chemotaxis is much easier to determine than when a spot of cAMP was placed on the surface of the agarose, as it should be straight downwards until the agar layer is reached. The cells are unable to penetrate the agar layer as the 1% agar is too solid for them to penetrate (see results section, chapter 5). This method therefore potentially also allows for investigation of the behaviour of cells at this agarose-cAMP agar interface in addition to providing a simple experimental setup for investigation of 4D (3D+time) chemotaxis.

3.10 4D Stack Registration

A common problem with time-lapse microscopy is that of focus drift[78,322,473]. This can be caused by a number of factors, most commonly the microscope focus mechanism slipping[322,613]. This problem was encountered in the images acquired using the custom build OCT microscope, with the extent of the slippage between ~10 μm and ~150 μm dependent on the experiment. In an OCT B-scan (a side-on view), the focus drift appears as the image moving downwards over time. A fix was attempted, holding the stage in a fixed position by using pieces of metal to prop it up once the focus was found, however, although this worked to a certain extent and reduced the magnitude of the slippage (to approximately 50 μm maximum), some sample drift still remained, which required correction before cells could be accurately tracked.

A comparison between the axial positions of the first (0 minutes) and last (130 minutes) of an example stack is shown in Figure 3.9. Before software stack registration, the stack can be clearly seen to have shifted position in the side on view (Figure 39A). This movement is not seen after registration (Figure 3.9B).

Figure 3.9: Focus drift- original stack and corrected stack

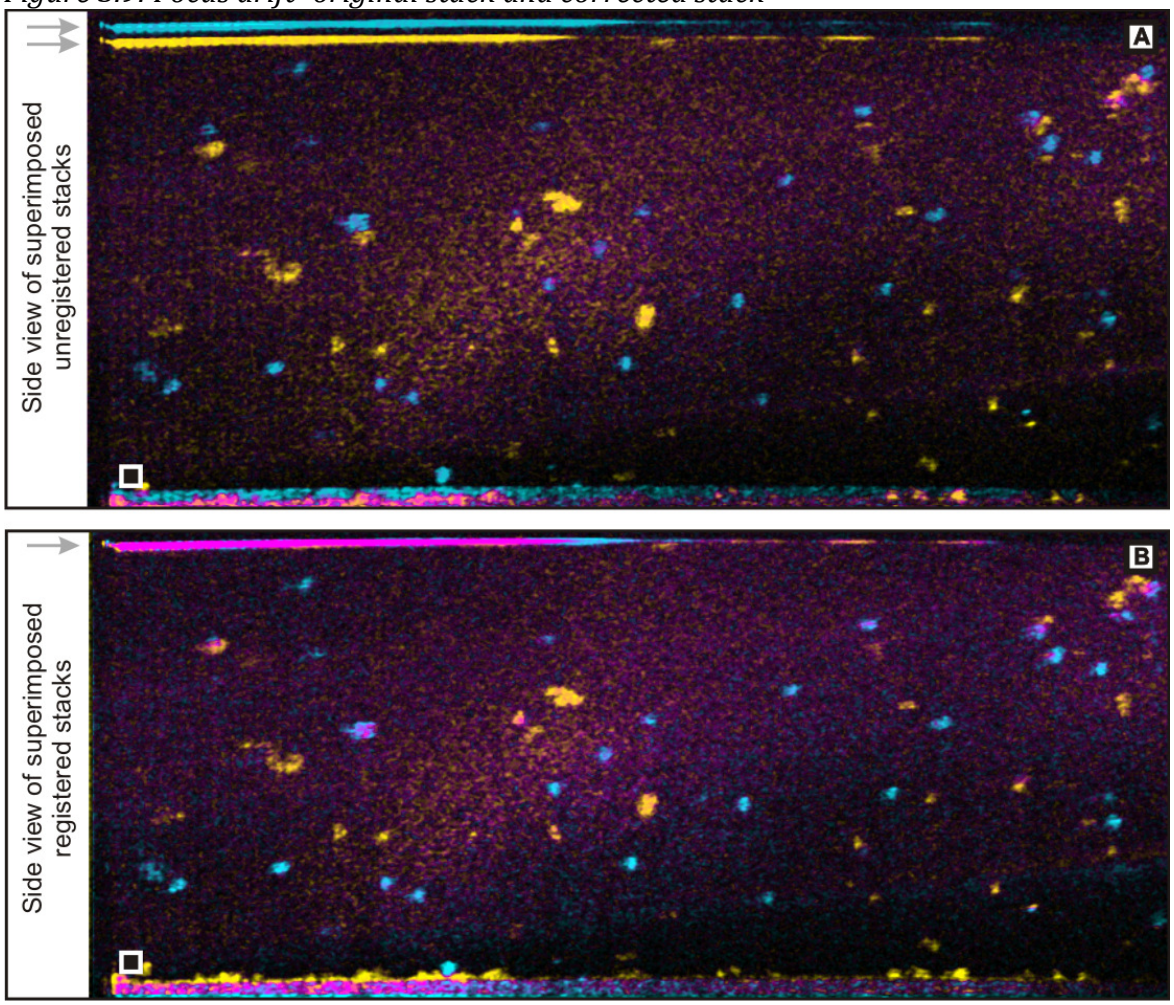

Figure 3.9: Superimposed false colour images of Ax2 cells pulsed for 5 hours, suspended in 0.5% agarose gel on a 1 µM cAMP agar base layer and imaged. Images are B-scan (side-on) views of slices summed over ~25 µm. The first time point, 0 minutes is yellow and the final time point, 130 minutes is blue. Magenta is seen where the yellow and blue exactly overlap. (A) Before software stack registration. (B) After software stack registration. The difference in position of the first and last slices on the tomogram is denoted with grey arrows. Scale bars are 20 µm.

Correction of this sample drift was attempted using software to align the stacks to one another after the tomograms were acquired and converted to the spatial domain. The first approach taken was to align sequential stacks to one another, beginning with the central stack, using a macro written in ImageJ. This macro made use of the plugins TurboReg, which aligns two images to one another, and StackReg, an extension of TurboReg, to align an entire stack of images sequentially, (Thévenaz P., Swiss Federal Institute of Technology, Lausanne, Switzerland), and PoorMan3Dreg which itself makes use of the aforementioned plugins (Liebling, M., California Institute of Technology, USA)[364,613] (see Appendix 3 for macro).

TurboReg uses an iterative algorithm, which attempts to determine the match between the two images and then distort the source image so that features in the source image are mapped to those in the target image[612,613]. It uses one of a number of user-specified transforms, which are implemented by use of matrix multiplication, and utilises polynomial spline interpolation, which the authors argue offers a good compromise between accuracy and speed, to align the source image with respect to the target image[613]. The transforms which the user can select between are a translation, rigid body, scaled rotation or affine transform. All of these transforms are performed by use of an affine transformation matrix, but vary in their degrees of freedom, so if a translation, rigid body or rotation is specified then the transform is restricted accordingly. For example, if, by inspection, the stacks only appear to move with respect to one another and do not warp or skew (as seen with the stage slippage) a translation would be sufficient for alignment[223,613]. Choice of 'affine transform' under these circumstances could result in artefacts as the algorithm attempts to correct some of the motion between the stacks by shearing, skewing, rotation etc. By use of 'translation', the algorithm is restricted in how it can transform the image to be registered; in this example, to a translation.

The TurboReg algorithm uses an image pyramid approach to register the images based on their pixel intensities[613]. This method is designed to reduce the time and computational cost of pattern recognition by separation of the original image into a set of images filtered into spatial frequency bands. This is achieved by iteratively subsampling the image. In order to avoid aliasing, the original image is smoothed (by convolution with a low pass filter) to remove the high frequency components prior to resampling. The algorithm uses a polynomial spline approach to generate the pyramid, as for the geometric transforms applied, in order to ensure internal consistency of the algorithm[613,629]. The patterns in the images are first matched using the lowest resolution image in the pyramid to register the coarse features in the image. The transformations applied are then passed to the higher resolution level of the pyramid, with

appropriate scale factors, so that only small corrections to accommodate the finer details present in the higher resolution images. This reduces the time and computational cost of pattern matching, as the majority of the iterations for registration use the low resolution images which are greatly reduced in amount of data. Additionally, it also reduces the chance of incorrect registration, which could occur if only the highest resolution images were registered because of the algorithm having an increased possibility of finding a local match between the images, a false minimum difference, which is not actually the optimum global match[3,613,629].

The degree of match between the two images is measured as the integrated squared difference of the intensity values between the source and the target image, i.e. the residual variance between the intensities of the source image and the target image (ε^2)[75,613]. This can be written as a function

$$\varepsilon^2 = \left\| f_R(x) - Q_p\{f_T(x)\} \right\|^2 \quad \text{(xii)}$$

where f_R is the reference data (target image), f_T is the test data (source image to be registered), and $Q_p\{f\}$ is a spatial transformation of parameters represented by p[75,360,613]. At each point of comparison the transformation parameters (p) are updated and applied to the test data (f_T), to find the optimum transformation to match the two images. Therefore, when the images match, the value of this function (ε^2) should be at a minimum with respect to p. The authors use an algorithm based on the Levenberg-Marquardt algorithm to calculate this minimum, by solving $\partial\varepsilon^2/\delta p = 0$[75,613,694].

The Levenberg-Marquardt algorithm, postulated initially by Levenberg in 1944 and rediscovered and improved upon by Marquardt in 1963, is a widely used optimisation algorithm which provides a solution minimising a non-linear function, using a least squares approach to assess the fit[75,400,613]. This algorithm initially approximates a steepest descent approach, a slow but robust method, until the solution is close to a local minimum and the residuals are small so that a quadratic estimation of the local curvature can be made, whereupon it then becomes the Gauss-Newton optimisation, a faster but less stable method. This switch between methods is achieved by use of a damping factor (λ), which is updated at each step to become smaller if the residuals decrease sufficiently and increased if the residuals do not. In this way, the Levenberg-Marquardt algorithm provides a stable and fast solution to nonlinear least squares minimisation[400,694].

The first step involves providing the algorithm with an initial estimate for p, the parameter vector. In this case, the initial condition is $p = p_0$, i.e. no transformation applied. It should be noted that if there are multiple minima and the initial estimate is far from the final solution, the algorithm will fail to converge. The multiresolution pyramid approach reduces the chance of this, as mentioned above[400,613].

The aim of the algorithm is to iterate and at each step produce values of p, updated by a step of δ_p, which aims to minimise ε^2 and therefore converge to a local minimum. The algorithm must be constrained by some pre-set parameters in order to define when iteration stops. These are the degree to which the match should be perfect (a minimum ε^2 value) and the lower limit in the amount of improvement gained between iterative steps (a minimum δ_p value)[612,613]. When the algorithm stops, the last updated parameter vector (δ_p) is taken to be the solution. In brief, the algorithm performs the calculation to determine the incremental step δ_p by taking the first order approximation (linear approximation) of the model curve and then calculating the Jacobian matrix (J), which represents the first order partial derivatives. The Hessian (H), a matrix containing the second order partial derivatives, which gives the local curvature of a function, can be obtained from the Jacobean matrix, under this linear approximation[400,694]. Solving for the minimum by setting the derivative with respect to δ_p to zero yields linear equations, which can be solved for δ_p[694]. The equation to determine the update between iterations, which blends elements of gradient descent and Gauss-Newton iteration is

$$p + \delta_p = p - (H + \lambda diag[H])\, \partial\varepsilon^2/\delta p \qquad \text{(xiii)}$$

$p + \delta_p$ is the updated parameter. p is the current parameter vector. λ is the damping factor, a factor which is updated with each iteration of the algorithm and reduces the influence of the gradient descent part of the algorithm. This value is increased when the error is reduced. $diag[H]$ is the diagonal of the Hessian matrix, which scales the gradient by the curvature of the function acting to create larger increments in $p + \delta_p$ where the gradient is smaller; and $\partial\varepsilon^2/\delta p$ is the derivative of ε^2 with respect to p[400,512,694].

In TurboReg, the transformation applied, to minimise the difference between the images, thus registering them, is saved, and can be called by other ImageJ plugins[612,613]. Specific details of the modifications to the Levenberg-Marquardt algorithm applied in the TurboReg

algorithm, implemented to improve the speed of the algorithm, are outlined in the paper Thévenaz, P. et al, 1998[613].

PoorMan3Dreg works by collapsing each time point to a single image by use of a projection and aligning the projected stacks using the TurboReg plugin. The user is given the choice of a translation, rigid body, rotation or affine transform to align the data and a choice of 'average intensity', 'max intensity' or 'sum slices' for the projection. The 'maximum intensity' projection and a translation were found to work best with my OCT data. The plugin requires all of the slices from the stacks to be aligned and the reference stack to be placed into a single stack, which was achieved using ImageJ. The number of slices in each of the original stacks to be aligned must also be specified, in order for the plugin to know where in the concatenated stack one original stack ends and the other begins. After selection of transformation and projection type, the stack to be aligned and the reference stack are projected and the transformation is calculated by TurboReg and saved. The transformation, calculated for a projected single image, is then sequentially applied to each slice of the original stacks, resulting in alignment of these two stacks in the y-direction (up and down in an OCT B-scan) and the x-direction (left and right in an OCT B-scan). As this plugin is not able to align the stacks in the z-direction (into and out of the plane in an OCT B-scan), due to this dimension being collapsed down (z-projected) in the initial part of the plugin, it cannot be said to register truly in 4D[364]. However, as the drift in the OCT images is largely axial, this method worked well on the OCT image stacks. In any data set where there was any drift in the z-direction, the stack was resliced from the right, aligned using the above method, and resliced again to return it to its original orientation.

Sequential alignment of the stacks was seen to result in some jitter between stacks, so a macro was written to align all of the stacks iteratively to the central stack, which performed better (see Appendix 4 for macro), removing the jitter.

In some cases it was necessary to adjust the 'minimum' parameter in the TurboReg plugin, which describes the minimum resolution which the lowest resolution image in the multiresolution pyramid can be, in order to achieve a better alignment of the stacks[612,613]. Unfortunately, in several cases, the algorithm used in the TurboReg failed to properly align the stacks. In this case, stacks were aligned using a macro based on a modified version of the macro to find the substratum location used with the 3D data (see Appendix 5 for macro). This macro first crops the image in half, keeps the bottom half, and then finds the interface in the manner described above for the 2D data (finding the maximum intensity value). It is

necessary to crop the image in half first so that only one interface is detected, as the images contain two interfaces and both interfaces cause high peaks of approximately the same value in the intensity spectrum of the pixels. Due to variations between images within a stack, the maximum value in one stack might be the bottom interface and the maximum in another stack being the top interface. This would result in the top of one image within the stack being aligned to the bottom of the other image. The bottom half was chosen for cropping merely because in the 4D chemotaxis experiments this was the location of the chemoattractant. The alignment works on a simple basis, taking the indices of the found maximum and cropping a certain area around it. The result is stacks of the same size with the maximum at the same pixel indices on each stack.

One problem with this method is that it was necessary to keep the total height of the stacks the same for proper comparison between time points. If the macro were to simply crop at the interface, the size of the stacks would increase, as the index of the maximum, and the position of the image on the stacks descended. In order to overcome this, a set size was cropped around the interface, resulting in aligned stacks of the same height. Furthermore, this method is unable to compensate for any motion other than axial focus drift. If the stacks aligned by this method had any lateral motion between time points (this was rare, but some small lateral drift was sometimes seen), the stacks were then aligned again using the method which uses the TurboReg plugin, which appears to perform best on my OCT images when there are only small differences between temporally adjacent image stacks.

Finally, if stacks were unable to be aligned by any of the above automated methods, an ImageJ macro was written to allow shifting of all of the slices of a stack by an amount which is input by the user. This method requires manual input for each stack as the amount of shift (in pixels) has to be previously measured by comparison of the stack to be shifted with a reference stack by eye, and input into the macro manually (see Appendix 6 for macro). Therefore, this method is extremely time-consuming for the user, as it requires constant manual measurement and input, but is useful for final alignment of stacks which failed to be properly aligned using the other methods.

3.11 Chapter 3 Summary

Resolutions were calculated and measured for our OCT microscope in order to ensure that they were sufficient for imaging ~10 μm diameter *Dictyostelium cells*. Sampling areas were decided on by trying different areas and choosing one that allowed a number of cells and desired features, such as streams and mounds, to be seen. Once this was a set, an appropriate sampling density was chosen in order to ensure a good SNR and meet the resolution limit of the system. The first problem identified as a part of the project was that of aberrations seen in the images caused by the objective lens. This lens was replaced with a stock telecentric objective manufactured by Thorlabs (Thorlabs, Inc., USA) which improved the distortions seen in the images. Another unanticipated problem was that of the standard image processing algorithm introducing striping artefacts into the images. This was solved by Dr Bernd Hofer of the Biomedical Imaging group at OPTOM, Cardiff University[260]. In order to image cells in 4D, it was necessary to set the cells in a 3D construct. Agarose was chosen as a suitable material in which to suspend cells, due to its melting and gelling temperature, among other considerations, while a base of 1 μM cAMP agar provided the chemoattractant source for chemotaxis experiments.

The final major issue identified during the course of the project was the most troubling one and proved to be the most challenging to overcome. The focus drift in the microscope was initially negligible and became worse in time, likely due to mechanical wear and tear in the focusing mechanism. This issue only became noticeable when comparing images from consecutive time points. Due to the processing times required (for the data stacks to be transformed from the spectral to the spatial domain and then further processed for easy visualisation of 3D time-lapse, involving collapsing the volumetric data to a single transversal image for all of the time points and then importing the 2D images as a time series), a number of image sequences were taken before this issue was noticed. The first approach to fix the stage in place failed to completely solve the issue, although an improvement was seen, so software solutions were investigated and attempted. Using these it was possible to register the stacks, with some iteration.

The development of these methods and protocols enable Optical Coherence Tomography to be used as a method to investigate cell migration and aggregation in 3D (2D+time) and in 4D (3D+time), revealing insights into cell behaviour and the mechanisms regulating cell motility under these conditions, which are inaccessible to conventional microscopy techniques without staining or otherwise tagging the cell.

Chapter 4: Ax2 *Dictyostelium* cells on opaque substrates

4.1 Chapter 4 Aims

As investigations into the multicellular behaviour of *Dictyostelium* largely use nitrocellulose or agar surfaces, on which cells are developed, and studies of individual cell behaviour are usually performed on glass or plastic substrates with the cells suspended in KK2 buffer, any effects that these differing substrates and experimental conditions have on the behaviour of the cells are relevant when direct comparisons between results from these different assays are made. This chapter aims to answer the question of whether OCT is a useful tool for studying cell migration on opaque substrates and obtaining quantitative data describing this process, and whether the differing experimental conditions of two commonly used assays have any effect on Ax2 *Dictyostelium* cell migration.

4.2 Cells and their surrounding environment

The effects of substratum and surrounding environment on cell behaviour have been of interest to cell biologists since the early twentieth century[106,118,164,244,660]. As outlined in the introduction, the environment in which cells are grown can have a great effect on their behaviour, morphology, adhesion and proliferation[24,95,119,419,477,577,707]. However, many of these environments and engineered substrates are opaque, and therefore inaccessible to conventional microscopy techniques. Therefore, due to limitations in imaging and other technologies, this area of research remained a niche, with most cells being grown and experimented on, on glass or plastic surfaces. With the advent of new technologies in more recent years, great interest has been shown in the effects of environment on cells, and in the potential to drive cell behaviour to the desired outcome using biomaterials and other engineered substrates.[14,24,124,283,305,554].

Research into this area is largely concentrated on mammalian cells, particularly directed differentiation and increasing cell viability, driven by the tissue engineering and stem cell industries[283,305,311,419,688]. Studies of cell migration have been fewer, and often predominantly focused on cancer cell invasion[232,626,663]. However, the phenomenon of contact guidance has long been known and it is recognised that cell migration can be influenced by environment and substratum topography[106,118,137,152,240,303,305,482]. The effects of different substrates on cell behaviour have been explored for many years, yet the detailed mechanisms behind this complex process have yet to be fully elucidated[14,106,468].

OCT is an imaging technique which was initially used for imaging the eye, but has since diversified into other areas, particularly skin, dental and cardiac imaging[7,567,609]. Due to there being no requirement for cell labelling and the non-invasive nature of the technique, it has shown promise for imaging cells and tissue on opaque surfaces as well as for characterisation of scaffold and substrate properties[56,359,371,467,597,606,608,689].

4.3 *Dictyostelium discoideum*, development, environment and assays

The environment surrounding the cell is able to have an effect on the character of its migration. In addition to the chemoattractant cAMP, phototaxis towards light can play a role in the directed migration of *Dictyostelium* cells[55,423]. Temperature and chemical cues (for example, the presence or absence of oxygen and pH) can also have effects, as can micron-scale topographical features[18,55,150]. *Dictyostelium* mutants with deficits in aggregation and development have been created in order to aid understanding of the processes within a cell that regulate chemotaxis and migration[530,651]. The behavioural effects of these mutations, or the effects of pharmacological treatments, are studied either by development assays on nitrocellulose or agar where the cells aggregate and develop naturally; or by chemotaxis assays involving individual cells on glass or plastic[143,651,709].

4.3.1 *Dictyostelium* developmental assays

The behaviour of *Dictyostelium* cells in a large cell population is commonly observed by seeding of cells onto a surface of either agar, or 0.45 μm pore nitrocellulose filters resting on prefilters, soaked to saturation[55,492]. Under these conditions the cells are in contact with buffer underneath, but are in contact with air above. The behaviour of the multicellular aggregates can then observed by inverted light microscopy, imaging though the agar, or with a stereo microscope and a time series can be recorded with an appropriate camera[143,569]. *Dictyostelium* cells can also be developed under KK2 buffer, often on glass or plastic Petri dishes, allowing for easier imaging, for example with DIC microscopy, although this is less common[128,648]. The above assays allow comparison of the multicellular behaviour of *Dictyostelium* mutants or drug-treated cells with the expected behaviour seen in their parent wild-type strain or untreated

cells[143,488,595,648] and often focus on any morphological differences which can be seen in the mounds, slugs (if formed) and culminants[488,530,595,651].

4.3.2 Dictyostelium chemotaxis assays

Typical *Dictyostelium* chemotaxis assays focus on the observation of the behaviour of single cells on a glass or plastic substratum[416,611,651,669]. These cells are rendered chemotactically competent, often by artificial pulses of 100 nM cAMP at 6 minute intervals, the approximate interval at which *Dictyostelium* cells are exposed to their own intrinsic signal during development[611,625]. This enables all of the cells to experience the same level of cAMP stimulation; something which may not happen during starvation and subsequent development, due to the cells being different distances from the origin of the local cAMP oscillations. Cells are then placed into a transparent chamber for imaging, usually made of glass or plastic completely immersed in a buffer[611,669,708,709]. After the cells have settled, chemoattractant is placed at one side, with buffer at the other, and the movement of single cells towards the chemoattractant is observed and/or imaged with light microscopy, frequently DIC microscopy[611,709]. The behaviour of individual cells is often quantified, by use of tracking software, and comparisons between the behaviour of individual wild-type and mutant or drug-treated cells are frequently performed[611,665].

4.4 The two different experimental configurations

I have considered two common assays with *Dictyostelium*, which have been briefly outlined; on a smooth surface such as glass or plastic, and on a surface with a rougher texture, a nitrocellulose filter. The surfaces, nitrocellulose, agar and polystyrene plastic imaged with scanning electron microscopy (SEM), as outlined in the methods section, are shown in Figure 4.1. The difference in roughness (caused by differences in the scale of the irregularities in the material) between the surfaces (Figure 4.1A-C) and structure of the nitrocellulose surface can be clearly seen (Figure 4.1B, E, G)[24]. Both the agar and plastic Petri dishes have smooth surfaces under SEM at low and medium magnifications (Figure 4.1 A&C, D&F). It should be noted, however, that the agar required dehydration prior to SEM imaging[11,440]. As a 1.8% KK2 agar gel (as used for experimentation) is ~98% KK2 buffer, which itself is largely comprised of water, much of the original content of the agar is lost due to this dehydration,

and the structure may appear different due to shrinkage[306,603,650]. Although texture has previously been seen in images of agar and agarose, it has emerged that this porosity may itself be an artefact of dehydration, as hydrated samples imaged by use of an environmental SEM do not show these pores[306,443,603]. Additionally atomic force microscopy of agar surfaces has indicated that agar surfaces are of a smoothness comparable to glass[584]. The nitrocellulose appears completely different to the agar and plastic surfaces under SEM, with a grainy appearance at low magnification (Figure 4.1B), which at medium magnification is rough in appearance and mesh-like (Figure 4.1E). At high magnification the nitrocellulose filter can be seen to be comprised of multiple pores (Figure 4.1E&G). A yellow scale marker of 10 μm shows the approximate diameter of *Dictyostelium* cells, to give an idea of the scale of the pores and surface features of the nitrocellulose relative to the cells (Figure 4.1G).

Figure 4.1 Electron microscopy images of nitrocellulose filter and plastic Petri dish

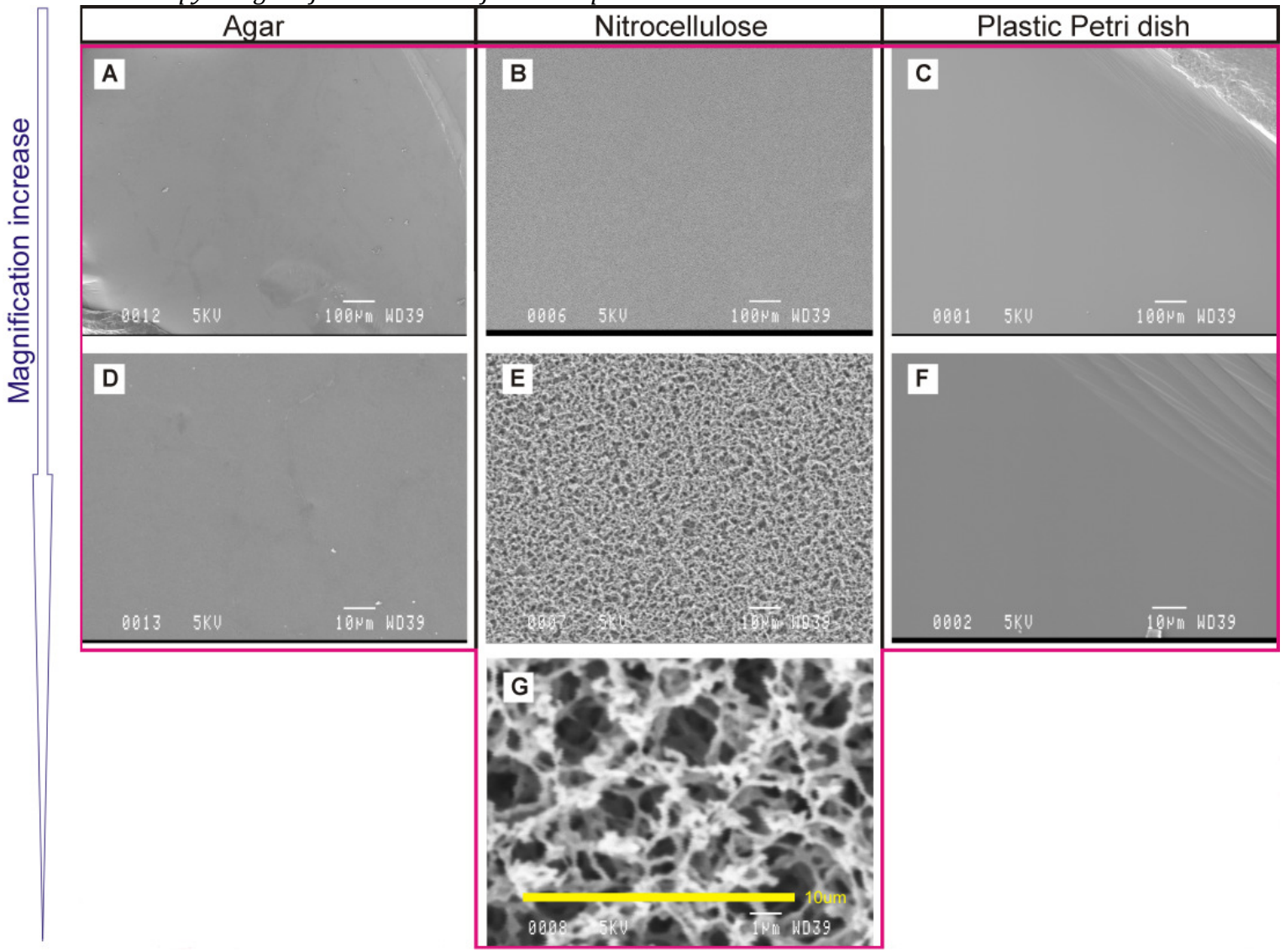

Figure 4.1: Electron microscopy images (enface) of (A&D) Agar (B, E, H) Nitrocellulose filter (C&F) Polystyrene Petri dish. (A-C) At low magnification (D-F) Medium magnification (H) High magnification, nitrocellulose only, as the polystyrene and agar images did not reveal any additional detail. (B, E, G) The nitrocellulose filter is grainy in appearance. At higher magnification levels the pores comprising the filter can be resolved. (G) A 10 µm scale bar in yellow shows the approximate diameter of a *Dictyostelium* cell to give an idea of the scale of the features on the nitrocellulose filter relative to the size of the cell.

The above assays, for development and chemotaxis, can be performed alone or in parallel to examine the motility and morphology of a mutant or drug-treated cell line, but a comparison with the expected behaviour, i.e. the behaviour of the untreated wild-type parent strain, is important for proper analysis of the functional effects[611,665]. While this is a valid test of the effects of the drug or mutation under certain controlled conditions, what is not taken account of are any effects of the different substrata on the cell behaviour. Most often, studies of multicellular aggregates of *Dictyostelium* are performed when the cells are on a substratum of agar or nitrocellulose, while the behaviour of individual cells is considered when the substrate is of glass or plastic[143,395,416,595,611,708]. Due to the non-transparency of the nitrocellulose substrate, and to a certain extent agar, single cell imaging on a nitrocellulose filter is inaccessible to the types of microscopy commonly used for imaging of single cell behaviour in glass chambers or on plastic Petri dishes, namely DIC, or occasionally phase contrast microscopy[665,669,682]. While it is possible to image single cells on opaque surfaces with epifluorescent microscopy techniques, this requires the introduction of additional processing steps into the experimental protocol[473]. It is also possible for dyes to interfere with the normal functioning of a cell, or introduce artefacts[49,126,473]. Therefore, single cell analysis is generally performed on glass or plastic transparent surfaces.

In order to see if there is an effect of the environment on the behaviour of the cells under these conditions, which are frequently used assays, cells have been imaged with OCT, which allows visualisation of cells on opaque substrates, on a nitrocellulose filter resting on pre-soaked (with KK2 buffer) Millipore prefilters and under KK2 buffer on a plastic Petri dish. The cells were seeded at the same density under both conditions, tracked using 2D-DIAS software, and subjected to subsequent statistical analysis. A nitrocellulose filter was chosen for these comparative experiments instead of agar, as the surface of the filter appears more different in texture, stiffness and topography to the plastic polystyrene, from which cell culture dishes are made, than agar, under SEM (Figure 4.1). The rationale behind this was that

the supposition that the greater the difference between the topography and texture of the surfaces, the increased likelihood of their having different effects on cell behaviour.

4.5 Ax2 cells imaged with OCT on a nitrocellulose filter, on KK2 agar and on a plastic Petri dish

Ax2 *Dictyostelium* cells were imaged on a nitrocellulose filter, KK2 agar and under KK2 buffer on a plastic Petri dish using the OCT microscope. Software written automatically collapsed the images into the enface plane at a small area around the substrate (~25 μm) for ease of visualisation. En face images were required to track the migration of the cells over the surface of their substrata with 2D-DIAS. OCT images of the enface and side-on appearance, and a 3D projection by Amira (Visage Imaging, USA) of these substrata, with Ax2 *Dictyostelium* cells seeded on them, are shown in Figure 4.2. The surfaces appear to have a different texture, with the nitrocellulose filter surface having a brighter and grainier appearance than the agar, and the plastic surface appearing almost invisible, but the differences between the nitrocellulose and the other surfaces is not as obvious as under electron microscopy, and the pores of the filter cannot be resolved (Figure 4.2). The appearance of the agar is rougher under OCT microscopy than that of the polystyrene plastic surface (Figure 4.2B-C). This is not seen in the SEM images (Figures 4.1B-C), and may appear in the OCT images due to light scatter from the arrangements of cross-linked and aggregated polymers which comprise the agarose gel[306,330,589,603,636]. The enface images also show a more textured appearance to the nitrocellulose surface, when compared to the agar, with the polystyrene Petri dish having almost no visible texture (Figure 4.2). The Ax2 *Dictyostelium* cells of approximately 10 μm diameter, which become longer and thinner when polarized, appear in the OCT images as bright spots against a darker (less scattering) background, on the agar, nitrocellulose and plastic Petri dish surfaces (Figure 4.2). These can be followed in time-lapse to obtain information about the characteristics of migration in the cell followed.

Figure 4.2 OCT images of agar, nitrocellulose and plastic surfaces seeded with Ax2 cells

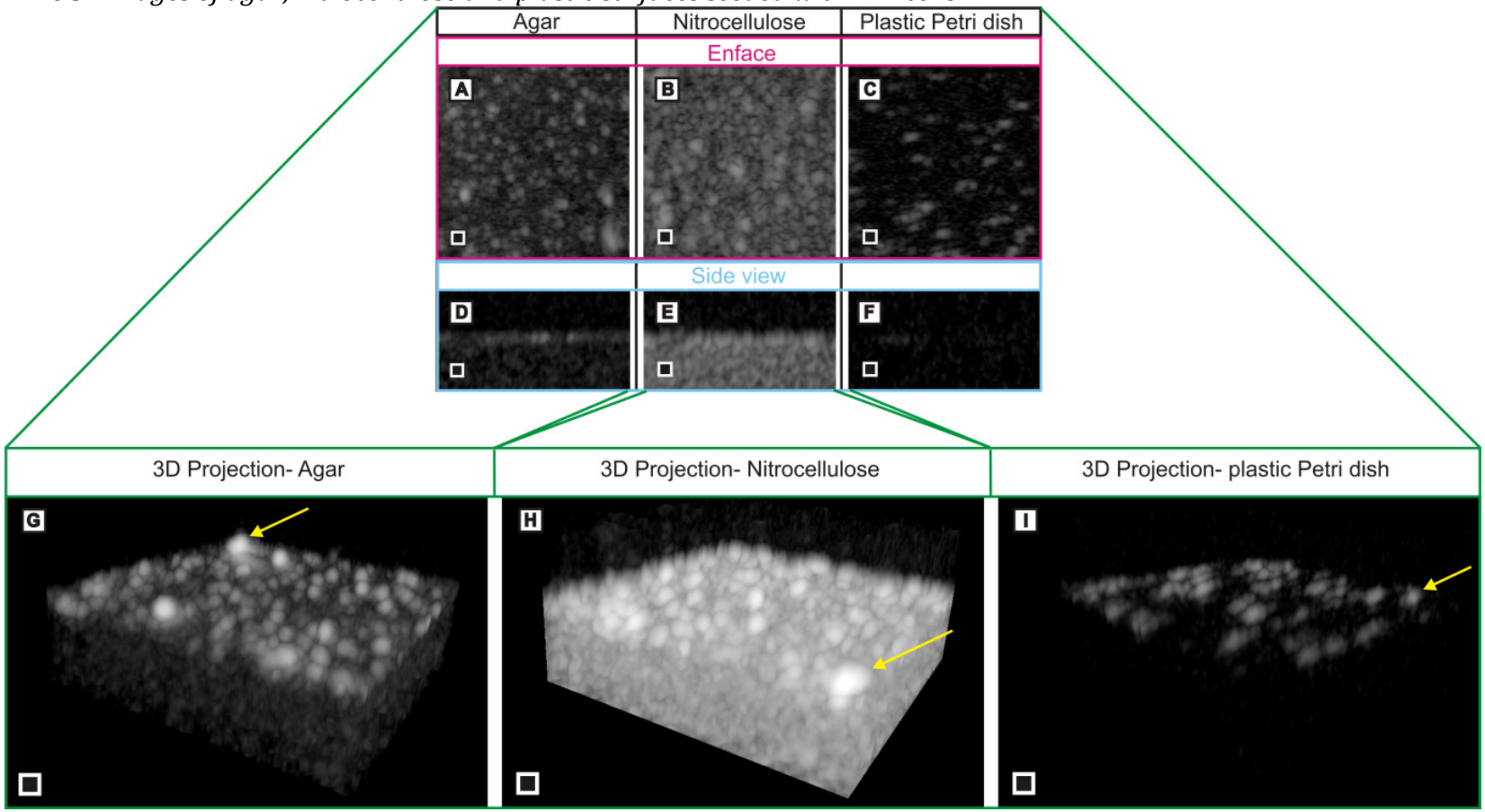

Figure 4.2: (A-C) Enface (one slice at the surface), (D-F) B-scan (side) (one slice from the beginning of the stack) and (G-I) 3D Projection OCT images (with Amira software (Visage Imaging, USA)) of (A, D, G) KK2 agar, (B, E, H) a nitrocellulose filter and (C, F, I) a plastic Petri dish, all seeded with Ax2 cells. The bright spots are cells and cellular debris, an example cell is indicated with a yellow arrow in each 3D image. The surfaces appear different in these images, but surface details cannot be properly resolved. Scale bars are 20 µm.

4.6 Ax2 Dictyostelium cells under two different conditions

Images of Ax2 *Dictyostelium* cells migrating on a nitrocellulose filter and on a plastic Petri dish under KK2 buffer were acquired every 30 seconds. These two surfaces were chosen as they are commonly used substrates for assaying development of *Dictyostelium* cells. As these assays generally allow the cells to intrinsically signal to one another after starvation, and do not rely on extrinsic application of cAMP, the Ax2 cells were seeded under starvation conditions 6 hours prior to imaging and allowed to spontaneously release waves of cAMP, their natural response to these conditions. 20 minutes of time-points were used for analysis, as this is sufficient time for visualisation of chemotaxis of *Dictyostelium* cells (slower moving cells would require much longer times to track effectively)[215,348,611]. The image stacks were collapsed into the enface plane by use of ImageJ macros prior to tracking and subsequent analysis, as described in the Methods section.

For the nitrocellulose filter surface, three different experiments performed on different days were used for the analysis, while for the plastic Petri dish substrate, two different experiments performed on different days were used. In order to determine if any effects of surface were restricted to cells exhibiting migration of a certain character, cells were assigned to two different groups based on features of their migration, and then manually outlined and tracked. These groups were called 'chemotaxis' or 'random movement'. *Dictyostelium* cells are motile when they are not chemotactic, but this motion is characterised by different features to chemotaxis[18,196,304,657]. It is a non-directional movement and involves pseudopods being extended at points all over the cell membrane[196,657,682]. The result is a cell which crawls around, exploring its environment in a seemingly random manner, although it has been argued that this process is not in fact entirely random[196,304]. It should be noted that although this usually refers to cells which are unstimulated, i.e. in the vegetative state, whilst the cells in my experiment had all been allowed to develop for 6 hours and so should have received some stimulation with cAMP[18,143]. The cells which I classified as randomly moving, for the purpose of this experiment, were those which were not moving directly towards a source of chemoattractant, but were motile.

The criteria used for classifying the type of movement were as follows: 1) the cells were motile, 2) cells which were moving towards a large multicellular aggregate, or towards a stream were classified as chemotactic, as the multicellular aggregate acts as a focal point for chemoattractant release in *Dictyostelium*, where the cAMP signal can be relayed from cell to cell over a distance of ~50 μm between cells[111,134]. Cells which were not moving towards a

multicellular aggregate or stream were classified as moving randomly. Cells which were possible to track with confidence through all the time-points were chosen for analysis. The same criteria were used for both conditions. Enface images of Ax2 cells on nitrocellulose filters are shown in Figure 4.3 and on Petri dishes under KK2 buffer in Figure 4.4. On the right hand side of the image, the tracks for randomly moving cells are shown in blue and for chemotaxing cells in yellow, superimposed on the first time point of the experiment. On the left hand side of the image, all of the time-points (41 acquisitions over 20 minutes) were summed together. This shows the general trend of the cell movement over the course of the time-points analysed, including cell streaming and location of formation of multicellular aggregates. Figure 4.5 shows the tracks superimposed on to one another, all starting from the same starting point (indicated by a yellow circle). The tracks have been reoriented so that the main direction of migration points upwards. The differences between the chemotactic cells and the randomly moving cells can be clearly seen with the chemotactic cells moving faster and more directly than the randomly moving cells. Any differences between the cells on the nitrocellulose filter and on the plastic Petri dish are difficult to visualise or assess qualitatively. Therefore quantitative analysis was performed.

For these experiments, speed was chosen as the first parameter for quantitative measurement as it has previously been shown to be affected by substrate topography on a nanoscale, with the trend that increased surface roughness increases cell migration speed[118,683]. Persistence, a measure of how directly the cell moved i.e. how much the cell turned while it was migrating with a higher value indicating more direct movement, was selected as the second parameter; as it was anticipated that, with the phenomenon of contact guidance in mind, topographical features on the surface could affect the cell's direction of motion, either by impeding it, or by providing additional surface for the cell to grip on to[106,118,683]. Indeed, the persistence of Schwann cells has previously been shown to be affected by alignment of strongly defined topographical features such as grooves and plateaus[422]. The speed of the cells in μm/min and the persistence of the cells, in μm/min-degrees, were calculated from tracks using 2D-DIAS (Soll Technologies Inc, Iowa, USA). These measured speeds and persistences, of the Ax2 cells under the two conditions of on a nitrocellulose filter and under KK2 buffer on a plastic Petri dish, are shown in Table 1 for randomly moving cells and for chemotaxing cells.

Figure 4.3: Ax2 cells on nitrocellulose filters

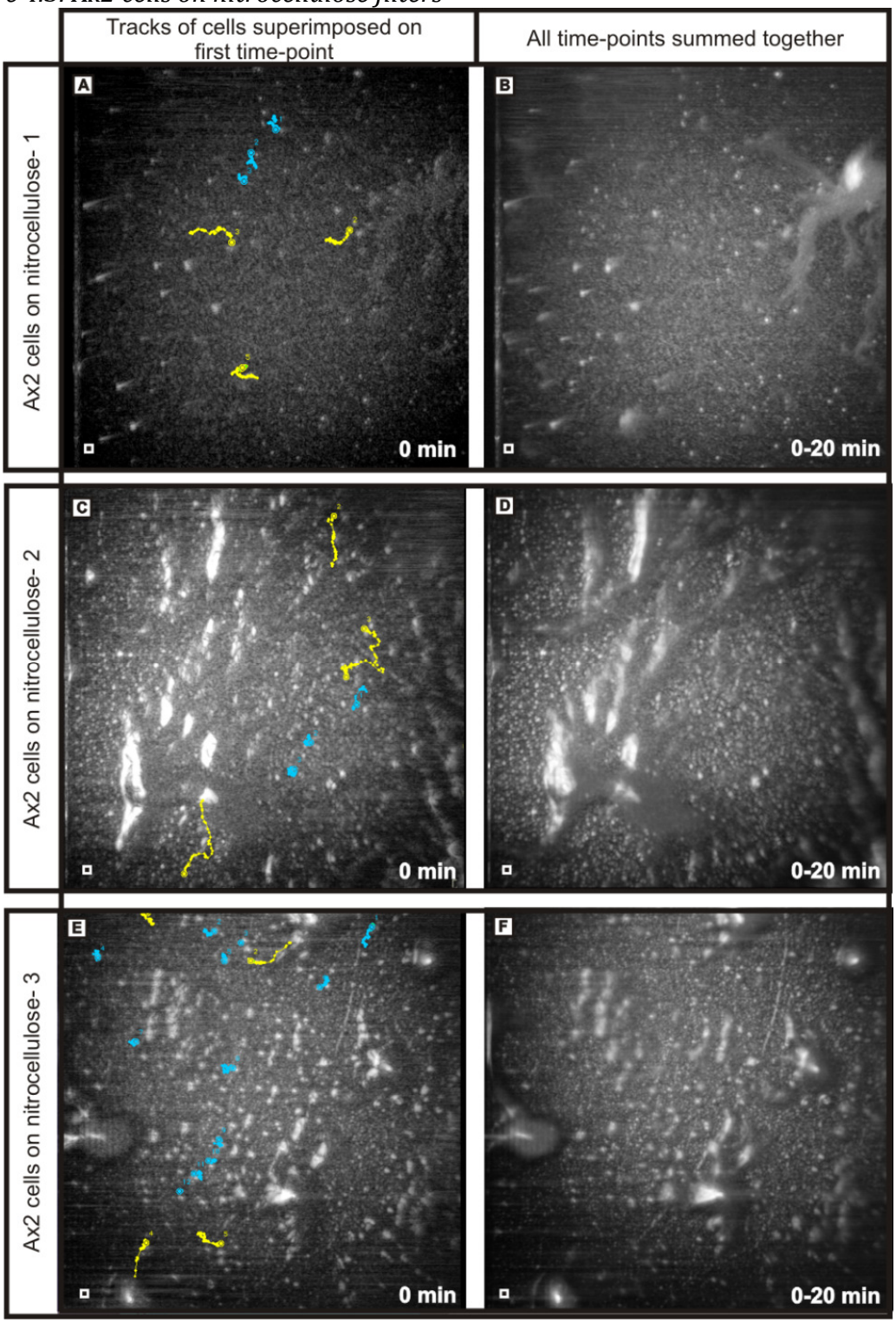

Figure 4.3: Ax2 cells imaged every 30 seconds over 20 minutes, 6 hours after seeding on a pre-soaked nitrocellulose filter. Stacks were collapsed into the enface plane and summed over ~20 µm for each time point. Three different experiments, (A-B) Experiment 1 (B-C) Experiment 2 (D-E) Experiment 3. (A, C, E) Cell tracks traced by 2D-DIAS superimposed on an image of the initial time point of the experiment. Yellow- chemotaxis tracks, Blue- random cell movement tracks. (B, D, F) Enface images summed over all time points with ImageJ showing the movement of the cells. Scale bars are 20 µm.

Figure 4.4: Ax2 cells under buffer on a plastic Petri dish

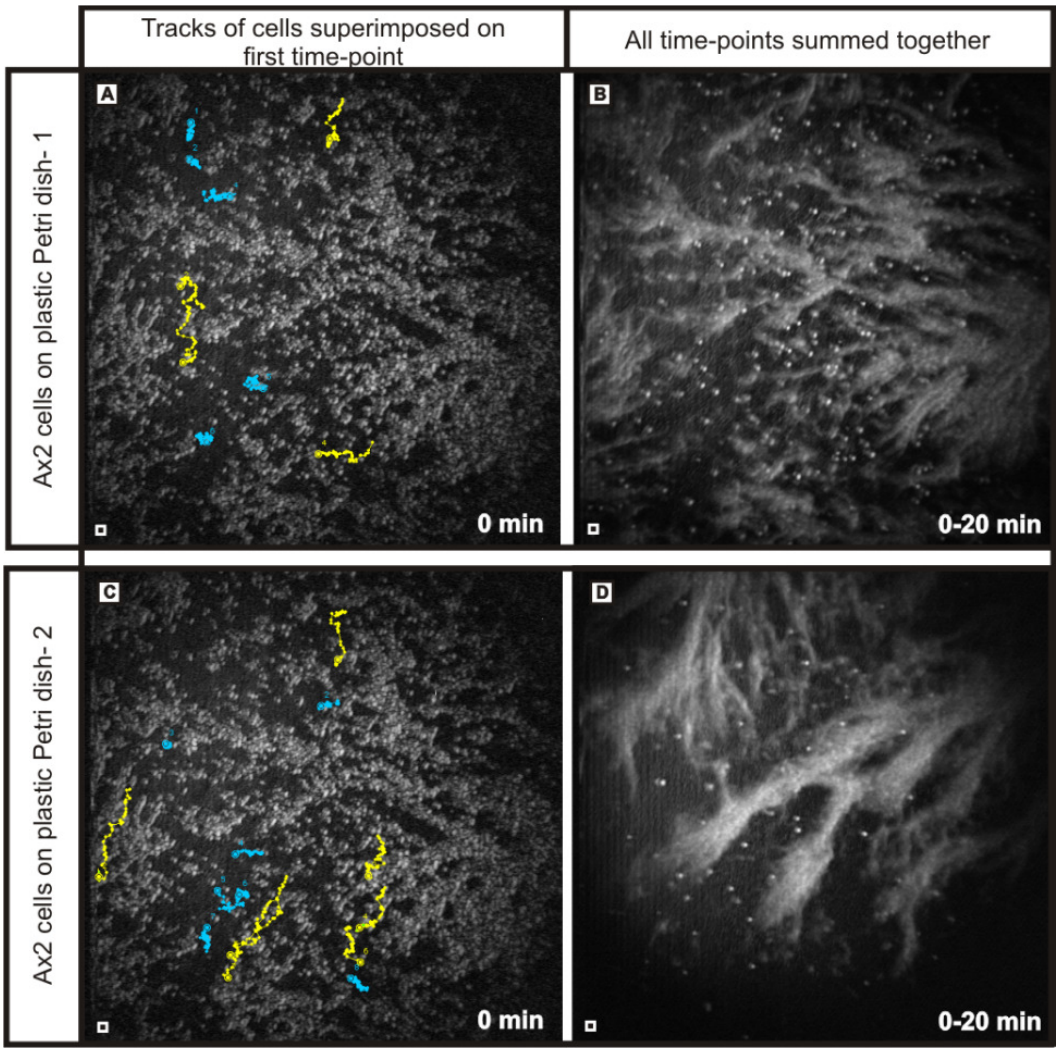

Figure 4.4: Ax2 cells imaged every 30 seconds over 20 minutes, 6 hours after seeding on a plastic Petri dish under KK2 buffer. Stacks were collapsed into the enface plane and summed over ~20 µm for each time point. Two different experiments, (A-B) Experiment 1 (B-C) Experiment 2. (A&C) Cell tracks traced by 2D-DIAS superimposed on an image of the initial time point of the experiment. Yellow- chemotaxis tracks, Blue- random cell movement tracks. (B&D) Enface images summed over all time points with ImageJ showing the movement of the cells. Scale bars are 20 µm.

Figure 4.5: Ax2 cell tracks on nitrocellulose and on a plastic Petri dish- chemotaxis and random movement

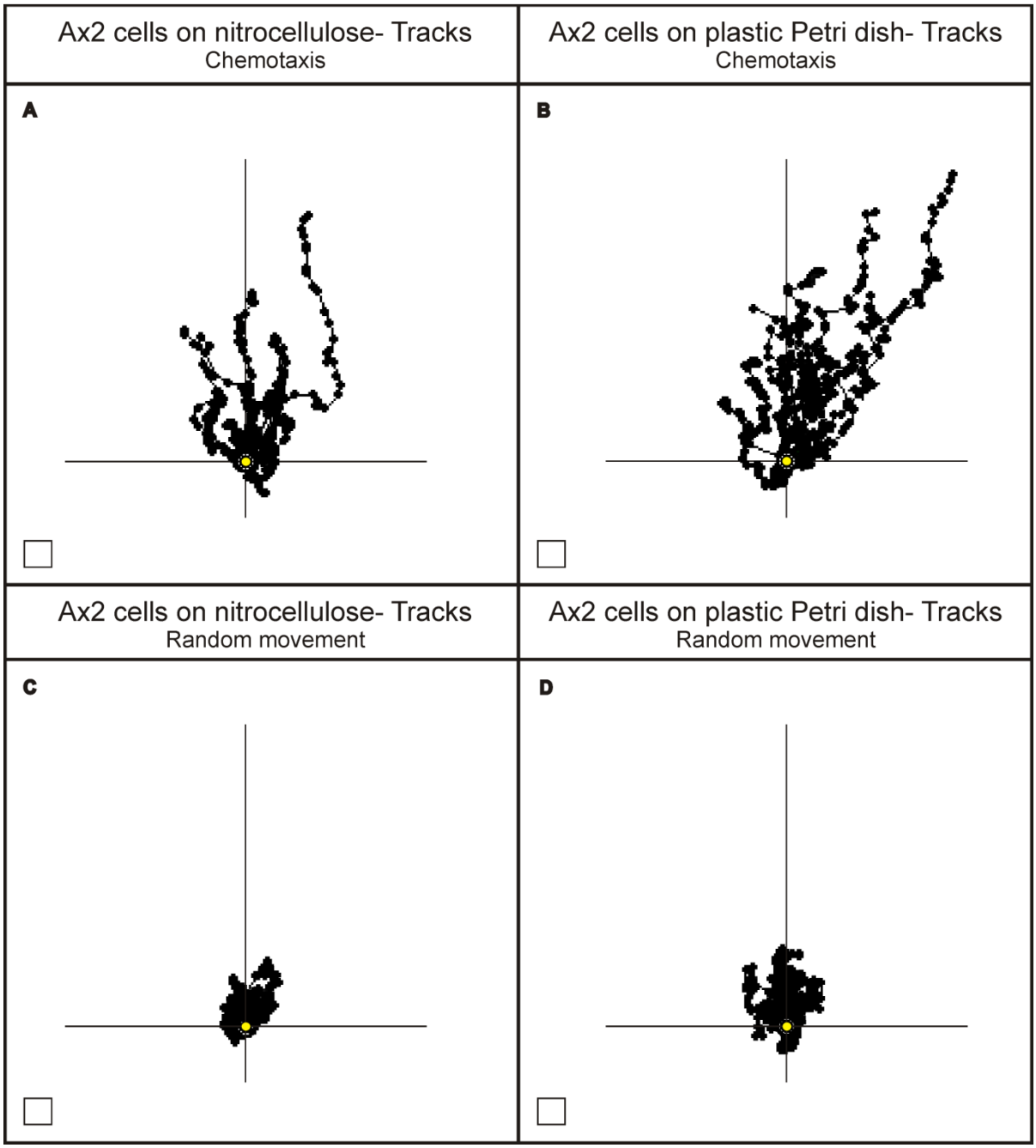

Figure 4.5: Superimposed tracks of Ax2 cells all starting from the same point and oriented so that the main direction of migration points upwards. Each track generated using 2D-DIAS software. Yellow dot indicates the starting point of the cell track. (A&C) On nitrocellulose. (B&D) On plastic Petri dish under KK2 buffer. (A-B) Chemotaxis. (C-D) Randomly moving cells. The cells can be seen to have moved further and more directly (i.e. turned less) when chemotactic than when randomly moving. Scale bars are 20 μm.

Table 1: Ax2 cells on two different surfaces- Chemotaxis, Random movement and Results of Statistical Analyses

Condition	Speed (μm/min)	Nitrocellulose vs plastic Petri dish Ax2 cells Speed	Persistence (um/min-degrees)	Nitrocellulose vs plastic Petri dish Persistence	Chemotaxing vs Randomly moving Ax2 cells Speed	Chemotaxing vs Randomly moving Ax2 cells# Persistence
Ax2 on nitrocellulose filter -random	3.35±1.21 (2.96±0.99)	**Random movement** U=38 Z=|2.96| p=0.03*	0.28±0.13 (0.26±0.15)	**Random movement** U=66 Z=|1.78| p=0.075	**Nitrocellulose Filter** U= 10 Z=|4.00| p<0.001*	**Nitrocellulose Filter** U= 8 Z=|4.09| p<0.001*
Ax2 on plastic Petri dish -random	5.03±1.86 (4.31±1.38)		0.40±0.20 (0.30±0.25)			
Ax2 on nitrocellulose filter -chemotaxis	6.95±1.99 (6.52±1.24)	**Chemotaxis** U=24 Z=|2.40| p=0.017*	0.81±0.36 (0.70±0.51)	**Chemotaxis** t=|-1.49| (dF=20) p=0.150	**Plastic Petri dish** U= 13 Z=|3.26| p<0.001*	**Plastic Petri dish** U= 8 Z=|3.57| p<0.001*
Ax2 on plastic Petri dish -chemotaxis	9.08±2.20 (8.30±3.9)		1.06±0.45 (1.00±0.51)			

Table 1: Grand means (±SD) and medians (±interquartile range) calculated from the mean values obtained for each cell. Medians in brackets. Random movement- Nitrocellulose filter n=18. Plastic Petri dish under buffer n=12. Chemotaxis- Nitrocellulose filter n=11. Plastic Petri dish under buffer n=11. Summary of the results of statistical analysis for Ax2 cells under two different conditions and between the two different conditions, * indicates significance at 95% CI.

In order to confirm that there were significant differences between the speed and persistence of the chemotactic cells and the randomly moving cells, i.e. that the two groups exhibiting different migration characteristics were significantly different from one another and therefore should not be combined into a single group, Mann-Whitney tests were performed, as the data were non-normal by inspection of a plot of the distribution and by Anderson-Darling tests at the 95% confidence level. The results show significance between the two groups (random vs chemotaxis) at a 95% confidence interval (CI) under all conditions (speed and persistence on a filter and speed and persistence on a polystyrene Petri dish) and are summarised in Table 1. The chemotactic group moved further and faster than the random movement group, and also turned less. This indicates that, regarding speed and persistence, the cells in the two groups were moving in a significantly different manner from one another, and could therefore be considered as two separate groups with different migration characteristics. The effect of substrata (nitrocellulose vs plastic) and environment (air vs KK2) on speed and persistence in these two cell populations was then assessed by statistical analysis. Where data were normal, a two-tailed T-test was used for statistical analysis and where data were not normal a Mann-Whitney rank-sum test was used[188].

Box and whisker plots showing the distributions of speed and persistence of the cells on the two different substrata are shown in Figure 4.6. These plots illustrate the differences seen between the conditions diagrammatically. Here it can be seen that there appears to be a larger difference in speed between the cells on the nitrocellulose and the cells on the plastic Petri dish than in persistence. Differences between the randomly moving and chemotactic cells can also be visualised by comparison across graphs, with the randomly moving cells having slower speed and decreased persistence.

Figure 4.6 Box and whisker plots of Ax2 cells in 3D (2D+time) under different conditions

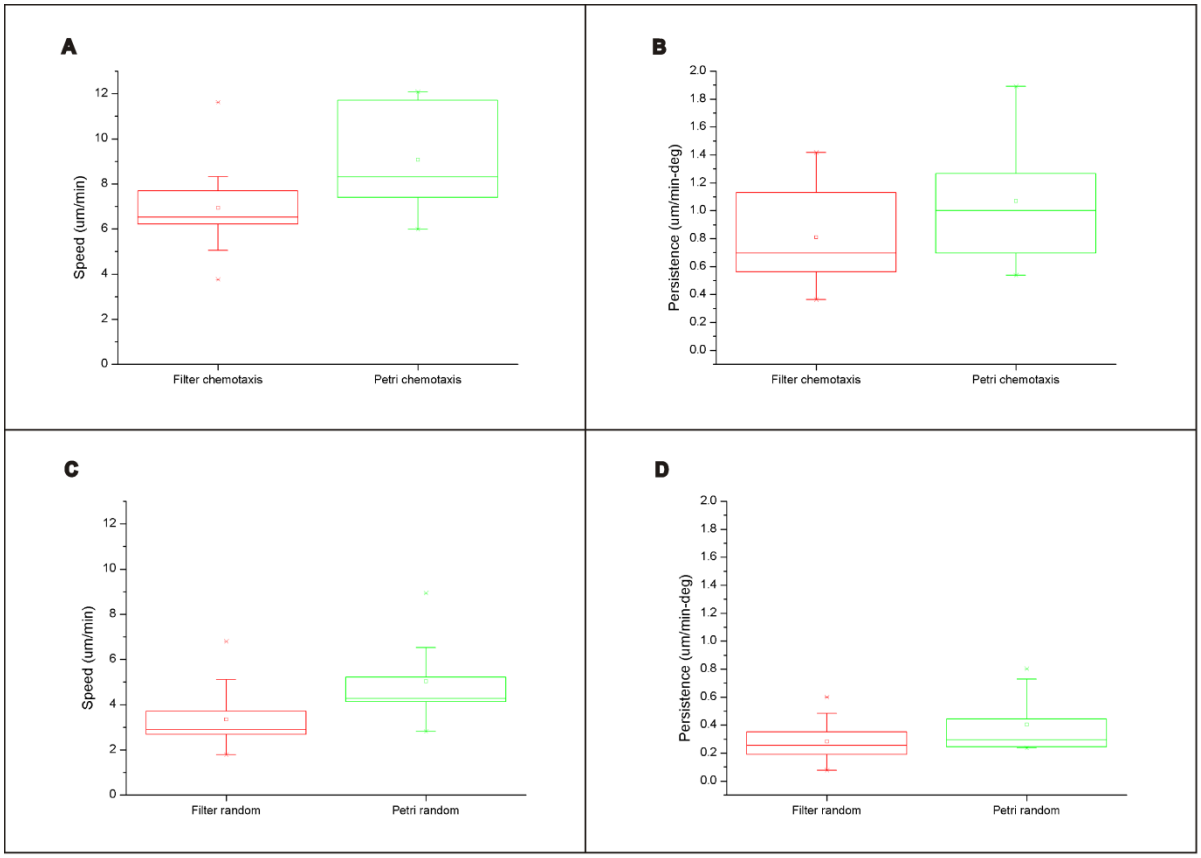

Figure 4.6: Box and whisker plots to show the distributions of speed (A&C) and persistence (B&D) of Ax2 cells left to aggregate for 6 hours under KK2 buffer on a plastic Petri dish and on a nitrocellulose filter. (A&B) show chemotaxing cells and (C&D) show cells moving in a random manner. The box shows the interquartile range, with the median value as a line across the middle. The small square box inside the boxplot is the mean. Whiskers represent the 5th-95th percentile of the data. Crosses represent the 1st and 99th percentile of the data. Data were obtained on three separate days for the cells on a nitrocellulose filter and on two separate days for the cells under buffer on a plastic Petri dish.

From Table 1, it can be seen that the speed of the randomly moving cells on the plastic polystyrene surface was greater than the speed on the filter by 1.68±3.07 μm/min and the persistence was also higher, with a value of 0.40±0.20 μm/min-degrees for the cells on the plastic surface and 0.28±0.13 μm/min-degrees on the nitrocellulose. This indicates that the randomly moving cells in the Petri dish under buffer were moving faster and turning less than on the nitrocellulose surface. For statistical analysis, the distribution of results for the speed on both the nitrocellulose filter and the Petri dish were significantly non-normal (Anderson-Darling test at 95% confidence, Nitrocellulose filter- p=0.021, Petri dish- p=0.019) The distribution of the results for the persistence was normal for the nitrocellulose filter but not for the Petri dish (Anderson-Darling test at 95% confidence, Nitrocellulose filter- p=0.422, Petri dish- p=0.005), so Mann-Whitney non-parametric rank-sum tests were used to test both parameters. The results of statistical analysis of the effect of the different conditions on the speed and persistence of randomly moving Ax2 *Dictyostelium* cells are summarised in Table 1. No significant difference is seen in the persistence between the two conditions of a nitrocellulose filter and a plastic Petri dish for randomly moving cells, as U=66, Z=|1.78| p=0.075, which is outside the 95% confidence level for significance (nitrocellulose n=18, Petri dish n=12). However, a significant difference at the 95% confidence interval is seen between the speed of the randomly moving cells under the two different experimental configurations, U=38, Z=|2.96|, p=0.03 (nitrocellulose n=18, Petri dish n=12).

From Table 1, it can be seen that the speed is 2.13±4.19 μm/min greater for the chemotaxing cells on the Petri dish than for those on the nitrocellulose. The persistence is 0.25±0.81 μm/min-degrees higher for the chemotaxing cells on the Petri dish, which indicates that the cells on the nitrocellulose filter were turning more. The distribution of the speed of the chemotaxing cells on the nitrocellulose was normal, but the cells on the Petri dish were non-normal (Anderson-Darling test at 95% confidence, Nitrocellulose filter- p=0.178, Petri dish- p=0.044) so a Mann-Whitney test is used for statistical analysis. The distributions for the persistence of both the nitrocellulose filter and the Petri dish conditions were normal (Anderson-Darling test at 95% confidence, Nitrocellulose filter- p=0.345, Petri dish- p=0.495) and a Levene's test indicated that the variances were equal (Levene's test p=0.576 (>0.05), F=0.324). Therefore a two-tailed Student's T-test was performed to see if the different conditions had any significant effect on the persistence of the cells. Table 1 summarises the results of statistical tests to see the effect of two different experimental conditions on the speed and persistence of chemotactic Ax2 cells. The Student's two-tailed T-test indicated that there was no significant difference at the 95% confidence level between the

persistences of the two groups of chemotactic cells, as p=0.150 (>0.05) (t=|-1.49|, 20 dF). A significant difference was found between the speed of the chemotaxing cells at the 95% confidence level, U=24, Z=|2.40|, p=0.017 with n=11 for the nitrocellulose filter and n=11 for the Petri dish.

4.7 Chapter 4 Discussion

Dictyostelium cells were successfully resolved and imaged with OCT at 800 nm wavelength on both transparent and opaque surfaces of agar, nitrocellulose and polystyrene plastic. The cells appeared to be well-adhered to the substrate in each case, and did not float away or become detached, even when disturbed, e.g. by moving the plate to the microscope for imaging. The differences in the textures of these surfaces were shown by use of electron microscopy and were also seen to a lesser extent in the OCT images. It was proposed that the different topological, chemical and other features of the surfaces may influence the migration of *Dictyostelium* cells.

In order to probe the effects of different environments on the behaviour and migration characteristics of cells, it is not enough to simply image the cells. The cells must be imaged with sufficient spatial and temporal resolution to enable tracking of cells with confidence throughout the duration of the required experimental period. The resolutions in my experiments were sufficient to allow manual outlining of motile cells by eye and the subsequent creation of tracks from these outlines with 2D-DIAS software . In addition, the technique used to visualise the cells should not interfere with the behaviour and vitality of the cells. OCT is widely considered to be a non-invasive technique which does not require any labelling or preparation of the cells[149,208,337]. Furthermore, in my experiments, laser power on the sample was kept below 1.8mW and switched off automatically between acquisitions, in order to keep any effect of laser light on the cells to a minimum. The cells were imaged migrating in time-lapse on both a nitrocellulose filter and on a polystyrene plastic Petri dish under KK2 buffer and subsequently successfully imported into software for cell-tracking (2D-DIAS), tracked, and analysed to obtain quantitative information. This chapter demonstrates that OCT microscopy can be used to image migrating cells on non-transparent substrates, resolving them with sufficient power to allow them to be tracked, chemotactic parameters to be measured and differences between experimental conditions detected. For example, between the speed and persistence of cells classified as chemotactic (moving more directly

and more rapidly) and randomly moving (moving more slowly and turning more); and between the speed and persistence of cells in different extracellular environments within these groups.

The experiments in this chapter show that, while these experiments do not detect a significant effect of the different surfaces (plastic Petri dish or nitrocellulose filter) and different conditions (surrounded by buffer vs on buffer and surrounded by air) on the persistence of Ax2 cells starved and subsequently allowed to develop for 6 hours, speed of these cells was shown to be significantly higher on the plastic surface under buffer than on the nitrocellulose filter. This effect was seen for both chemotactic and randomly moving cells, suggesting that the effect of surface seen here is not dependent on whether cells are moving slowly and turning more, or faster and in a more directional manner. This suggests an effect on basic cell motility rather than specifically on directional migration.

Prior experiments, by Arcizet et al with vegetative state *Dictyostelium* cells on microscale polydimethylsiloxane (PDMS) indicated an effect of topography on these cells, reducing the amount of directed cell motion when compared to flat surfaces, and therefore resulting in decreased persistence[18]. Speed was also found to be reduced overall when micropillars were present, although when the cells were moving in a more directed manner, the cells on the micropillar surface exhibited increased velocity[18,21,410]. It should be noted, however, that these experiments focused on comparisons of the effects of microfabricated structures against flat surfaces manufactured of the same material on cells in the vegetative state[18]. The structure of the nitrocellulose pores in my experiments is on the order of nanometres and the cells have been starved. Experiments by Li et al with aggregation stage *Dictyostelium* cells on amine functionalised surfaces found that the speeds of these cells were similar to those of similar cells on glass[18,361]. It would therefore seem that the effects of topography on *Dictyostelium* cells are considerably variable, depending on the physical, mechanical and chemical properties of the surfaces on which they are seeded and environments in which they are placed; and additionally on their developmental stage, as certain genes are developmentally regulated[333,528,646].

In the context of the scope of literature on the influence of macro-, micro- and even nano-topography on cell behaviour, it may seem somewhat surprising that no effect was seen on the persistence of *Dictyostelium* cells under the two different environmental conditions, however, much of these studies have focused on viability, growth, adhesion and differentiation, rather than specifically on migration, with increased surface roughness on the

submicron- to nano-scale having positive effects on these processes[24,95,118,688]. Nevertheless, contact guidance is a well-known phenomenon, and alignment of cells along topological features would certainly be expected to interfere with the persistence of the migration path taken by a cell, and this has been shown to be the case in the response of *Dictyostelium* cells to an etched glass interface[212]. Additionally, some studies have found that increased surface roughness can have positive effects on cell motility, increasing movement speed[118,119,327,626]. However, the elastic and chemical properties of the surface, as well as the scale and type of patterning have been shown to affect contact guidance[327,62688,200,373,482,510,626]. Nitrocellulose filters may not have the correct features for the occurrence of this phenomenon in *Dictyostelium*. Although contact guidance has been seen with ridges and grooves of down to approximately 70 nm, almost an order of magnitude smaller than the 450 nm (0.45 μm) pore sizes of the nitrocellulose filters, possibly other features of the surface do not promote this behaviour in Ax2 *Dictyostelium* cells[327,373,610]. Additionally, most of the literature available on cell-substrate interactions and contact guidance focuses on mammalian cells, largely due to the stem cell, biomaterial and tissue engineering industries; furthermore, on many different types of cells and cell lines, from neurones through muscle cells to leucocytes, with particular emphasis on tissue engineering applications[24,283,422,456]. It should not be forgotten that the effects of surface topography and functionalization on cells has been shown to vary by cell type, even among mammalian cells, and that, while *Dictyostelium* shares many cellular signalling molecules with higher eukaryotic organisms, there are still a number of differences at the genetic level and in protein sequences[88,134,200,373,510]. For example, in the context of cell-substrate interactions, no homologs of integrins have yet been found in *Dictyostelium*, although other adhesion receptors have been discovered, and force traction experiments have clearly shown that *Dictyostelium* cells are able to adhere to and generate force on their substrata[37,43,109,114,187,376]. The natural environments of *Dictyostelium* cells and mammalian cells are also quite unalike[55]. It may not be appropriate to apply information gained from mammalian cells to *Dictyostelium* and vice versa. Caution should also be applied in the interpretation of the results within the narrower context of *Dictyostelium* migration, and development assays, for example, these results for a nitrocellulose filter resting on saturated prefilters cannot be applied to cells on a dry nitrocellulose filter, as these physical and hydration properties can affect cell behaviour[24,118].

Broadly, there are two possible reasons why no significant differences are seen in cell persistence between the two environments, either the environments exert exactly the same effect on persistence, or they exert several different effects which in some manner interact to

the same effect on the cellular scale. The surfaces appear different to the human eye, and under electron (Figure 4.1) and atomic force microscopy, and also different in texture when touched by a human finger. Nonetheless, it cannot be said whether all of these textural differences necessarily translate well to the cellular level[118,548]. It should be noted here that is possible to quantify the roughness of a surface from an image of that surface, by use of texture analysis, a process whereby a surface can be described in terms of deviation from the ideal by a number of mathematical parameters[125,285,401,437,481]. Although these parameters have been reasonably well-characterised for 2D-surfaces and are used in some national standards, texture can be difficult to define[285,401,437,481]. Therefore, although texture analysis was not used here, as it can be complex, often utilising various methods of statistical analysis to select appropriate texture features to suit the particular application; it may represent a useful avenue for future study when investigating the effects of surfaces on cell behaviour[285,290,481].

An analysis of the physical and chemical properties of the two surfaces was considered to be outside the scope of this experiment and therefore was not undertaken, but by observation it was seen that the nitrocellulose was more flexible and deformable than the polystyrene. The literature reveals that cells migrate faster on stiffer substrates, and this was seen in this chapter, with cells moving faster on polystyrene plastic surfaces. However, this appears to refer primarily to gels and matrices, and while it was possible to bend the nitrocellulose filter by hand, it is a solid material and is unlikely to be significantly deformable[136,303,372,626,662,688]. Neither material could be considered to be 'soft', which may cause problems with the stability of cell-substrate interactions, as they become disrupted by the traction force generated by the moving cell[24,167]. Extremely high hydrophilicity may also disrupt the formation of cell-surface interactions, as cell-surface binding proteins are not well adsorbed under these conditions[24,453]. From the manufacturer's website, nitrocellulose was said to be a hydrophilic surface, although the degree of hydrophilicity is not given[166]. The polystyrene Petri dish is also likely to be hydrophilic, due to it being manufactured for cell culture[24,516]. Cells adhere optimally to reasonably (i.e non-extreme) hydrophilic surfaces, because of adsorption of any proteins mediating cell-substrate interactions[24]. Both the nitrocellulose filter and polystyrene Petri dish are likely to fall into this category, as they are designed for cellular compatibility. The porosity of nitrocellulose was given as 79%, as it is composed of small pores of 0.45 μm. The polystyrene Petri dish does not have pores of this size, as can be seen from the EM microscopy images (Figure 4.1)[166]. Osteoblasts and corneal epithelial cells display increased adherence when seeded on a membrane with nano- and sub-micron- scale pores[240,707]. However, this could be because the basement membrane on which mammalian cells typically

rest in vivo is on the order of tens to hundreds of nanometres and the artificial structure mimics their natural environment[240]. *Dictyostelium* cells are not found on this type of structure in nature and so potentially have not developed this type of response.

Dictyostelium cells have been shown to be able to swim when not adhered to a substrate, however, this is not likely to be occurring in the experimental configurations used here as the cells were left to attach to their substrata for 6 hours prior to imaging[27,32,640]. Therefore, the living cells should be adhered to their substrates and not swimming freely in buffer[187]. Additionally, the OCT images were cropped at 25 μm around the interface, so any cells which were seen in the enface images were at a maximum of 25 μm from the substratum, which makes the cells which appear in the analysed images having no contact with the substratum improbable. Finally, the speed at which *Dictyostelium* swim was discovered to be in the region of 1 μm/min, a much slower speed than their speed of migration on glass, or their speed of migration measured in my experiments[27,32,309]. It is possible that the *Dictyostelium* cells on the plastic substrate under KK2 buffer are slightly less well adhered to the surface than those on the nitrocellulose filter. Cancer, epidermal melanocytes and *Dictyostelium* move slowly on cleaned glass because of very strong attachment, which can be reduced by coating with (human serum albumin) or mica (a non-adhesive mineral)[548,663]. Vegetative *Dictyostelium* sadA- mutants, which lack an adhesion receptor and are therefore poorly adhered to substrata are able to migrate, moving faster when compared to their wild-type counterparts[187,206]. Similarly TalinA mutants which have cytoskeletal defects and attach poorly to surfaces also show increased migration speed[79,448,622]. Potentially the Ax2 cells may be more strongly attached to the nitrocellulose surface than to the plastic Petri dish surface, resulting in a reduced movement speed[640]. This explanation does not, however, account for the fact that no significant difference was seen between the persistences of the cells under the different experimental conditions. The sadA- mutants also exhibit reduced persistence[187]. Therefore, it might be expected that the faster moving cells on plastic under KK2 buffer might have similarly reduced persistence. This was not seen, with mean persistence actually being higher for the cells on the plastic Petri dish than on the nitrocellulose filter, although this difference was not found to be significant at the 95% confidence level.

An alternative possibility to explain the reduced speed of *Dictyostelium* cells on a nitrocellulose surface relative to that seen on a plastic Petri dish surface, is that on this substratum the cells take increasing time to anchor to the surface, resulting in a slower measured speed. The edges of the pores of the filter are thin (<0.5 μm wide) and separated by holes which are microns

apart. This is illustrated in Figure 4.7, the nitrocellulose filter at the highest magnification with the edges reproduced here and marked with orange arrows, for clarity. *Dictyostelium* pseudopodia have been shown to be approximately 5 μm in size[59,581,582,641]. Because of these large gaps and the relatively small size of the edges of the pores, the pseudopodia may have to extend further or possibly even alter direction in order to adhere to the substratum properly, subsequently allowing the cell to move[210,582,640,657]. Bunemann et al have argued that the process of cell adhering to the substratum plays only a small role in the migration speed of *Dictyostelium* cells, postulating a model whereby detachment of the cell from the substratum is the rate-limiting step in cell migration speed, which contradicts what I have outlined here[76,287]. However, their model relies on there being a fixed number of potential adhesion points randomly distributed around the membrane of the cell, which are always located at a point where they are able to easily attach to the substrate[76,210]. As I have suggested, this may not be the case on the nitrocellulose surface.

Figure 4.7: Electron microscopy image of the nitrocellulose filter

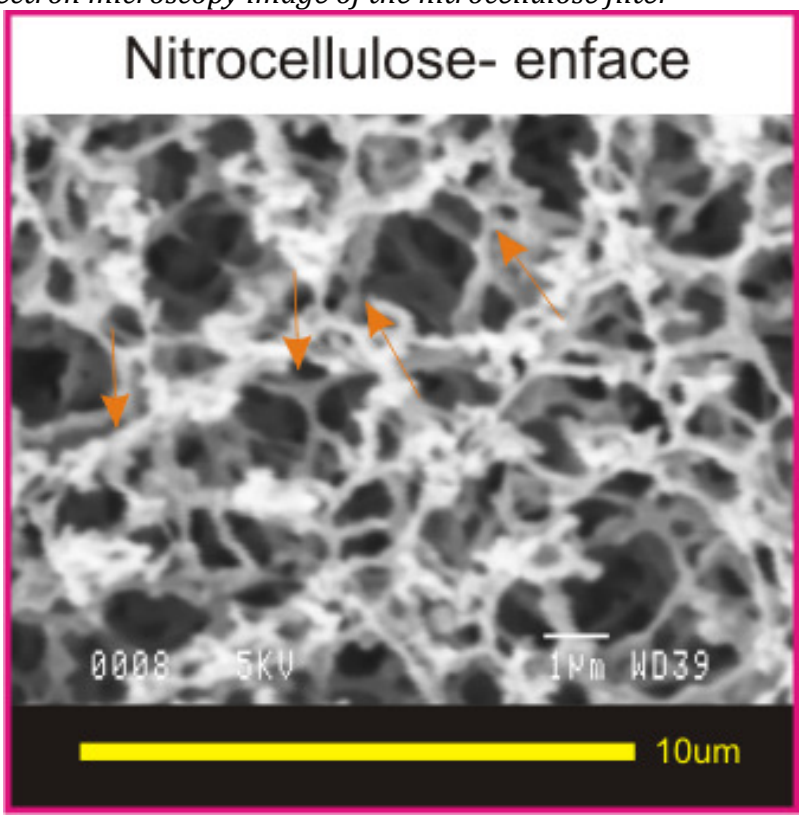

Figure 4.7: Electron microscopy image at high magnification from Figure 4.1 made larger and annotated for clarity of explanation. Orange arrows show the approximate edges of two pores which appear to exceed 1 μm in diameter. A scale bar showing the approximate diameter of a *Dictyostelium* cell is shown beneath the image in yellow.

Another possible explanation for an observed reduction in speed, but not in persistence of the *Dictyostelium* cells on the nitrocellulose filter is that the cells moved through the pores of the filter instead of over the top of the surface. It is possible for cells to squeeze through gaps of up to 10% of their diameter and, although the pore size of the filter is stated as 0.45 μm diameter, the electron microscopy images revealed a meshwork structure of several layers with pores on each layer of a couple of microns in diameter (Figure 4.7, orange arrows)[48,145]. As I have tracked the cells on the surface in the enface plane only and have summed around the surface over approximately 20 μm, I have tracked only the motion of the cells over the surface. If the cells are migrating through the pore of the nitrocellulose rather than directly over the surface, with motion in the horizontal as well as lateral plane, then their actual path length exceeds that which has been tracked by this method (Figure 4.8). If this is the case, then their actual speed may not be reduced but only the apparent speed, calculated from this method of tracking, because they have actually moved a greater distance than has been tracked (i.e. their displacement over the surface is less than their actual path length, Figure 4.8). It is not possible to determine whether or not this is the case with this microscopy technique as the nitrocellulose filter too highly scattering, making it extremely difficult to resolve cells from the background within its pores, and the resolution of the system is insufficient to resolve the pores of the nitrocellulose.

With *Dictyostelium* being a commonly used model for the study of chemotaxis and cell motility, and a significant difference in speed between both chemotaxing and randomly moving *Dictyostelium* cells on two different commonly used substrata seen, caution should be applied when comparing results from cell migration experiments performed on different substrates.

Figure 4.8: Diagram of cell migration through nitrocellulose pores

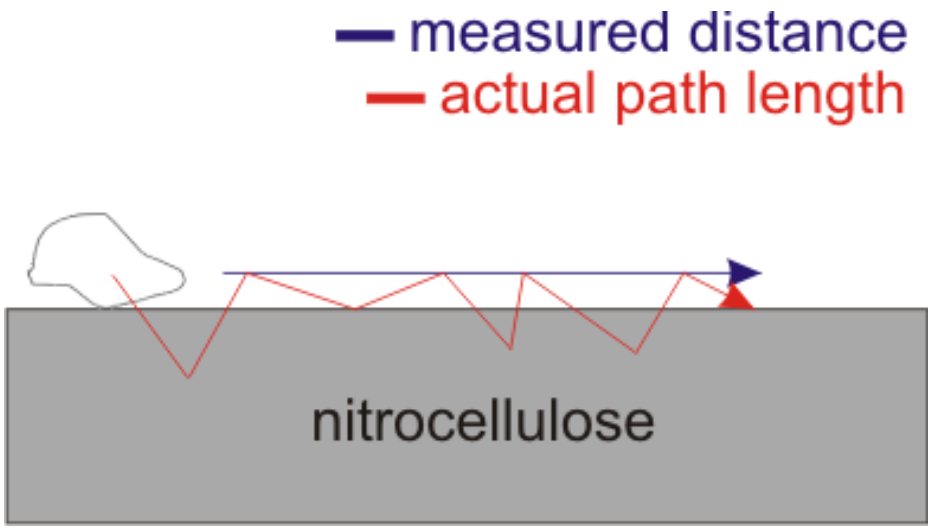

Figure 4.8: Schematic of a cell migrating through pores of nitrocellulose below the surface. The actual distance the cell moves is shown in red, while the measured distance by which the cell displaces across the surface is shown in blue. The measured distance is less than the actual distance moved by the cell, which results in a lower measured speed for this cell than the actual speed.

4.8 Chapter 4 Summary

Chapter 4 aimed to explore the possibility of imaging single migrating *Dictyostelium* cells on opaque surfaces, which is not readily achievable without staining for conventional light microscopy techniques; and subsequently to use this tool and the methods and protocols developed to investigate the effects of two different experimental conditions on Ax2 cell migration, both random motion and chemotaxis. The motivation behind this was to allow for a fairer comparison of results obtained, as individual cells are usually studied on glass, while the behaviour of multicellular aggregates is commonly explored on nitrocellulose filters or agar surfaces. Initially the utility of the label-free non-invasive technique of OCT for imaging motile cells on opaque substrates with sufficient spatial and temporal resolution to enable them to be tracked and subjected to quantitative analysis with complimentary software tools was demonstrated. Subsequently experiments comparing the effects of two commonly used development assays on the speed and persistence of Ax2 *Dictyostelium* cells were performed. It was discovered that there was no effect of substrate (nitrocellulose or plastic) and surrounding medium (plastic and KK2 buffer or nitrocellulose and air) on the persistence of Ax2 cells classified into groups as randomly moving or chemotactic, but a significant difference was found between the speeds of the cells in both groups, with the cells on the plastic Petri dish moving faster. This result should be considered when drawing conclusions from cross-comparisons of cell motility experiments under different conditions and on different substrates.

Chapter 5: Ax2 *Dictyostelium* migration and chemotaxis in 4D (3D+time)

5.1 Chapter 5 Aims

As the natural environments of both *Dictyostelium* (soil) and mammalian cells (tissue) are complex three-dimensional (3D) environments, bearing little resemblance to the planar glass substrates commonly used for cell culture and experiments, there is increasing interest in both culturing and experimenting with cells within 3D environments[55,172,606]. The goals of this chapter were to image Ax2 *Dictyostelium* cells within the three-dimensional environment of an agarose gel, and follow their migration in time-lapse. This was in order to explore whether this environment offers a useful way to present *Dictyostelium* cells in 3D and if OCT can be used to effectively study cell migration under these conditions. Additionally, to determine what information can be obtained from these OCT images on the character of cell migration in four-dimensions (3D+time) and how this migration and chemotaxis compares to what is seen on 2D surfaces.

5.2 Dictyostelium discoideum aggregation- why a 3D environment

As mentioned in chapter 4, one of the common methods by which cell chemotaxis and motility is investigated in *Dictyostelium* is through development assays, whereby starved *Dictyostelium* cells aggregate by chemotaxis and come together to form 3D multicellular structures comprised of thousands of cells[143]. Throughout this process, cells are attracted to one another by the chemoattractant cAMP propagating in waves over long distances[140,571,572,667]. Successful development is dependent on the proper control of cell migration and gene expression by this dynamic signal, so investigation of the mechanisms of this signal is essential for a full understanding of *Dictyostelium* chemotaxis and development[140,667]. To this end, these propagating waves can be visualised in both brightfield and darkfield microscopy images, although darkfield microscopy is most commonly used as the waves are more visible in this configuration[140,143,521]. The cAMP signals can be seen as waves because of the response of the cells to this signal[522]. After they receive the cAMP signal the cells respond by first rounding up (the cringe response) and then by releasing cAMP themselves, polarizing and moving directly towards the source[216,521,659,667]. However, after a few minutes, they stop both responding to and releasing cAMP, becoming insensitive to this signal[667]. Meanwhile, the local cAMP molecules diffuse away and the cells secrete a cAMP phosphodiesterase, which degrades the local cAMP[26,357]. The cAMP concentration begins to fall, which causes the cells to become re-sensitized to cAMP, in preparation for the arrival of

the next wavefront of cAMP[466,667]. The result of this is that cells switch between being polarized (more scattering) and unpolarized (rounded and less scattering) with the propagation of the cAMP waves, and this change can be visualised under microscopy as changes in light scattering caused by the population of cells changing morphology in a co-ordinated manner[104,388,571,572,667].

The processes of chemotaxis, aggregation and development of *Dictyostelium* have been well-studied on 2D planar surfaces, and to a certain extent within more complex environments, such as on soil plates, microstructured surfaces or under-agarose[18,142,492,544,682]. Although it is generally known that cells experience a complex three-dimensional environment in nature, and efforts have been made to replicate this in the laboratory, often there has been significant difficulty in visualising motile cells within these environments, due to the opacity of the matrix and the need to obtain rapid volumetric images[614,691]. Furthermore, some experimental protocols require destruction of the sample at the experimental end-point, precluding the possibility for time-lapse analysis[63,172,513,614,682].

In chapter 4, I have shown that *Dictyostelium* cell behaviour differs depending on the substrata on which the cells rest. This is likely due to differences in the physical properties of the surfaces in question (nitrocellulose and polystyrene plastic)[11,100,108,18]. Exploration of the effects of substratum topography and physiochemical properties on cell behaviour can be extremely useful, particularly in directed differentiation of stem cells, and development of biomaterials. Additionally, these investigations could go some way towards unravelling the mechanisms of cell motility and chemotaxis, particularly with reference to cell-substrate adhesion[419-421]. However, in collapsing the natural 3D environment of a cell to only 2D some information will be lost[142]. Furthermore, it appears that mammalian cells exhibit different behaviour and genetic expression on 2D surfaces than in their more natural 3D environment[15,30,45,95,221,461,477,607]. As *Dictyostelium* shares many genes and signalling molecules in common with mammalian cells, and a similar paradigm of cell movement, most markedly with leucocytes and neutrophils, the added dimensionality of a 3D environment may have an effect on the migration and chemotaxis of *Dictyostelium* cells[202,466,497]. Indeed, growth of *Dictyostelium* mutant cells on soil plates, a more natural 3D environment, has previously revealed phenotypes which were not apparent on 2D planar agar surfaces[492]. Therefore, in order to investigate the potential of an agarose gel, a widely available frequently used biocompatible substance, to act as a 3D environment in which to place *Dictyostelium* cells, Ax2 *Dictyostelium* cells were seeded within an agarose gel and imaged aggregating and chemotaxing

with OCT, which offers a non-invasive, label-free method for investigation of cell behaviour within 3D matrices[56,411,606]. To explore the possibility for this 3D environment to exert effects on cell migration, the time-lapse images were tracked and quantitative information on cell motility parameters was obtained, which was then compared to cells on 2D substrata.

5.3 Agarose- a 3D environment for Dictyostelium cells

Agarose is a hydrocolloid, originally derived from red algae and seaweeds[515]. Purified from agar, which consists of agarose (the gelling fraction) and agaropectin, it is a complex polysaccharide where the exact structure is dependent on the species from which it was originally derived. However, it is mainly comprised of alternating, galactose residues, linked together to form long polysaccharide chains, which aggregate to form double helices, joined together by hydrogen bonds[20,194,306,589,604]. It is frequently used in molecular biology and tissue engineering because of its biocompatibility and useful physical properties, such as thermo-reversibility, formation of resistant gels at low concentrations, the ability to vary the size of the mesh by alteration of the concentration of the agarose, and high hysteresis (difference between melting and gelling temperature)[174,286,312,339,443,451,515,616]. Low melting-point agarose was chosen as the material in which to place the *Dictyostelium* cells because of these properties, as discussed in chapter 3.

5.4 Ax2 cell aggregation and development in a 0.5% agarose gel

Figures 5.1 and 5.2 show Ax2 *Dictyostelium* cells which were placed within the three-dimensional environment of a non-nutrient 0.5% agarose gel, and imaged after 10 hours had elapsed with OCT, as described in the methods section, migrating and coming together in time-lapse (Figure 5.1A-F&K-P, Figure 5.2A-F over 2 hours). This demonstrates that *Dictyostelium* cells are able to signal to one another effectively, as they spontaneously undergo aggregation, and migrate within the three-dimensional environment of an agarose gel, and can form multicellular structures under these conditions[312,492]. The cells are shown at the streaming stage of development, and, although the majority of the streams formed at interfaces, either between the agarose and the air (Figure 5.1) or between the agarose and agar (Figure 5.2), some of the streams clearly extended through the agarose (Figure 5.1A-B&K-L) yellow arrows), confirming that Ax2 *Dictyostelium* cells are able to migrate through agarose in

multicellular cell streams. Streaming typically occurs at around 8-10 hours post-starvation in Ax2 *Dictyostelium* cells[109,190,492]. Multicellular formation had already begun by the initial acquisition time point, at 10 hours after starvation, with mound formation at around 12 hours of development (the final acquisition time-point), which is approximately the same time-scale as seen in development of these cells on a 2D surface[109,139,186,492]. As OCT is non-invasive and there is no fluorescent tagging of the cells, so photobleaching cannot occur, it is possible to follow the cells for a long time-period with no loss of signal intensity[473,508]. Figure 5.1G-J, shows Ax2 cells followed over a period of 5 hours of imaging (acquisition every 2 minutes). By the final time-point of the experiment, 15 hours after seeding within the non-nutrient agarose, the cells had formed a tight aggregate which had displaced approximately 50-60 μm from its original position (Figure 5.1I). The formation of a tip can be clearly seen (Figure 5.1I), indicating that the prestalk cells are able to differentiate and become sorted in this experimental configuration[139,572]. *Dictyostelium* development was not followed for any longer in this experiment due to limited space on the acquisition computer's hard drive for saving images.

Figure 5.1: Ax2 Dictyostelium cell streaming at the agarose surface

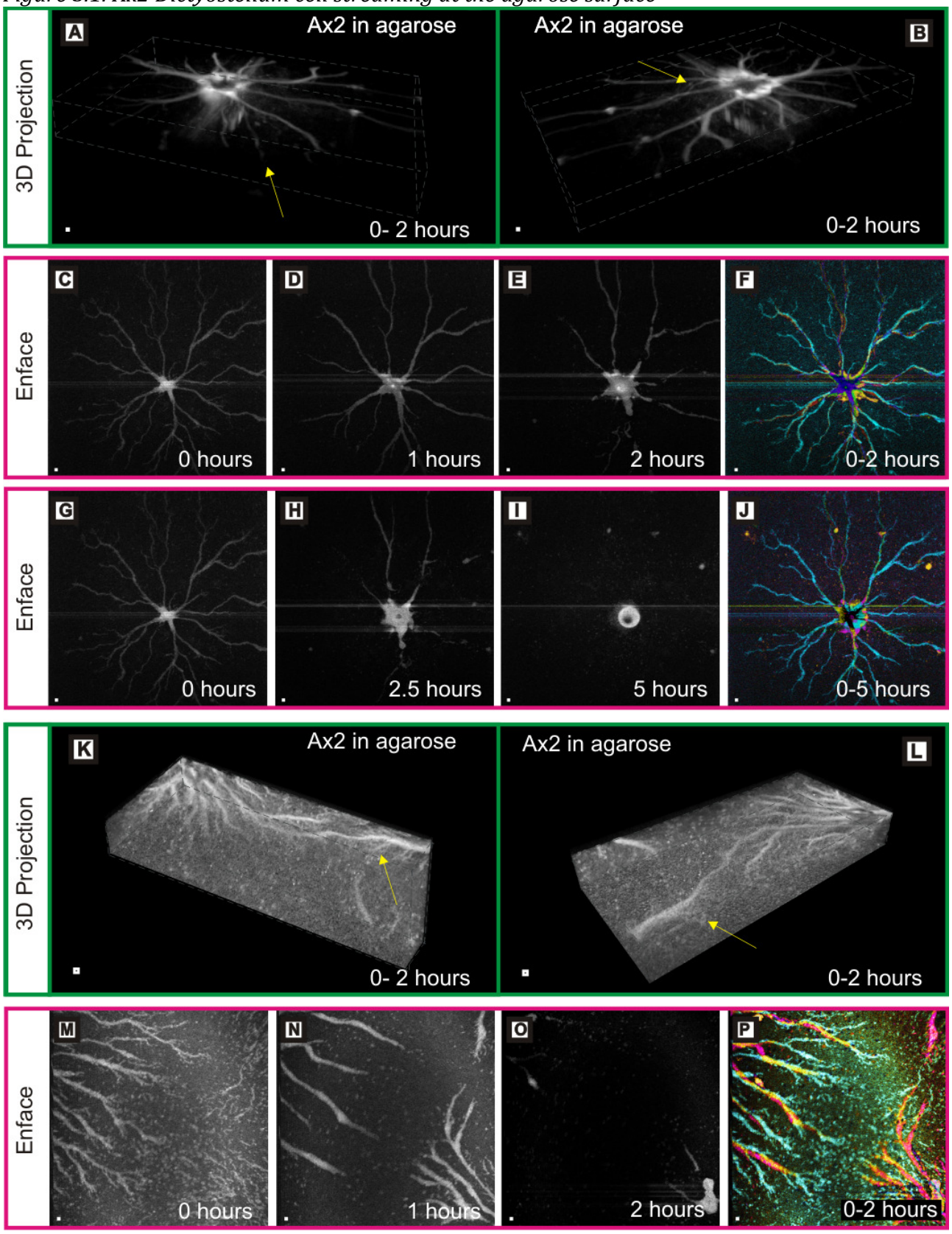

Figure 5.1: Two experiments from two different days showing Ax2 cells in 0.5% agarose on an agar base layer imaged ~10 hours after seeding. Images were acquired every 2 minutes (120 seconds). Cell streams are clearly seen at the surface of the agarose and within the agarose. (A-B&K-L) Volumetric renderings of the cells within and on the surface of the agarose generated using Amira software (Visage Imaging, USA). All of the time points are summed together using standard deviation in ImageJ to show the general trend of cell movement. Grey guidelines denote the edges of the image for ease of visualisation. Yellow arrow points to an example stream which extends below the surface of the agarose. (C-F&G-J&M-P) Images collapsed into the enface plane and summed over ~20 µm. (C,G&M) At 0 minutes (D&N) At 60 minutes (1 hour) (E&O) At 120 minutes (2 hours) (H) at 150 minutes (2.5 hours) (I) at 300 minutes (5 hours). (F&P) Superimposed enface false colour images of slices summed over ~20 µm, blue- 0 minutes, magenta- 60 minutes (1 hour) and yellow- 120 minutes (2 hours). (J) Superimposed enface false colour images of slices summed over ~20 µm, blue- 0 minutes, magenta- 150 minutes (2.5 hours) and yellow- 3000 minutes (5 hours). Scale bars are 20 µm.

Figure 5.2: Ax2 Dictyostelium cell streaming at the agarose- agar interface

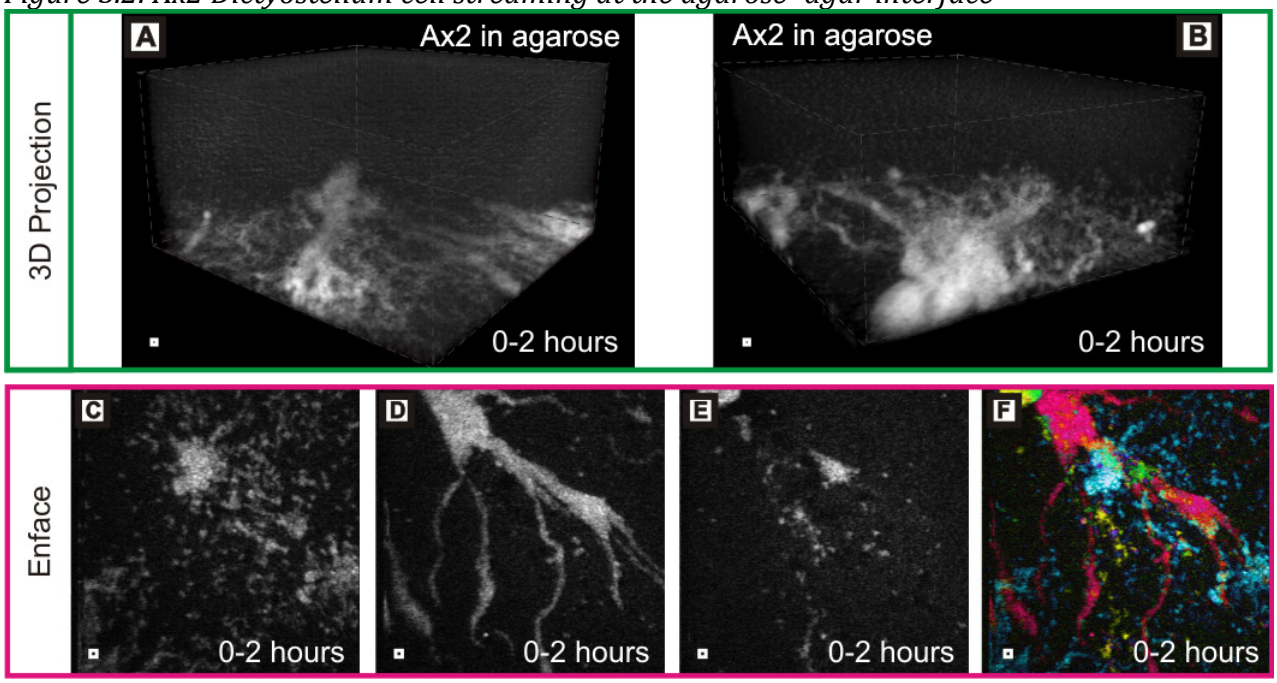

Figure 5.2: Ax2 cells in 0.5% agarose on an agar base layer imaged ~10 hours after seeding. Images were acquired every 1 minute over 120 minutes. Cell streams can be clearly seen at the interface between the agarose and the agar base. (A-B) Volumetric renderings of the cells within and on the surface of the agarose. Grey guidelines denote the edges of the image for ease of visualisation. (C-E) Images collapsed into the enface plane and summed over ~20 µm. (C) At 0 minutes (D) At 60 minutes (E) At 120 minutes. (F) Superimposed enface false colour images of slices summed over ~20 µm, blue- 0 minutes, magenta- 60 minutes and yellow- 120 minutes. Scale bars are 20 µm.

5.5 Ax2 cell-cell signalling within a 0.5% agarose gel

As the Ax2 cells aggregated in a manner comparable to that seen on 2D substrata, it has been inferred that they were able to signal effectively through the agarose gel[312,338]. Under starvation conditions, during multicellular development, cAMP pulses are released by *Dictyostelium* cells, and these pulses synchronise with one another, resulting in extracellular waves of cAMP originating from the centre of each aggregation point[572]. These waves can be visualised as optical density waves during development[143,571,572]. The optical density waves are caused by coordinated changes in cell morphology and motility occurring in a synchronous fashion in multiple cells as a result of cAMP signalling and can therefore give insights into the mechanisms of cell-cell signalling during the process of aggregation and development[143,357,572]. In order to see if these waves could be visualised propagating through the cells within a 3D environment in the OCT images, image subtraction was performed, whereby each image was subtracted from the following one. This was to enhance the differences between the two images, enabling the waves to be seen more clearly[142,572]. Figure 5.3 shows these wave fronts visualised as dark and light stripes seen within the streams, occurring at the surface of (Figure 5.3A-H, yellow arrows) and within the agarose (Figure 5.3A-B&I-J, orange arrows and yellow arrows), moving in time, demonstrating that Ax2 cells are able to signal to one another through the agarose and that the optical density waves, which represent the propagated cAMP signal as experienced by the cells, can be visualised using OCT[357,522].

Figure 5.3: Ax2 cells in 0.5% agarose cAMP waves

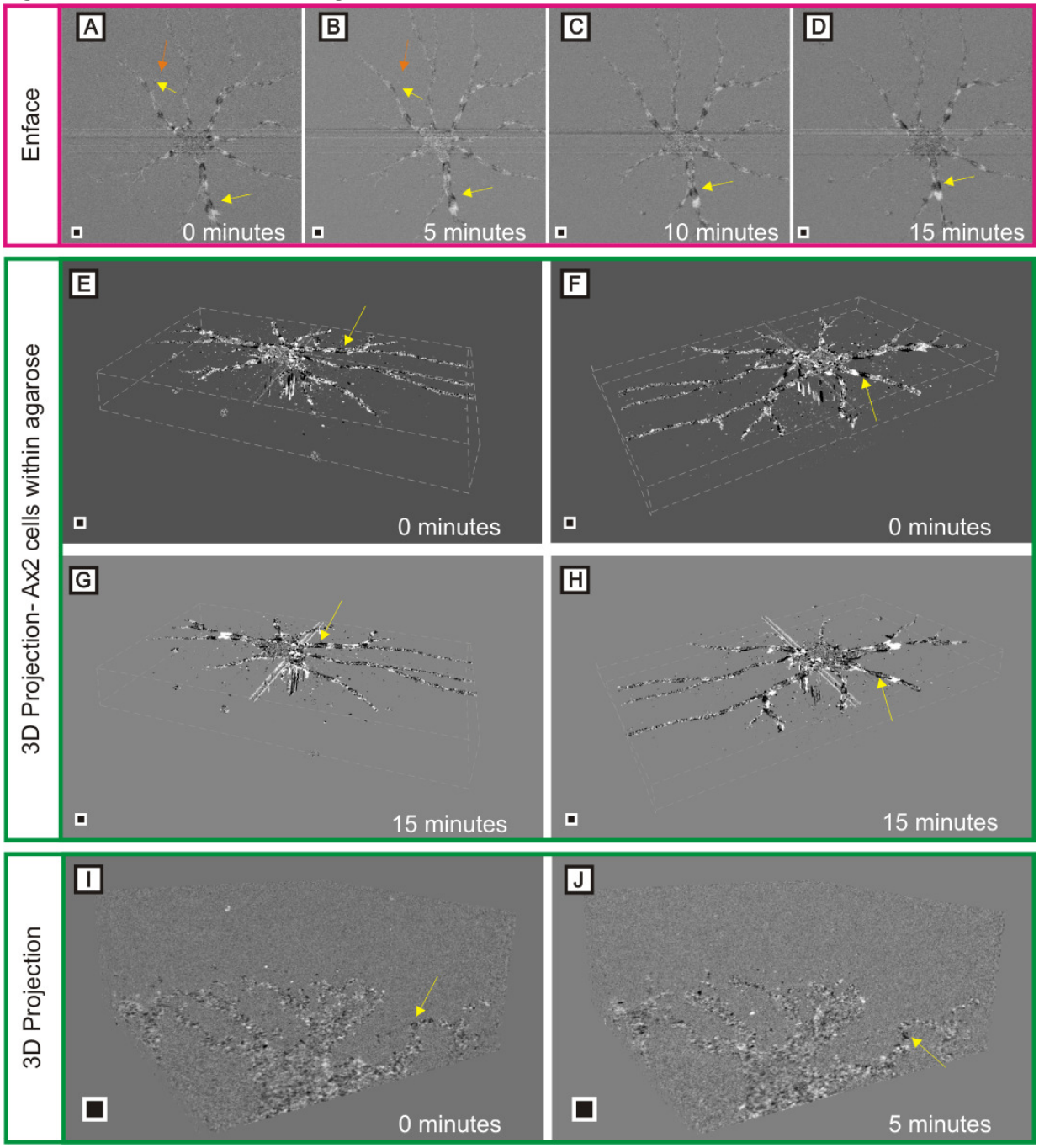

Figure 5.3: Optical density waves seen in a stream of Ax2 cells suspended within 0.5% agarose gel on a base of agar. Image subtraction has been used to enhance the visibility of these waves[572]. Yellow arrows show an example of a dark area (less scattering) consisting of multiple cells acting in a coordinated manner within the stream moving in time. Orange arrow indicates the remains of a stream which was below the surface of the agarose. (A-D) Streams occur largely on the surface of the 0.5% agarose, so images were collapsed into the enface plane using ImageJ and summed over ~30 µm round the surface of the agarose. A representative sample of 4 images is shown starting from approximately 680 minutes (11.33 hours) after initiation of starvation. 5 minutes elapse between consecutive images. (E-H) 3D projections from 2 different angles (E&G and F&H), created using Amira

software at the initial time point (E-F) and final time point (G-H) shown in the enface images. Grey guidelines show the edges of the volume for ease of visualisation. (I-J) Two volumetric images (Amira generated) from a different experiment on a different day, 5 minutes apart showing the movement of a dark area of cells in time, within a stream within inside the agarose gel. Scale bars are 100 μm.

5.6 Chemotaxis of Ax2 cells in 4D within a 0.5% agarose gel

Having explored the motility of Ax2 *Dictyostelium* cells within a 0.5% agarose gel and shown that cells are able to signal through the agarose and aggregate together to form streams and multicellular aggregates, I decided to attempt to visualise the chemotaxis of these cells within the agarose. Individual cell behaviour was difficult to assess in the previous experiments, as there were few single cells remaining outside of multicellular aggregates by the commencement of imaging. Additionally, previous work had suggested that sometimes cells fail to develop within an agarose gel, and that when development did occur, different colonies were not found to be at the same developmental stage[312]. Although I did not see this in my development experiments with Ax2 cells, this did not preclude the possibility of this happening. Therefore, in order to ensure that all of the cells were at the same developmental stage and were not aggregated by the initiation of imaging, the cells were pulsed prior to imaging, as described in the methods section, and subsequently placed within 0.5% agarose on a layer of 1 μM cAMP agar, which acted as a chemoattractant. The result was a diffusion-based gradient of cAMP from the bottom of the agarose to the top, as discussed in chapter 3 (illustrated for clarity in Figure 5.4)[341].

Figure 5.4: The cAMP gradient

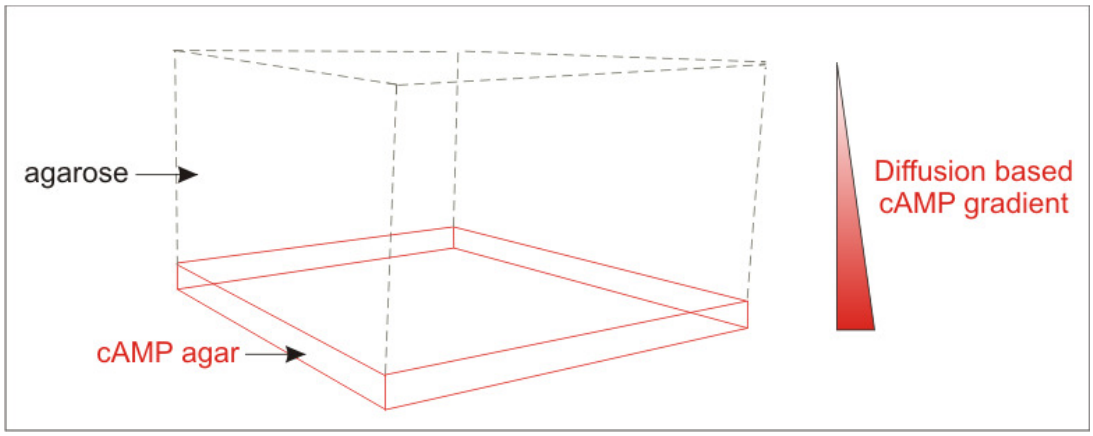

Figure 5.4: The 1 µm cAMP agar below the 0.5% agarose. The cAMP diffuses from the base agar layer through the agarose establishing a diffusion-based gradient.

Cells were imaged 30 minutes after they were set within the agarose, in order to allow a gradient to establish. As can be seen in Figure 5.5, the Ax2 *Dictyostelium* cells began moving from the initial acquisition time-point (Figure 5.5A&B) indicating that the cAMP gradient was established by the beginning of the time-lapse experiment. Cells near the top of the agarose in these experiments were able to detect the cAMP signal and move downwards towards the cAMP agar both near the beginning (Figure 5.5A&B) and throughout the entire time course of the experiment (Figure 5.5C).

With OCT microscopy, Ax2 *Dictyostelium* cells can be resolved as bright spots within the darker background of the agarose gel (Figure 5.6). For some cells, cell shape can also be resolved, i.e. elongated morphology instead of rounded morphology can be seen. An example elongated cell can be seen indicated with a yellow arrow in Figure 5.6B. With the spatial resolution limit of the system measured at ~5 µm, however, on occasion the cells appeared as bright spots of less discernible morphology (Figure.5.6D&F). Yet this is sufficient for tracking population cell migration, as it allows the cell to be localised within the volume and its movement within the volume followed[576,685].

Figure 5.5: Ax2 cell chemotaxis within a 0.5% agarose gel- the cAMP gradient

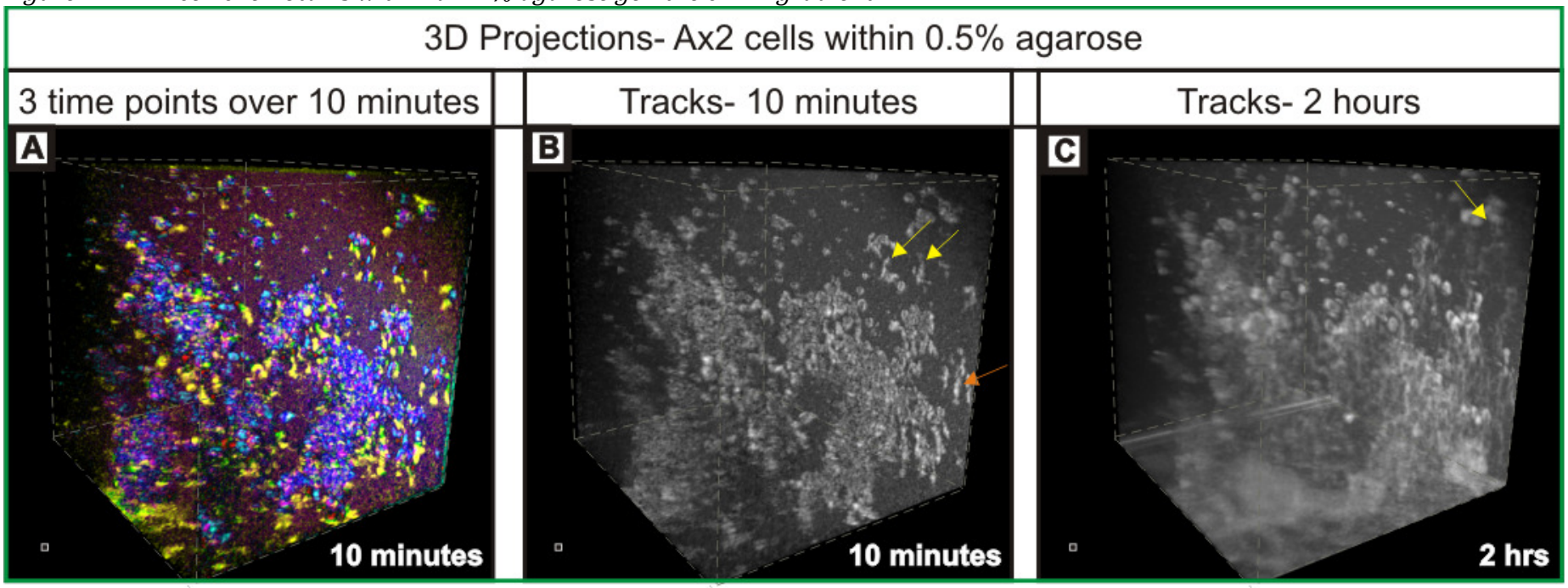

Figure 5.5: Volumetric images of Ax2 cells chemotaxing within 0.5% agarose gel. (A-B) over 10 minutes (C) over 120 minutes (2 hours). (A) Superimposed false colour image, blue- 0 minutes, magenta- 5 minutes, yellow- 10 minutes) (B) images from 0 minutes to 10 minutes summed over all time points using the standard deviation projection in ImageJ. Yellow and orange arrows point to tracks from cells moving downwards over this time period (yellow- cells high up within the agarose, orange- cells lower down within the agarose), showing that the cells within the agarose are able to detect and respond to the cAMP gradient from the beginning of acquisition. (C) images from 0 minutes to 120 minutes (the entire period of acquisition) summed over all time points using the standard deviation projection in ImageJ. Yellow arrow indicates an example track from a cell, high up within the agarose (Far from the cAMP source) moving downwards, showing that the cells seeded high up within the agarose are able to detect and respond to the cAMP gradient. Grey guidelines show the edges of the volumetric images (generated using Amira software (Visage Imaging, USA)). Scale bars are 20 μm.

Turning to temporal resolution, volumetric images were acquired of 1000x1000 μm with 800x800 sampling points (in x and y). This size was initially chosen to capture the multicellular stages of *Dictyostelium* cell development. However, the number of sampling points necessitated by an image of this size, in order to meet desired sampling levels (discussed in chapter 3), and the subsequent time required to save tomograms of this size meant that the images could only be acquired at 2 minute (120 second) intervals, even with use of a striped RAID array[139,379]. Although it may have been possible to acquire images every 105 seconds with this spatial sampling density (800x800), if saving were delayed for any reason, for example due to the computer processor and RAM being occupied with other tasks, imaging of the next tomogram would not start until saving of the previous tomogram had completed. Practically, when this was trialled, it resulted in image sequences with time-points which were an unknown time apart, anywhere from the specified 105 seconds up to 115 seconds apart, dependent on how long the previous tomogram had taken to complete the full acquisition and saving sequence. Therefore 120 seconds was chosen between time-points, by experimental iteration, for acquiring time-lapse images of volumes with 800x800 sampling points, as it allowed imaging to commence at the specified time, and not to be delayed by any increased time saving the previous tomogram. This temporal resolution, combined with a spatial resolution of ~5 μm, which allowed cells to be resolved at a minimum as spherical bright spots (Figure 5.5), is sufficient for localising chemotaxing cells and tracking them within an agarose gel, as I will show in this chapter.

Figure 5.6: Ax2 Dictyostelium cells suspended within a 0.5% agarose gel

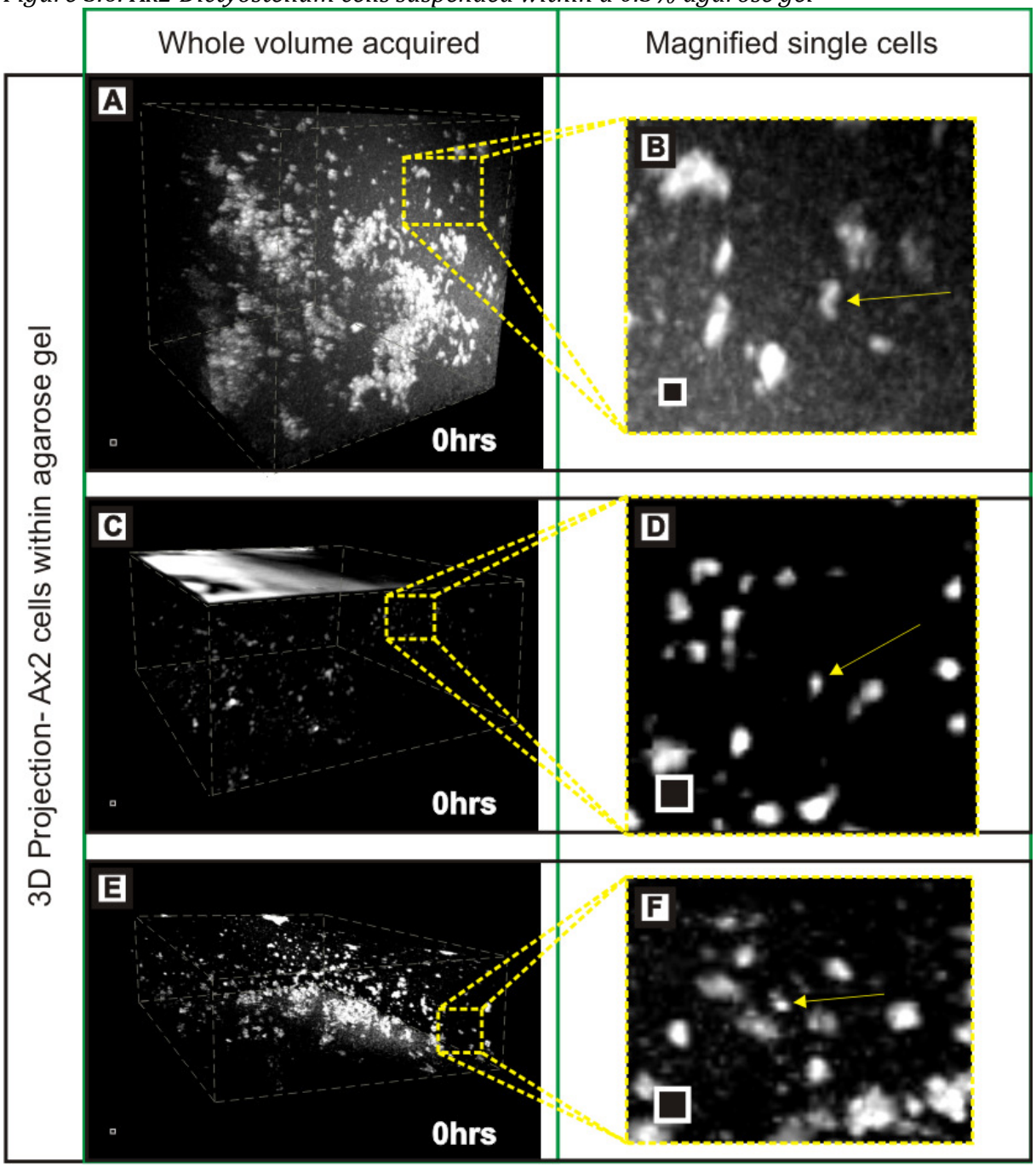

Figure 5.6: 3D projections of Ax2 cells seeded within a 0.5% agarose gel, generated with Amira software (Visage Imaging, USA). Grey guidelines delineate edge of volumes for ease of visualisation. (A, C, E) Entire volume acquired. Yellow area indicates area magnified in (B, D, F). (B) Chemotaxing cell with elongated shape. (D&F) Chemotaxing cells which can be seen as single bright points. Scale bars are 20 μm.

5.7 Chemotaxis of Ax2 cells in 4D within a 0.5% agarose gel- temporal resolution

Although tracking cells can be accomplished when cells are resolved as bright spots with a temporal resolution of 120 seconds (2 minutes), some more detailed information is unfortunately lost such as more detailed information about the shape of the cell track and information about cell shape changes within the two minute intervals. With this in mind, a tomogram was acquired with the size of the volume decreased to 100x1000 μm (in x and y), by setting the galvanometric mirrors to scan over a smaller area. 80x800 sampling points were acquired to keep the spatial sampling density identical to that of the larger volumetric images. This sampling density permits image stacks to be acquired and saved successfully every 10 seconds, allowing for experimental determination of the trade-off between increased temporal resolution, and decreased size of volume acquired.

Figure 5.7 shows a volumetric image of Ax2 cells within a 0.5% agarose gel on a base of 1 μM cAMP agar, acquired with a reduced size and an increased temporal sampling rate (to every 10 seconds). The initial time-point is shown in Figure 5.7A&B with the tracks of the migrating cells, generated using the Analyse Particles plugin in ImageJ, in Figure 5.7(C&D). As seen in the previous 4D chemotaxis time series (Figure 5.5), the general trend of cell movement was in the downwards direction, towards the cAMP agar (Figure 5.7A-D). A section outlined in green in Figure 5.7C is magnified in Figure 5.7(E-G). These magnified images show the appearance of a selected area of cells suspended within the agarose gel. The contrast between the cells and the background was made clearer by use of a thresholded binary mask (in ImageJ) (Figure 5.7F), enabling the cells to be more easily distinguished from the background by eye, and the morphology of the cells clearer. The tracks of the cells in this magnified area are shown in Figure 5.7G, moving down towards the cAMP agar. The yellow box in Figure 5.7(E-F) was further magnified in Figure 5.7(H-K). The cells were thresholded from the background using a binary mask and then outlined using the Analyse Particles plugin in ImageJ. A bicellular aggregate was followed over a 20 second period, during which it split to form two single cells (Figure 5.7H-J). This aggregate split and re-formed several times over the entire experimental time course (2 hours, data not shown). The outline of this aggregate, traced from 5940 seconds (99 minutes) after image acquisition begun to 7200 seconds (over a period of 1260 seconds (21 minutes)) is shown in Figure 5.7K. Its morphology at each time-point can be seen, superimposed over the cell outlines from the other time-points. Its general trend of motion was in the downwards direction, towards the cAMP agar, however, it stops

migrating downwards and instead migrates laterally for a short period (Figure 5.7K, orange arrow) of approximately 85 seconds. This period of only lateral movement is shown in Figure 5.7L, where the morphology of the migrating bicellular aggregate is shown over this reduced timespan. The bicellular aggregate did not change position with respect to the cAMP agar, but was limitedly motile, changing shape (Figure 5.7L).

Figure 5.7: Ax2 cell chemotaxis within 0.5% agarose- temporal resolution of 10 seconds

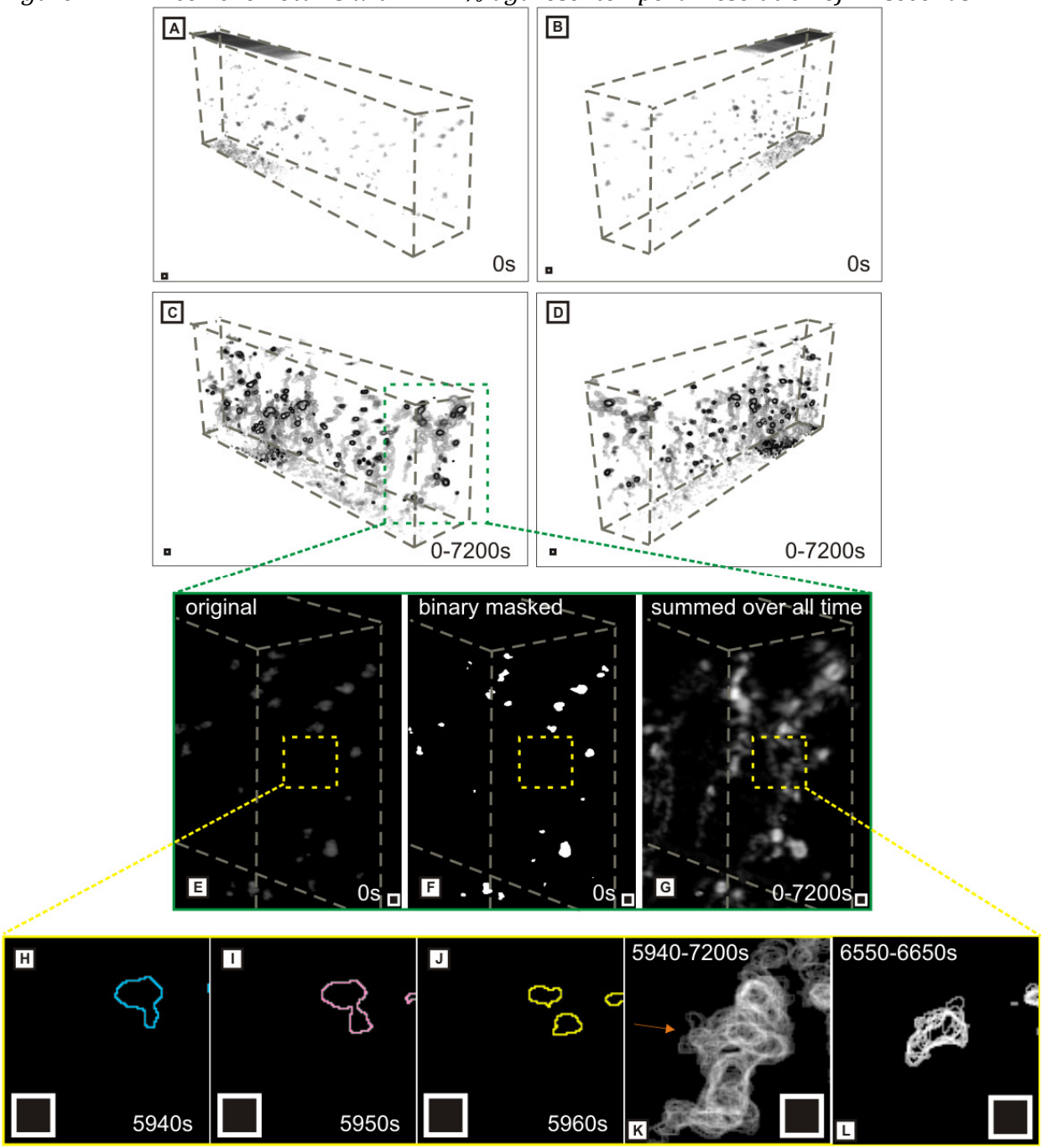

Figure 5.7: Ax2 cells within 0.5% agarose on a base layer of 1 µM cAMP agar. Images acquired every 10 seconds for 7200 seconds (2 hours). Grey guidelines delineate the edges of the larger volumetric images for ease of visualisation. (A-D) Volumetric images of the Ax2 cells within the agarose from two different angles. (A-B) Initial time point. (C-D) Objects thresholded from the background and outlined using the Analyse Particles plugin in ImageJ followed by summing using the standard deviation projection over all time points. The tracks of the cells can be seen. (E-G) zoomed in area, indicated by green box in (C). (E) Initial time-point. (F) Initial time-point with a binary mask applied to outline the cells. (G) All of the time-points (7200 seconds, 2 hours) summed together using the standard deviation projection in ImageJ to show the cell tracks and overall pattern of cell migration. (H-K) Zoomed in

images of a bicellular aggregate, which splits to form two cells, over the course of 20 seconds from the area outlined with the yellow box in (E-G). Outlines of the cells generated in ImageJ using a binary mask and then outlined using the Analyse Particles plugin. (H-J) An example single cell at 5940 seconds (99 minutes, 1.65 hours) after the beginning of image acquisition- blue, and for 20 seconds afterwards (5950 seconds- magenta, 5960 seconds- yellow). (K) 5940 seconds (99 minutes, 1.65 hours) to 7200 seconds (120 minutes, 2 hours) after commencement of image acquisition summed together using the standard deviation projection in ImageJ. The morphology of the cells and the migration path of the cells can be seen. Orange arrow indicates a point where the cell stops migrating downwards and shifts position in the same vertical position, before resuming motion downwards towards the cAMP agar. (L) Bicellular aggregate from 6550 seconds (~109 minutes, ~1.82 hours), followed over 100 seconds. The cell does not significantly displace from its original starting point towards the cAMP agar, but is motile, changing shape and shifting position. Scale bars are 20 μm.

Returning to the entire imaging area of 100x1000 μm, cell tracks generated using a binary mask to separate the cells from the background and then outlined using the Analyse Particles plugin in ImageJ are shown from two different angles in Figure 5.8A-B. The time-series, obtained by acquiring every 10 seconds over 7200 seconds (2 hours), was imported into Volocity software for tracking, as described in the methods section, in order to obtain quantitative information describing cell chemotaxis. The tracks generated from this volume calculated by Volocity are shown in Figure 5.8C, from two different angles. It appears from the output generated by Volocity (Figure 5.8C) that certain cells have been considered by the software as two separate objects, with one terminating partway through the time-sequence and the other beginning at this point (Figure 5.8C indicated by orange arrows and yellow arrow). This is likely explained by the fact that cells which become multicellular and then disaggregate again to single cells, such as the example shown in Figure 5.7H-J cannot be tracked during the bicellular stage as the volume then exceeds the volume thresholding applied within the Volocity software; which was applied to restrict analysis to objects of the approximate size of single cells (see methods section for details of this thresholding). This was a necessary step to ensure tracking of only individual cells, and exclude any multicellular aggregates which formed during the course of the experiment, as a natural response of the *Dictyostelium* cells to the presence of cAMP. Cells were excluded from analysis if their track did not span the entire timespan of the chosen experimental duration, in order to ensure a fair comparison, as there may be differences in the experimental conditions (i.e. altered cAMP gradient and levels of enzymes released by the cells) between the beginning time-point and

end time-point of the experiment[682]. Thus cells which are not tracked for the entire duration may be subject to different experimental conditions and exhibit differences in the grand mean quantitative chemotactic parameter values as a direct result of this. Unfortunately, this also results in the exclusion from analysis of cells such as those shown in Figure 5.7H-J, even though if their tracks were summed together they would span the whole course of the experiment. Evidently, constraining the tracking algorithm by size and also filtering the results in this manner excludes cells which become multicellular aggregates during the course of the experiment, and cells which come into contact with other cells at any point during the experiment. The main outcome of this is in severely reducing the number of tracks which meet the volume and track time-span criteria and thus are available for analysis.

Figure 5.8D-E shows plots of the tracks, generated with Volocity software, which span the entire time-course of the experiment (2 hours). Only 4 tracks from a total of 77 successfully tracked objects were tracked for the entire experiment (2 hours). The mean velocity of these tracked cells was 0.10±0.04 μm/second (median 0.10±0.05 μm/second) and the mean meandering index was 0.03±0.04 (median 0.01±0.01). Meandering index is a measure, between 1 and 0, of how much a cell deviated from a straight path while migrating and is calculated from displacement/track length. A value of 1 indicates that a cell was moving in a straight line. These chemotactic parameters were chosen, because both of these parameters have previously been shown to be affected by the substratum and environment of a cell[106,119,410,483,563,683]. Additionally, between them these parameters describe the path of a cell. For example, path length can be simply calculated from velocity over a known time. From this value, with a known meandering index, displacement could also be calculated. It can therefore be seen that velocity, describing how fast a cell was moving, and meandering index, describing how directly a cell moved towards its destination, together provide a good description of cell migration. The values obtained for these few successfully tracked Ax2 *Dictyostelium* cells indicated that these cells were able to migrate through the agarose, but did not take a very direct path, so their translocation from their starting point was small, as can be seen in Figure 5.8D-E.

Figure 5.8: Ax2 cell chemotaxis within 0.5% agarose- temporal resolution of 10 seconds- Quantitation

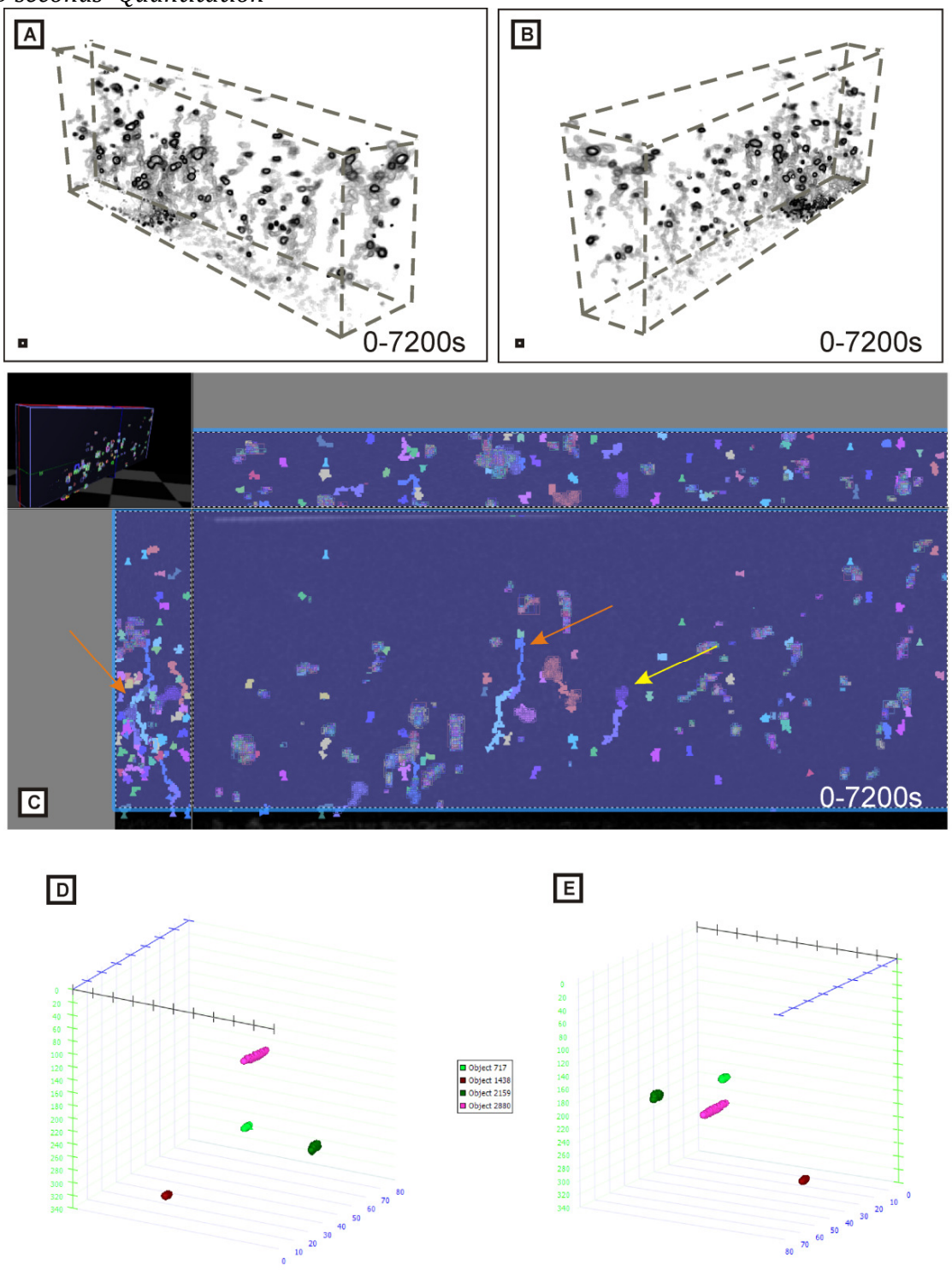

Figure 5.8: Ax2 cells chemotaxing within a 0.5% agarose gel on a base of 1 µM cAMP agar. (A-B) Volumetric images of the Ax2 cells within the agarose from two different angles generated using Amira software. Objects thresholded from the background and outlined using the Analyse Particles plugin in ImageJ followed by summing using the standard deviation projection over all time points. The tracks of the cells can be seen, for comparison with (C) Output from Volocity showing the cell

tracks calculated by the software- Top left- entire volume (surface), Top right- enface view (single plane), Bottom left- X-Y view (B-scan), Bottom right X-Z view. Orange arrows point a track which has been split by the software into two separate tracks. Yellow arrow points to another track which has been split. (D-E) Plots of 4 cell tracks from two different angles calculated using Volocity software, which could be tracked over the entire 7200 seconds (2 hour) timespan. X axis is black, Y axis is green, Z axis is blue. Scale bars are 20 μm.

5.8 Chemotaxis of Ax2 cells in 4D within a 0.5% agarose gel- tracking and quantification

Although I have shown that OCT can be used to image a few cells with increased temporal resolution, which potentially gives access to more detailed information on cell morphology and the temporal dynamics of cell chemotaxis, the periodicity of a naturally occurring cAMP wave has previously been shown to be 5-7 minutes, which suggests that a temporal resolution of 2 minutes is sufficient to track the overall pattern of cell chemotaxis[542,619]. A major drawback of increasing the temporal resolution was the corresponding decrease in the volume of the image stack which could be successfully acquired and saved. This, in combination with the necessity to constrain the tracking algorithm to exclude artefacts, resulted in very low numbers of cells successfully tracked throughout the entire time course of the experiment. To properly represent the typical behaviour of Ax2 cells within an agarose gel, and to reduce the effect of any cells exhibiting unusual behaviour (i.e. outliers), which may be seen within a population, it was necessary to track larger numbers of cells than could be acquired with this reduced volume[188,410]. Therefore, larger volumes of 1000x1000 μm (with 800x800 sampling points, in x and y) were acquired, with image stacks 2 minutes (120 seconds) apart. These were the same imaging parameters as chosen for observation of multicellular development, earlier in this chapter.

The cells were set within 0.5% agarose on a bed of 1 μM cAMP agar, as described in the methods section, with images acquired on three different days to show repeatability of results. Chemotaxis of these cells is shown over a period of 2 hours in Figure 5.9. At the initial time-point, many individual cells were seen (Figure 5.9A,C,E- blue colour). By the final time-point (120 minutes) (Figure 5.9A,C,E- yellow colour) there were far fewer individual cells and more multicellular aggregates, most commonly located on the cAMP agar base. Figure 5.9 (B,D&F) shows all of the images, acquired over the entire 120 minutes, summed together indicating the general trend of cell motion, and also some distinct cell tracks (Figure 5.9B,D,F- yellow

arrows). As expected, the cell movement was mostly in the downwards direction, towards the chemoattractant. Once the cells reached the cAMP agar layer, which was too solid for them to penetrate, they started to aggregate, streaming along this layer and forming clumps of many cells, the mound stage of development This was not unexpected, as primed by cAMP, *Dictyostelium* development was initiated[143].

By inspection, by 1 hour, the majority of the cells present in the images acquired at the beginning of these experiments had aggregated and formed multicellular structures, particularly at the agarose-cAMP agar interface, and far fewer single cells were available for tracking (Figure 5.10A-C, experiments performed on three different days). As I was interested in exploring individual cell migration, and had set parameters within the Volocity software to exclude objects above this size, cells could not be tracked once they were no longer individual units. Although more individual cells which were originally outside of the imaging area entered the acquisition volume during the time-lapse experiment, new objects appearing in the images were excluded. Tracks which did not cover the entire time span of the experiment were also excluded. These restrictions were introduced to reduce the possibility of artefacts from non-cellular object being tracked. Therefore, Ax2 cells were tracked for a time period of 1 hour, to obtain information on the characteristics of individual Ax2 cell chemotaxis within a 3D environment. Over this 1 hour period, the grand mean velocity of the cells was 0.13±0.06 μm/s (median= 0.13 μm/s, interquartile range= 0.05 μm/s). The grand mean meandering index, a measure of how directly a cell moved, i.e. how much it deviated from moving in a straight line, was found to be 0.18±0.09. (median= 0.17, interquartile range= 0.12). The chemotactic index was calculated as described in the methods section. This was found to be -0.16±0.55 (grand mean) (median= -0.22., interquartile range= 0.87).

Figure 5.9: Ax2 cells chemotaxing within a 0.5% agarose gel on a 1 μM cAMP agar base

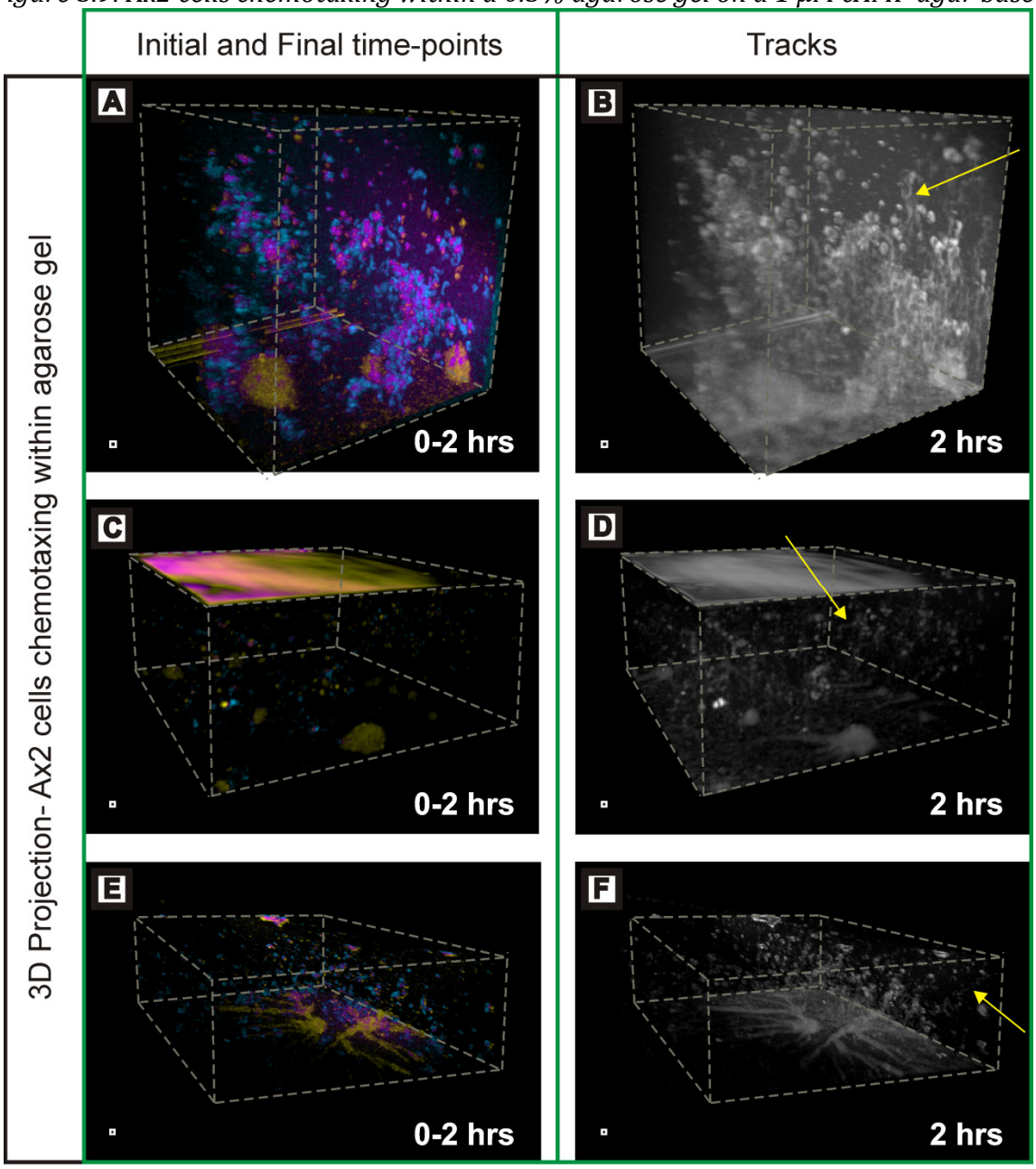

Figure 5.9: Three different experiments performed on different days showing Ax2 cells within a 0.5% agarose gel on a base of cAMP agar. Time-lapse experiments of the cells migrating images every 2 minutes over 2 hours (A-B) First experiment (C-D) Second experiment (E-F) Third experiment. (A, C, E) Superimposed false colour images of the first and last time point of the experiment. 0 minutes- blue, 120 minutes (2 hours)- yellow. Magenta indicates stationary objects or objects that are located in the same area in the first and final images. (B, D, F) All of the time points summed together using the standard deviation projection in ImageJ. Yellow arrows point to an example of a track in each experiment which can be clearly seen. Grey guidelines show the edges of the acquired volumes, for ease of visualisation. Scale bars are 20 μm.

Figure 5.10: Ax2 cells in 0.5% agarose at 1 hour and 0 hours after initial time-point

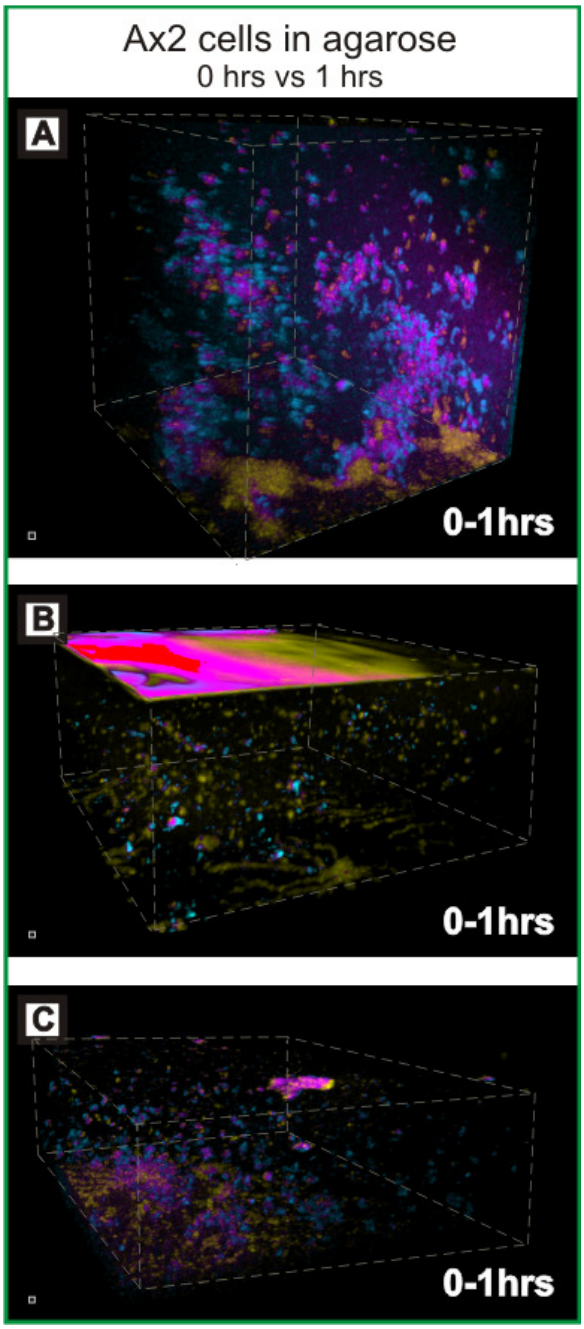

Figure 5.10: (A-C) Ax2 cells imaged chemotaxing in time-lapse within a 0.5% agarose gel. Volumes rendered using Amira software (Visage Imaging, USA). Superimposed false colour coded images- Blue- 0 minutes, Yellow- 60 minutes (1 hour). Magenta is seen where objects overlap (are in the same position) at both time-points. There are more individual blue objects than yellow or magenta objects indicating that there are more individual cells at the initial time point than at 60 minutes (1 hour). There are more multicellular aggregates in yellow- 60 minutes (1 hour) into imaging. Grey guidelines show the edges of the volumes for ease of visualisation. Scale bars are 20 μm.

5.9 Ax2 cells under different conditions- velocity and meandering index

In Chapter 4, Ax2 cells were imaged migrating and chemotaxing on two different substrata. In this chapter this has been extended into the 4th dimension, and chemotaxing cells have been imaged within an agarose gel. In Chapter 4 I showed an effect of the surrounding environment on the cell speed, but not on persistence. Here, this analysis is extended to include the agarose environment. The parameters chosen for comparison were velocity (in μm per second) and meandering index. Velocity was calculated from the speed (in μm per minute) output by 2D-DIAS software. Meandering index is a measure of how directly a cell moves. The higher the value, the less a cell deviates from a straight line while migrating. It was calculated manually for the data on the 2D surfaces using meandering index= displacement/track length, with data output from 2D-DIAS[476]. As cells selected from the time-lapse images in Chapter 4 were assigned to the chemotaxis group only if they were moving directly towards a source of chemoattractant, the tracks generated for the Ax2 cells chemotaxing within the agarose were subjected to a filter based on chemotactic index, calculated as described in the methods section from the cosine of the angle between the cell track and the direction of the chemoattractant source. Cells with a chemotactic index of less than +0.75 were excluded, so that only cells with a trajectory where the vector pointed mostly downwards, i.e. towards the cAMP agar, were analysed. This was to ensure fair testing, that cells from the 3D (2D+time) and 4D (3D+time) data were subjected to the same selection criteria. As the experiments from chapter 4 spanned a time period of 20 minutes, only 20 minutes of time-points for the Ax2 cells within the agarose were tracked and subsequently analysed. The results are summarised in Table 2.

Table 2: Ax2 cells chemotaxing on two different surfaces and within a 0.5% agarose gel- Results and Statistical Analyses

Condition	Velocity (μm/s)	Meandering Index
Ax2 on nitrocellulose filter	0.12±0.03 Median: 0.11±0.02	0.59±0.19 Median: 0.65±0.27
Ax2 on plastic Petri dish	0.15±0.04 Median: 0.14±0.07	0.62±0.12 Median: 0.56±0.20
Ax2 in agarose gel	0.14±0.04 Median: 0.14±0.06	0.36±0.19 Median: 0.34±0.25
Ax2 nitrocellulose filter vs agarose	t=|1.650| dF=127 p=0.10	U=262 Z=|3.26| p=0.001*
Ax2 plastic Petri dish vs agarose	U=547 Z=|0.86| p=0.39	U=172 Z=|4.23| p<0.001*

Table 2: Grand means (±SD) and medians (±interquartile range) calculated from the mean values obtained for each cell. Nitrocellulose filter n=11. Plastic Petri dish under buffer n=11. Agarose n=118. Summary of the results of statistical analysis between Ax2 cells within agarose and Ax2 cells on two surfaces, a nitrocellulose filter and a plastic Petri dish. * indicates significance at 95% CI.

The mean velocity was highest on the plastic Petri dish surface at 0.15±0.04 μm/s, 0.01±0.08 μm/s, higher than within the agarose gel. The mean velocity in the agarose gel was 0.02±0.07 μm/s higher than on the nitrocellulose filter. The mean meandering index was highest on the plastic surface at 0.62±0.12, 0.03±0.31 higher than on the nitrocellulose filter. The meandering index is lowest on the agarose surface at 0.36±0.19, 0.23±0.38 lower than on

the nitrocellulose filter. Box plots showing the distributions for all of the above conditions and summarising the data are shown in Figure 5.11.

Figure 5.11: Ax2 cells under different experimental conditions

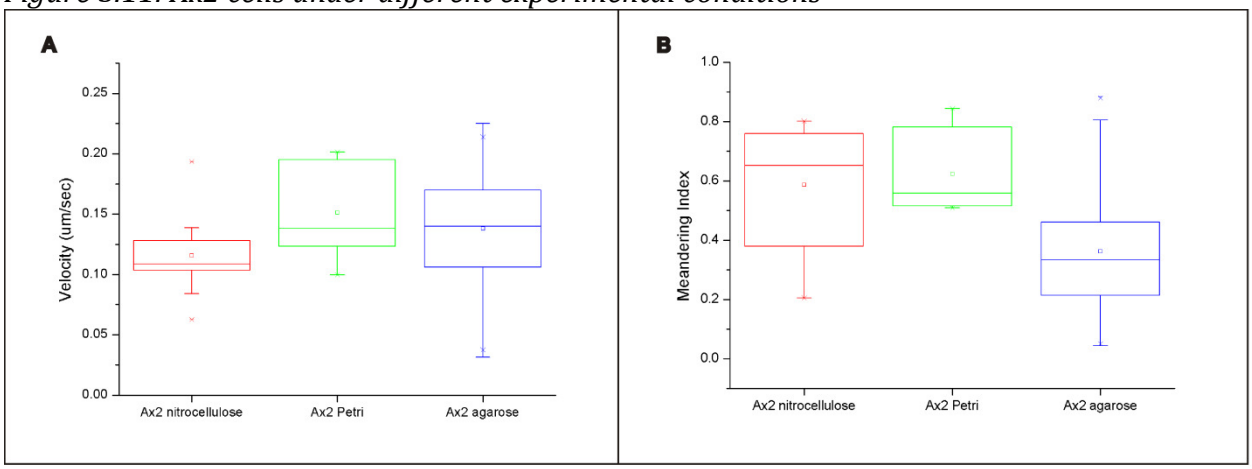

Figure 5.11: Box and whisker plots showing the distributions of velocity (A) and meandering index (B) of Ax2 cells chemotaxing on a nitrocellulose filter, on a plastic Petri dish and within a 0.5% agarose gel over 1200 seconds (20 minutes). The box shows the interquartile range, with the median value as a line across the middle. The small square box inside the boxplot is the mean. Whiskers represent the 5th-95th percentile of the data. Crosses represent the 1st and 99th percentile of the data. Data were obtained on three separate days for the cells on the nitrocellulose filter and within the 0.5% agarose and on two separate days for the cells under buffer on the plastic Petri dish.

The distributions for the velocity of both the nitrocellulose filter and the agarose conditions were normal (Anderson-Darling tests at 95% confidence, Nitrocellulose filter- $p=0.178$, Agarose- $p=0.310$) and a Levene's test indicated that the variances were equal (Levene's test $p=0.90(>0.05)$, Test Statistic=2.923). Therefore a two-tailed Student's T-test was performed to compare the velocity of the cells under these two conditions. The distribution for the velocity on the Petri dish was non-normal (Anderson-Darling test at 95% confidence, $p=0.044$, (<0.05)), so a Mann-Whitney U test was performed to compare the velocity of the agarose and the Petri dish. The results of the statistical analyses are summarised in Table 2. A Kruskal-Wallis one way analysis of variance by ranks was performed between all of the conditions, and there was found to be no significant difference between all of the groups at the 95% confidence interval, $H=5.01$, $dF=2$, $p=0.82$. Subsequently, Mann-Whitney tests revealed that the velocities of the cells on the nitrocellulose filter and within the agarose, and

also between the cells on the plastic Petri dish surface and within the agarose did not appear to be different (Table 2) (nitrocellulose vs agarose t=|1.65|, dF=127, p=0.10, Petri dish vs agarose U=547, Z=|0.86|, p=0.39). The mean (and median) velocity of the cells within agarose lies between the values for the cells on the nitrocellulose and plastic surfaces. Hence, although there is a significant difference between the velocity of Ax2 cells on a nitrocellulose filter and on a Petri dish (chapter 4), the differences in velocity between the cells on both of these surfaces and the cells within the agarose are insufficient to reach significance at the 95% confidence level[188].

The distribution of the meandering index on the nitrocellulose filter was normal (Anderson-Darling test at 95% confidence, p=0.217), but the distributions for the Petri dish and the agarose were non-normal (Anderson-Darling tests at 95% confidence, Petri dish- p=0.032, Agarose- p=0.005, (<0.05)), so Mann-Whitney rank sum tests were performed for comparison of the cells suspended in the agarose with cells on the nitrocellulose filter and Petri dish. The results are summarised in Table 2. A Kruskal-Wallis one way analysis of variance performed between all of the conditions, revealed significant differences between the conditions at the 95% confidence level, H=24.71, dF=2, p<0.001. Subsequent Mann-Whitney U-tests indicated significant differences between the meandering indices of the cells in agarose and on both the nitrocellulose at the 95% confidence interval (U=262, Z=|3.26|, p=0.001) and the plastic Petri dish (U=172, Z=|4.23|, p<0.001) surfaces.

5.10 Chapter 5 Discussion

5.10.1 Ax2 cell development in 4D

The processes of both individual and collective cell migration are important in multicellular organisms, such as mammals, for development and organogenesis, and also play a role in ongoing physiological processes such as wound healing[270,294,461,518]. Furthermore, aberrant collective migration may also be involved in the metastasis of cancer cells[270,294]. Therefore, an understanding of these processes is of great interest. Many studies have explored the process of single cell and collective cell migration on 2D surfaces, but it is recognised that this environment does not necessarily provide a good model of cells within their natural environments[61,142,172,461,493,572,659]. *Dictyostelium*, which lies at the interface between single celled and multicellular organisms, undergoes a developmental process of aggregation, involving individual cell migration and collective cell migration such as cell streaming, which shares

features with mammalian cell collective migration[29,410,526,658]. In combination with its robust nature and accessible genetics, *Dictyostelium* is therefore a useful model organism to investigate this process.

I have shown that Ax2 *Dictyostelium* cells are able to signal to one another through an agarose gel, as they undergo spontaneous aggregation, and that the propagation of this signal, cAMP waves, can be visualised as optical density waves. I have also shown that they are able to migrate and come together within the three-dimensional environment of an agarose gel as both individual cells and as multicellular aggregates. Although a previous study had shown that development of Ax2 cells under these conditions was asynchronous and that some groups of cells failed to develop at all, this was not seen in my experiments[312,447]. There are several possible explanations for this discrepancy. The first is that of measurement bias. I began imaging at 10 hours after initiation of starvation conditions, by which point some cell aggregation had already taken place. When selecting an area for imaging in my experiments, I selected an area which contained a multicellular aggregate, but between these aggregates there were many areas which contained very few or no cells. It may be that in this way I selected out areas which failed to develop, although visual inspection of the sample by eye before and after imaging revealed that multiple aggregates formed and were at approximately the same stage of development. A photograph illustrating an example of this is shown in Figure 5.12; orange arrows indicate examples of cell streaming. By eye the cells appear to have been at approximately the same stage of development (Figure 5.12).

Figure 5.12: Photograph of Ax2 cell streaming in 0.5% agarose

Figure 5.12: Ax2 cells within a 0.5% agarose gel at approximately 12 hours after seeding. Examples of cell streaming seen on the surface of the agarose are indicated with orange arrows. By eye the cells over the entire plate appear to be at approximately the same developmental stage.

The second possible reason is that I used a lower concentration of agarose to that used in the other study. I used 0.5% agarose, while Knecht et al used 1% agarose[602]. Properties of agarose gels such as pore size and strength of the gel are known to depend on the concentration of the agarose[31,286,515]. Therefore, it is possible that the 1% agarose exerted effects on the *Dictyostelium* cells such as preventing some cells from aggregating and delaying development, because of its increased rigidity or smaller pore size of the polysaccharide network, which are not seen when the concentration is reduced to 0.5%. Additionally, although both studies used low melting point agarose (which is high-purity) the origins of the agarose may be different, resulting in slightly different chemical compositions[42,515]. As chemical properties of the environment are able to exert effects on cell behaviour, it is possible that the presence or absence of certain chemical groups in the polysaccharide chain, or increased or decreased numbers of these could contribute to the difference in observed behaviour[327,62688,200,373,510,626]. Thirdly I used $1.9x10^7$ cells in 3 ml of agarose, while Knecht et al used $3\text{-}5x10^5$ cells in 5-10 ml

of agarose. *Dictyostelium* cells have a mechanism by which they are able to sense their own density, both as vegetative cells and as starving cells. The secreted glycoprotein conditioned medium factor (CMF) is released by cells which are starved at high densities, but not by those starved at low cell densities[108,227,250]. This factor is essential for cAMP signalling and cell aggregation[227,250,695]. The differences in cell density may therefore contribute to the differences seen in *Dictyostelium* development. Finally, Knecht et al originally used agarose which contained growth medium, so the cells were not plated under starvation conditions and did not begin to develop for several weeks. The cells could have originally been plated at varying densities throughout the agarose or divided at different rates and therefore exhausted their supply of medium at different rates, potentially explaining the asynchronous development. As my cells were seeded within the agarose under starvation conditions, these factors would not influence cell development in my experiments[312].

It was thought that the gel may present a more challenging environment to the cells than simply moving through air or buffer, as these are environments of minimal resistance, and therefore potentially impede the cells and slow development[329,682]. However, this was not seen to be the case, with the timescale of development of the Ax2 *Dictyostelium* cells within agarose similar to that of these cells previously observed on 2D surfaces, at least for the period of time the cells were followed with OCT (5 hours)[211,286,369,371]. This indicates that it is likely that the cells do not find the 0.5% agarose to be an impediment to either their movement or their signalling. *Dictyostelium* cells can be developed under agarose and imaged by inverted light microscopy[682,263,368,389]. While this does not represent a true 3D environment, as the cells are not completely surrounded by agarose and the cells move in a single plane along their glass substratum and furthermore are artificially flattened by the agarose layer, it should be noted that under these conditions *Dictyostelium* has been shown to fail to develop beyond aggregates, unless the agarose is removed, although contrary to this Nicol et al reported successful formation of flattened slugs under 2% agarose[2,302,447,682]. In my experiments, *Dictyostelium* did develop past the aggregation stage, as I observed, by eye, that fruiting bodies had formed by the following day after experimentation. However, it is most likely that, as seen during the course of my imaging, the cells moved up to the surface during aggregation, and completed their development in the air, as the fruiting bodies appeared to be on the surface of the agarose (data not shown, as the full fruiting body was too large to completely capture). Nonetheless, the occurrence of fruiting bodies on the surface of the agarose is not a surprising finding, as previous studies have shown that developing *Dictyostelium* cells are able to migrate up a gradient of oxygen (within agar) and orient themselves in a particular pattern

with respect to this gradient[592]. However, it therefore cannot be said from my experiments whether *Dictyostelium* is able to complete development fully within an agarose gel.

It has been shown in this chapter that *Dictyostelium* cells seeded under starvation conditions within an agarose gel on a base of KK2 agar preferentially form streams at interfaces, either the agarose-air interface or the agar-agarose interface. The movement of the cells towards the air is unsurprising, as in the wild *Dictyostelium* cells must sporulate to disperse to other areas in search of additional food sources[160]. This distribution of spores is aided when at the surface of the soil as the spores can then attach themselves to the coat of a passing animal[55,66]. It would therefore be expected that *Dictyostelium* cells would preferentially migrate upwards towards the surface, and up the gradient of oxygen, as it has been shown that they are chemotactic to oxygen[493,585,592]. However, previous studies have shown that in the absence of other cues *Dictyostelium* in fact migrates downwards during development, potentially due to the effect of gravity[52,160]. This finding is explained by the fact that *Dictyostelium* is phototactic and thermotactic, suggesting that in the wild the organism uses light and heat as environmental cues during development[52,53,55,249,578,674]. It is thought that it is at this slug stage of *Dictyostelium* development, a later stage than in my experiments, that *Dictyostelium* orients itself towards the surface of the soil, using these thermotaxis and phototaxis as guidance cues[52,55,249,674]. Nonetheless, *Dictyostelium* single cells have also been shown to be phototactic, and the brief duration of the scanning laser light source may be enough to bias the motion of cells near the top of the agarose upwards[301]. This would result in an accumulation of cells at the top surface of the agarose, potentially explaining why aggregates form there. One way in which this could be tested would be by assessing the response of both chemotactically competent and vegetative *Dictyostelium* cells within an agarose gel to different wavelengths and intensities of light, from a variety of different directions. As to why the cells also form streams along the bottom of the agarose at the agar-agarose interface, it may be that some migrating cells reach this interface and, unable to migrate further in the vertical direction as when migrating downwards they cannot penetrate the agar layer, they instead migrate along it, until sufficient numbers accumulate to form an aggregation centre. As Arcizet et al have previously found that vegetative *Dictyostelium* cells are attracted to micropillars, it may be that the cells have an attraction to the agar layer which, upon localising to it by chance, induces them to stay along this surface, rather than returning to the agarose environment[18]. Nonetheless, although streaming also occurs largely at these interfaces, streams can also form through the agarose. This is probably caused by the chemotaxis of cells that had not already reached the interface

towards the larger concentration of cells which had, which comprised the aggregate and therefore centre of local chemoattraction.

The patterns of darkfield waves have previously been used to study the mechanisms by which *Dictyostelium* cells aggregate and differentiate to form fruiting bodies elevated by a stalk comprised of vacuolated stalk cells, as these waves reflect the propagated chemoattractant signal[143,460,571,572]. This type of propagating wave is also relevant to other systems, such as multicellular organisms, as spiral waves have been found to be a general feature of excitable systems, and have been shown in diverse organs and organisms, from xenopus oocytes to cardiac muscle and mammalian neocortex[122,267,343]. I have shown that with the aid of image subtraction to enhance the differences between subsequent images, OCT could potentially be used to investigate the signalling of *Dictyostelium* cells within the three-dimensional environment of an agarose gel, which could help to unravel the mechanisms of how cells signal to one another within a three-dimensional environment, and whether the patterns and characteristics of propagated cell-cell signalling waves vary when cells are in a more natural three-dimensional environment, compared to on 2D surfaces[382,460,571].

5.10.2 Ax2 cell chemotaxis in 4D

As Ax2 *Dictyostelium* cells had been shown to be motile within an agarose gel and additionally to be capable of cell-cell signalling through the gel with subsequent aggregation, agarose was determined to be a useful material in which to set *Dictyostelium* cells for investigation of cell motility. However, simply placing the cells within a non-nutrient agarose gel and allowing them to aggregate through a process of natural chemotaxis has several drawbacks; such as lack of control on the developmental stage of the cell, as it is possible cells may develop at different rates within the agarose; a lack of individual cells to follow, as most of the cells comprise multicellular aggregates; and inability to establish a reproducible cAMP gradient within the agarose, as the cells may aggregate at either the top or the bottom of the agarose, as I have shown. In order to overcome these limitations, the cells were pulsed prior to setting within the agarose, in order to ensure that all cells were aggregation competent and at the same developmental stage; the cells were imaged at 30 minutes after setting within the agarose, so there were still many individual cells to follow; and a base layer of 1 μM cAMP agar was used to establish a diffusion based gradient. Agarose has been shown to be a useful material in which to establish a gradient, as it is capable of stabilizing chemoattractant

gradients, both spatially and in time[338,341]. Previous studies have made use of this property of agarose, either by placing cells on an agar or agarose surface at a certain distance from a drop of chemoattractant and allowing diffusion to establish the gradient, or by placing cells on agar or agarose made with a set concentration of chemoattractant and allowing the cells to naturally degrade the chemoattractant by secretion of enzymes, resulting in a gradient of chemoattractant increasing away from the cells[54,318,329,523,617]. These methods have proved useful for analysis of multicellular cell behaviour, for example *Dictyostelium* cell streaming, but individual cell behaviour is difficult to assess, in part due to the difficulty of acquiring images of sufficient resolution with conventional microscopy techniques, such as DIC microscopy[410]. To this end, OCT was employed to image individual cells chemotaxing within agarose, as described in the methods section.

To investigate the potential for investigation of detailed behaviour of individual cells within an agarose gel with OCT, Ax2 cells were imaged chemotaxing within an agarose gel with images acquired every 10 seconds. From these images it can be seen that the morphology of individual cells can be determined and cells can be seen to be elongated, oriented downwards towards the cAMP, indicating that *Dictyostelium* cell polarization occurs under these experimental conditions. Individual cells and aggregates of two or three cells can be seen to migrate vertically, then pause in their migration, making only small lateral movements, and then continue migration at speed (an example was shown in Figure 5.7K-L). This pause may correspond to the peak of the passing cAMP wave, as this has previously been shown to be inhibitory to cell translocation, although in my experiments, the bicellular aggregate followed was still motile, moving around a confined local area in a lateral direction[619,667,701]. More likely, this stationary period, which is approximately 85 seconds long, instead corresponds to the end of the tail of the cAMP wave, where the cAMP gradient is low and falling, as prior experiments have indicated that cell migration towards an aggregation centre occurs over a period restricted to the rising portion of the cAMP wave[213,619,667,701,702]. The cAMP waves in Ax2 cells have a periodicity of approximately 5-7 minutes[542]. Therefore it is possible be that this period corresponds to a gap between the cAMP waves, where the cell aggregate is unable to detect a cAMP gradient and is therefore not directly chemotaxing at this point, but remains motile, as motility is intrinsic to *Dictyostelium* cells[142,416,542,664]. Nonetheless, chemotaxis in *Dictyostelium* cells has previously been shown to be oscillatory, with periods of approximately 1-2 minutes between peak velocities, and it appears from my results that cells within agarose exhibit similar cyclical periods of migration[132,143,216,664,667].

It is also possible, with this temporal resolution of 10 seconds, to see individual cells coming together and moving as bicellular aggregates for a short while, before parting again and moving as separate entities. This may indicate that the cells find it easier to migrate through the gel when they exert additional force as an object of larger mass. Alternatively it could be due to the ability of the cells to sense one another in the local vicinity and exhibiting a natural tendency to aggregate at this developmental stage[108,143]. It may also be that the cells are not in actual fact aggregated, but that one cell is very closely following the other for a period of time and the cells merely appear as a single object due to lack of spatial resolution. This may indicate that one cell acts as a trailblazer, carving a path through the agarose, which the other cell then follows, rather than creating a path of its own. As to why the cells sometimes split apart again, this could be due to initially sensing one another and aggregating, but then receiving a signal of different characteristics, larger, and perhaps with different temporal or spatial dynamics, originating from the local multicellular aggregate, which overrides the signal mediating local aggregation and the cells move towards the larger aggregate[658,667]. It should be noted that this explanation implies that the spatial gradient of chemoattractant set up by the cAMP from the cAMP agar diffusing through the agarose can be overridden by local cell-mediated cAMP signalling. Alternatively it may be that it is easier for individual cells to move through the increased challenge of a 3D agarose environment due to having reduced surface area and reduced mass as individual cells. The cells may struggle to co-ordinate the application of appropriate forces to migrate efficiently as bicellular or multicellular aggregates, as co-ordination of forces has shown to play an important role in *Dictyostelium* migration[133,279,374,381,414].

Although acquisition of images every 10 seconds enabled detailed information about individual cell migration of a selected few cells to be obtained, it did not allow many cells to be successfully tracked with the tracking software employed (Volocity, PerkinElmer), with only 4 out of 77 tracks generated that spanned the entire image acquisition period. I have previously mentioned in the results section that this is due to the necessity to constrain the tracking algorithm to exclude multicellular aggregates from analysis, in combination with the tendency of the cells to periodically form bicellular aggregates, and have shown an example of a track which has been split by the software into two separate tracks because of this. Therefore, ensuring sufficient numbers of cells tracked to allow for an overview of the characteristics of Ax2 *Dictyostelium* cell chemotaxis within an agarose gel required a corresponding increase in the size of volume acquired, which in order to keep the spatial sampling density constant necessitated a reduction in the temporal sampling frequency. This

meant that volumes could be acquired at intervals of every 2 minutes, which as Ax2 cAMP wave have previously been shown to have a period of 5-7 minutes (a minimum of 4 minutes by completion of aggregation), is sufficient to track the overall trajectory and speed of migration, even though access to more detailed information, such as what behaviour the cell exhibits between these two time-points, is unfortunately lost[135,542,658,664].

Imaging of Ax2 *Dictyostelium* cells for 1 hour within an agarose gel at 2 minute intervals, allowed a total of 470 tracks to be generated from 3 separate experiments performed on three separate days, all of which spanned the entire 1 hour period. The grand mean velocity was found to be 0.13±0.06 μm, which equates to ~7.8 μm/min, which is approximately the same speed as cells chemotaxing on glass surfaces[640]. This indicates that it is unlikely that the cells are swimming through the agarose as the speed at which they swim is much lower (1-3 μm/min, or ~4 μm/min, dependent on the experimental configuration), providing support for the fact that the cells do not perceive the agarose as a liquid[27,32,640]. The cells also do not move fast enough to be 'gliding' (~17 μm/min), and are therefore likely adhered to the agarose gel[640]. The grand mean chemotactic index was -0.16±0.55. This means that, although it appeared as though the net direction of motion was in the downwards direction, in actuality approximately half of the cells were moving in an upward net direction, away from the cAMP agar, over the 1 hour period. This could be because the cells which were migrating downwards reached the cAMP agar layer during the course of this 1 hour and then began moving laterally or reversed direction and moved upwards. This would result in an overall trajectory which was not directly downwards. This idea is supported by the grand mean meandering index being 0.18±0.09, indicating that the cells which were tracked were not migrating in very straight lines and changed direction during their translocation. Another possibility is that the multicellular aggregates formed during the course of the experiment, as a natural response of *Dictyostelium* cells to the presence of cAMP, began producing cAMP waves of their own, which resulted in additional sources of chemoattractant, potentially interfering with the ability of the individual cells to respond to the spatial gradient of cAMP set up by diffusion of cAMP from the agar through the agarose[213]. However, recent work by McCann et al showed that, if a signal is propagated by cell-cell signalling, such as has been shown to occur in Ax2 cells within agarose in my development experiments, the cells should merely propagate the signal from the cAMP source[410]. Therefore, alternatively it may be that the cells which migrated first, possibly even before commencement of imaging, perturbed the gradient of cAMP through the agarose, firstly by merely passing through the agarose and disturbing the agarose itself, and secondly through degradation of the cAMP by secreted cAMP

phosphodiesterases[26,538]. If this occurred, following cells would therefore experience an uncertain gradient of cAMP. Not only could this directly result in less direct chemotaxis for the following cells, as the direction of the source of the chemoattractant is less certain, but could also result in the following cells then responding to secreted gradients of cAMP released by neighbouring cells, promoting cell aggregation and indirectly causing less directed migration towards the known source of the cAMP, the cAMP agar, because these cells will move away from this cAMP source towards other more local sources, and therefore change direction during chemotaxis. This idea is supported by the observations of Laevsky et al who directly saw this effect of reduced directionality and chemotactic index in 'follower' *Dictyostelium* cells migrating under 0.5% agarose, which the authors attributed to disturbance of the gradient by the leading cells[329].

In chapter 4, I investigated the effects of two different substrata on the motility of Ax2 *Dictyostelium* cells and discovered an effect on cell speed but not on cell persistence. In this chapter I have extended this analysis to compare the velocity and meandering indices of these cells chemotaxing within an agarose gel with chemotaxis on a nitrocellulose filter and on a polystyrene Petri dish over a period of 20 minutes. I have discovered that the agarose does not appear to present an impediment to the velocity of Ax2 cells, as no significant difference was found between the cells within the agarose gel and the cells on either the polystyrene plastic or on the nitrocellulose surfaces. Although there is a significant difference between the velocities of cells on these surfaces (chapter 4), the cells within the agarose had a velocity which lies between these two values and so no significant difference is seen when the cells in the agarose are compared to either of these two conditions. However, although the cells within the agarose appeared to move as rapidly as on 2D surfaces, they did not move as directly, with significant differences seen between the meandering indices for the cells within agarose and the cells on the plastic and on the nitrocellulose surfaces. By 20 minutes into image acquisition, the cAMP gradient between the agar and agarose would have established and should not have yet been degraded, and by inspection of the volumes by eye in time-lapse, it can be seen that not many multicellular aggregates had formed, so it is unlikely that there were any significant confounding cAMP signals present[496]. Therefore it appears that the agarose presents an impediment to *Dictyostelium* cells chemotaxing in a straight line. This may either represent a problem with the propagation or detection of the cAMP gradient within the gel, or with the motility of the cell through agarose. The latter seems the most likely explanation, as the experiments with developing *Dictyostelium* showed that cAMP waves could be visualised propagating through cells within agarose. Additionally, when the image sequence

is viewed by eye, a dramatic downwards migration of the cells is seen under these experimental conditions, which is not seen in the absence of cAMP agar, indicating that the cells are able to both detect and respond to the chemoattractant gradient.

As agarose gels have been shown to be non-homogenous in structure, it is possible that, during the course of their migration through the gel, cells encountered patches of the agarose which they were unable to penetrate, or which they chose not to penetrate, perhaps preferring to take a less challenging route, which forced them to change direction[174,589]. This agrees with the effects of micropillars on directly moving vegetative state *Dictyostelium* cells scale seen by Arcizet et al[18,21]. Although their experiments used vegetative state cells, these cells are known to have two distinct modes of migration, directed migration and randomly moving migration[21,258,410,657]. While the randomly moving cells preferred to localise to micropillars rather than to the planar surface because of the increased surface area available to them in this location, the cells which were moving more directly and therefore more similarly to the chemotaxing cells in my experiments were deflected by the micropillars, which reduced their directional movement[18]. Alternatively, as *Dictyostelium* cells have previously been shown to respond to cyclic stretching of their substratum with changes in both speed and direction of migration, local changes in the elastic properties of the agarose could result in changes in cell orientation, such as those seen in my results, although it should be noted that a 30% stretching ratio was used in these experiments and it would be unlikely to find such large differences in elasticity between two adjacent areas within agarose[280,372,443,616]. Additionally, cells exert a force on their substratum when they migrate, which could also cause local changes to the elasticity of the agarose gel, which in turn may exert an effect on the chemotaxing cells. Due to the relative magnitude of the forces involved this is not likely to occur with individual cells, but may play a role when many cells are migrating together such as in multicellular aggregates or cell streams[132,329,374,443].

While there have been a number of studies investigating the migration of mammalian cells within 3D environments, the breadth of different cell types, from fibroblasts to tumour cell lines, and the number of different matrices in which the cells are set make comparisons difficult to draw[48,172,461,479,677,680,698]. For example, mammalian fibroblasts migrate more directionally in three-dimensions, which the authors suggest is an effect of the structure of the matrix in which the cells were placed[462]. This directly contradicts my findings with *Dictyostelium* within an agarose gel, but it cannot be said if this is a result of the fact that different cell types were used, or that these cells were set within different gels. Just because we have included

another dimension does not negate the previous research showing the importance of physiochemical surface properties on cell behaviour[24,88,95,118,172,200,373,510,626,688]. Additionally, it is not always possible to say whether a characteristic of cell migration within a 3D matrix is as a result of the fact that the cells are set within a 3D environment and are therefore surrounded on all sides by substrate, or whether it is that the environment has very different physical, chemical and rigidity properties to the more commonly used 2D planar surfaces. In light of the research indicating the potential for restrictive environments to alter gene expression and cause cytoskeletal remodelling and the range of effects of biomaterials on cell behaviour, it seems most likely that both the different properties of the materials in which cells are embedded in 3D, generally gels and matrices, as opposed to the more rigid 2D surfaces, and the fact that the cell is surrounded on all sides, play a role in establishing the morphology, migration and other behaviour of a cell within a 3D matrix[36,172,305,340,372,443,446,554,677,681,698].

Chemotaxis assays can be performed under agarose, and these assays have previously been used to investigate *Dictyostelium* chemotaxis[120,329,338]. This environment appears to present an environment of increased challenge to *Dictyostelium*, as certain mutants display an impaired ability to move under these conditions[338,339,445]. It may more closely approximate the natural conditions of *Dictyostelium* than studies performed on 2D surfaces such as glass, plastic or nitrocellulose as the cells are in contract with the agarose above and the plastic surface of the Petri dish beneath. However, these conditions, which usually utilise 1-2% agarose, cause *Dictyostelium* cells to become flattened, resulting in the redistribution of myosin II and actin[329,446]. Although it has been argued that the under agarose assay may approach the conditions which *Dictyostelium* cells find themselves within their natural environment of soil, it should be noted that one of the differences which has been found between cells grown in 2D and cells grown within the more natural environment of 3D matrices is that cells in 3D are rounder and less flattened and spread than cells on 2D surfaces[117,235,329,479,579,679,680,682]. Therefore the flattening of the cells by the agarose seen in the under agarose chemotaxis assays utilising higher concentrations of agarose may not in fact be found within a truly 3D environment. However, chemotaxis assays with cells under 0.5% agarose have also been performed, and under these conditions the cells are less flattened (8 μm tall rather than 4 μm tall under higher concentrations of agarose). NC4A2 cells under 0.5% agarose were shown to move consistently at speeds of 6.4 μm/min, however, Ax2 cells were found to move at 7.4μm/min, which is similar to their speed within a 0.5% agarose gel (7.8 μm/min)[328,329]. These under agarose experiments showed direction changes of approximately 16.7 degrees between time steps of 1 minute indicating that the cells were migrating in a direct manner, which does not

agree with my measurements of meandering index of Ax2 cells chemotaxing within 0.5% agarose[328]. While this may reflect an effect of the different environments of the two assays, because the under agarose studies used the chemoattractant folate rather than cAMP which interacts with a different cell surface receptor on the *Dictyostelium* cell membrane, it is not possible to draw any firm conclusions about environmental effects from this comparison[69,129,239,329,639].

As growing cells within three-dimensional environments has been shown to have a variety of different effects on their behaviour, probably due both to the dorsal side of the cell being constrained and to the physiochemical and elastic properties of the matrix in which they are placed, and the natural environment of *Dictyostelium* cells is a three-dimensional one, the potential of an agarose gel to offer a three-dimensional environment in which to investigate the migratory behaviour of *Dictyostelium* cells has been demonstrated[31,248,513]. Furthermore, the utility of the non-invasive interferometric imaging technique of OCT for imaging of cells under these conditions, in order to obtain qualitative and quantitative data on the features of cell migration within this matrix has been shown[56].

5.11 Chapter 5 Summary

Multicellular aggregation, followed by development, is an important stage in the life cycle of *Dictyostelium*, as the culmination of this process leads to dispersal in search of new food sources[51,55]. While this process has been well studied in time-lapse on 2D substrata, this aggregation has not yet been explored within true 3D environments[142,329,658]. This chapter has shown that OCT can be used to follow the aggregation and development of *Dictyostelium* cells within a 3D agarose gel, including the potential to image propagating optical density waves, representing the propagating cAMP signal, and to investigate the manner in which *Dictyostelium* cells aggregate in this more complex environment. As the cells are not labelled in any way, there is no toxicity to the cell or photobleaching, indicating that this microscopy technique could potentially be used to follow this process over extended periods of time.

Chemotaxis within this 3D agarose gel environment was accomplished, by setting up a diffusion-based gradient within the agarose, by use of a base of 1 μM cAMP agar. The images acquired were subjected to qualitative assessment and subsequently imported into tracking software and tracked to obtain quantitative information on the character of cell chemotaxis within a 3D environment. The exploration of environment on *Dictyostelium* cell behaviour begun in chapter 4 was then extended to the fourth dimension, and an effect of this 3D agarose environment on the meandering index, a measure of how directly a cell moved during its translocation, was found. No effect was seen on the velocity of the cells, which indicated that the cells are able to move through the gel at normal speed but find direct motion somewhat impeded, potentially due to the increased challenge of navigating this 3D environment.

Chapter 6: Role of myosin II in *Dictyostelium* in 4D migration and chemotaxis

6.1 Chapter 6 Aims

This chapter aimed to explore the effects of the three-dimensional environment of an agarose gel on the migration and chemotaxis of *Dictyostelium* cells lacking the gene encoding Myosin II. This was in order to determine if this 3D assay was a useful method to investigate phenotypes of *Dictyostelium* mutant cell strains; moreover, to assess the possibilities offered by this 3D environment to probe the migration and chemotaxis of mutant cells, and to obtain quantitative information to describe these migration characteristics.

6.2 Motility of Myosin II null cells in Dictyostelium

Cell motility is a complex process regulated by remodelling of the actin-myosin cytoskeleton. Much of what is known about cell motility comes from the creation of *Dictyostelium* mutants and observation of their phenotypes. This is due to their rapid growth, ease of culture and conserved signalling pathways with mammalian cells, in combination with the relative ease of generation of mutants[271,299,544]. Visualisation and comparison of the behaviour of mutant cells with their parent strain, particularly mutations in cytoskeletal components or known signal transduction molecules, can be useful to determine the role of the missing protein in cell aggregation and development.

Dictyostelium cells lacking the myosin heavy chain have a pronounced mound-arrest phenotype[128,313]. Pre-spore cells are able to differentiate, but tip formation does not occur and development never proceeds beyond the tight aggregate stage[139,314]. When mixed with wild-type cells, in a chimeric aggregation assay, mhcA- (Myosin heavy chain A null) cells will complete development, but the number of fruiting bodies is far fewer than would be expected for the initial number of cells[313]. Imaging studies have revealed that the mhcA- cells localise to the edges of streams where they are apparently dragged along with the wild-type cells in order to complete the developmental process and have also shown that they are absent from the mound tip[313,314,564]. At the mound stage, mhcA- cells have been shown to become stuck in place, 'jiggling' on the spot[139]. Previous work has indicated that mhcA- cells have difficulty moving in under 0.5% agarose assays, with only a few cells entering the more restrictive environment of the agarose, and most of them remaining in the trough cut into the agarose in which they were originally placed[328]. Those that do enter the agarose, show significantly reduced ability to chemotax, stopping at a distance of 500 μm after approximately 4 hours and not chemotaxing any further, over the duration of the 9 hour experiment, compared to the

wild-type cells covering a distance of 3000 μm over the same time period[328,329]. MhcA- cells under 1% agarose do not enter the under-agarose environment of the assay, indicating that, despite the presence of chemoattractant on the other side of the agarose, this environment is too restrictive for them to penetrate[328]. The above phenotypes have been attributed to a lack of cortical integrity of mhcA- cells helping to explain why they struggle to migrate under 0.5% agarose and are unable to move within the restrictive environments of mounds and under-1% agarose[139,314,328]. Furthermore, myosin II plays a critical role in retraction the uropod, the rear of the cell, and mhcA- cells have been seen to have difficulty retracting their uropod both under agarose and under buffer, slowing their migration, and sometimes resulting in cell fragmentation[279,328,414].

Examination of mhcA- cells on glass under buffer has revealed that these cells exhibit reduced speed, reduced persistence, both when chemotaxing and in basic cell motility, and reduced chemotactic index in response to a chemoattractant gradient[255,374,582,593,702]. While myosin II is not thought to be directly involved in the generation of pseudopodia, it does appear to have a role in the regulation of this complex process[255,582,593,702]. Myosin heavy chain null mutants extend pseudopodia all over the cell and not just localised to the leading edge, which may be due to misregulated spatial localisation of Ras and its downstream signalling molecules[197,350]. The result is that they exhibit chemotactic defects, involving increased turning and reduced speed[197,582,668]. Cells lacking myosin II have also been shown to have impaired ability to respond to a spatial chemoattractant gradient and complete inability to respond to a temporal gradient, such as those released by aggregation centres during *Dictyostelium* development, which may contribute to their developmental defects[255,668,702]. Recent work has shown the importance of a properly organised cytoskeleton in both the synthesis of cAMP and response to a cAMP gradient, which may help to explain this impairment[569]. Moreover, traction force cytometry measurements have revealed that these cells exert abnormal patterns of force on their substrata and show delays in the cycles of force generation required for cell translocation[132,374,414].

Therefore, although the mechanisms behind myosin II function in *Dictyostelium* remain to be fully elucidated, it has been established to be essential for fast and directed cell migration on 2D substrata, both in basic cell motility and in response to a chemoattractant.

6.3 mhcA- cell development in 0.5% agarose gel

MhcA- (Myosin heavy chain A null) *Dictyostelium* cells were set within 0.5% agarose and imaged 8 hours later, with images acquired every 3 minutes (180 seconds) over a 2 hour (120 minutes, 7200 second) period, as described in the methods section. Figure 6.1(A-C) shows volumetric images of the mhcA- cells within the agarose from three different angles. All of the acquisition time-points (2 hours) have been summed together using the 'standard deviation' projection in ImageJ, as described in the methods section. This allows tracks to be seen from moving objects (as shown in Chapter 5 and later in this chapter). Cell tracks from cells moving on the surface of the agarose indicated by yellow arrows are shown in Figure 6.1B. Figure 6.1A-C shows the cells and multicellular aggregates within the agarose gel, which appeared stationary over the acquisition period. Figures 6.1A&B show the edges of the volumetric image better, while Figure 6.1C better shows the cells inside the agarose gel. Superimposed colour-coded enface images at the surface of the agarose, and at ~50 μm below the surface (both summed over ~10 μm) in Figure 6.1D(I) and E respectively; blue- 0 minutes, red- 60 minutes (3600 seconds) and yellow- 120 minutes (7200 seconds), show that there was motion seen on the surface of the agarose (Figure 6.1D(I)), but not within the agarose (at ~50 μm depth) (Figure 6.1E). A white arrow in Figure 6.1D(I) points to a motile cell on the surface of the agarose. The cross-sectional view (Figure 6.1D(II)) indicates that there was no lateral movement seen over the entire experimental time-period (2 hours).

In order to see if cell development and motility was arrested or merely delayed, the same experimental sample of mhcA- cells within 0.5% agarose was kept hydrated and covered overnight, and was imaged at 24 hours after commencement of the initial imaging, over 2 hours, acquiring every 3 minutes (Figure 6.2). All of the time-points were summed together using the standard deviation projection in ImageJ, which shows any tracks generated by moving objects (Figure 6.2). The entire volume is shown in Figure 6.2A. No tracks were seen within the agarose in Figure 6.2A. Enface images from the volume at the surface (Figure 6.2B) and at ~50 μm below the surface of the agarose (slices summed over ~10 μm) (Figure 6.2Ci) show cells still moving on the surface (Figure 6.2B) indicated with a yellow arrow, but not within the agarose (Figure 6.2C(I&II)). A cross-sectional view (slices summed over 20 μm from the middle of the stack) reveals that there was no lateral motion of the objects within the agarose (Figure 6.2C(II)).

Figure 6.1: mhcA- cell aggregation in agarose

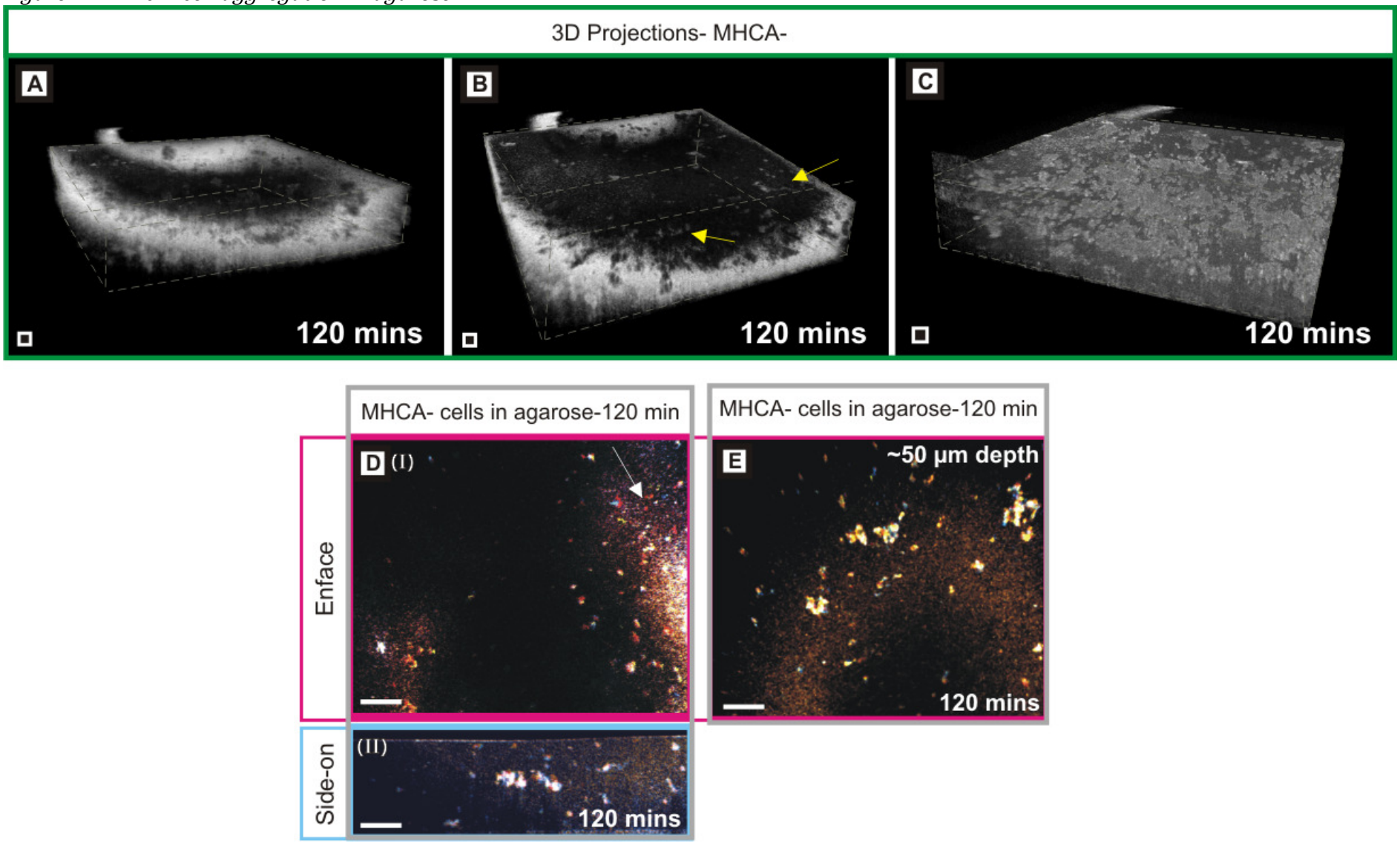

Figure 6.1: mhcA- cells in 0.5% agarose on an agar base layer imaged every 3 minutes over 120 minutes (A) Volumetric rendering (using Amira) of mhcA- cells summed over all time points (120 minutes) using the standard deviation projection in ImageJ. The cells within the agarose do not move. (B) Same image as A from a slightly different viewpoint showing the surface better. Yellow arrows point to examples of tracks created by cells moving on the surface of the agarose. (C) Volumetric rendering from a third viewing angle, better showing the cells within the agarose. All time-points summed over 120 minutes using the standard deviation projection in ImageJ. No cell tracks are seen within the agarose. (D-E) Superimposed false colour images (A) blue- 0 minutes, red- 60 minutes (3600 seconds) and yellow- 120 minutes (7200 seconds) (D(I) Enface image of mhcA- cells on the surface of the agarose, slices summed over ~10 μm, some cell movement is seen on the surface of the agarose. An example of this motion is indicated with a white arrow. (D(II)) Cross-sectional sum of B-scans over ~20 μm from the middle of the stack showing mhcA- cells do not appear to move vertically within the agarose. (E) Colour coded enface image of mhcA- cells summed over ~10 μm at ~50 μm below the surface of the agarose, no motion is seen. Scale bars are 100 μm.

Figure 6.2: mhcA- cell aggregation in agarose- 24hr

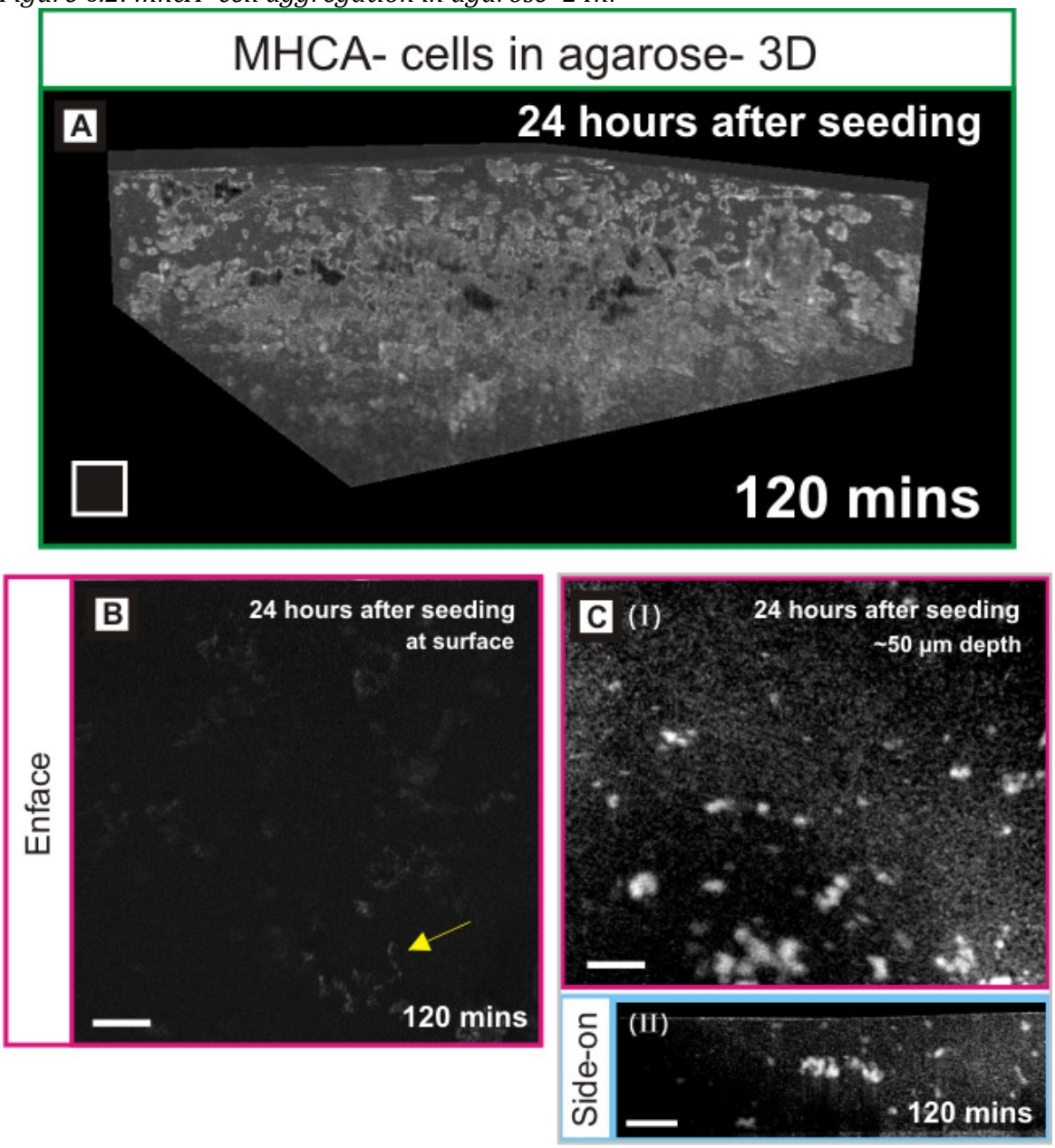

Figure 6.2: mhcA- cells within 0.5% agarose at 24 hours after the initial imaging point shown in the previous figure. Images acquired every 3 minutes (180 seconds) over 0-120 minutes (7200 seconds) (A) Volumetric image generated with Amira software showing all of the time-points of the experiment summed together using the standard deviation projection in ImageJ. (B) En face image (slices summed at ~10µm around the surface) of all of the time points of image acquisition (2 hours) summed using the standard deviation projection in ImageJ. Yellow arrow shows a moving cell on the surface of the agarose. (C(I&II)) Sum of all time points, every 3 minutes over 0-120 minutes in (I) en face (slices summed at ~10µm at ~50 µm below the surface) and (II) cross-sectional (slices summed over ~20 µm from the middle of the stack) planes at 24 hours after seeding. mhcA- cells have not developed within the agarose. No movement is seen over the course of the imaging. Scale bars are 100 µm.

While most of the experiments so far have focused on the axenic mutant of *Dictyostelium* Ax2, the parent strain of the myosin null cells, which I used for my experiments was JH10, an axenic thymidine auxotroph[238]. Therefore the results from experiments with the mhcA- cells have been compared with behaviour of JH10 cells (grown in axenic medium supplemented with thymidine), in order to ensure a fair comparison. Differences have previously been shown to exist in the behaviour of migrating axenic and true wild-type (solely bacteriovore) strains of *Dictyostelium* and in the gene expression profiles of cells grown under different conditions (on bacteria or in Axenic medium)[55,297,574]. The JH10 strain is originally derived from the Ax3 strain of *Dictyostelium*[238,404]. This strain is independent in origin from the Ax2 strain and is different genetically[199,375]. Therefore, the relevant parent strain (in this case JH10) should be used when comparing mutant and wild-type cell behaviour[394].

Although JH10 cells have previously been found to move poorly in under-agarose assays, they appear to move with comparable speed and directionality to Ax2 cells when placed within a 0.5% agarose gel[328]. This could potentially be attributed to the need for the cells to exit the trough in the under-agarose assay, whereas in my experimental configuration the cells are already set within the agarose and do not need to move from a less restrictive environment to an environment of increased challenge but merely need to exert enough force to initiate migration within the gel.

JH10 and mhcA- cells were seeded within a 0.5% agarose gel, as described in the methods section, and left under these starvation conditions for 8 hours prior to imaging. Image sequences were acquired over a 2 hour (120 minute, 7200 second) period at 2 minute (120 second) intervals. Volumetric images are shown in Figure 6.3. Figure 6.3A-B JH10 cells, and Figure 6.3C-D mhcA- cells. Experiments performed on two separate days for both strains. All of the time-points were summed together using the standard deviation projection in ImageJ, which shows tracks generated by moving objects. Tracks can be clearly seen in the JH10 images and some example tracks are indicated by yellow arrows (Figure 6.3A-B). The single JH10 cells were able to signal to one another and migrate within the agarose (Figure 6.3A-B- yellow arrows), aggregate together, and move as multicellular aggregates within cell streams (Figure 6.3A-B- orange arrows), and outside of cell streams (Figure 6.3A-B- pink arrows). The objects within the agarose in the mhcA- volumes appear stationary and no cell streaming was seen. (Figure 6.3C-D).

Figure 6.3: JH10 and mhcA-cell aggregation in agarose

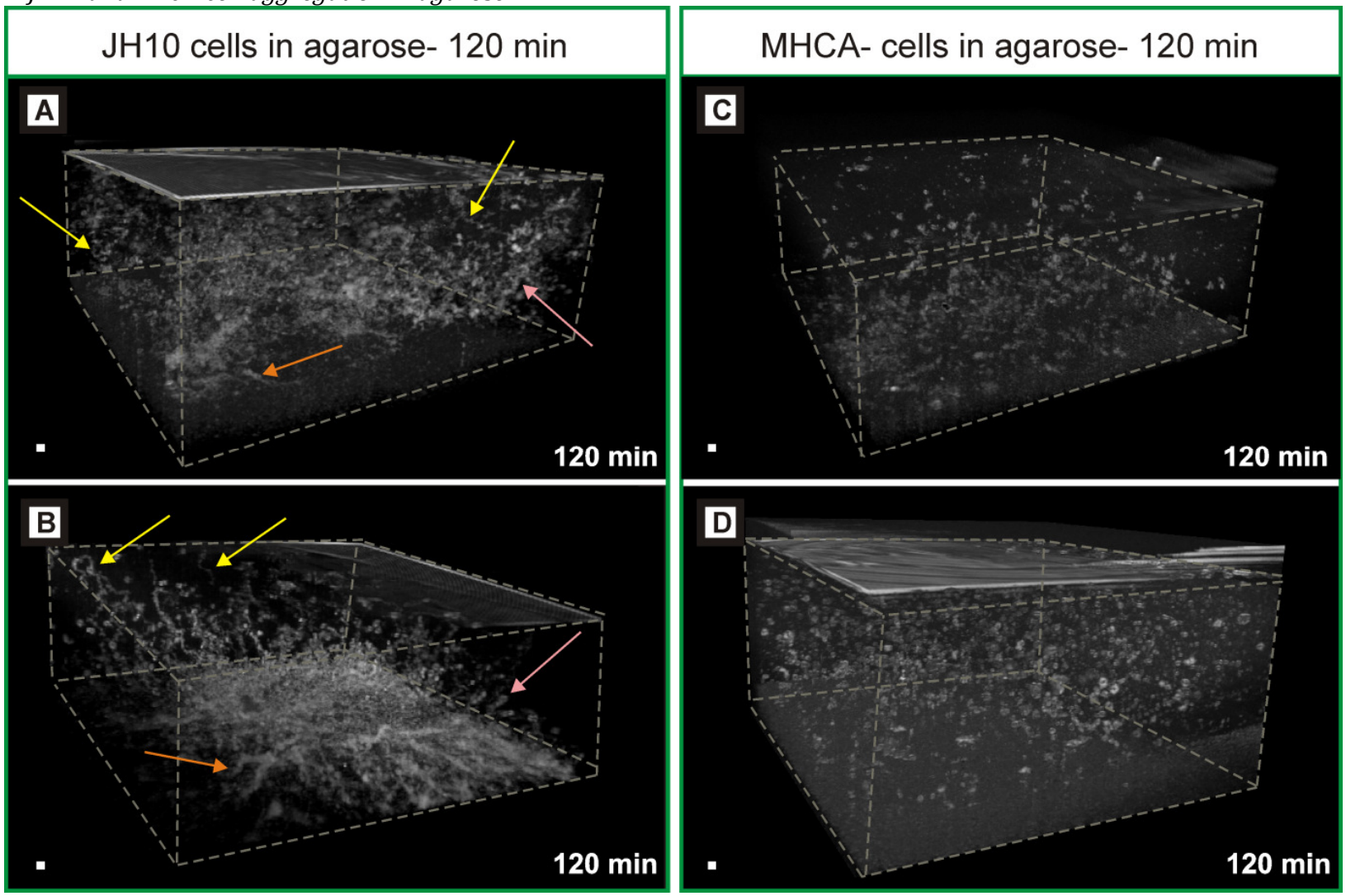

Figure 6.3: (A-B) JH10 and (C-D) mhcA- cells suspended in 0.5% agarose on an agar base layer, images acquired on two separate days for each of the cell strains. Images acquired every 2 minutes (120 seconds) over 2 hours, (120 minutes, 7200 seconds). Volumetric images generated using Amira software. Grey guidelines delineate the edges of the volumetric images for ease of visualisation. Images were acquired every 2 minutes over 120 minutes. Images summed over all time-points (2 hours) using standard deviation in ImageJ over 120 minutes to show the tracks of the cells and the general trend of cell motion. Yellow arrows illustrate tracks of cells moving in time in the JH10 images. Orange arrows indicate streams seen within the JH10 images. Pink arrows indicate tracks generated by migrating multicellular aggregates. No tracks are seen in the mhcA- images. Scale bars are 20 μm.

The evidence up to this point may lead one to conclude that mhcA- cells are unable to move within a three-dimensional 0.5% agarose gel environment; and as this is a challenging environment to navigate and these mutants have severe cytoskeletal deficits, this may not seem surprising[18,209,329,445,682]. However, a closer inspection of the volumes reveals that this is in fact not the entire story. Figure 6.4 shows the volumes from Figure 6.3, with the colour-coded areas (yellow, orange and pink) outlined by the boxes in Figure 6.4A&B magnified in Figures 6.4C-H. In Figures 6.4C&E, three example multicellular aggregates, by size comprised of two or three cells (Figure 6.4C- indicated by orange arrows) or a few more cells (Figure 6.4E- indicated by pink arrows), are shown over 4 minute (240 second) periods. The cells are colour-coded and superimposed with blue as the first time-point, magenta 2 minutes (120 seconds) later and yellow a further 2 minutes later. The multicellular aggregates change shape and morphology, in Figure 6.4C, migrating a short distance, and in Figure 6.4E briefly contacting another multicellular aggregate (yellow). Figures 6.4D&H show the multicellular aggregates from Figures 6.4C&E respectively, summed over the entire image acquisition time (2 hours). From these images it can be seen that the smaller multicellular aggregates indicated by the orange arrows in Figure 6.4C-D, although they changed shape and migrated a short distance, did not move far from their initial position over the entire 2 hour acquisition period, and so appeared to have not moved when considering the entire time-sequence collapsed to a single image. The larger aggregates indicated with pink arrows in Figure 6.4E-F changed morphology and even contacted another multicellular aggregate briefly, but did not shown any translocation from their initial position. Therefore, although the majority mhcA- multicellular aggregates do not translocate within agarose, it can be seen from Figure 6.4C-F that they were motile, changing morphology, and that the smaller aggregates could migrate,

although only over a short distance. Furthermore, these motile cells do not form cell streams or progress further with development (as seen previously in Figures 6.1&6.2).

Turning to the behaviour of single mhcA- cells within agarose, a single migrating mhcA- cell is shown, as an example, in Figure 6.4G-H. All of the time-points of the image acquisition (every 2 minutes for 2 hours) were summed together to show the tracks of moving objects. The beginning and end of the cell's track is indicated by yellow arrows in Figure 6.4G, and the path taken by the cell has been manually traced on the image in Figure 6.4H for clarity. The cell entered the magnified area of the image at 70 minutes (4200 seconds) after image acquisition begun, so the track of the cell spans 50 minutes (3000 seconds). This is one example of a few migrating mhcA- cells within the volumes, but there are not many, and there are certainly far fewer than seen with the JH10, parent strain, which is why on inspection of the whole volume it did not appear as though mhcA- cells were able to move within 0.5% agarose gel, as these few motile cells were easily missed. Therefore, in order to properly explore the motility of mhcA- cells within an agarose gel, quantitative information about the characteristics of this migration must be obtained.

Figure 6.4: mhcA-cell aggregation in agarose- additional details

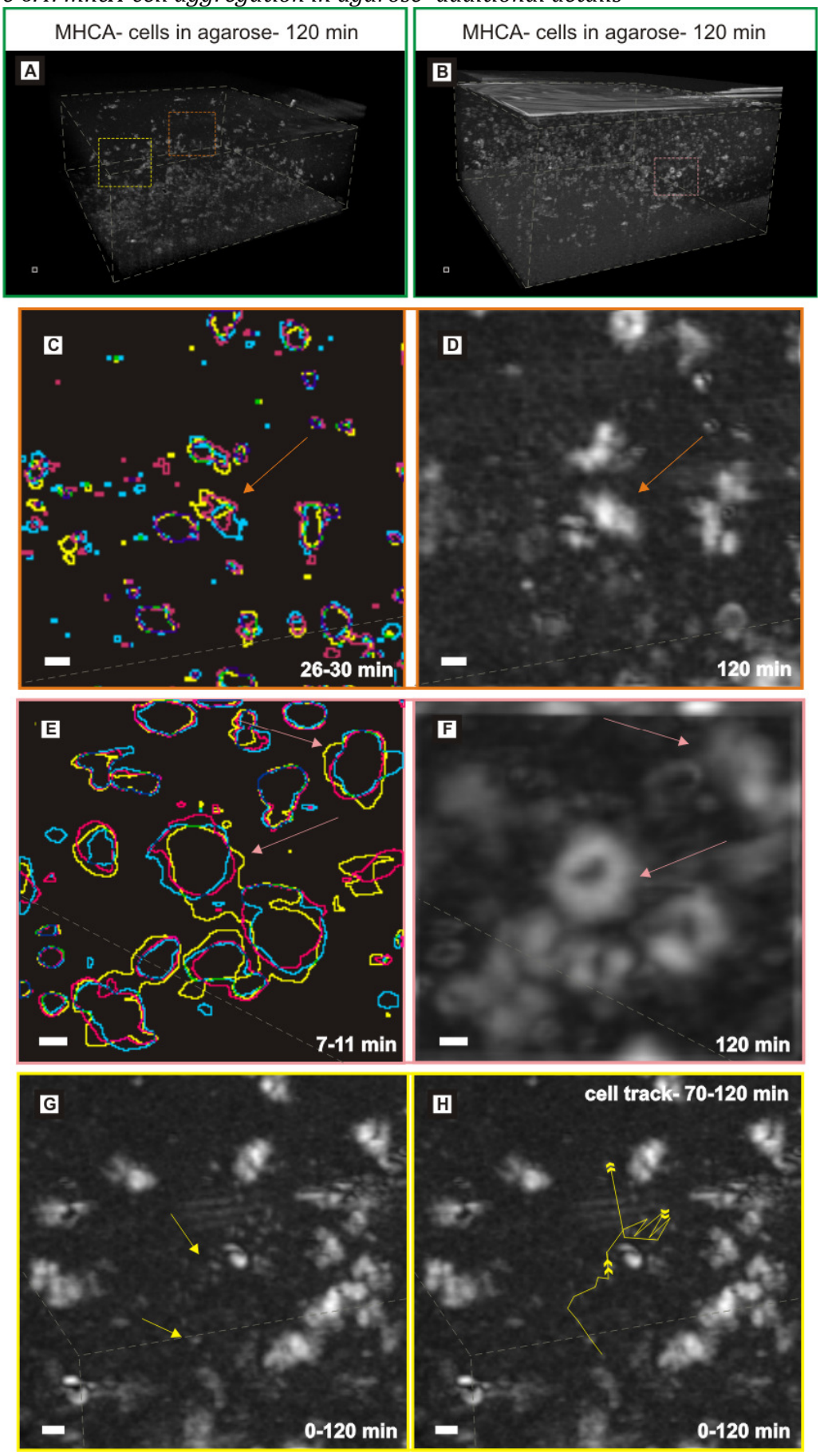

Figure 6.4: Volumetric images generated using Amira software of mhcA- cells suspended in 0.5% agarose on an agar base layer. Grey guidelines delineate the edges of the volumetric images for ease of visualisation. Images were acquired every 2 minutes (120 seconds) over 120 minutes (7200 seconds). (A-B) mhcA- cells within agarose- entire volume. Image sequences acquired on two separate days. Outlined areas magnified in: yellow and orange, (G-H) and (C-D) respectively; pink, (E-F). (C) Three superimposed colour-coded images, 2 minutes (120 seconds apart), from 26 minutes (1560 seconds) to 30 minutes (1800 seconds) after the beginning of image acquisition, 26 minutes- blue, 28 minutes (1680 seconds)- magenta, 30 minutes- yellow. The cell aggregate changes shape and moves a small distance. (D) All time-points, 120 minutes, summed together using the standard deviation projection in ImageJ. The object followed over 4 minutes (240 seconds) in C appears stationary in D, so does not move any further than the short distance shown in C, over the entire acquisition time. (E) Three superimposed colour-coded images, 2 minutes (120 seconds apart), from 7 minutes (420 seconds) to 11 minutes (660 seconds) after the beginning of image acquisition, 7 minutes- blue, 9 minutes (540 seconds)- magenta, 11 minutes- yellow. The cell aggregates indicated by pink arrows change shape, but do not migrate any distance. (F) All time-points, 120 minutes, summed together using the standard deviation projection in ImageJ. The objects followed over 4 minutes (240 seconds) in E, indicated by pink arrows appear stationary in F, so do not move any distance from its initial starting point. (G-H) a single mhcA- cell motile within the agarose magnified. Yellow arrows indicate the approximate beginning and end of the track. (G) All time-points, 120 minutes, summed together using the standard deviation projection in ImageJ. The cell appears in the cropped image area at ~70 minutes (4200 seconds) after the beginning of acquisition and the track extends from this time point until the end of acquisition (120 minutes) (H) With a yellow track, manually generated, showing the path of the cell (which is seen over a time period of 50 minutes (3000 seconds) from 70 minutes (4200 seconds) after the beginning of image acquisition, for ease of visualisation. Scale bars are 20 μm.

6.4 JH10 and mhcA- chemotaxis in 0.5% agarose gel

To further explore the motility of mhcA- cells, as compared to their parent strain JH10, within a 0.5% agarose three-dimensional environment, it was necessary to track cells within the agarose and obtain quantitative information on the characteristics of the cell migration. As seen above, JH10 cells formed small, then larger multicellular aggregates, and began cell streaming, while mhcA- cells left under starvation conditions for the same amount of time formed small cell aggregates. In order to eliminate any variation in chemoattractant signalling and concentration which may arise as a result of these marked differences and to ensure that all cells were at the same stage of development, cells were exposed to extrinsic pulses of cAMP at regular intervals for 6 hours. They were then suspended within a 0.5% agarose gel,

which was resting on a 1 μM cAMP agar base layer. A diffusion based extrinsic cAMP gradient was then allowed to establish for 30 minutes prior to the commencement of image acquisition, with images then acquired every 2 minutes for 2 hours. Experiments were performed on three separate days for both the JH10 and mhcA- cells. Image stacks were subsequently imported into Volocity Quantitation software (PerkinElmer, USA) for tracking and to obtain quantitative information on the character of cell chemotaxis within an agarose gel, and to allow for a comparison of the migration of JH10 and mhcA- cells under these conditions. The tracking algorithm was constrained by the parameters outlined in the methods section, to restrict tracking of objects to single cells and to minimise potential artefacts.

Figure 6.5 shows the JH10 (Figure 6.5A-C) and mhcA- (Figure 6.5D-F) cell stacks used for analysis. A volumetric rendering of the images, summed together over all time-points (2 hours) using the standard deviation projection in ImageJ to show the cell tracks, is shown in Figure 6.5Ai-Fi). An example of a cell track is indicated in each volume with a yellow arrow. Figure 6.5Aii-Fii shows the tracks generated by the Volocity software: top left- volume, top right- enface image, bottom left- side view (X-Y), bottom right side view (X-Z). By inspection it can be seen that the tracks generated by the software appear longer for the JH10 cells than for the mhcA- cells. Table 3 is a summary of the velocity and meandering index of the JH10 and mhcA- cells tracked chemotaxing within agarose. In order to reduce errors from tracks generated by artefacts, only cell tracks which spanned the entire image acquisition period were included in the analysis. These parameters were chosen for analysis, as together they describe the track of a cell, in terms of how fast a cell is able to move, and how much it deviates from migrating in a straight line, as discussed in chapter 5.

Figure 6.5: JH10 and mhcA- cells in agarose tracked with Volocity software over 2 hours

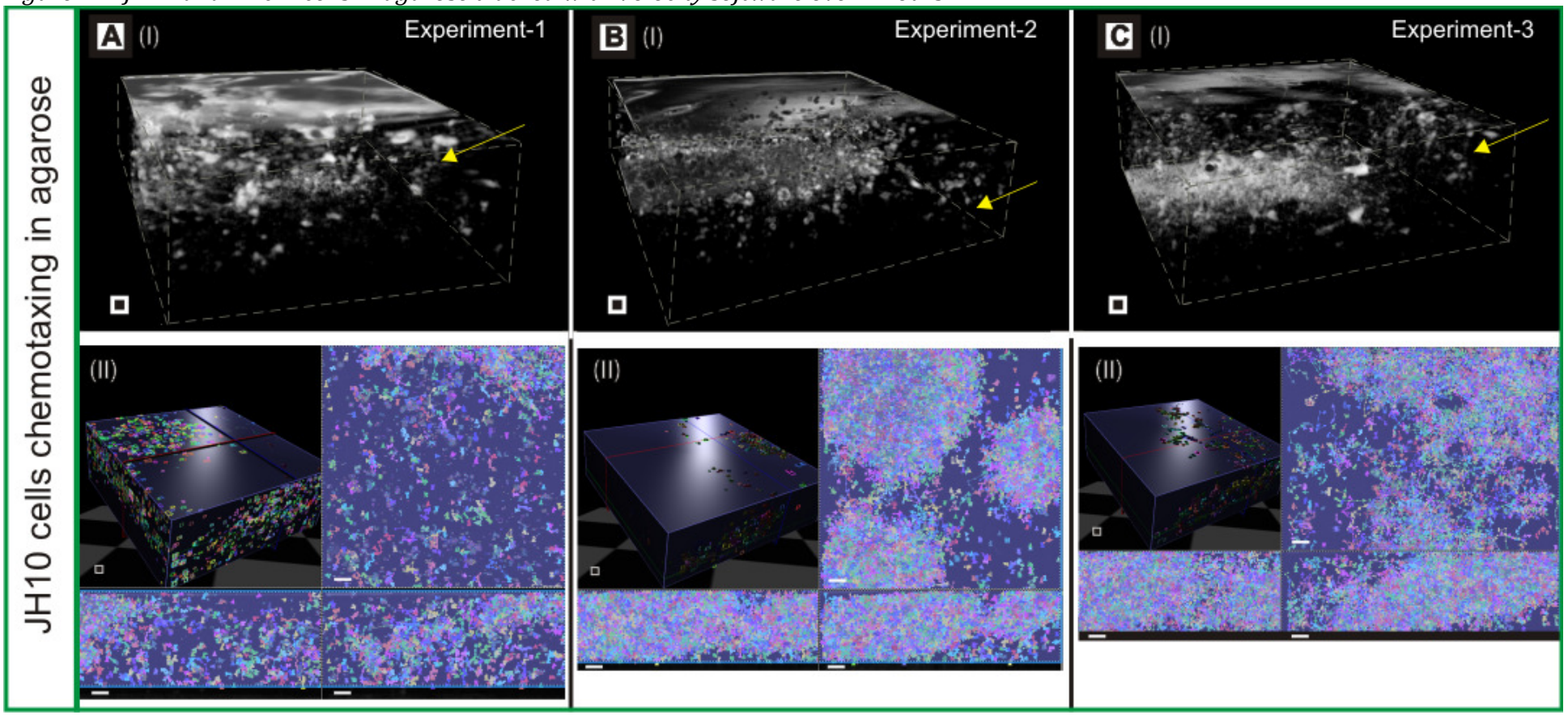

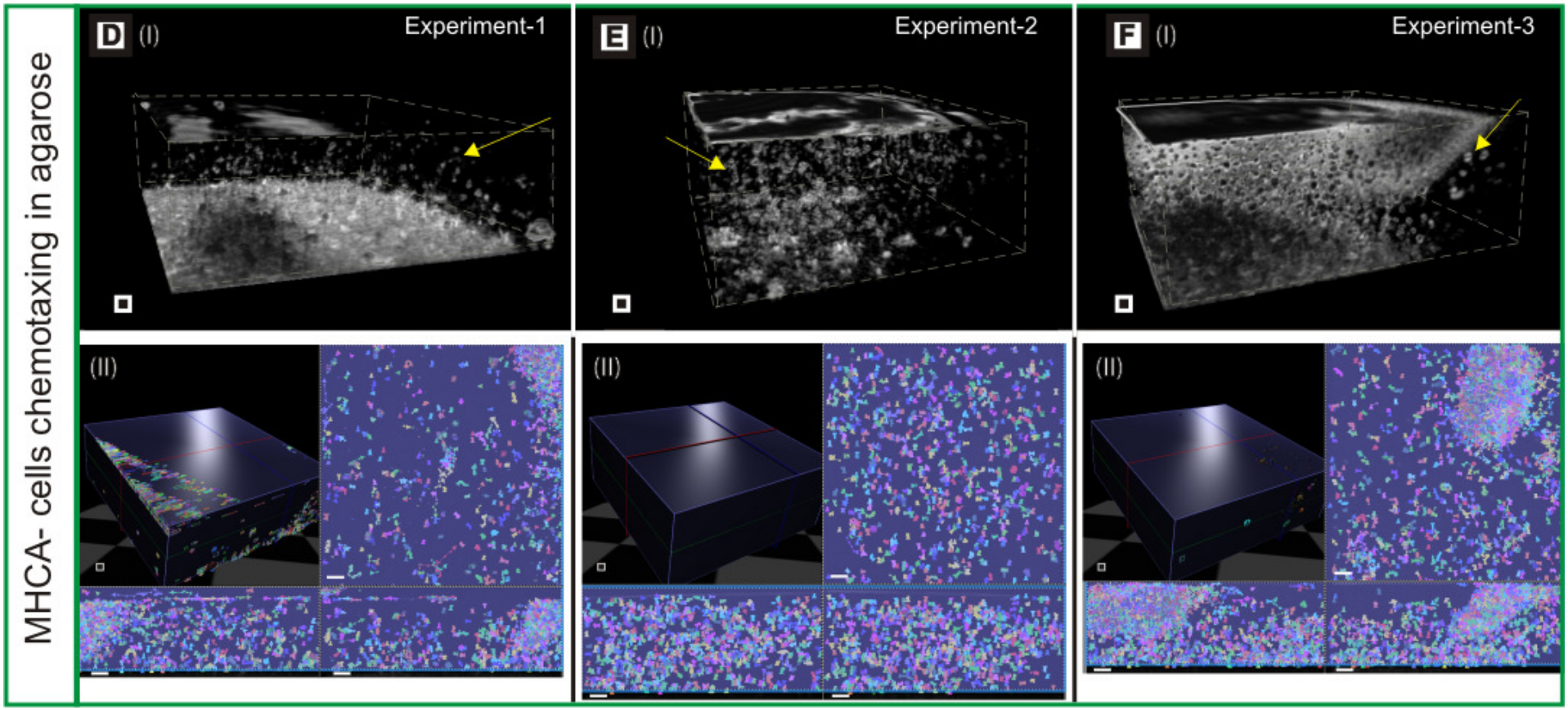

Figure 6.5: JH10 and mhcA- cells pulsed for 5 hours and seeded within 0.5% agarose on a bed of 1 µM cAMP agar. Images were acquired every 2 minutes over 120 minutes. Grey guidelines delineate the edges of the volumetric images for ease of visualisation. (A-C) JH10 cells, images acquired on three separate days. (D-F) mhcA- cells, images acquired on three separate days. (A-F(I)) Volumetric rendering of cells within the agarose summed using standard deviation projection in ImageJ for visualisation of tracks. Yellow arrows point to example tracks seen. (A-F(II)) Output from Volocity software after tracking showing the objects Volocity finds from the input parameters, and the tracks plotted by the software- Top left- entire volume (surface), Top right- enface view (single plane), Bottom left- X-Y view (B-scan), Bottom right X-Z view. By visual inspection the mhcA- tracks can be seen to in general be shorter than the JH10 tracks. Scale bars are 100 µm.

The results are summarised in Table 3, from which it can be seen that the mean velocity of the JH10 cells was 0.13±0.03 μm/s, 0.09±0.08 μm/s more than the mhcA- cells, where the mean velocity was 0.04±0.05 μm/s. The meandering index of the JH10 cells was also higher than that of the mhcA- cells, at 0.12 ±0.06, 0.04±0.12 higher than for the mhcA- cells, which had a meandering index of 0.08±0.06.

As there were a number of multicellular aggregates within the agarose, particularly in the JH10 experiments, which release cAMP as part of the natural developmental process of *Dictyostelium*, it is possible that some cells within the JH10 experiments were exposed to a cAMP gradient originating from these aggregates, and rather than move towards the cAMP agar instead moved towards these aggregates, as discussed for the Ax2 cells in chapter 5. Alternatively, the leading cells may disrupt the chemoattractant spatial gradient in the agarose, resulting in less directed migration for those following, as discussed in chapter 5. This also may happen to a certain extent within the mhcA- experiments, although this is less likely, as we have seen above that mhcA- cells are impaired in cell development within an agarose gel and fewer cells are motile (Figures 35-37). This reduced motility, resulting in the formation of fewer aggregation centres and less disruption of the cAMP spatial gradient, may offer an explanation for why the chemotactic index of mhcA- cells (mean= 0.40±0.49, median= 0.55±0.71) was found to be 0.399±1.03 higher than that of JH10 cells (mean= 0.001±0.54, median= 0.02±0.90) under these conditions. This difference is significant at the 95% confidence interval (Mann-Whitney test U= 187032, Z= 14.17, $p<0.001$).

To exclude the possibility of the differences in the chemotactic parameters between the JH10 and mhcA- cells being mediated by differences in proportion of actively chemotaxing cells (cells moving towards the cAMP source) and cells which were moving in other directions, the data were subjected to a filter on the basis of chemotactic index, calculated as described in the methods section. Cells with a chemotactic index of less than 0.75 (not moving towards the cAMP agar) were excluded from analysis in the CI filtered data, so that only cells where the general direction of motion was towards the cAMP agar were included in the analysis for this filtered data. The means and medians for this data are summarised in Table 3 (CI filter). The differences seen in chemotactic parameters between the JH10 and mhcA- cells persisted in the data filtered in this way, with the CI filtered JH10 cells having a mean velocity of 0.19±0.04 μm/s, which was 0.17±0.06 μm/s higher than that of the mhcA- cells, at 0.02±0.02 μm/s; and also a higher meandering index of 0.10±0.06, 0.03±0.11 higher than the 0.07±0.05 meandering index of the mhcA- cells.

In order to see if there was any effect of filtering the data on the basis of chemotactic index on the chemotactic parameters of each cell strain, i.e. to test if filtering had any significant effect on the velocity and meandering indices of the cells, the filtered datasets were compared to the unfiltered datasets, for both the JH10 and mhcA- cells. All distributions of the data were significantly non-normal (Anderson-Darling tests $p<0.005$ for all), so Mann Whitney tests were performed by way of comparison. The JH10 cells showed significant differences at the 95% confidence level between the unfiltered and filtered data for both velocity ($U=56639$, $Z=|2.81|$, $p=0.005$) and meandering index ($U=49549$, $Z=|4.69|$, $p<0.001$). The mhcA- cells also showed significant differences at the 95% confidence level (velocity- $U=32398$, $Z=|5.69|$, $p<0.001$; meandering index- $U=39517.5$, $Z=|2.66|$, $p=0.008$). This shows that the cells which were chemotaxing directly downwards towards the cAMP source had different velocities and meandering indices than the whole (unfiltered) population of cells, which indicated that there are potential differences between the migration character of cells within an agarose gel chemotaxing directly towards the known source of cAMP agar, and those where the overall trajectory was not towards this known source.

The differences between the JH10 and mhcA- cells, both unfiltered and chemotactic index filtered were tested using Mann-Whitney tests, as all of the probability distributions of the data were significantly non-normal (Anderson-Darling tests, all: $p<0.005$). The results are summarised in Table 3, with significant differences at the 95% confidence interval seen between the JH10 and the mhcA- cells for velocity and meandering index in both the unfiltered and data filtered on the basis of chemotactic index ($p<0.001$). Box plots of the velocity and meandering index of JH10 and mhcA- cells, for both the unfiltered and chemotactic index filtered data are shown in Figure 6.6. Figure 6.6A-B unfiltered data, A- velocity, B- meandering index; Figure 6.6C-D chemotactic index filtered data, C- velocity, D- meandering index.

Figure 6.6: Box and whisker plots of chemotaxis parameters of JH10 and mhcA- cells within 0.5% agarose- over 2 hours

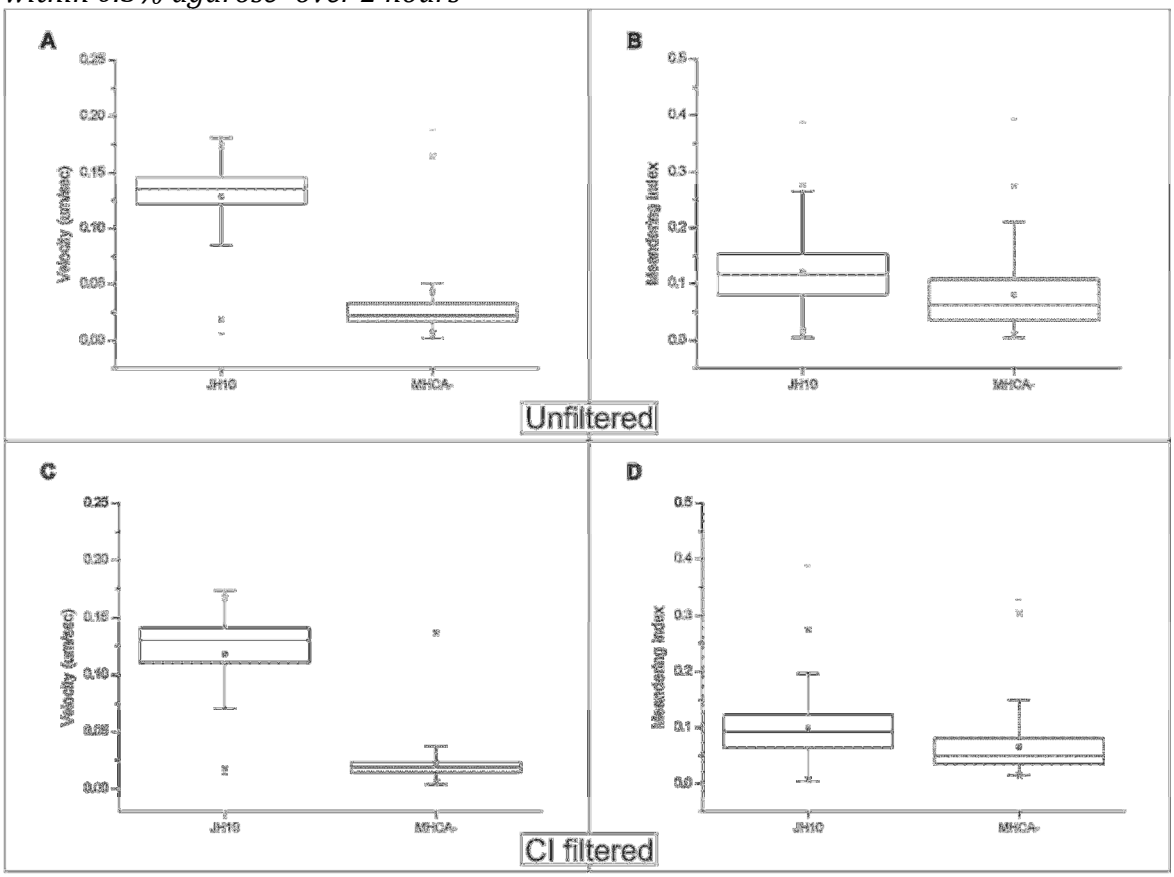

Figure 6.6: Box and whisker plots showing the distributions of (A&C) velocity and (B&D) meandering index of chemotaxing JH10 and mhcA- cells pulsed for 6 hours, suspended within 0.5% agarose on a 1 μM cAMP base layer, and imaged over 2 hours (120 minutes, 7200 seconds). Acquisition was every 2 minutes (120 seconds). (A-B) Unfiltered data. (C-D) Data filtered on the basis of chemotactic index, to include only tracks where the net direction of motion was in the downwards direction, towards the cAMP agar (excluded tracks with a chemotactic index of <0.75). The box shows the interquartile range, with the median value as a line across the middle. The small square box inside the boxplot is the mean. Whiskers represent the 5th-95th percentile of the data. Crosses represent the 1st and 99th percentile of the data. Data were obtained on three separate days. The data were truncated to exclude any tracks which did not span the entire 2 hour image acquisition period.

Table 3: JH10 cells and mhcA- cells migrating within a 0.5% agarose gel over 2 hours- Results and Statistical Analyses

Condition	Velocity (µm/s)	CI filter Velocity (µm/s)	Meandering Index	CI filter Meandering Index
JH10 in agarose gel	0.13±0.03 (0.14±0.03)	0.19±0.04 (0.13±0.03)	0.12±0.06 (0.12±0.07)	0.10±0.06 (0.09±0.06)
mhcA- in agarose gel	0.04±0.05 (0.02±0.02)	0.02±0.02 (0.02±0.009)	0.08±0.06 (0.06±0.07)	0.07±0.05 (0.05±0.05)
JH10 vs mhcA- in agarose	U=79223.50 Z=|25.37| P<0.001*	U=751.00 Z=|13.13| P<0.001*	U=179290.50 Z=|14.97| P<0.001*	U=5181.00 Z=|6.49| P<0.001*

Table 3: Grand means (±SD) and medians (±interquartile range), in brackets, calculated from the mean values obtained for each cell. JH10 in agarose n=1159. mhcA- in agarose n=558. JH10 in agarose chemotactic index filtered n=116. mhcA- in agarose chemotactic index filtered n=164. Summary of the results of statistical analysis for JH10 cells and mhcA- cells, * indicates significance at 95% CI.

6.5 JH10 and mhcA- aggregation in agarose- bimodal velocity

Plots of the probability density functions of the JH10 and mhcA- cell velocities reveal two peaks, indicating that the data may be bimodal. This was also found for the data which had been filtered by chemotactic index (CI >0.75, as described in the previous section). Furthermore the density plots for both filtered and unfiltered data have similar patterns (Figure 6.7). This indicates that this bimodal pattern of motion was not restricted by chemotactic index of the migrating cells, i.e. that this bimodality does not arise as a result of differences in velocity between cells which are moving directly towards the cAMP source and cells which are not.

Hartigan's dip tests were performed which indicated that the velocity of the cells was significantly bimodal at the 95% confidence interval for all of the data. JH10 unfiltered data p= 0.01, mhcA- unfiltered data p=0.04, JH10 CI filtered data p=0.03, mhcA- CI filtered data p=0.02 (all <0.05)[247,387,505]. This may indicate that there were two populations of cells, a slow moving group and a faster moving group within the overall motile cell population.

Figure 6.7: Probability density plots of the velocity of JH10 and mhcA- cells within 0.5% agarose over 2 hours

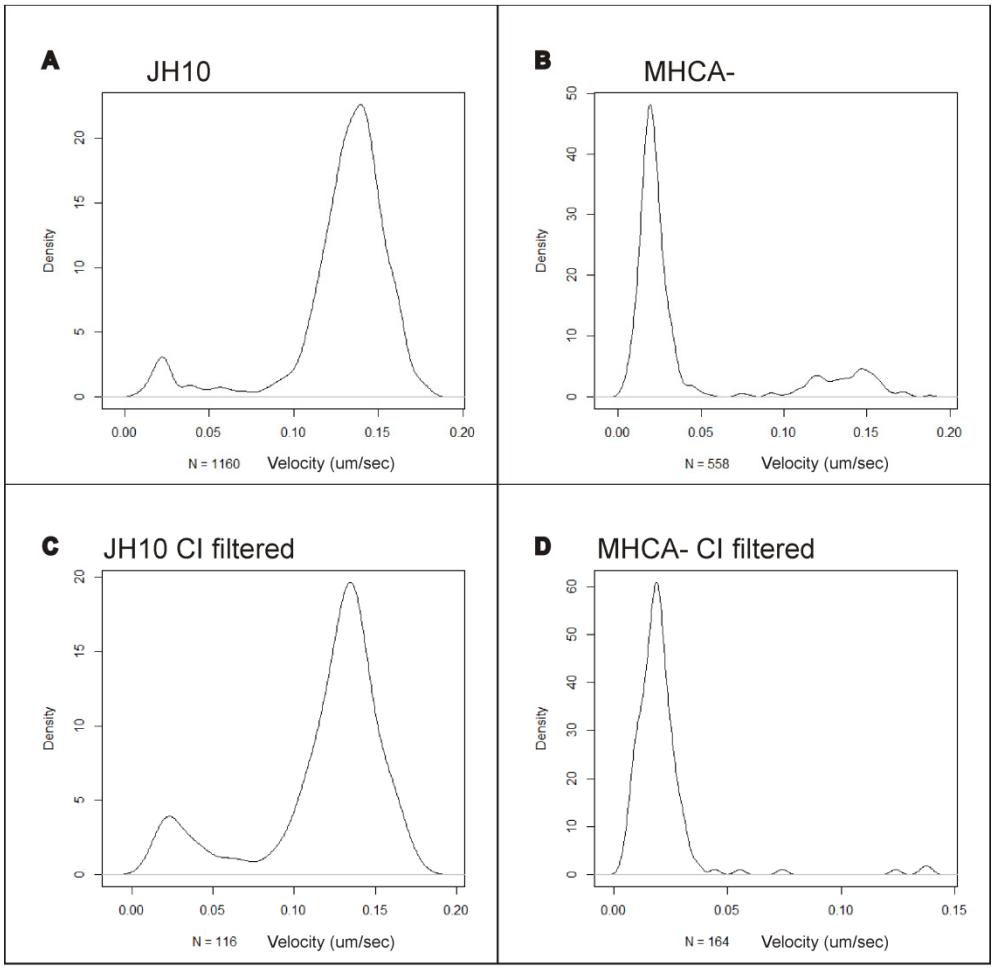

Figure 6.7: Probability density plots, generated, using R statistical software, of the velocity of (A) JH10, (B) mhcA-, tracked over 2 hours (C-D) Data filtered to exclude data with a chemotactic index of less than 0.75. (C) chemotactic index filtered JH10 cell velocity. (D) chemotactic index filtered mhcA- cell velocity, tracked over 2 hours.

The data for the overall population of cells were divided into two groups by velocity, in roughly the middle, with cells with a velocity greater than or equal to 0.075 μm/s placed into the high velocity filtered group, and cells with a velocity of less than 0.075 μm/s placed into the low velocity filtered group. Out of an initial population of 1159 tracks, 1074 of the JH10 cells (92.7%) had a velocity ≥0.075 μm/s and 85 (7.3%) had a velocity <0.075μm/s. Of the original 558 mhcA- cells, successfully tracked over the entire 2 hour time-series, 107 (19.2%) had a velocity ≥0.075 μm/s and 451 (80.8%) had a velocity <0.075μm/s. In order to see whether the large difference in velocity of the overall population of cells seen between the JH10 and mhcA- cells may be due to this difference in proportion of fast-moving to slow-moving cells, rather than due to any difference in the ability of cells to migrate, the velocity and meandering indices of the JH10 and mhcA- cells were compared for both slow-moving and fast-moving cells, filtered as described above. The data and results of statistical analysis are summarised in Table 4. Box plots of the data are shown in Figure 6.8.

The distributions of the high velocity filtered JH10 cells were non-normal at the 95% confidence level (velocity $p=0.013$, meandering index $p<0.005$, chemotactic index $p<0.005$), so although the distributions for the mhcA- cells were normal for velocity and meandering index (Anderson-Darling tests at 95% confidence, velocity $p=0.176$, meandering index $p=0.052$, chemotactic index $p=0.018$), Mann-Whitney tests were used to compare the data. The distributions for both the JH10 and mhcA- low velocity filtered cells were non-normal for all of the chemotactic parameters to be compared (Anderson-Darling tests at 95% confidence interval, velocity, meandering index and chemotactic index for both JH10 and mhcA-, $p<0.005$), therefore Mann-Whitney tests were used to compare the velocity, meandering index and chemotactic index between the two cell strains.

The mean velocity of the fast moving JH10 cells was 0.14±0.02 μm/s, 0.03±0.07 μm/s higher than that of the fast moving mhcA- cells, which had a mean velocity of 0.11±0.05 μm/s. This difference in velocity was not found to be significant at the 95% confidence level, $U=55633.0$, $Z=|0.56|$, $p=0.58$.

The mean velocity of the slow moving cells was 0.03±0.02 μm/s for the JH10 cells and 0.02±0.01 for the mhcA- cells, a difference of 0.01±0.03. Despite the fact that this difference is small, a Mann-Whitney test revealed that it was significant at the 95% confidence level, $U=10764.5$, $Z=|6.42|$, $p<0.001$. This is likely attributable to the fact that the Mann-Whitney test is a comparison of the sum of ranks and is therefore not only sensitive to changes in the absolute values of medians, but also to the spread and shape of the distributions being

compared[188,245]. These distributions are summarised as box plots in Figure 6.8 from which it can be seen that the shape and spread of the distributions of the mean velocities between the fast-moving JH10 and mhcA- cells are quite similar, but that they are quite different for the slow-moving cells. The above Mann-Whitney tests indicate that the fast moving mhcA- move with the same velocity as the fast moving JH10 cells, but the slow moving mhcA- cells move significantly slower than the slow JH10 cells.

No significant difference was seen between the meandering indices for the slow moving cells ($U=18647.0$, $Z=|0.40|$, $p=0.69$). However, although there is not much apparent difference between the absolute values of mean and median, a significant difference was found to exist between the meandering indices of the fast moving cells ($U=49269.0$, $Z=|2.45|$, $p=0.01$), with the JH10 cells moving more directly with a mean meandering index of 0.12 ± 0.05, compared to the mhcA- cells mean meandering index of 0.11 ± 0.05. As the Mann-Whitney test is a rank-sum test, which involves ranking the data and then summing the ranks for each variable, this significant difference likely reflects a difference in the distribution of results, with the JH10 cells having a significantly higher number of large values for meandering index (mean rank=599.17) than the mhcA- cells (mean rank=514.46)[188,245,391]. Although this is not readily apparent upon inspection of the box plots by eye (Figure 6.8), it should also be noted that a large number of samples increases the statistical power of a test thereby reducing the chance of a type II error, where no significant difference is found even if one exists[188,189].

Figure 6.8: Box and whisker plots of the velocity and meandering index of JH10 and mhcA- cells within 0.5% agarose over 2 hours- velocity filters

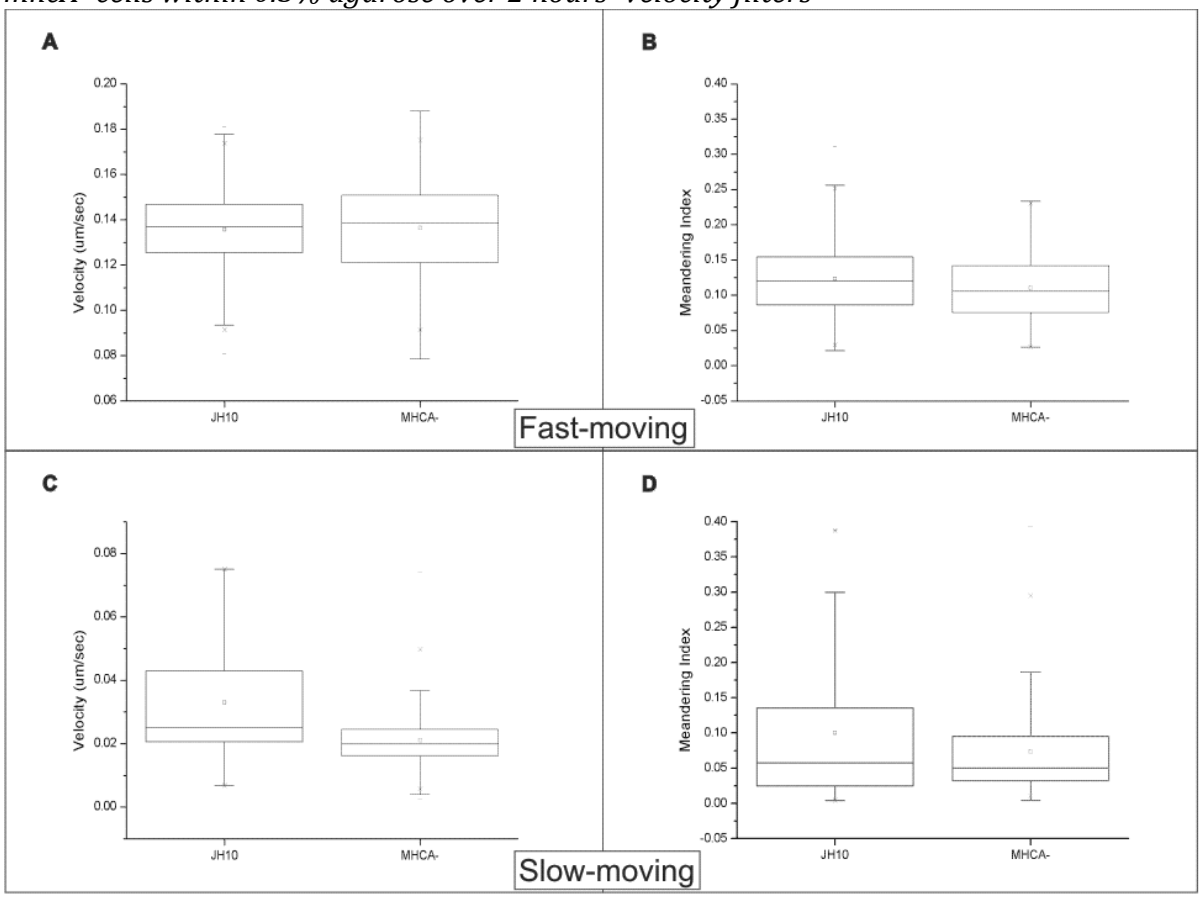

Figure 6.8: Box and whisker plots showing the distributions of (A&C) velocity and (B&D) meandering index of chemotaxing JH10 and mhcA- cells pulsed for 6 hours, suspended within 0.5% agarose on a 1 µM cAMP base layer, and imaged over 2 hours (120 minutes, 7200 seconds). Acquisition was every 2 minutes (120 seconds). Data filtered on the basis of velocity. (A-B) high velocity filter (fast moving cells) >0.75 µm/s. (C-D) low velocity filter (slow moving cells <0.75µm/s). The box shows the interquartile range, with the median value as a line across the middle. The small square box inside the boxplot is the mean. Whiskers represent the 5th-95th percentile of the data. Crosses represent the 1st and 99th percentile of the data. Data were obtained on three separate days. The data were truncated to exclude any tracks which did not span the entire 2 hour image acquisition period.

Table 4: JH10 cells and mhcA- cells migrating within a 0.5% agarose gel over 2 hours filtered by velocity- Results and Statistical Analyses

Condition	High velocity filter (≥0.075)		Low velocity filter (<0.075)	
	Velocity (μm/s)	Meandering Index	Velocity (μm/s)	Meandering Index
JH10 in agarose gel	0.14±0.02 (0.14±0.02)	0.12±0.05 (0.12±0.07)	0.03±0.02 (0.03±0.02)	0.10±0.10 (0.06±0.11)
mhcA- in agarose gel	0.11±0.05 (0.13±0.07)	0.11±0.05 (0.10±0.07)	0.02±0.01 (0.02±0.01)	0.07±0.06 (0.05±0.06
JH10 vs mhcA- in agarose	U=55633.00 Z=|0.56| P=0.58	U=49269.00 Z=|2.45| P=0.01*	U=10764.50 Z=|6.42| P<0.001*	U=18647.00 Z=|0.40| P=0.69

Table 4: Grand means (±SD) and medians (±interquartile range), in brackets, calculated from the mean values obtained for each cell. High velocity filtered JH10 in agarose n=1074. mhcA- in agarose n=107. Low velocity filtered JH10 in agarose n=85. mhcA- in agarose n=451. Summary of the results of statistical analysis for JH10 cells and mhcA- cells, * indicates significance at 95% CI.

Mann-Whitney tests revealed significant differences in the meandering indices between the two velocities for both the JH10, U=29148.5, Z=|55.6|, p<0.001, and mhcA- cells, U=12525.5, Z=|7.7|, p<0.001, indicating that the fast-moving cells moved more directly than the slow moving cells. The significance of the difference in meandering indices can be better understood by inspection of the displacement of the two populations of cells, both fast-moving and slow-moving. Box plots of the displacement for the slow-moving and the fast-moving JH10 and mhcA- cells are shown in Figure 6.9. These illustrate that although there were a few slow-moving cells in both the JH10 and the mhcA- cell populations which

translocated over 100 μm, indicating that they moved with a consistently slow pace, mainly in a single direction, the majority of the slow moving cells were almost non-motile, displacing only a few microns from their starting point. Conversely, although there were a few fast moving cells which did not translocate far, the majority of the fast moving cells displaced over 100 μm from their starting points for both the JH10 and mhcA- cells.

Figure 6.9: Box and whisker plots of the displacement of JH10 and mhcA- cells within 0.5% agarose over 2 hours- velocity filtered

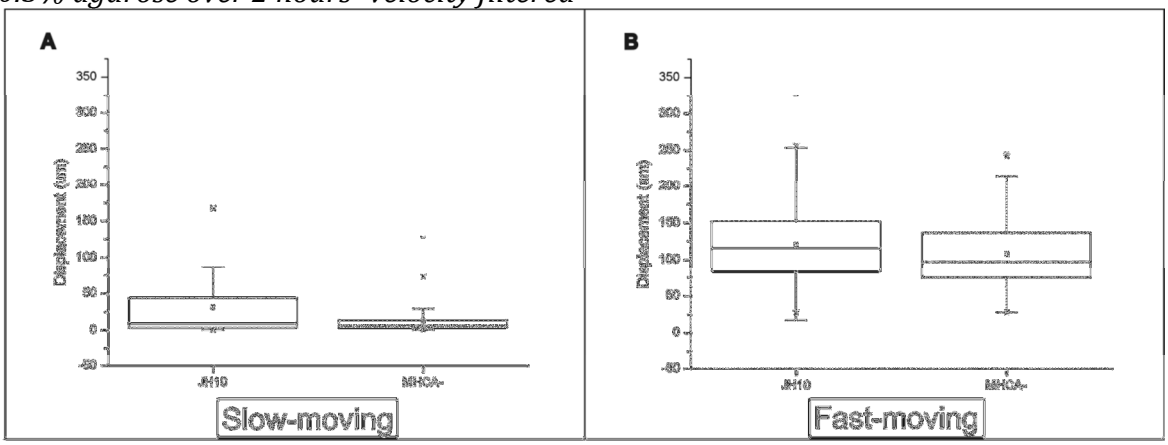

Figure 6.9: Box and whisker plots showing the distributions of displacement of chemotaxing JH10 and mhcA- cells pulsed for 6 hours, suspended within 0.5% agarose on a 1 μM cAMP base layer, and imaged over 2 hours (120 minutes, 7200 seconds). Acquisition was every 2 minutes (120 seconds). (A) low velocity filter (slow moving cells <0.75μm/s). (B) high velocity filter (fast moving cells) >0.75 μm/s. The box shows the interquartile range, with the median value as a line across the middle. The small square box inside the boxplot is the mean. Whiskers represent the 5th-95th percentile of the data. Crosses represent the 1st and 99th percentile of the data. Data were obtained on three separate days. The data were truncated to exclude any tracks which did not span the entire 2 hour image acquisition period.

Dictyostelium mhcA- cells were seen above to have a strong bias towards slow movement, with only a small (<20%) proportion exhibiting fast movement. This is contrary to the behaviour of their parent strain where >90% of the cells are classified as fast-moving. Earlier in this chapter I have shown differences in the behaviour of multicellular aggregates between JH10 and mhcA- cells, whereby mhcA- aggregates were unable to move and do not form cell streams, but JH10 aggregates could move, and form streams. Over the 2 hour time course of the chemotaxis experiment, cell aggregates can be seen to have formed by the end of the 2 hour time period (Figure 6.10). In order to ensure that the differences between the

proportion of slow-moving to fast-moving cells seen above cannot be attributed to the differences in behaviour of JH10 and mhcA- in response to the presence of multicellular aggregates, or to cells joining multicellular aggregates during the course of the experiment and thus being eliminated from analysis, cells were additionally tracked over a period of 30 minutes. By 30 minutes into acquisition, not many multicellular aggregates had formed, streaming had not begun in the JH10 datasets, and the numbers of multicellular aggregates or clumps of cells were similar for the JH10 and mhcA- cells (Figure 6.11).

Figure 6.10: JH10 and mhcA- cells within 0.5% agarose at 2 hours after acquisition began- multicellular aggregates within the agarose

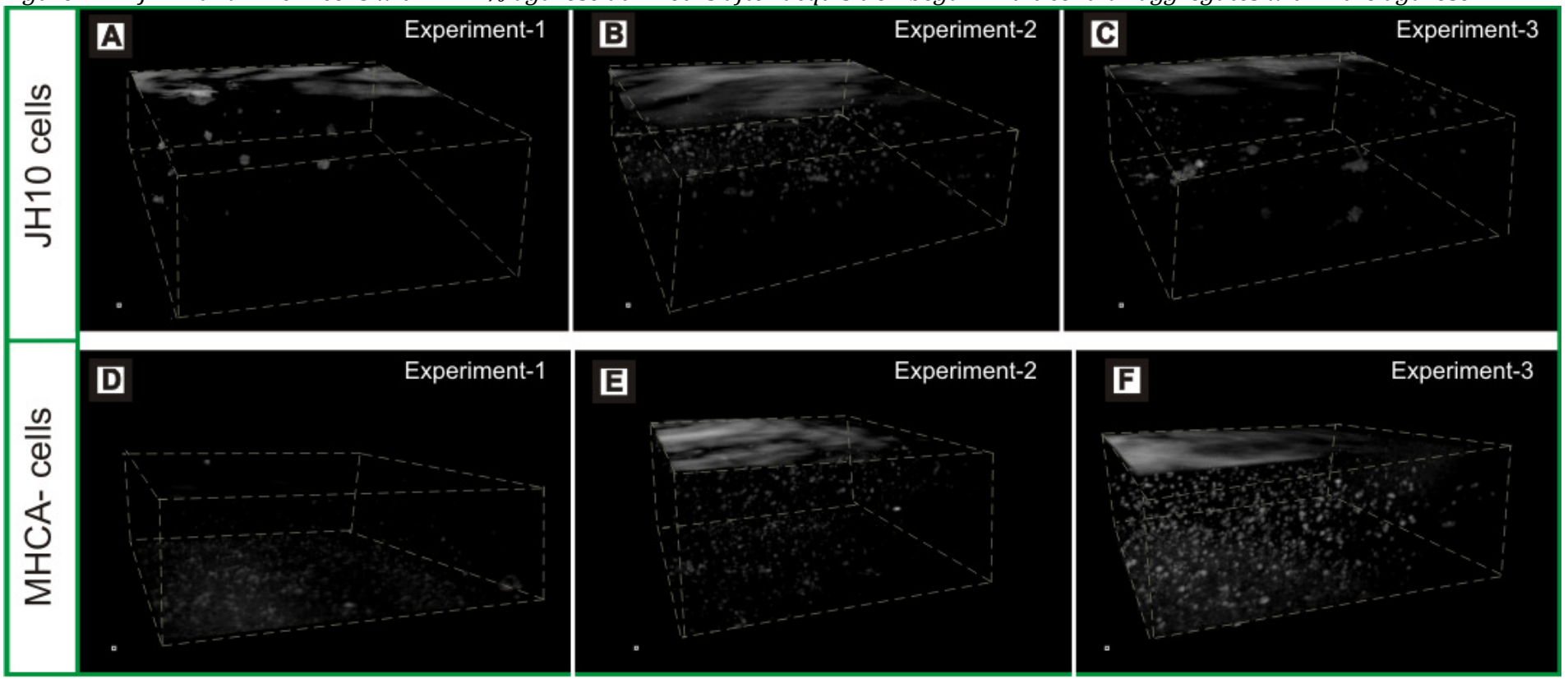

Figure 6.10: Volumetric rendering of JH10 (A-C) and mhcA- (D-F) cells generated using Amira software within 0.5% agarose on a base of 1 µm cAMP agar. Grey guidelines indicate the edges of the volumes for ease of visualisation. Three different experiments performed on three different days. The cells at 120 minutes (2 hours) after commencement of image acquisition. There are differences in the number of multicellular aggregates and the pattern of their distribution. The JH10 volumes show a few large aggregates and cell streams. There are many more aggregates in the mhcA- volumes and they are smaller. There are also no cell streams. JH10 and mhcA- cells. Scale bars are 20 µm.

Figure 6.11: JH10 and mhcA- cells within 0.5% agarose at 30 minutes after acquisition began

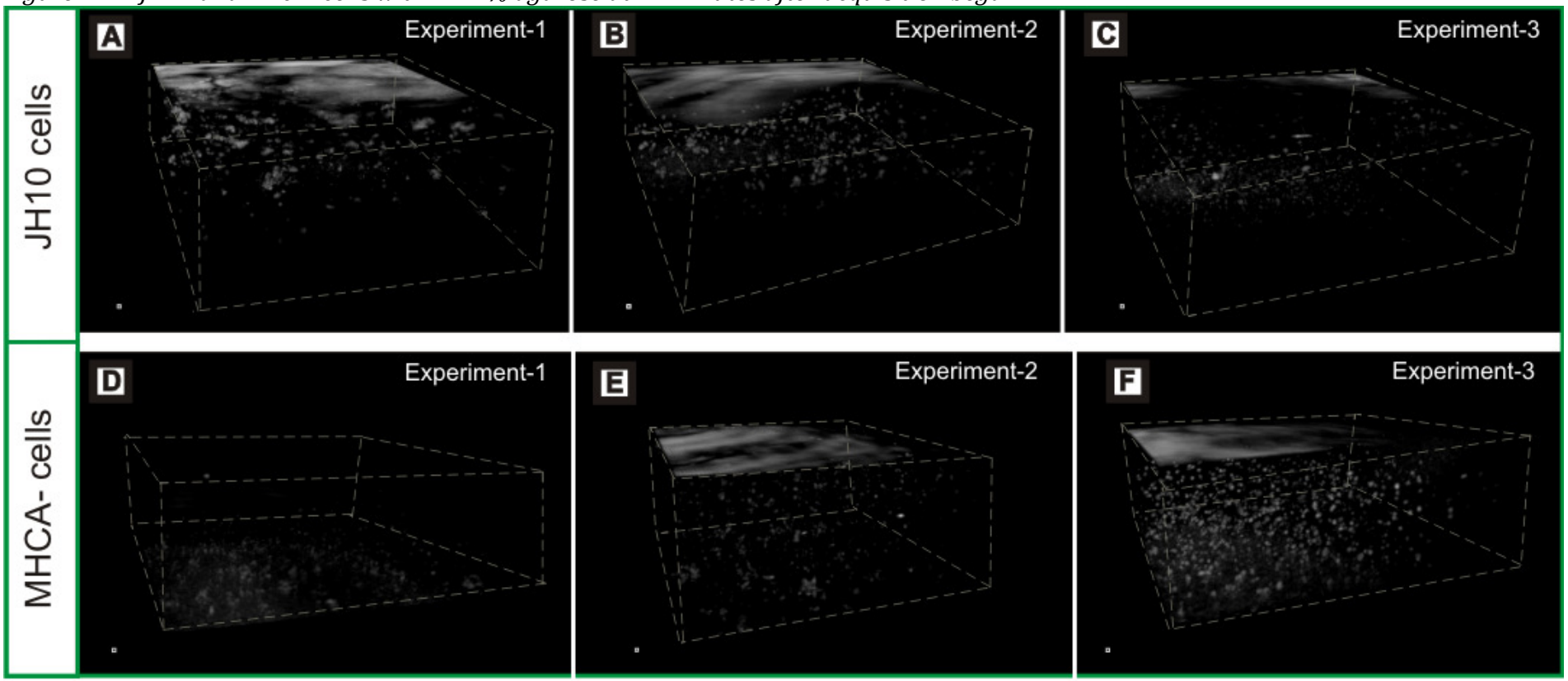

Figure 6.11: Volumetric rendering of JH10 (A-C) and mhcA- (D-F) cells generated using Amira software within 0.5% agarose on a base of 1 µm cAMP agar. Grey guidelines indicate the edges of the volumes for ease of visualisation. Three different experiments performed on three different days. The cells at 30 minutes after commencement of image acquisition. There are not many multicellular aggregates and the number and size of aggregates is similar for both the JH10 and mhcA- cells. Scale bars are 20 µm.

Hartigan's dip tests indicated that the velocity of the cells was significantly bimodal at the 95% confidence interval for all of the data over the course of 30 minutes. JH10 unfiltered data p= 0.02, mhcA- unfiltered data p=0.03, JH10 CI filtered data p=0.02, mhcA- CI filtered data p=0.03 (all <0.05)[247,387,505]. Therefore the bimodal behaviour of the velocity of the cells was still seen over this truncated time period and was also seen in cells over this truncated time period which were moving directly towards the cAMP agar (CI filter >0.75, as before), as can be seen from the probability density plots (Figure 6.12). This indicates that this pattern of cell velocity can be seen both in cells which are moving directly towards the cAMP source and the entire population as a whole, and over 30 minutes as well as over 2 hours.

Figure 6.12: Probability density plots of the velocity of JH10 and mhcA- cells within 0.5% agarose over 30 minutes

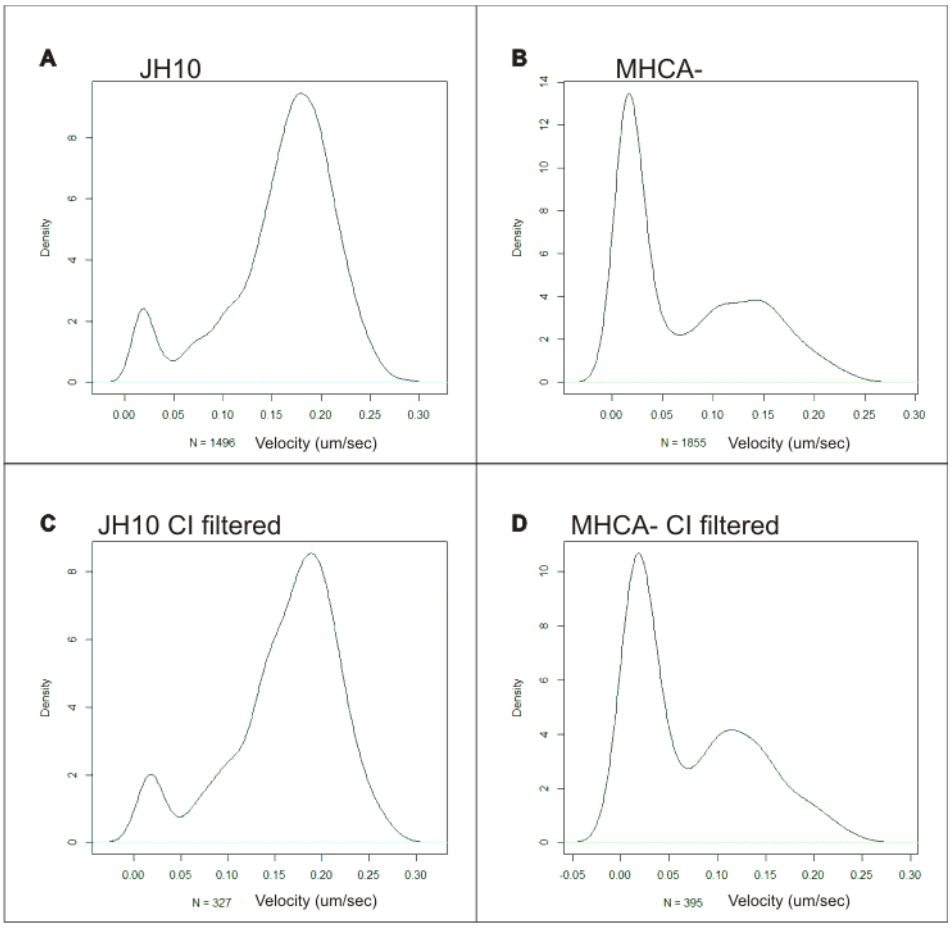

Figure 6.12: Probability density plots, generated, using R statistical software, of the velocity of (A) JH10, (B) mhcA-, tracked over 30 minutes (C-D) Data filtered to exclude data with a chemotactic index of less than 0.75. (C) chemotactic index filtered JH10 cell velocity. (D) chemotactic index filtered mhcA- cell velocity, tracked over 30 minutes.

The velocity and meandering indices of the JH10 and mhcA- cells over 30 minutes and the results of the statistical analyses are shown in Table 5. All data were significantly non-normal (Anderson-Darling tests at 95% confidence level, all $p<0.005$), so Mann-Whitney U tests were performed. Box plots of the velocity and meandering indices of the JH10 and mhcA- cells tracked over a period of 30 minutes are shown in Figure 6.13, graphically illustrating the differences in the population chemotaxis parameters between the two cell strains. As before, both the velocity and meandering index of the JH10 cells was significantly higher at 0.16 ± 0.06 μm/s and 0.27 ± 0.13 respectively (grand mean values) than that of the mhcA- cells at 0.07 ± 0.07 μm/s and 0.21 ± 0.14 respectively (grand mean values), showing that the JH10 cells moved faster and more directly than the mhcA- cells.

Figure 6.13: Box and whisker plots of the velocity and meandering index of JH10 and mhcA- cells within 0.5% agarose over 30 minutes

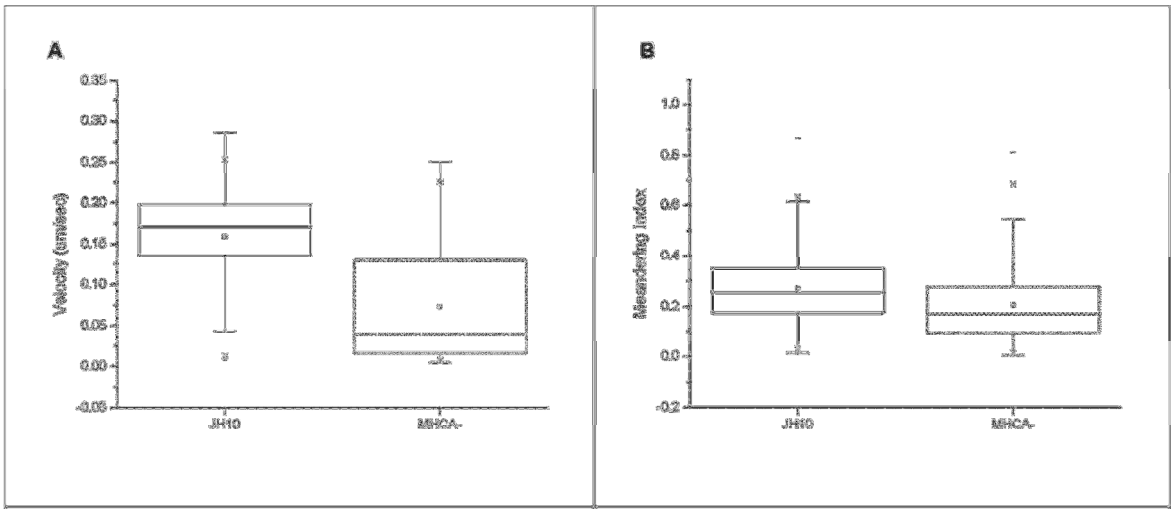

Figure 6.13: Box and whisker plots showing the distributions of (A) velocity and (B) meandering index of chemotaxing JH10 and mhcA- cells pulsed for 6 hours, suspended within 0.5% agarose on a 1 μM cAMP base layer, and imaged over 30 minutes (1800 seconds). Acquisition was every 2 minutes (120 seconds). The box shows the interquartile range, with the median value as a line across the middle. The small square box inside the boxplot is the mean. Whiskers represent the 5th-95th percentile of the data. Crosses represent the 1st and 99th percentile of the data. Data were obtained on three separate days. The data were truncated to exclude any tracks which did not span the 30 minutes period of tracking.

Table 5: JH10 cells and mhcA- cells migrating within a 0.5% agarose gel over 30 minutes- Results and Statistical Analyses

Condition	Velocity (μm/s)	Meandering Index
JH10 in agarose gel	0.16±0.06 (0.17±0.06)	0.27±0.13 (0.26±0.18)
mhcA- in agarose gel	0.07±0.07 (0.04±0.11)	0.21±0.14 (0.17±0.18)
JH10 vs mhcA- in agarose	U=464238.50 Z=|33.16| P<0.001*	U=949492.50 Z=|15.73| P<0.001*

Table 5: Grand means (±SD) and medians (±interquartile range), in brackets, calculated from the mean values obtained for each cell. JH10 in agarose n=1469. mhcA- in agarose n=1855. Summary of the results of statistical analysis for JH10 cells and mhcA- cells, * indicates significance at 95% CI.

6.6 Chapter 6 Discussion

Previous experiments have shown that although *Dictyostelium* cells deficient in myosin II are motile, they exhibit impaired chemotaxis on 2D planar surfaces, having a reduced speed, reduced cell polarisation and lower chemotactic indices than their parent strain[314,668]. They have additionally been shown to exert abnormal patterns of force on their substrata and greatly slowed cycles of force generation in comparison to wild-type cells[374,414]. The more restrictive environment of an under-agarose assay has also revealed impaired migration under these conditions, with cells lacking myosin II unable to move under agarose concentrations of greater than 0.5% and migrating slowly and translocating only a short distance under 0.5% agarose[328,682]. I have extended the study of the phenotypes of myosin II null cells to the third-dimension, to investigate what this environment of increased challenge can reveal.

6.6.1 mhcA- development in 4D

I have shown that mhcA- failed to complete development within agarose, never progressing beyond the stage of aggregates, and did not form cell streams within agarose, unlike their wild-type counterparts. As aggregation has previously been shown to be delayed in mhcA- cells, unsurprisingly considering their lower chemotactic speed and efficiency, the sample of mhcA- cells within agarose was imaged again at 24 hours after initiation of starvation, to see if further development had occurred[255,314,394,593,668]. No further development was seen in within the agarose throughout the duration of this image sequence, indicating that the mhcA- cells were not merely delayed in this process of development, but that development is completely arrested at this point, although a motile cell seen on the surface of the agarose shows that the mhcA- cells were still alive and motile. This is additionally supported by the fact that, although by eye I frequently observed fruiting bodies on the surface of the agarose of both Ax2 and JH10 cells the day after imaging, I did not see this with the mhcA- cells. This result agrees with the well-known mound-arrest phenotype that *Dictyostelium* myosin heavy chain null cells have been shown to exhibit and with the observation of Laevsky et al, that mhcA- cells stop chemotaxing after a period of approximately 4 hours, possibly due to reduced cortical integrity of these cells caused by their cytoskeletal deficits[128,313,328]. Although mhcA- cells under buffer have previously been shown to be able to form streams, the cells within the streams have been shown to be disordered, in contrast to wild-type cells which show some patterns of organisation[162]. Although, it should be noted that this organisation may not be an

important factor in development, as Doolittle et al did not see this ordered pattern in their experiments with Ax2 cells, which completed development normally[139]. More recently Heid et al found that mhcA- cells were unable to form streams in buffer, although the cells were able to form multiple aggregates[255]. This agrees with what I have seen with mhcA- cells within agarose, as under these conditions no cell streaming was seen, but aggregates were formed. Furthermore, Heid et al demonstrated the inability of mhcA- cells to respond to temporal gradients of cAMP, such as those released from aggregation centres during the natural development process; an observation supported by Driscoll et al who observed wave-like characteristics in the migration of wild-type cells responding to a wave of cAMP, but did not see these waves in mhcA- cells, and further contributing to a possible explanation for why this strain fails to complete development within an agarose gel[150,255,328,701,702].

Multicellular aggregates within the 0.5% agarose initially appeared to be fully immobile. However, closer inspection of the images revealed that the smaller mhcA- multicellular aggregates were motile, but did not translocate far from their original position, while the larger multicellular aggregates, composed of three to four cells by size, changed morphology on the spot but did not translocate. This agrees with the observations of Doolittle et al, who fluorescently labelled some mhcA- cells and imaged the process of development[139]. They observed that the cells became stuck at the mound stage, once the cells became tightly packed, and 'jiggled' on the spot[139]. Indeed, from my results, it seems as though when mhcA- cells formed aggregates of more than two or three cells (by size), they became stuck in the agarose and jiggled on the spot. Doolittle et al, and others, attribute the jiggling of the mhcA- cells within the mound to a lack of cortical integrity in mhcA- cells, possibly caused by the inability of the mhcA- cells to properly regulate crosslinking of F-actin and stabilise the cytoskeleton during motility[314,374,414]. Although F-actin has been shown to move towards the rear of the cell independently of the action of myosin II, this movement is five times slower[211,686]. Therefore, while mhcA- cells are able to regulate F-actin to a certain extent, possibly through the action of cortexillin I or other actin binding proteins, involved in maintaining cytoskeletal integrity, such as the bundling protein α-actinin and gelation factor ABP120, it appears as though proper regulation of the actin cytoskeleton is a myosin II dependent process[127,211,255,381,414,425,450,686]. Consequently, although there is no question that the cytoskeleton of mhcA- cells is impaired, and that this lack of cortical integrity is likely to play a role in the impaired migration exhibited by mhcA- cells, it cannot be said from developmental assays whether the multicellular aggregates are unable to translocate far within agarose, or whether this lack of translocation can be attributed to an inability of the cells to

respond to the temporal dynamics of naturally occurring cAMP waves, as has previously been shown in this mutant strain by Heid et al[255]. However, from observation of the mhcA- cells in volumetric images in time-lapse placed within an extrinsic spatial gradient of cAMP, it can be seen that the multicellular aggregates exhibit the same behaviour as in the development assays, with the smaller aggregates translocating a short distance and the larger aggregates jiggling on the spot. This lends support to the idea that it is not impairment in response to a signal which dictates this behaviour of mhcA- cells, but rather a physical difficulty in traversing their environment.

At first glance it appeared as though individual mhcA- cells were also trapped within the agarose gel, unable to migrate, with cell movement seen only on the top surface. However, closer inspection revealed that certain individual mhcA- cells were able to migrate within the 3D environment of a 0.5% agarose gel. The numbers of migrating cells were far fewer than seen in the corresponding parent strain, JH10, explaining why they are easily missed and indicating a clear phenotype of these cells in 3D migration. Moreover, it appears that the mhcA- individual cells were able to move a significant distance within the agarose. The migration also exhibited a period of direct movement, before the cell changed direction repeatedly for a short while before migrating more directly again, but in a different direction. This pattern of periods of increased cell speed and persistence has been observed in unstimulated mhcA- cells has by Heid et al[255]. In their experiments, the faster and more persistently moving mhcA- were shown to have single pseudopods, which, although they were abnormal in shape and size when compared to the parent strain, JH10, contrasted with the slower and more randomly moving mhcA- cells, which were seen to form several pseudopods concurrently[255]. Lombardi et al have also observed that some vegetative mhcA- cells are able to move as fast as some of the slower moving parent strain[374]. They attributed these periods to the development of an asymmetry of forces between the front and rear of the cell, arising by chance in mhcA- cells, which in their model is what allows a cell to propel itself along a surface[374]. This contrasts with the forces generated by non-directionally motile mhcA- cells which are not asymmetric, but instead distributed all around the membrane of the cell[414]. It is conceivable that a similar asymmetry of forces is required to propel the cell during 3D cell migration, and development of these by chance, potentially aided by gravitational forces in a 3D environment, could explain the periods of rapid and directed migration seen in a few starved individual mhcA- cells within an agarose gel[204,205,414].

Although certain individual mhcA- cells appeared to be able to move within 0.5% agarose, during development, the numbers of motile cells were severely reduced in comparison to the number of motile cells seen during JH10 development. Multicellular behaviour was also compromised, with the mhcA- cells exhibiting no cell streaming, impaired motility of multicellular aggregates, and failure to progress in development beyond the stage of aggregates. A marked difference was seen in the cell behaviour during natural development between the mhcA- cells and their parent strain, JH10, showing that development of mutant cell lines within an agarose gel may prove a useful tool for qualitative investigation of mutant phenotypes within a three-dimensional environment.

6.6.2 mhcA- chemotaxis in 4D

I have shown that the velocity of individual mhcA- cells was significantly reduced within an agarose gel compared to that of JH10 cells, the parent strain. The speed of mhcA- cells has been previously seen to be reduced both in cells under buffer on glass surfaces, cells on gelatin surfaces and cells under agarose on polystyrene surfaces[328,374,414,668]. The impairment in migration speed is thought to be due to difficulty of mhcA- cells in retracting their rear, and in maintaining single dominant pseudopod although a potential additional role of myosin II in extension of pseudopodia has been recently postulated[76,279,381,414]. MhcA- cells also display delayed cycles of force generation and migration and unusual patterns of cell contractility. This is potentially due to impaired cytoskeletal integrity, in addition to difficulties in retraction of the cell rear. Impaired cortical integrity could result in inability to properly stabilise the forces which govern cell motility, resulting in dysregulation of these forces and reduced cell velocity[131,374,414,582]. However, it should be noted that this low group velocity may also arise because many of the mhcA- cells simply never initiate movement. MhcA- cells under agarose and on gelatin surfaces have previously been shown to exhibit low numbers of migrating cells[131,328].

The population meandering index of mhcA- cells was similarly significantly reduced in comparison to their parent strain. Previous work has shown that mhcA- cells have misregulated pseudopodial dynamics, which result in them generating a number of secondary pseudopods in addition to their primary pseudopod[255,582,593,668]. They also show abnormal morphology and aberrant patterns of contractile force exerted on their substrata, which may correspond to a deficit in cell polarity[254,374,414]. Therefore their low directionality is likely due to

an inability to supress formation of new pseudopodia and to retract existing ones, resulting in changes in direction as the different dominant pseudopods arise[255,350,582,657,668].

The observed reduction in speed and directness of mhcA- cell migration agrees with previous work with these cells on glass under buffer, on plastic under agarose and on gelatin surfaces in air[254,314,374,414,593,668]. This indicates that setting cells within agarose can be used as an assay to obtain quantitative information on the characteristics of cell migration within a 3D environment, allowing for comparison of mutant phenotypes with their parent strain.

I have found that the chemotactic index is higher for the mhcA- cells than for the JH10 cells. However, by eye, the mhcA- cells were overwhelmingly non-motile, and quantitative data revealed a large proportion of very slow moving cells, which did not translocate far from their original position and additionally did not migrate with a very straight path. As the measured resolution of my OCT microscope was ~5 μm, mean displacement of mhcA- cells was 6.14±9.1 μm and the median was 1.84±5.9 μm, the trajectories of these cells calculated using the Volocity software are unlikely to represent any significant attempt to move towards the cAMP source, and rather to be artefacts generated from attempting to calculate a trajectory for an almost non-motile cell which changes morphology (and therefore potentially centroid position) in time (illustrated in Figure 6.14). Therefore, although chemotactic index (calculated as described in the methods section) may represent an effect of chemotaxis, as mhcA- cells have previously been shown to be weakly chemotactic, gravity may be playing a role in biasing these cells towards movement in the downwards direction, and it is questionable whether chemotactic index, has any real meaning for these non- or extremely limitedly-motile cells, which do not translocate from their original position[52,55,255].

Figure 6.14: Tracking a cell which does not translocate

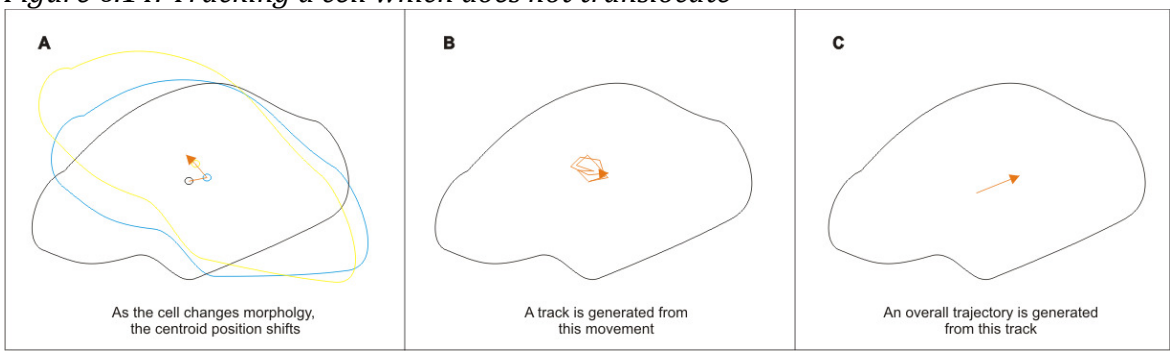

Figure 6.14: Illustration of tracking the centroid of a cell which does not migrate. The drawing represents the boundary of the cell with the centroid in the middle. (A) The centroid position of the cell shifts as the cell changes morphology; different time-points are illustrated by different colours. (B) The centroids are tracked and an overall track of the cell is generated. (C) The overall trajectory of this track is generated, which does not necessarily reflect any net migration of the cell in this direction.

Nonetheless, in order to be certain that the differences seen between the mhcA- and JH10 cells could not potentially be attributed to differences in the numbers of cells migrating directly towards the source and cells which were moving in other directions, the data were filtered to exclude cells which were not migrating directly towards the chemoattractant source. As a side-effect, this showed that there were significant differences in the velocity and meandering indices between the cells which were moving directly towards the cAMP agar and the whole population of cells. The velocity of the JH10 cells was higher in the cells moving towards the chemoattractant, but the meandering index was lower. This indicates that the cells moving directly towards the source were faster, but did not move as directly. The increase in speed is likely explained by elimination of cells which were not able to sense the chemoattractant gradient and were therefore not chemotaxing, as chemotaxing cells have been shown to move faster than cells which are not exposed to a gradient of chemoattractant[645]. The decrease in directed movement could be attributed to the presence of multicellular aggregates on the cAMP agar, which formed over the course of the 2 hour duration of the experiment. This resulted in cells initially migrating directly downwards towards the cAMP agar and then changing direction to orient towards a multicellular aggregate. Furthermore cells which initially migrated directly downwards could not penetrate the cAMP agar layer and once they reached it were therefore forced to change orientation and move along it. Both the velocity and the meandering index were significantly reduced in the mhcA- cells with the highest chemotactic indices, but, as discussed above, in a population of

largely non-motile cells, this parameter does not necessarily describe useful information about the migration character of the cell, and therefore could potentially be explained by chance variation. However, although attempts were made to exclude cells on the cAMP base layer from analysis by selection of an ROI for analysis which did not include this area, it is possible that some cells which were using the cAMP agar base as an aid to migration, i.e. a substratum on which to rest, were tracked, potentially resulting in increased motility and directionality in cells which rather than moving directly downwards were moving in the perpendicular direction, along the agar base layer. Even so, the differences between the JH10 and mhcA- cells were apparent, and similar in pattern in both the cells filtered on the basis of chemotactic index and the unfiltered entire population of cells. Therefore, the differences in velocity and meandering index between the two strains are likely to be a feature of impaired motility of mhcA- cells within an agarose gel, rather than attributable to differences in the proportion of cells responding to the spatial chemoattractant gradient.

The probability density function of the mhcA- cell velocity showed a small proportion of the cells which were able to move almost as fast within the agarose as the JH10 cells. The meandering index of these fast-moving mhcA- cells was significantly reduced in comparison to the JH10 fast-moving cells, potentially indicating that although this population of cells was able to move as fast as the JH10 fast moving cells, they still did not move as directly, indicating a possible role of myosin II in directed cell migration. This lack of directionality in mhcA- cells has been postulated to arise from pseudopods forming all around the cell membrane and not being restricted to the leading edge[150,350,593]. Traction cytometry experiments are consistent with this, revealing that motile mhcA- cells generate force on their substratum by contracting all around the cell membrane, unlike wild-type cells which generate force-asymmetries between front and back[374,414]. Although mhcA- cells exhibiting faster migration have previously been shown to extend a single pseudopod, rather than the multiple pseudopodia seen in the average slower moving and less directional mhcA- cells, these pseudopods were broader in shape and extended from the dorsal surface of the cell body, unlike the pseudopods extended by wild-type cells[255]. The pseudopodia of these faster mhcA- cells additionally showed far less stability than the pseudopods of their wild-type counterparts[255]. As cells have been shown to orient themselves towards their dominant pseudopod, dynamically changing pseudopodia arising from a lack of proper cytoskeletal organisation and inability to correctly retract pseudopodia could account for reduced directionality of fast-moving mhcA- cells[150,255,279,381,414,465,569,657].

Lombardi et al have previously found that vegetative mhcA- cells are able to move as fast as wild-type cells for short periods of time (<3 minutes) on gelatin surfaces[374]. This has been similarly observed by Heid et al, who also saw periods of increased cell persistence in mhcA- cells on glass under buffer[255]. However, I have shown that a proportion of the mhcA- cells exhibit this fast-moving phenotype over a 2 hour time period, indicating that the ability of certain mhcA- cells to move rapidly within a 3D environment is not restricted to transient bursts, but holds for a period of at least 2 hours. This is a surprising finding for a number of reasons. Primarily, previous work has shown that mhcA- cells are impaired in chemotaxis and migration speed both on 2D planar surfaces under buffer and under-agarose[254,287,374,414]. Secondly, mhcA- cells have been shown to exhibit abnormal pseudopodial dynamics and show poor co-ordination of forces required to generate movement[133,254,287,374,414]. Thirdly, cells lacking myosin are thought to be incapable of bleb-driven cell migration, which has been proposed as a mechanism by which cells may migrate within restrictive environments[92,204,520,586,693]. Finally, these cells are thought to lack the cortical integrity to migrate effectively within restrictive environments as they are unable to sufficiently deform the agarose gel to migrate beneath it[287,328,414]. Therefore, while in this context it is unsurprising that a large proportion of the mhcA- cells are non- or limitedly-motile, the question arises of why a proportion of the cells are able to consistently migrate for a 2 hour period with speeds similar to those of their wild-type parent strain within the 3D environment of a 0.5% agarose gel.

Myosin II has been shown to play an important role in retraction of the rear of the cell during chemotaxis[279,287]. Indeed, Laevsky et al noted in their under 0.5% agarose chemotaxis assay, that mhcA- cells had difficulty in retraction of the rear of the cell, an observation since supported by experimental observations of pseudopodial dynamics of mhcA- cells under buffer and with traction force microscopy[255,279,328]. Under agarose, this impaired retraction appeared to result in elongated cells, which were caused by the body of the cell continuing to migrate, while the rear of the cell remained adhered to the substratum[328]. In some cells this was observed to result in cellular fragmentation because of the rupture of the elongated stretch of cell, however, other mhcA- cells did not break apart[328]. Laevsky et al also observed in their under-agarose chemotaxis assay, that the mhcA- cells which successfully exited the trough and penetrated the agarose had a speed of approximately 2/3 of the wild-type strain[328,329]. Wessels et al showed in their initial experiments that mhcA- cell speed in chemotaxis to a spatial gradient of cAMP was reduced by approximately 1/3, which was again seen by Heid et al[255,328,668]. Therefore, it appears as though mhcA- cells may be able to migrate

faster when their dorsal surface is in contact with agarose. Possibly the agarose provides a support mechanism for the cells, aiding them to stabilise their impaired cytoskeleton, and also providing additional points of anchorage for the cell to its surrounding material. This in turn could allow them to more rapidly generate sufficient force to retract their uropod than on 2D substrata, although the negative side of this increased cortical tension would be that it occasionally results in cellular fragmentation, which was seen by Laevsky et al[328]. Extending this to the third-dimension where the cell is completely surrounded by agarose potentially provides additional support, as well as additional anchorage points for the cell to adhere to the environment, which could potentially offer an explanation for why the mhcA- fast-moving cells are not significantly reduced in speed. It should be noted, however, that the under-agarose assay may be intrinsically biased towards fast-moving cells as, if these cells are phenotypically different in some manner from the general population of mhcA- cells which allows them to better overcome the barrier of the agarose gel, then only these cells would contribute to the measurement of population speed, and this could be an alternative reason for the observed smaller reduction in mhcA- cell speed in the under-agarose assay when compared to under buffer.

Myosin II null cells are known to have difficulties in retracting their rear, both on 2D glass surfaces and under agarose on plastic, a required step for cell migration[279,328,414]. However, agarose provides a more deformable and elastic environment than glass or polystyrene[31,616]. Differences in adhesion of the cells to the 2D glass or plastic surface and the 3D agarose gel, may result in retraction of the rear of the cell, a myosin mediated process, being of less importance or less difficult, and therefore less of an impediment to cell speed during chemotaxis[137]. Cell migration additionally requires proper co-ordination of forces, and this is impaired in cells lacking the myosin heavy chain[279,374,414]. Generation of opposing forces between the front and the rear of the cell have been shown to be important for the cell to move[374,414]. The generation of these forces has been shown to occur in a cyclical manner, and one of the reasons for the slow migration speed of mhcA- cells is that these cycles are reduced in frequency[150,414]. Potentially, being held within a 3D gel allows asymmetry of forces to develop more easily, due to the extra dimensionality allowing for extra axes along which asymmetries can develop. These prior force cytometry studies have, however, relied on cells exerting forces on a 2D substratum. In this experimental configuration cells have defined pseudopods and uropods as well as defined dorsal and ventral surfaces. In 3D the dorsal and ventral surfaces are all in contact with and potentially adhered to the matrix in which the cell is embedded. This may affect the manner in which a cell defines a rear and a front.

Furthermore the forces exerted by these structures in 3D may differ from models established from measurements in 2D. Novel 3D traction force microscopy could potentially enable measurement of the forces applied by mhcA- *Dictyostelium* cells within 3D gels, enabling exploration of the mechanisms behind their 3D migration and chemotaxis[198,351].

Nonetheless, it appears as though the difference in speed between the JH10 and mhcA- cells within an agarose represents a difference in proportion of slow-moving to fast-moving cells, rather than an absolute reduction in population speed in the mhcA- cells. Therefore there may be two phenotypically different populations of cells migrating within the agarose, a slow-moving group and a fast-moving group.

6.6.3 Two cell populations?

The probability density functions of the velocity of both the JH10 and mhcA- cells within an agarose gel were found to be significantly bimodal, indicating that there may be two distinct populations of cells characterised by different velocities. To see if this pattern was simply a result of cells moving directly towards the cAMP source moving faster than cells moving in other directions, as chemotaxing cells have been previously shown to move faster than non-chemotaxing cells, a chemotactic index filter was applied to the data to exclude cells which were not moving directly towards the cAMP agar[645]. The bimodal pattern persisted in the filtered data, indicating that this bimodality cannot be explained by differences in the behaviour of cells which are directly chemotaxing towards the cAMP source and those which are not.

In their under- 0.5% agarose chemotaxis assay, Laevsky et al noted that mhcA- cells were able to migrate for 4 hours before ceasing to migrate, which may be caused by a gradual breakdown in the structure of the cells, due to their cytoskeletal deficits[328]. As the 3D environment may have presented an increased challenge to the cells than the under-agarose assay, it was considered possible that the reason for the increased number of non-motile mhcA- cells could have been attributed to breakdown of the fast-moving cells over the 2 hour course of the experiment, resulting in apparently low velocity, i.e. a fast-moving phase followed by a non-motile phase after cell breakup. Although the size constraints placed on the algorithm precluded this, as small cell fragments would not be tracked, and only cells where the tracks spanned the entire 2 hour time course were tracked, the cells were additionally tracked over a 30 minute period, to eliminate this possibility. The pattern of bimodality was

seen to persist in cells tracked for only 30 minutes, which confirmed that the large number of slow-moving cells is unlikely to be due to fast-moving cells breaking apart and ceasing movement. Additionally, as there are very few multicellular aggregates within the agarose at 30 minutes, this indicates that the presence or absence of multicellular aggregates and any potential confounding signals generated by these do not play a role in this bimodal behaviour of cell velocity.

Dictyostelium cells have recently been shown to be able to swim, by using their pseudopods and other small actin-rich structures as 'paddles', which have previously been termed eupodia[210,627]. The speed of this swimming has been found to vary between ~1-4 μm/min, dependent on the conditions of the experimental work[27,32,640]. The grand mean velocity of the slow-moving population of cells in my experiments was found to be 0.02±0.01 μm/s or 1.2 μm/min. Although the grand mean displacement of both the JH10 and mhcA- cells in my experiments was small, at 15.3 μm over a 2 hour period (JH10 grand mean= 31.3±40.9 μm, mhcA- grand mean= 12.3±14.5 μm), it can be seen from the box plots generated that a few cells displaced much further, up to ~150 μm, meaning that they migrated in a relatively straight path at a consistently slow speed. These cells could potentially be swimming through the agarose rather than undergoing a more conventional form of motility. This would mean that they are less adhered to their environment than the faster-moving population of cells, which crawl through the agarose[32]. Although it is not possible to determine why these cells may choose to make use of this alternative mechanism of cell motility characterised by less adherence and slower-motility, fibroblasts have recently been shown to alter their migration characteristics dependent on the elastic properties of their matrix, therefore, local differences in the agarose could potentially contribute to the mode of migration selected by the *Dictyostelium* cells[479].

However, although there are a few cells which migrate with a consistently low velocity, yet eventually cover distances in excess of 100 μm, the majority of the cells do not translocate very far from their original position. As velocity is a measure of total cell displacement over total time, tracking the centroid of a cell which jiggles about in place, or moves around in the same local area would result in a cell measured as having a slow velocity. Therefore the majority of the slow-moving population of cells could represent cells which are, either through choice or necessity not moving within the agarose, but are jiggling, i.e. changing morphology and making small motions, and occasionally making small translocation within the agarose, but not migrating far from their original position, similar to the behaviour of the mhcA- bicellular aggregate in the development section of the results. Therefore, it seems that

the majority of cells exhibit two modes of motility within an agarose gel, a fast-moving motility characterised by large cell displacements and a slow-moving motility characterised by very small cell displacements. This pattern is also seen in cells filtered on the basis of chemotactic index, indicating that this effect is independent of whether the overall trajectory of the cells is directly towards the source of chemoattractant or in another direction. This points to a feature of basic cell motility rather than in chemoattractant sensing, although a role of directional sensing cannot be completely excluded as all of this experimental work was done in the presence of a spatial chemoattractant gradient.

The bimodality could potentially be explained by the inhomogeneity of the agarose gel reported by Stellwagen et al, resulting in some cells becoming trapped in particular parts of the agarose gel[589]. MhcA- cells have previously been shown to be unable to migrate on adhesive surfaces, becoming trapped, when wild-type cells were motile[287]. Furthermore, a lack of cytoskeletal tension and integrity, and inability to retract the rear of the cell could potentially explain why more mhcA- cells become trapped than JH10 cells, which may be able to free themselves and move onward[287,328,414,589]. However, as these inhomogeneities were found to be on the order of the size of molecules, on the order of nm rather than cells, on the order of μm, this likely does not provide a comprehensive explanation[590].

A bimodal distribution of motility has been previously found to exist in freshly starved *Dictyostelium* cells, which was shown to correspond to differences in intracellular calcium levels[23,230]. Cells with a low calcium content were found to move at ~7 μm/min and cells with a high calcium content at ~10 μm/min[230]. These differences in cell speeds were postulated to be caused by slower moving cells being partially differentiated down the pre-spore pathway and faster moving cells down the pre-stalk pathway, as high calcium ion levels have previously been shown to result in an increase in stalk cells in the fruiting body and low levels to an increase in spore cells in the fruiting body[33,230]. Although these differences in motility are less than seen in my experiments, where the slow moving cells had a grand mean velocity of 0.02±0.01 μm/s or 1.2 μm/min (JH10= 0.03±0.02 μm/s; mhcA-=0.02±0.01 μm/s) and the fast moving 0.13±0.02 μm/s or 7.8 μm/min (JH10= 0.14±0.02; mhcA-= 0.11±0.05 μm/s), it may be that the agarose acts to impair both fast-moving and slow-moving cells somewhat, with the slow-moving cells more affected by the increased challenge of the 3D environment than the fast-moving population, especially as Laevsky et al observed similar speeds of their wild-type cells (Ax2) under 0.5% agarose (7.4±1.9 μm/min)[328]. The chemical properties of the agarose could also differentially affect these populations of cells, as ammonia (NH_3) has

previously been shown to differentially affect the response of two distinct populations of cells, prestalk cells and anterior-like cells (ALC) to a cAMP gradient and the differential effects of physical and chemical properties of an environment on cells have been well documented[118,130,177,355]. The troughs in between the peaks in velocities seen in the probability density functions of the slow-moving and fast-moving cell groups appeared more pronounced in the cells tracked over 2 hours compared to the cells tracked over 30 minutes. This indicates that there may be a progressive increase in the difference between the two populations of cells, fast-moving and slow-moving, over time, which is consistent with increased cell differentiation over time, potentially along the prestalk and prespore pathways. However, prestalk cells, which are the faster moving, have previously been shown to comprise less than 20% of the final number of cells in mounds, and while this is approximately the percentage of fast-moving cells seen within the mhcA- image sequences, the JH10 fast-moving cells make up greater than 90% of the total population[190,230,447,621]. Therefore, rather than myosin II biasing cells towards slower movement, it may be that agarose biases cells towards the faster-moving stalk differentiation pathway through a myosin II dependent mechanism. As prestalk and prespore cells have been shown to be differentially adhesive, perhaps this effect could be mediated through surface adhesion as cells within agarose are potentially adhered to the agarose on all sides, compared to on 2D surfaces where only the ventral surface is in contact with the environment[176,331,470]. Prespore cells have been shown to be more adhesive than prestalk cells, so potentially could become more easily trapped within the restrictive environment of an agarose gel, helping to explain why the slow-moving cells do not translocate great distances[176,331,459]. Still, this explanation of the cells being differentiated down different pathways is unlikely as, by eye, the JH10 cells formed fruiting bodies which were normal in appearance, whereas, if the fast-moving cells become stalk cells, a stalk-heavy phenotype would be expected to emerge[296,298,386,447]. However, it could potentially be possible for a more normal pattern of prespore to prestalk cells to establish within the JH10 cell population later in development, as transdifferentiation between prestalk and prespore cells has been shown to be able to occur at the slug stage of development[386,507]. Potentially, treatment of the cells with DIF-1 prior to setting within the agarose, inducing the stalk phenotype, could help to support or rule out this explanation[319,431].

Cells have previously been shown to be capable of varying mechanisms of movement and morphology dependent on the circumstances and environment in which they find themselves. Cell adhesion, matrix elasticity and stiffness, matrix composition and contractility of the cell have all been shown to cause cells to change morphology and migration mode, demonstrating

that cells have significant plasticity in their modes of motility, potentially aiding them to migrate in restrictive environments and contributing to the metastasis of cancer[203,462,479,490,537,679]. Membrane blebbing has recently attracted attention as a novel way in which cells are able to move, and this type of motion has been shown in *Dictyostelium* cells, as well as in a variety of mammalian cells[173,203,335,377,537]. While this mode of cell migration is postulated to play a role in the migration of cells in restrictive environments, potentially providing a way for them to squeeze through pores in matrices and migrate directionally in a 3D environment, blebbing is not found to occur in the absence of myosin II and therefore cannot explain the ability of mhcA- *Dictyostelium* cells to migrate within the 3D environment of an agarose gel[92,93,173,204,377,520,586,693]. However, if this type of motility aids cell migration within a 3D matrix, the lack of blebbing-mediated motility in mhcA- cells may help to explain the reason that this cell population is biased towards slow-moving cells with very low displacement, while the JH10 cells, potentially able to make use of this mode of motility, exhibit a large population of highly motile cells. Myosin II has been shown to be important at the stage of retraction of the bleb[93]. Therefore it is possible that the jiggling motion exhibited by the mhcA- cells within the agarose, with small periodic translocations, arise from extension of blebs, which the cell is then unable to properly retract due to lack of myosin II mediated cortical tension[92,93,287].

Petrie et al have recently discovered a novel lobopodial based cell migration mode in fibroblasts, which was dependent on both the dimensionality (i.e. 2D vs 3D) and the elasticity of the matrix in which the cells were placed[479]. This type of migration was shown to be myosin II dependent, and therefore cannot be used by mhcA- cells to migrate in 3D, but may potentially be used by JH10 cells[692]. Cells were demonstrated to be able to switch between two modes of migration, dependent on the changing properties of the environment in which they were placed[479]. Although this type of cell migration may not be present in *Dictyostelium* cells, it illustrates the potential of 3D environments to aid in uncovering previously unknown forms of cell migration.

Therefore, although it appears that the reason for this bimodal behaviour and mechanisms behind it, and the reason for the bias in the mhcA- cell experiments towards slow movement remain to be fully elucidated, the possibility for 3D environments to reveal additional phenotypes and potentially uncover new modes of migration in motile cells demonstrates the importance of microscopic techniques for visualisation of 3D cell migration and chemotaxis. I

have shown that OCT offers a non-invasive technique to achieve this, without the need for sample staining and processing.

6.7 Chapter 6 Summary

Myosin heavy chain null cells (mhcA-) exhibit known and well-characterised deficits in chemotaxis and development on 2D surfaces and under-agarose[139,255,328,668]. The exploration of their phenotype was further explored within the increased challenge of a 3D agarose gel. The mhcA- cells did not complete development, arresting at the stage of aggregates, which agreed with previously observed multicellular phenotypes of mhcA- cells[139]. MhcA- cells additionally showed an inability to move when in aggregates of a few cells, restricted mobility in aggregates of two or more cells, and slowed mobility as individual cells and bicellular aggregates. These phenotypes have been previously attributed to a lack of cortical integrity in mhcA- cells caused by their cytoskeletal deficits[328]. A small proportion of mhcA- individual cells were discovered to be motile within the agarose, so a diffusion-based chemoattractant gradient of cAMP was established within the agarose to investigate further.

Directionality and speed of chemotaxing mhcA- cells were found to be significantly reduced in comparison to their parent strain JH10. This pattern persisted in cells filtered to exclude cells which were not moving directly towards the chemoattractant, indicating that it likely primarily represents a deficit in cell motility rather than specifically in proportion of cells responding to the chemoattractant. However, a number of the mhcA- cells were found to move with the same speed as the JH10 cells. The reason for this is currently unclear, although it may potentially be due to differences in patterns of cell adhesion in 3D compared to 2D, or to the support of the agarose gel aiding stabilisation of the cell cortex.

Differences in population speed between the mhcA- cells and the JH10 cells were found to be due to different numbers of fast-moving and slow-moving cells within the whole population, rather than due to consistently slower migration of mhcA- cells. This indicated the existence of two populations of cells characterised by low and high velocities respectively, with myosin Ii acting to bias cells towards faster migration. This could potentially be the result of cells selecting two different modes of migration characterised by different levels of adhesion to their environment. Although the reason for this bimodal distribution of population velocities and the bias of mhcA- cells towards slow-movement remains to be elucidated, this chapter aimed to demonstrate that setting cells within agarose provides a potentially useful three-dimensional environment in which to explore both multicellular and individual cell motility of *Dictyostelium* mutant strains and potentially uncover new patterns of cell migration. Furthermore, that these phenotypes can be visualised without the need for cell labelling, using OCT.

Chapter 7: Discussion and Conclusions

7.1 Aims of this work

The main aim of this work is to assess the utility of Optical Coherence Tomography for visualisation of cells on non-transparent 2D surfaces and within 3D structures and to develop methods and protocols by which this can be accomplished. In addition, to subsequently explore the migration and chemotaxis of cells under these conditions and obtain quantitative information on the character of this motility, in order to establish what can be learned about cell migration using this microscopic technique.

7.2 Optical Coherence Tomography

Throughout this thesis, I have explored the potential of Optical Coherence Tomography as a tool for cell biology. As a microscopic technique which gives access to structural information, it is ideal for studying the dynamics of whole cell migration, particularly on opaque substrates and within 3D environments. Technology is continually progressing and these advances can improve the performance of OCT microscopes. For example, CCD cameras have become faster and more sensitive since the beginning of this project which would allow more rapid acquisition of images. Solid state drives have become faster and offer larger storage capacities, enabling saving time to be sped up. Furthermore, light sources have become increasingly more stable, and capable of broader bandwidths, resulting in increased axial resolution[178,630]. Novel signal processing techniques have been developed, which can enable superior depth penetration and reduced loss of focus with increasing depth i.e. interferometric synthetic aperture microscopy, and offer increased imaging depth range, i.e. dispersion encoded full range OCT[262,511]. Due to advances in laser technology, swept source OCT has now overtaken FD-OCT in terms of speed and, in combination with the reduced signal roll-off seen with this configuration, offers a significant advantage over FD-OCT for 3D volumetric imaging in time-lapse[498,672].

However, OCT does not allow access to functional information. Investigation of biological processes has benefited greatly from a drive towards multimodal imaging. Combining techniques with different depth penetrations, different resolutions and different contrast can enable a sample to be understood in much greater detail or from different perspectives[56,64,70,687,700]. OCT has recently been combined with confocal fluorescent microscopy, multiphoton microscopy, photoacoustic tomography and CARS microscopy[56,68,700,705]. As the technique requires no staining or sample processing, it lends itself

well to combination with other similar non-invasive techniques, as well as imaging modalities requiring staining such as fluorescent microscopy, for imaging of both in vivo and in vitro samples. As a primarily structural imaging technique, OCT can be useful not only for whole cell tracking as an independent modality, but also in multimodal microscopes for combination with techniques which yield functional but limited or no structural information. Although there are a number of potential challenges associated with designing and creating multimodal microscopes, such as less precisely optimised optics and increased image acquisition time, the possibilities offered by the simultaneous acquisition from two different imaging modalities make this an attractive area for future research[606,705].

7.3 Experimental configuration

Due to difficulties in establishing an extrinsic spatial chemoattractant gradient on a nitrocellulose filter, the experiments in chapter 4 made use of the natural propensity for *Dictyostelium* cells to create a temporal gradient as part of their developmental programme, and explored the response of the cells to this gradient. However, better control of the chemoattractant gradient is desirable because cell behaviour in response to different concentrations and to spatial and temporal gradients varies[582,583,667]. Therefore, an avenue of research for future investigation of cell motility on opaque 2D substrata is in establishing a repeatable and controllable gradient of chemoattractant. Microfluidic techniques potentially offer a method by which a highly reproducible gradient can be created over a wide concentration range[41,169,546]. Furthermore, the gradient can be varied both spatially and in time, giving great flexibility and allowing for investigation of cell responses to precisely controlled chemoattractant gradients[41,169,546]. Additionally, as the chemoattractant gradient is established and maintained by continuous flow, there is no possibility for factors secreted by the cells to influence their behaviour[113,638]. Therefore, a future direction in the investigation of *Dictyostelium* single cell migration on 2D substrata is the design of a microfluidic chamber, which allows different materials to be placed within, so that the response of cells to repeatable and well controlled gradients can be measured on different surfaces.

Agarose offered a simple 3D environment in which to present the cells for imaging. Furthermore, the physical and chemical properties of this gel can be altered, for example the elastic properties of agarose can be varied by addition of gelatin[443,706]. As differences in elasticity have been shown to affect cell migration and differentiation, agarose potentially

offers a useful gel in which the effects of different matrix properties on *Dictyostelium* cells could be investigated[168,280,479,563]. However, agarose unfortunately suffers from shrinkage as it dehydrates, a problem which, despite covering my experimental sample with clingfilm, I observed in some datasets. Other biocompatible gels and matrices are available, such as Matrigel™, reconstituted basement membrane, PuraMatrix™, a peptide-based hydrogel, and CyGel™, a micellular gel[34,35,555,616]. As discussed in chapter 3, Matrigel™ does not set at the required temperature for *Dictyostelium* cells[35]. PuraMatrix™, has low pH of 2-2.5, which requires time to equilibrate, so is not suitable for setting cells within just prior to imaging[34,555]. However, CyGel™ is liquid when cooled and gelatinous when warmed to room temperature, and could potentially offer an alternative matrix in which to present *Dictyostelium* cells for imaging within a 3D environment, although it is unknown if this gel may also dehydrate and shrink[44,503]. Additionally, there are a number of synthetic matrices in which cells can be set, for example, polyethylene glycol (PEG)[616]. The advantages of such matrices is that they allow for great control over the mechanical properties of the gel and these properties are very reproducible[616]. Experiments investigating the effects of 3D environments on cells have made use of various different matrices, of varying properties[616]. In light of the growing body of evidence that matrix properties such as elasticity, stiffness and matrix composition can affect the adhesion and motility of cells, future work should attempt to determine the optimum reproducible matrix for observation of 3D *Dictyostelium* cell behaviour[168,280,479,563].

Time-lapse microscopy is known to suffer from problems with focus drift, and the problem of registering stacks to compensate for this is not trivial in 4D (3D+time)[78,263,322,473]. The potential advantages of tracking cells within a 3D environment, as it enables cells to be studied in a more natural context and potentially enables access to additional information about cell migration such as the discovery of different modes of migratory behaviour, have been established[198,479]. Therefore, while it is possible to manually register stacks, this is time consuming and becomes a near impossible task with increasing number of experimental time-points, and so there is a clear need for automated stack registration in 4D. I have made use of several different methods and ImageJ plugins to align my stacks during this work, including collapsing the entire stack to a 2D image prior to registration, cropping images at a set distance around the agar-agarose interface and manual registration, and have written ImageJ macros to accomplish this[364,613]. However, these methods are not fully robust and a need to develop a robust algorithm for 4D stack registration is indicated from this work.

7.4 Concluding Remarks

I have discovered in chapter 5 that *Dictyostelium* cell development is not delayed within an agarose gel. Furthermore, the cells preferentially form aggregates and cell streams at interfaces. The reason for this is currently unclear, but longer term imaging, from the initiation of starvation through to culmination, may enable capture of the initial formation of these aggregation centres, which could aid understanding of the mechanisms behind this process. Similar to the phenotype previously seen on 2D surfaces, in chapter 6 *Dictyostelium* cells lacking the myosin heavy chain failed to complete development or form cell streams within an agarose gel, unlike their parent strain, JH10[139,255]. This phenotype has been attributed to difficulty of the cells migrating within the restrictive multicellular environment of the mound[139]. Agarose appears to present an impediment to motility of cells lacking the myosin heavy chain, as these cells are overwhelmingly non- or limitedly-motile. It therefore potentially offers an environment of varying restrictiveness, dependent on the concentration of agarose, in which to further explore the reasons for this lack of motility.

The potential for commonly used substrates for aggregation and development of *Dictyostelium* to affect the speed of cell migration and chemotaxis on 2D surfaces was uncovered in chapter 4. Moreover, this was extended to exploration of migration and chemotaxis in 3D in chapter 5, wherein it was discovered that *Dictyostelium* cells within an agarose gel are not significantly slowed, but are impaired in their ability to migrate in a straight line. In chapter 6, I have uncovered two distinct populations of *Dictyostelium* cells characterised by different velocities, a slow-moving group and a fast-moving group. Additionally, I have found that myosin II plays an important role in the migration of *Dictyostelium* cells within an agarose gel, as cells lacking myosin II are biased towards slow movement. Although, a small proportion of cells lacking myosin II were able to move with speeds similar to their parent strain, indicating that the role of myosin II in 3D cell migration in *Dictyostelium* is more complex than in allowing fast migration by increasing cortical tension and rather pointing to a role in the facilitation of fast migration.

In mammalian cells, myosin II contraction mediated contraction has been shown to play a role in the formation of mature focal adhesions, but not in transient ones formed during cell migration[100,325]. *Dictyostelium* cells migrate rapidly and therefore do not form these longer lasting cell-substrate contacts, which may help to explain why *Dictyostelium* mhcA- cells are able to migrate in 3D, while myosin IIA was found to be required for epithelial cell migration[202,566]. Nonetheless, *Dictyostelium* cells do form attachments to their substrata, which

are likely to be important in enabling them to exert forces required for cell migration on their surrounding environment, particularly on 2D substrates of complex topography, such as their natural environment of soil, and within 3D matrices. Although no homologs of integrins have been found in *Dictyostelium*, a number of other molecules involved in cell-substrate adhesion have been uncovered. TM9/Phg1 and SadA have both been shown to be involved in substrate adhesion in *Dictyostelium*[37,187]. SadA is also associated with the actin cytoskeleton through association with cortexillin I and ABP50, actin binding proteins[321]. TM9/Phg1 (a kinase) and SadA, have recently been shown to exert their effects on cell-substrate adhesion through regulating expression and stability of Sib (similar to Integrin Beta) and also controlling its translocation to the cell membrane[206]. Sib, so called because it shares some features in common with Integrins, known cell-surface adhesion receptors in mammalian systems, may mediate its effects by interaction with Talin[113,114,206]. Talin, known to be involved in the formation of focal adhesions in mammalian cells, also plays an important role in *Dictyostelium* cell-substrate adhesion as mutants lacking this gene display reduced adhesion to surfaces, aberrant transmission of force to their substratum and a fast 'gliding' motility[220,448,622,623,640]. An unconventional myosin of class VII, has also been shown to play a role in *Dictyostelium* cell adhesion and in regulation of the actin cytoskeleton[219,618]. Moreover, cell-substrate adhesions have been shown to be affected by the adhesivity of the environment in which the cell was grown, where a more adhesive substratum appears to downregulate expression of proteins involved in adhesion[113]. Furthermore, *Dictyostelium* cells secrete a factor inhibiting adhesion, which results in cells at high densities being less adhesive than cells at low densities[113].

What emerges is that there is a complex interplay between the dynamics of the cell cytoskeleton and the formation of adhesions between a cell and its surrounding environment. The mechanisms behind this process are currently not well understood, and contradictory information is sometimes obtained from different studies, potentially due to differences in matrix properties or cell types[248]. However, it is clear that further exploration of the mechanisms of cell-environment interactions, with cytoskeletal and adhesion mutants, both in 3D and on 2D non-transparent surfaces has the potential to uncover additional modes of cell motility and probe the mechanisms behind them[18,479,520]. *Dictyostelium*, a system of reduced complexity in comparison to mammalian systems, but with conserved cellular transduction mechanisms, represents a useful model in which to investigate how cell behaviour can be affected by the dimensionality of its environment, and enable greater understanding of the mechanisms and processes underlying chemotaxis and basic cell motility[544]. Furthermore, with

the methods and protocols developed in this work, OCT offers a valuable microscopic tool for visualisation of cell motility and chemotaxis under these conditions.

7.5 Final Summary

For convenience of visualisation with conventional light microscopy, such as phase contrast or DIC, studies of chemotaxis and cell behaviour have generally relied on the use of monolayers of cells on 2D transparent substrates, usually glass or plastic, although it is increasingly apparent that this observed behaviour does not necessarily relate well to the behaviour of cells within their more natural 3D environment[461,583,611,665]. OCT has been demonstrated as a valuable microscopic technique for the visualisation of both individual and multicellular migration and chemotaxis on 2D substrates and within 3D environments. The volumetric images obtained were subjected to analysis with tracking software and differences were shown in the migratory characteristics of cells under three different environmental conditions. Furthermore, the potential for this technique, with the developed experimental protocols, to probe the migration and chemotaxis of mutant cell strains within 3D environments and compare it to that of the parent strain was shown. The methods and protocols developed within this work enable investigation of the behaviour and migration of cells in 4D and on 3D non-transparent surfaces, allowing assessment of the effects of different substrata and different environments on cells and potentially enabling greater understanding of the processes of cell migration, aggregation and morphogenesis.

Bibliography

1 *dictyBase*, <http://dictybase.org/> (2011).

2 *PART I: Development Under Agarose*, <http://homepages.uconn.edu/~mb2225vc/MCB_2225/Expt_6a__Development_of_Dictyostelium_Under_Agarose.html> (2012).

3 Adelson, E. H., Anderson, C. H., Bergen, J. R., Burt, P. J. & M.Ogden, J. Pyramid methods in image processing. *RCA Engineer* **29**, 33-41 (1984).

4 Adler, D. C. *et al.* Three-dimensional endomicroscopy of the human colon using optical coherence tomography. *Opt. Express* **17**, 784-796 (2009).

5 Afonso, P. V. & Parent, C. A. PI3K and Chemotaxis: A Priming Issue? *Sci. Signal.* **4**, pe22 (2011).

6 Aizawa, H., Fukui, Y. & Yahara, I. Live dynamics of *Dictyostelium* cofilin suggests a role in remodeling actin latticework into bundles. *J. Cell Sci.* **110**, 2333-2344 (1997).

7 Alex, A. *et al.* Multispectral in vivo three-dimensional optical coherence tomography of human skin. *J. Biomed. Opt.* **15**, 026025 (2010).

8 Allavena, P. & Mantovani, A. Immunology in the clinic review series; focus on cancer: tumour-associated macrophages: undisputed stars of the inflammatory tumour microenvironment. *Clinical & Experimental Immunology* **167**, 195-205 (2012).

9 Amos, W. B. & White, J. G. How the Confocal Laser Scanning Microscope entered Biological Research. *Biol. Cell* **95**, 335-342 (2003).

10 An, L., Li, P., Shen, T. T. & Wang, R. High speed spectral domain optical coherence tomography for retinal imaging at 500,000 A-lines per second. *Biomed. Opt. Express* **2**, 2770-2783 (2011).

11 Anderson, T. F. Techniques for the preservation of three-dimensional structure in preparing specimens for the electron microscope. *Trans. N. Y. Acad. Sci.* **13**, 130-134 (1951).

12 Andrew, N. & Insall, R. H. Chemotaxis in shallow gradients is mediated independently of PtdIns 3-kinase by biased choices between random protrusions. *Nat Cell Biol* **9**, 193-200 (2007).

13 Anjard, C. & Loomis, W. F. Cytokinins induce sporulation in *Dictyostelium*. *Development* **135**, 819-827 (2008).

14 Anselme, K., Ponche, A. & Bigerelle, M. Relative influence of surface topography and surface chemistry on cell response to bone implant materials. Part 2: Biological

aspects. *Proceedings of the Institution of Mechanical Engineers, Part H: Journal of Engineering in Medicine* **224**, 1487-1507 (2010).

15 Antoine, B. *et al.* Gene expression in hepatocyte-like lines established by targeted carcinogenesis in transgenic mice. *Exp. Cell Res.* **200**, 175-185 (1992).

16 Araki, T., van Egmond, W. N., van Haastert, P. J. M. & Williams, J. G. Dual regulation of a *Dictyostelium* STAT by cGMP and Ca2+ signalling. *J. Cell Sci.* **123**, 837-841 (2010).

17 Araujo, J. C. *et al.* Comparison of hexamethyldisilazane and critical point drying treatments for SEM analysis of anaerobic biofilms and granular sludge. *J. Electron Microsc. (Tokyo)* **52**, 429-433 (2003).

18 Arcizet, D. *et al.* Contact-controlled amoeboid motility induces dynamic cell trapping in 3D-microstructured surfaces. *Soft Matter* **8**, 1473-1481 (2012).

19 Arnison, M. R., Cogswell, C. J., Smith, N. I., Fekete, P. W. & Larkin, K. G. Using the Hilbert transform for 3D visualization of differential interference contrast microscope images. *J. Microsc.* **199**, 79-84 (2000).

20 Arnott, S. *et al.* The agarose double helix and its function in agarose gel structure. *J. Mol. Biol.* **90**, 269-284 (1974).

21 Asano, Y. *et al.* Keratocyte-like locomotion in amiB-null *Dictyostelium* cells. *Cell Motil. Cytoskeleton* **59**, 17-27 (2004).

22 Axel, L., Gonçalves, R. C. & Bloomgarden, D. Regional heart wall motion: two-dimensional analysis and functional imaging with MR imaging. *Radiology* **183**, 745-750 (1992).

23 Azhar, M., Manogaran, P. S., Kennady, P. K., Pande, G. & Nanjundiah, V. A Ca2+-Dependent Early Functional Heterogeneity in Amoebae of *Dictyostelium discoideum*, Revealed by Flow Cytometry. *Exp. Cell Res.* **227**, 344-351 (1996).

24 Bacakova, L., Filova, E., Parizek, M., Ruml, T. & Svorcik, V. Modulation of cell adhesion, proliferation and differentiation on materials designed for body implants. *Biotechnology Advances* **29**, 739-767 (2011).

25 Bachmann, A., Leitgeb, R. & Lasser, T. Heterodyne Fourier domain optical coherence tomography for full range probing with high axial resolution. *Opt. Express* **14**, 1487-1496 (2006).

26 Bader, S., Kortholt, A. & Haastert, P. J. M. V. Seven *Dictyostelium discoideum* phosphodiesterases degrade three pools of cAMP and cGMP *Biochem. J.* **402**, 153-161 (2007).

27 Bae, A. J. & Bodenschatz, E. On the swimming of *Dictyostelium* amoebae. *PNAS* **107**, E165-E166 (2010).

28 Bagorda, A. *et al.* Real-time measurements of cAMP production in live *Dictyostelium* cells. *J. Cell Sci.* **122**, 3907-3914 (2009).

29 Baldauf, S. L., Roger, A. J., Wenk-Siefert, I. & Doolittle, W. F. A Kingdom-Level Phylogeny of Eukaryotes Based on Combined Protein Data. *Science* **290**, 972-977 (2000).

30 Barralet, J. E. *et al.* Comparison of bone marrow cell growth on 2D and 3D alginate hydrogels. *Journal of Materials Science: Materials in Medicine* **16**, 515-519 (2005).

31 Barrangou, L. M., Daubert, C. R. & Allen Foegeding, E. Textural properties of agarose gels. I. Rheological and fracture properties. *Food Hydrocolloids* **20**, 184-195 (2006).

32 Barry, N. P. & Bretscher, M. S. *Dictyostelium* amoebae and neutrophils can swim. *PNAS* **107**, 11376-11380 (2010).

33 Baskar, R., Chhabra, P., Mascarenhas, P. & Nanjundiah, V. A cell type-specific effect of calcium on pattern formation and differentiation in *Dictyostelium discoideum*. *Int. J. Dev. Biol.* **44**, 491-498 (2000).

34 BDBiosciences. *BD™ PuraMatrix™ Peptide Hydrogel Guidelines for Use*, <http://www.bdbiosciences.com/external_files/dl/doc/manuals/live/web_enabled/354250Lpug.pdf> (2012).

35 BDBiosciences. *Guidelines for use Product: BD Matrigel™ Basement Membrane Matrix, 5 ml vial*, <http://www.bdbiosciences.com/external_files/dl/doc/manuals/live/web_enabled/356234_Guidelines.pdf> (2011).

36 Bell, S. E. *et al.* Differential gene expression during capillary morphogenesis in 3D collagen matrices. *J. Cell Sci.* **114**, 2755-2773 (2001).

37 Benghezal, M. *et al.* Synergistic Control of Cellular Adhesion by Transmembrane 9 Proteins. *Mol. Biol. Cell* **14**, 2890-2899 (2003).

38 Beningo, K. A., Dembo, M. & Wang, Y.-l. Responses of fibroblasts to anchorage of dorsal extracellular matrix receptors. *PNAS* **101**, 18024-18029 (2004).

39 Berlot, C. H., Spudich, J. A. & Devreotes, P. N. Chemoattractant-elicited increases in myosin phosphorylation in *Dictyostelium*. *Cell* **43**, 307-314 (1985).

40 Bérubé, K., Pitt, A., Hayden, P., Prytherch, Z. & Job, C. Filter-well technology for advanced three-dimensional cell culture: perspectives for respiratory research. *Altern Lab Anim* **38**, 49-65 (2010).

41 Beta, C. & Bodenschatz, E. Microfluidic tools for quantitative studies of eukaryotic chemotaxis. *Eur. J. Cell Biol.* **90**, 811-816 (2011).

42 Bhojwani, S. S. & Razdan, M. K. Chapter 4: Cell Culture in *Plant Tissue Culture: Theory and Practice (Studies in Plant Science)* (eds Sant Saran Bhojwani & M. K. Razdan) Ch. 4, (Elsevier Science Ltd; Rev. Ed edition (8 Nov 1996), 1996).

43 Biname, F., Pawlak, G., Roux, P. & Hibner, U. What makes cells move: requirements and obstacles for spontaneous cell motility. *Mol. Biosyst.* **6**, 648-661 (2010).

44 BiostatusLimited. *CyGEL™ ...a liquid when cooled and a gel when warmed...* <http://www.biostatus.com/product/cygel/> (2012).

45 Birgersdotter, A., Sandberg, R. & Ernberg, I. Gene expression perturbation in vitro—A growing case for three-dimensional (3D) culture systems. *Semin. Cancer Biol.* **15**, 405-412 (2005).

46 Bissell, M. J., Hall, H. G. & Parry, G. How does the extracellular matrix direct gene expression? *J. Theor. Biol.* **99**, 31-68 (1982).

47 Blaser, H. *et al.* Migration of Zebrafish Primordial Germ Cells: A Role for Myosin Contraction and Cytoplasmic Flow. *Dev. Cell* **11**, 613-627 (2006).

48 Blow, N. Cell migration: our protruding knowledge. *Nat Meth* **4**, 589-594 (2007).

49 Boddington, S. *et al.* Labeling Human Mesenchymal Stem Cells with Fluorescent Contrast Agents: the Biological Impact. *Mol. Imaging Biol.* **13**, 3-9 (2011).

50 Boer, J. F. d. Spectral/Fourier Domain Optical Coherence Tomography in *Optical Coherence Tomography: Technology and Applications* (eds Wolfgang Drexler & James G. Fujimoto) Ch. 5, 147-175 (Springer-Verlag, 2008).

51 Bonner, J. T. The migration stage of *Dictyostelium*: Behavior without muscles or nerves. *FEMS Microbiol. Lett.* **120**, 1-7 (1994).

52 Bonner, J. T., Chiang, A., Lee, J. & Suthers, H. B. The possible role of ammonia in phototaxis of migrating slugs of *Dictyostelium discoideum*. *PNAS* **85**, 3885-3887 (1988).

53 Bonner, J. T., Davidowski, T. A., Hsu, W. L., Lapeyrolerie, D. A. & Suthers, H. L. B. The Role of Surface Water and Light on Differentiation in the Cellular Slime Molds. *Differentiation* **21**, 123-126 (1982).

54 Bonner, J. T., Kelso, A. P. & Gilmor, R. G. A new approach to the problem of aggregation in the cellular slime molds. *Biol. Bull.* **130**, 28-42 (1966).

55 Bonner, J. T. & Lamont, D. S. Behavior of cellular slime molds in the soil. *Mycologia* **97**, 178-184 (2005).

56 Boppart, S. A., Yang, Y. & Wang, R. K. Optical Coherence Tomography in Tissue Engineering in *Optical Coherence Tomography: Technology and Applications* (eds Wolfgang Drexler & James G. Fujimoto) Ch. 29, 889-917 (Springer-Verlag, 2008).

57 Bosgraaf, L. *et al.* A novel cGMP signalling pathway mediating myosin phosphorylation and chemotaxis in *Dictyostelium*. *EMBO J.* **21**, 4560-4570 (2002).

58 Bosgraaf, L. *et al.* A novel cGMP signalling pathway mediating myosin phosphorylation and chemotaxis in *Dictyostelium*. *EMBO J.* **21**, 4560-4570 (2002).

59 Bosgraaf, L. & Van Haastert, P. J. M. Navigation of Chemotactic Cells by Parallel Signaling to Pseudopod Persistence and Orientation. *PLoS ONE* **4**, e6842 (2009).

60 Bosgraaf, L. & van Haastert, P. J. M. The regulation of myosin II in *Dictyostelium*. *Eur. J. Cell Biol.* **85**, 969-979 (2006).

61 Bosgraaf, L. *et al.* RasGEF-containing proteins GbpC and GbpD have differential effects on cell polarity and chemotaxis in *Dictyostelium*. *J. Cell Sci.* **118**, 1899-1910 (2005).

62 Boucheny, C., Bonneau, G.-P., Droulez, J., Thibault, G. & Ploix, S. A perceptive evaluation of volume rendering techniques. *ACM Trans. Appl. Percept.* **5**, 1-24 (2009).

63 Boyden, S. The Chemotatic Effect of Mixtures of Antibody and Antigen on Polymorphonuclear Leucocytes. *The Journal of Experimental Medicine* **115**, 453-466 (1962).

64 Brackmann, C. *et al.* Coherent anti-Stokes Raman scattering microscopy of human smooth muscle cells in bioengineered tissue scaffolds. *J. Biomed. Opt.* **16**, 021115 (2011).

65 Braet, F., De Zanger, R. & Wisse, E. Drying cells for SEM, AFM and TEM by hexamethyldisilazane: a study on hepatic endothelial cells. *J. Microsc.* **186**, 84-87 (1997).

66 Brannstrom, A. & Dieckmann, U. Evolutionary dynamics of altruism and cheating among social amoebas. *Proc. R. Soc. Lond. B Biol. Sci.* **272**, 1609-1616 (2005).

67 Bray, D. F., Bagu, J. & Koegler, P. Comparison of hexamethyldisilazane (HMDS), Peldri II, and critical-point drying methods for scanning electron microscopy of biological specimens. *Microsc. Res. Tech.* **26**, 489-495 (1993).

68 Bredfeldt, J. S., Vinegoni, C., Marks, D. L. & Boppart, S. A. Molecularly sensitive optical coherence tomography. *Opt. Lett.* **30**, 495-497 (2005).

69 Breshears, L. M., Wessels, D., Soll, D. R. & Titus, M. A. An unconventional myosin required for cell polarization and chemotaxis. *PNAS* **107**, 6918-6923 (2010).

70 Breunig, H. G. *et al.* Combining multiphoton and CARS microscopy for skin imaging. in *Proc. SPIE 7903, Multiphoton Microscopy in the Biomedical Sciences XI.* 79031A (SPIE).

71 Brezinski, M. E. Optical Coherence Tomography Theory in *Optical Coherence Tomography: Principles and Applications* Ch. 5, (Academic Press, 2006).

72 Brock, D. A., Douglas, T. E., Queller, D. C. & Strassmann, J. E. Primitive agriculture in a social amoeba. *Nature* **469**, 393-396 (2011).

73 Brown, M. E. & Bridgman, P. C. Myosin function in nervous and sensory systems. *J. Neurobiol.* **58**, 118-130 (2004).

74 Bruhn, H. & Steinert, M. *Dictyostelium*, a Tractable Model Host Organism for Legionella in *Legionella: Molecular Microbiology* (eds Klaus Heuner & Michele Swanson) Ch. 12, (Caister Academic Press, 2008).

75 Buckley, M. J., Eagleson, G. K. & Silverman, B. W. The estimation of residual variance in nonparametric regression. *Biometrika* **75**, 189-199 (1988).

76 Buenemann, M., Levine, H., Rappel, W.-J. & Sander, L. M. The Role of Cell Contraction and Adhesion in *Dictyostelium* Motility. *Biophys. J.* **99**, 50-58 (2010).

77 Burch, C. R. & Stock, J. P. P. Phase-Contrast Microscopy. *J. Sci. Instrum.* **19**, 71 (1942).

78 Bürglin, T. R. A two-channel four-dimensional image recording and viewing system with automatic drift correction. *J. Microsc.* **200**, 75-80 (2000).

79 Burridge, K. & Connell, L. Talin: A cytoskeletal component concentrated in adhesion plaques and other sites of actin-membrane interaction. *Cell Motil.* **3**, 405-417 (1983).

80 Cai, H. *et al.* Ras-mediated activation of the TORC2–PKB pathway is critical for chemotaxis. *The Journal of Cell Biology* **190**, 233-245 (2010).

81 Calamante, F. *et al.* Super-resolution track-density imaging studies of mouse brain: Comparison to histology. *Neuroimage* **59**, 286-296 (2012).

82 Calvo-Garrido, J. *et al.* Autophagy in *Dictyostelium*: Genes and pathways, cell death and infection. *Autophagy* **6**, 686-701 (2010).

83 CardiffUniversity. *Central Biotechnology Services*, <http://medicine.cf.ac.uk/cbs/> (2012).

84 Carrasco, S. *et al.* Enhancing the axial resolution of quantum optical coherence tomographyby chirped quasi-phase matching. *Opt. Lett.* **29**, 2429-2431 (2004).

85 Carroll, P. & James, J. Assaying Promoter Activity Using LacZ and GFP as Reporters in *Mycobacteria Protocols* Vol. 465 *Methods in Molecular Biology* (eds Tanya Parish & Amanda Claire Brown) Ch. 18, 1-14 (Humana Press, 2009).

86 Chalfie, M. Green Fluorescent Protein. *Photochem. Photobiol.* **62**, 651-656 (1995).

87 Chalfie, M., Tu, Y., Euskirchen, G., Ward, W. & Prasher, D. Green fluorescent protein as a marker for gene expression. *Science* **263**, 802-805 (1994).

88 Charest, J. L., García, A. J. & King, W. P. Myoblast alignment and differentiation on cell culture substrates with microscale topography and model chemistries. *Biomaterials* **28**, 2202-2210 (2007).

89 Charest, P. G. & Firtel, R. A. Big roles for small GTPases in the control of directed cell movement. *Biochem. J.* **401**, 377-390 (2007).

90 Charest, P. G. & Firtel, R. A. "TORCing" Neutrophil Chemotaxis. *Dev. Cell* **19**, 795-796 (2010).

91 Charest, P. G. *et al.* A Ras Signaling Complex Controls the RasC-TORC2 Pathway and Directed Cell Migration. *Dev. Cell* **18**, 737-749 (2010).

92 Charras, G. & Paluch, E. Blebs lead the way: how to migrate without lamellipodia. *Nat Rev Mol Cell Biol* **9**, 730-736 (2008).

93 Charras, G. T., Yarrow, J. C., Horton, M. A., Mahadevan, L. & Mitchison, T. J. Non-equilibration of hydrostatic pressure in blebbing cells. *Nature* **435**, 365-369 (2005).

94 Chehroudi, B., Gould, T. R. L. & Brunette, D. M. Effects of a grooved titanium-coated implant surface on epithelial cell behavior in vitro and in vivo. *J. Biomed. Mater. Res.* **23**, 1067-1085 (1989).

95 Chen, C. S., Mrksich, M., Huang, S., Whitesides, G. M. & Ingber, D. E. Geometric Control of Cell Life and Death. *Science* **276**, 1425-1428 (1997).

96 Chen, L. *et al.* PLA2 and PI3K/PTEN Pathways Act in Parallel to Mediate Chemotaxis. *Dev. Cell* **12**, 603-614 (2007).

97 Chen, P., Ostrow, B. D., Tafuri, S. R. & Chisholm, R. L. Targeted disruption of the *Dictyostelium* RMLC gene produces cells defective in cytokinesis and development. *The Journal of Cell Biology* **127**, 1933-1944 (1994).

98 Chen, X., Liu, Y. & Zhang, X. Topical insulin application improves healing by regulating the wound inflammatory response. *Wound Repair Regen.* **20**, 425-434 (2012).

99 Chisholm, R. L., Rushforth, A. M., Pollenz, R. S., Kuczmarski, E. R. & Tafuri, S. R. *Dictyostelium discoideum* myosin: isolation and characterization of cDNAs encoding the essential light chain. *Mol. Cell. Biol.* **8**, 794-801 (1988).

100 Choi, C. K. *et al.* Actin and [alpha]-actinin orchestrate the assembly and maturation of nascent adhesions in a myosin II motor-independent manner. *Nat Cell Biol* **10**, 1039-1050 (2008).

101 Choma, M. A., Suter, M. J., Vakoc, B. J., Bouma, B. E. & Tearney, G. J. Physiological homology between Drosophila melanogaster and vertebrate cardiovascular systems. *Dis Model Mech.* **4**, 411-420 (2011).

102 Choyke, P. L. *et al.* Toxicity of Organic Fluorophores Used in Molecular Imaging: Literature Review. *Mol. Imaging* **8**, 341-354 (2009).

103 Christenson, L., Mikos, A. G., Gibbons, D. F. & Picciolo, G. L. Biomaterials for Tissue Engineering: Summary. *Tissue Eng* **3**, 71-76 (1997).

104 Chuai, M., Dormann, D. & Weijer, C. J. Imaging cell signalling and movement in development. *Seminars in Cell & Developmental Biology* **20**, 947-955 (2009).

105 Chung, C. Y. & Firtel, R. A. Paka, a Putative Pak Family Member, Is Required for Cytokinesis and the Regulation of the Cytoskeleton in *Dictyostelium discoideum* Cells during Chemotaxis. *The Journal of Cell Biology* **147**, 559-576 (1999).

106 Clark, P., Connolly, P., Curtis, A. S., Dow, J. A. & Wilkinson, C. D. Topographical control of cell behaviour. I. Simple step cues. *Development* **99**, 439-448 (1987).

107 Clark, P., Connolly, P., Curtis, A. S., Dow, J. A. & Wilkinson, C. D. Topographical control of cell behaviour: II. Multiple grooved substrata. *Development* **108**, 635-644 (1990).

108 Clarke, M., Dominguez, N., Yuen, I. S. & Gomer, R. H. Growing and starving *Dictyostelium* cells produce distinct density-sensing factors. *Dev. Biol.* **152**, 403-406 (1992).

109 Coates, J. C. & Harwood, A. J. Cell-cell adhesion and signal transduction during *Dictyostelium* development. *J. Cell Sci.* **114**, 4349-4358 (2001).

110 Cobb, M. J. *et al.* Imaging of subsquamous Barrett's epithelium with ultrahigh-resolution optical coherence tomography: a histologic correlation study. *Gastrointest. Endosc.* **71**, 223-230 (2010).

111 Cohen, M. H. & Robertson, A. Chemotaxis and the early stages of aggregation in cellular slime molds. *J. Theor. Biol.* **31**, 119-130 (1971).

112 Comer, F. I., Lippincott, C. K., Masbad, J. J. & Parent, C. A. The PI3K-Mediated Activation of CRAC Independently Regulates Adenylyl Cyclase Activation and Chemotaxis. *Curr. Biol.* **15**, 134-139 (2005).

113 Cornillon, S., Froquet, R. & Cosson, P. Involvement of Sib Proteins in the Regulation of Cellular Adhesion in *Dictyostelium discoideum*. *Eukaryot. Cell* **7**, 1600-1605 (2008).

114 Cornillon, S. *et al.* An adhesion molecule in free-living *Dictyostelium* amoebae with integrin [beta] features. *EMBO Rep.* **7**, 617-621 (2006).

115 Crawley, S. W. *et al.* Autophosphorylation Activates *Dictyostelium* Myosin II Heavy Chain Kinase A by Providing a Ligand for an Allosteric Binding Site in the α-Kinase Domain. *J. Biol. Chem.* **286**, 2607-2616 (2011).

116 Cukierman, E., Pankov, R., Stevens, D. R. & Yamada, K. M. Taking Cell-Matrix Adhesions to the Third Dimension. *Science* **294**, 1708-1712 (2001).

117 Cukierman, E., Pankov, R. & Yamada, K. M. Cell interactions with three-dimensional matrices. *Curr. Opin. Cell Biol.* **14**, 633-640 (2002).

118 Curtis, A. & Wilkinson, C. New depths in cell behaviour: reactions of cells to nanotopography. *Biochemical Society symposium* **65**, 15-26 (1999).

119 Curtis, A. & Wilkinson, C. Topographical control of cells. *Biomaterials* **18**, 1573-1583 (1997).

120 Cutler, J. E. A Simple In Vitro Method for Studies on Chemotaxis. *Proceedings of the Society for Experimental Biology and Medicine. Society for Experimental Biology and Medicine (New York, N.Y.)* **147**, 471-474 (1974).

121 Das, S., Rericha, E. C., Bagorda, A. & Parent, C. A. Direct Biochemical Measurements of Signal Relay during *Dictyostelium* Development. *J. Biol. Chem.* **286**, 38649-38658 (2011).

122 Davidenko, J. M., Pertsov, A. V., Salomonsz, R., Baxter, W. & Jalife, J. Stationary and drifting spiral waves of excitation in isolated cardiac muscle. *Nature* **355**, 349-351 (1992).

123 Davis, B. J., Ralston, T. S., Marks, D. L., Boppart, S. A. & Carney, P. S. Autocorrelation artifacts in optical coherence tomography and interferometric synthetic aperture microscopy. *Opt. Lett.* **32**, 1441-1443 (2007).

124 Dawson, E., Mapili, G., Erickson, K., Taqvi, S. & Roy, K. Biomaterials for stem cell differentiation. *Advanced Drug Delivery Reviews* **60**, 215-228 (2008).

125 De Chiffre, L. *et al.* Quantitative Characterisation of Surface Texture. *CIRP Annals - Manufacturing Technology* **49**, 635-652 (2000).

126 De Clerck, L. S., Bridts, C. H., Mertens, A. M., Moens, M. M. & Stevens, W. J. Use of fluorescent dyes in the determination of adherence of human leucocytes to endothelial

cells and the effect of fluorochromes on cellular function. *J. Immunol. Methods* **172**, 115-124 (1994).

127 de Hostos, E. L. *et al. Dictyostelium* mutants lacking the cytoskeletal protein coronin are defective in cytokinesis and cell motility. *The Journal of Cell Biology* **120**, 163-173 (1993).

128 De Lozanne, A. & Spudich, J. Disruption of the *Dictyostelium* myosin heavy chain gene by homologous recombination. *Science* **236**, 1086-1091 (1987).

129 De Wit, R. J. W. & Bulgakov, R. Folate chemotactic receptors in *Dictyostelium discoideum* I. Ligand-induced conversion between four receptor states. *Biochimica et Biophysica Acta (BBA) - Molecular Cell Research* **886**, 76-87 (1986).

130 Decaestecker, C., Debeir, O., Van Ham, P. & Kiss, R. Can anti-migratory drugs be screened in vitro? A review of 2D and 3D assays for the quantitative analysis of cell migration. *Med. Res. Rev.* **27**, 149-176 (2007).

131 del Alamo, J. C. *et al.* Spatio-temporal analysis of eukaryotic cell motility by improved force cytometry. *PNAS* **104**, 13343-13348 (2007).

132 del Álamo, J. C. *et al.* Spatio-temporal analysis of eukaryotic cell motility by improved force cytometry. *PNAS* **104**, 13343-13348 (2007).

133 Delanoë-Ayari, H., Rieu, J. P. & Sano, M. 4D Traction Force Microscopy Reveals Asymmetric Cortical Forces in Migrating *Dictyostelium* Cells. *Phys. Rev. Lett.* **105**, 248103-248101-248104 (2010).

134 Devreotes, P. *Dictyostelium discoideum*: a model system for cell-cell interactions in development. *Science* **245**, 1054-1058 (1989).

135 Devreotes, P. & Janetopoulos, C. Eukaryotic Chemotaxis: Distinctions between Directional Sensing and Polarization. *J. Biol. Chem.* **278**, 20445-20448 (2003).

136 DiMilla, P. A., Barbee, K. & Lauffenburger, D. A. Mathematical model for the effects of adhesion and mechanics on cell migration speed. *Biophys. J.* **60**, 15-37 (1991).

137 Discher, D. E., Janmey, P. & Wang, Y.-l. Tissue Cells Feel and Respond to the Stiffness of Their Substrate. *Science* **310**, 1139-1143 (2005).

138 Dixit, R. & Cyr, R. Cell damage and reactive oxygen species production induced by fluorescence microscopy: effect on mitosis and guidelines for non-invasive fluorescence microscopy. *The Plant Journal* **36**, 280-290 (2003).

139 Doolittle, K. W., Reddy, I. & McNally, J. G. 3D Analysis of Cell Movement during Normal and Myosin-II-Null Cell Morphogenesis in *Dictyostelium*. *Dev. Biol.* **167**, 118-129 (1995).

140 Dormann, D., Kim, J.-Y., Devreotes, P. N. & Weijer, C. J. cAMP receptor affinity controls wave dynamics, geometry and morphogenesis in *Dictyostelium*. *J. Cell Sci.* **114**, 2513-2523 (2001).

141 Dormann, D. & Weijer, C. J. Chemotactic cell movement during *Dictyostelium* development and gastrulation. *Current Opinion in Genetics & Development* **16**, 367-373 (2006).

142 Dormann, D. & Weijer, C. J. Imaging of cell migration. *EMBO J.* **25**, 3480-3493 (2006).

143 Dormann, D. & Weijer, C. J. Visualizing *Dictyostelium* Development in *Dictyostelium discoideum protocols* (eds L. Eichinger & F. Rivero-Crespo) (2006).

144 Dorobantu, L. S., Goss, G. G. & Burrell, R. E. Atomic force microscopy: A nanoscopic view of microbial cell surfaces. *Micron* **43**, 1312-1322 (2012).

145 Downey, G. P. *et al.* Retention of leukocytes in capillaries: role of cell size and deformability. *J. Appl. Physiol.* **69**, 1767-1778 (1990).

146 Drexler, W. Cellular and Functional Optical Coherence Tomography of the Human Retina The Cogan Lecture. *Investigative Ophthalmology & Visual Science* **48**, 5340-5351 (2007).

147 Drexler, W. Ultrahigh-resolution optical coherence tomography. *J. Biomed. Opt.* **9**, 47-74 (2004).

148 Drexler, W. & Fujimoto, J. G. State-of-the-art retinal optical coherence tomography. *Prog. Retin. Eye Res.* **27(1)**, 45-88 (2008).

149 Drexler, W. *et al.* Ultrahigh-resolution ophthalmic optical coherence tomography. *Nat. Med.* **7**, 502-507 (2001).

150 Driscoll, M. K. *et al.* Cell Shape Dynamics: From Waves to Migration. *PLoS Comput. Biol.* **8**, e1002392 (2012).

151 Dundr, M., McNally, J. G., Cohen, J. & Misteli, T. Quantitation of GFP-fusion proteins in single living cells. *J. Struct. Biol.* **140**, 92-99 (2002).

152 Dunn, G. A. How do cells respond to ultrafine surface contours? *Bioessays* **13**, 541-543 (1991).

153 Dunn, K. W., Kamocka, M. M. & McDonald, J. H. A practical guide to evaluating colocalization in biological microscopy. *American Journal of Physiology - Cell Physiology* **300**, C723-C742 (2011).

154 Dytham, C. *Choosing and using statistics: a biologist's guide- 2nd Edition.* (Blackwell Science, 2003).

155 EdmundOptics. *Telecentricity and Telecentric Lenses in Machine Vision*, <http://www.edmundoptics.com/technical-support/imaging/telecentricity-and-telecentric-lenses-in-machine-vision/?&viewall> (2011).

156 Egelhoff, T. T., Croft, D. & Steimle, P. A. Actin Activation of Myosin Heavy Chain Kinase A in *Dictyostelium*. *J. Biol. Chem.* **280**, 2879-2887 (2005).

157 Egelhoff, T. T., Lee, R. J. & Spudich, J. A. *Dictyostelium* myosin heavy chain phosphorylation sites regulate myosin filament assembly and localization in vivo. *Cell* **75**, 363-371 (1993).

158 Egelhoff, T. T., Naismith, T. V. & Brozovich, F. V. Myosin-based cortical tension in *Dictyostelium* resolved into heavy and light chain-regulated components. *J. Muscle Res. Cell Motil.* **17**, 269-274 (1996).

159 Egner, A., Andresen, V. & Hell, S. W. Comparison of the axial resolution of practical Nipkow-disk confocal fluorescence microscopy with that of multifocal multiphoton microscopy: theory and experiment. *J. Microsc.* **206**, 24-32 (2002).

160 Eichinger, L. *et al.* The genome of the social amoeba *Dictyostelium discoideum*. *Nature* **435**, 43-57 (2005).

161 Eisenbach, M. & Lengeler, J. W. *Chemotaxis*. (Imperial College Press, 2004).

162 Eliott, S., Joss, G. H., Spudich, A. & Williams, K. L. Patterns in *Dictyostelium discoideum*: the role of myosin II in the transition from the unicellular to the multicellular phase. *J. Cell Sci.* **104**, 457-466 (1993).

163 Elmore, S. Apoptosis: A Review of Programmed Cell Death. *Toxicol. Pathol.* **35**, 495-516 (2007).

164 Elsdale, T. & Bard, J. Collagen substrata for studies on cell behavior. *The Journal of Cell Biology* **54**, 626-637 (1972).

165 Elzie, C. A., Colby, J., Sammons, M. A. & Janetopoulos, C. Dynamic localization of G proteins in *Dictyostelium discoideum*. *J. Cell Sci.* **122**, 2597-2603 (2009).

166 EMDMilliporeCorporation©. *MF-Millipore Membrane Filter*, <http://www.millipore.com/catalogue/item/habp04700> (2012).

167 Engler, A. J. *et al.* Myotubes differentiate optimally on substrates with tissue-like stiffness. *The Journal of Cell Biology* **166**, 877-887 (2004).

168 Engler, A. J., Sen, S., Sweeney, H. L. & Discher, D. E. Matrix Elasticity Directs Stem Cell Lineage Specification. *Cell* **126**, 677-689 (2006).

169 Englert, D. L., Jayaraman, A. & Manson, M. D. Microfluidic Techniques for the Analysis of Bacterial Chemotaxis in *Chemotaxis Methods and Protocols* (eds Tian Jin & Dale Hereld) Ch. 1, 1-23 (Human Press, 2009).

170 Esmaeelpour, M. *et al.* Three-dimensional 1060nm OCT: Choroidal thickness maps in normals and improved posterior segment visualization in cataract patients. *Investigative Ophthalmology & Visual Science* **51**, 5260-5266 (2010).

171 Evans, J. P., Garcia-Gonzalez, F., Almbro, M., Robinson, O. & Fitzpatrick, J. L. Assessing the potential for egg chemoattractants to mediate sexual selection in a broadcast spawning marine invertebrate. *Proceedings of the Royal Society B: Biological Sciences* **279**, 2855-2861 (2012).

172 Even-Ram, S. & Yamada, K. M. Cell migration in 3D matrix. *Curr. Opin. Cell Biol.* **17**, 524-532 (2005).

173 Fackler, O. T. & Grosse, R. Cell motility through plasma membrane blebbing. *The Journal of Cell Biology* **181**, 879-884 (2008).

174 Fakhri, N., MacKintosh, F. C., Lounis, B., Cognet, L. & Pasquali, M. Brownian Motion of Stiff Filaments in a Crowded Environment. *Science* **330**, 1804-1807 (2010).

175 Fass, L. Imaging and cancer: A review. *Molecular Oncology* **2**, 115-152 (2008).

176 Feinberg, A. P., Springer, W. R. & Barondes, S. H. Segregation of pre-stalk and pre-spore cells of *Dictyostelium discoideum*: observations consistent with selective cell cohesion. *PNAS* **76**, 3977-3981 (1979).

177 Feit, I., Medynski, E. & Rothrock, M. Ammonia differentially suppresses the cAMP chemotaxis of anterior-like cells and prestalk cells *Dictyostelium discoideum*. *Journal of Biosciences* **26**, 157-166 (2001).

178 FemtolasersGmbH. *Rainbow*, <http://www.femtolasers.com/fileadmin/documents/Leaflets/FS_rainbow.pdf> (2012).

179 Fercher, A. F. Inverse Scattering, Dispersion, and Speckle in Optical Coherence Tomography in *Optical Coherence Tomography: Technology and Applications* (eds Wolfgang Drexler & James G. Fujimoto) Ch. 4, 119-146 (Springer-Verlag, 2008).

180 Fercher, A. F. & et al. Optical coherence tomography - principles and applications. *Reports on Progress in Physics* **66**, 239 (2003).

181 Fercher, A. F., Hitzenberger, C. K., Drexler, W., Kamp, G. & Sattmann, H. In vivo optical coherence tomography. *Am. J. Ophthalmol.* **116**, 113-114 (1993).

182 Fercher, A. F., Hitzenberger, C. K., Kamp, G. & El-Zaiat, S. Y. Measurement of intraocular distances by backscattering spectral interferometry. *Opt Commun* **117**, 43-48 (1995).

183 Fercher, A. F. *et al.* Dispersion compensation for optical coherence tomography depth-scan signals by a numerical technique. *Opt Commun* **204**, 67-74 (2002).

184 Ferguson, G. J. *et al.* PI(3)K[gamma] has an important context-dependent role in neutrophil chemokinesis. *Nat Cell Biol* **9**, 86-91 (2007).

185 Fey, P., Gaudet, P., Pilcher, K. E., Franke, J. & Chisholm, R. L. dictyBase and the Dicty Stock Center in *Dictyostelium discoideum protocols* (eds L. Eichinger & F. Rivero-Crespo) (Humana Press, 2006).

186 Fey, P., Kowal, A. S., Gaudet, P., Pilcher, K. E. & Chisholm, R. L. Protocols for growth and development of *Dictyostelium discoideum*. *Nat. Protocols* **2**, 1307-1316 (2007).

187 Fey, P., Stephens, S., Titus, M. A. & Chisholm, R. L. SadA, a novel adhesion receptor in *Dictyostelium*. *The Journal of Cell Biology* **159**, 1109-1119 (2002).

188 Field, A. *Discovering Stastistics Using SPSS Second Edition.* (SAGE Publications Ltd, 2005).

189 Field, A. & Hole, G. *How to Design and Report Experiments.* (SAGE Publications Ltd, 2011).

190 Firtel, R. A. & Meili, R. *Dictyostelium*: a model for regulated cell movement during morphogenesis. *Current Opinion in Genetics & Development* **10**, 421-427 (2000).

191 Fisher, P. R., Merkl, R. & Gerisch, G. Quantitative analysis of cell motility and chemotaxis in *Dictyostelium discoideum* by using an image processing system and a novel chemotaxis chamber providing stationary chemical gradients. *The Journal of Cell Biology* **108**, 973-984 (1989).

192 Fishman, E. K. *et al.* Volume Rendering versus Maximum Intensity Projection in CT Angiography: What Works Best, When, and Why1. *Radiographics* **26**, 905-922 (2006).

193 Flannigan, D. J., Barwick, B. & Zewail, A. H. Biological imaging with 4D ultrafast electron microscopy. *PNAS* **107**, 9933-9937 (2010).

194 Foord, S. A. & Atkins, E. D. Y. New x-ray diffraction results from agarose: Extended single helix structures and implications for gelation mechanism. *Biopolymers* **28**, 1345-1365 (1989).

195 Fraley, S. I. *et al.* A distinctive role for focal adhesion proteins in three-dimensional cell motility. *Nat Cell Biol* **12**, 598-604 (2010).

196 Franca-Koh, J. & Devreotes, P. N. Moving Forward: Mechanisms of Chemoattractant Gradient Sensing. *Physiology* **19**, 300-308 (2004).

197 Franca-Koh, J., Kamimura, Y. & Devreotes, P. Navigating signaling networks: chemotaxis in *Dictyostelium discoideum*. *Current Opinion in Genetics & Development* **16**, 333-338 (2006).

198 Franck, C., Maskarinec, S. A., Tirrell, D. A. & Ravichandran, G. Three-Dimensional Traction Force Microscopy: A New Tool for Quantifying Cell-Matrix Interactions. *PLoS ONE* **6**, e17833 (2011).

199 Franke, J. & Kessin, R. A defined minimal medium for axenic strains of *Dictyostelium discoideum*. *PNAS* **74**, 2157-2161 (1977).

200 Fraser, S. A. *et al.* Sub-micron and nanoscale feature depth modulates alignment of stromal fibroblasts and corneal epithelial cells in serum-rich and serum-free media. *Journal of Biomedical Materials Research Part A* **86A**, 725-735 (2008).

201 Friedl, P. Dynamic imaging of cellular interactions with extracellular matrix. *Histochem. Cell Biol.* **122**, 183-190 (2004).

202 Friedl, P., Borgmann, S. & Bröcker, E.-B. Amoeboid leukocyte crawling through extracellular matrix: lessons from the *Dictyostelium* paradigm of cell movement. *J. Leukoc. Biol.* **70**, 491-509 (2001).

203 Friedl, P. & Wolf, K. Plasticity of cell migration: a multiscale tuning model. *The Journal of Experimental Medicine* **188**, 11-19 (2010).

204 Friedl, P. & Wolf, K. Tumour-cell invasion and migration: diversity and escape mechanisms. *Nat. Rev. Cancer* **3**, 362-374 (2003).

205 Friedl, P. & Zallen, J. A. Dynamics of cell-cell and cell-matrix interactions in morphogenesis, regeneration and cancer. *Curr. Opin. Cell Biol.* **22**, 557-559 (2010).

206 Froquet, R. *et al.* TM9/Phg1 and SadA proteins control surface expression and stability of SibA adhesion molecules in *Dictyostelium*. *Mol. Biol. Cell* **23**, 679-686 (2012).

207 Froquet, R., Lelong, E., Marchetti, A. & Cosson, P. *Dictyostelium discoideum*: a model host to measure bacterial virulence. *Nat. Protocols* **4**, 25-30 (2008).

208 Fujimoto, J. & Drexler, W. Introduction to Optical Coherence Tomography in *Optical Coherence Tomography: Technology and Applications* (eds Wolfgang Drexler & James G. Fujimoto) Ch. 1, 1-45 (Springer-Verlag, 2008).

209 Fukui, Y., De Lozanne, A. & Spudich, J. A. Structure and function of the cytoskeleton of a *Dictyostelium* myosin-defective mutant. *The Journal of Cell Biology* **110**, 367-378 (1990).

210 Fukui, Y. & Inoué, S. Amoeboid movement anchored by eupodia, new actin-rich knobby feet in *Dictyostelium*. *Cell Motil. Cytoskeleton* **36**, 339-354 (1997).

211 Fukui, Y., Kitanishi-Yumura, T. & Yumura, S. Myosin II-independent F-actin flow contributes to cell locomotion in *Dictyostelium*. *J. Cell Sci.* **112**, 877-886 (1999).

212 Fukui, Y., Murray, J., Riddelle, K. S. & Soil, D. R. Cell Behavior and Actomyosin Organization in *Dictyostelium* During Substrate Exploration. *Cell Struct. Funct.* **16**, 289-301 (1991).

213 Fuller, D. *et al.* External and internal constraints on eukaryotic chemotaxis. *PNAS* **107**, 9656-9659 (2010).

214 Funamoto, S., Meili, R., Lee, S., Parry, L. & Firtel, R. A. Spatial and Temporal Regulation of 3-Phosphoinositides by PI 3-Kinase and PTEN Mediates Chemotaxis. *Cell* **109**, 611-623 (2002).

215 Funamoto, S., Milan, K., Meili, R. & Firtel, R. A. Role of Phosphatidylinositol 3' Kinase and a Downstream Pleckstrin Homology Domain–Containing Protein in Controlling Chemotaxis in *Dictyostelium*. *The Journal of Cell Biology* **153**, 795-810 (2001).

216 Futrelle, R. P., Traut, J. & McKee, W. G. Cell behavior in *Dictyostelium discoideum*: preaggregation response to localized cyclic AMP pulses. *The Journal of Cell Biology* **92**, 807-821 (1982).

217 Gao, L. *et al.* Noninvasive Imaging beyond the Diffraction Limit of 3D Dynamics in Thickly Fluorescent Specimens. *Cell* **151**, 1370-1385 (2012).

218 Gargesha, M., Jenkins, M. W., Rollins, A. M. & Wilson, D. L. Denoising and 4D visualization of OCT images. *Opt. Express* **16**, 12313-12333 (2008).

219 Gebbie, L. *et al.* Phg2, a Kinase Involved in Adhesion and Focal Site Modeling in *Dictyostelium*. *Mol. Biol. Cell* **15**, 3915-3925 (2004).

220 Geiger, B., Spatz, J. P. & Bershadsky, A. D. Environmental sensing through focal adhesions. *Nat Rev Mol Cell Biol* **10**, 21-33 (2009).

221 Ghosh, S. *et al.* Three-dimensional culture of melanoma cells profoundly affects gene expression profile: A high density oligonucleotide array study. *J. Cell. Physiol.* **204**, 522-531 (2005).

222 Giusti, C. *et al.* Chapter 1 Analysis of Autophagic and Necrotic Cell Death in *Dictyostelium* in *Methods Enzymol.* Vol. Volume 446 (eds Zahra Zakeri Richard A. Lockshin Roya Khosravi-Far & Piacentini Mauro) 1-15 (Academic Press, 2008).

223 Glasbey, C. A. & Mardia, K. V. A review of image-warping methods. *Journal of Applied Statistics* **25**, 155-171 (1998).

224 Golé, L., Rivière, C., Hayakawa, Y. & Rieu, J.-P. A Quorum-Sensing Factor in Vegetative *Dictyostelium Discoideum* Cells Revealed by Quantitative Migration Analysis. *PLoS ONE* **6**, e26901 (2011).

225 Goley, E. D. & Welch, M. D. The ARP2/3 complex: an actin nucleator comes of age. *Nat Rev Mol Cell Biol* **7**, 713-726 (2006).

226 Gomer, R. H., Jang, W. & Brazill, D. Cell density sensing and size determination. *Development, Growth & Differentiation* **53**, 482-494 (2011).

227 Gomer, R. H., Yuen, I. S. & Firtel, R. A. A secreted 80×10^3 M_r protein mediates sensing of cell density and the onset of development in *Dictyostelium*. *Development* **112**, 269-278 (1991).

228 Gómez-Lechón, M. J. *et al.* Long-term expression of differentiated functions in hepatocytes cultured in three-dimensional collagen matrix. *J. Cell. Physiol.* **177**, 553-562 (1998).

229 Gould, C. J. *et al.* The Formin DAD Domain Plays Dual Roles in Autoinhibition and Actin Nucleation. *Current biology : CB* **21**, 384-390 (2011).

230 Goury-Sistla, P., Nanjundiah, V. & Pande, G. Bimodal distribution of motility and cell fate in *Dictyostelium discoideum*. *Int. J. Dev. Biol.* (2012).

231 Gray, D. C. *et al.* In vivo fluorescence imaging of primate retinal ganglion cells and retinal pigment epithelial cells. *Opt. Express* **14**, 7144-7158 (2006).

232 Gray, R. S., Cheung, K. J. & Ewald, A. J. Cellular mechanisms regulating epithelial morphogenesis and cancer invasion. *Curr. Opin. Cell Biol.* **22**, 640-650 (2010).

233 Griffith, L. M., Downs, S. M. & Spudich, J. A. Myosin light chain kinase and myosin light chain phosphatase from *Dictyostelium*: effects of reversible phosphorylation on myosin structure and function. *The Journal of Cell Biology* **104**, 1309-1323 (1987).

234 Grinvald, A. & Hildesheim, R. VSDI: a new era in functional imaging of cortical dynamics. *Nat. Rev. Neurosci.* **5**, 874-885 (2004).

235 Gruber, H. & Hanley, E. Human disc cells in monolayer vs 3D culture: cell shape, division and matrix formation. *BMC Musculoskeletal Disorders* **1**, 1 (2000).

236 Guillame-Gentil, O. *et al.* Engineering the Extracellular Environment: Strategies for Building 2D and 3D Cellular Structures. *Advanced Materials* **22**, 5443-5462 (2010).

237 Guillotin, B. & Guillemot, F. Cell patterning technologies for organotypic tissue fabrication. *Trends Biotechnol.* **29**, 183-190 (2011).

238 Hadwiger, J. A. & Firtel, R. A. Analysis of G alpha 4, a G-protein subunit required for multicellular development in *Dictyostelium*. *Genes & Development* **6**, 38-49 (1992).

239 Hadwiger, J. A., Lee, S. & Firtel, R. A. The G alpha subunit G alpha 4 couples to pterin receptors and identifies a signaling pathway that is essential for multicellular development in *Dictyostelium*. *PNAS* **91**, 10566-10570 (1994).

240 Hajicharalambous, C. S. *et al.* Nano- and sub-micron porous polyelectrolyte multilayer assemblies: Biomimetic surfaces for human corneal epithelial cells. *Biomaterials* **30**, 4029-4036 (2009).

241 Hale, G. M. & Querry, M. R. Optical Constants of Water in the 200-nm to 200-microm Wavelength Region. *Appl. Opt.* **12**, 555-563 (1973).

242 Halova, I., Draberova, L. & Draber, P. Mast cell chemotaxis Chemoattractants and signaling pathways. *Frontiers in Immunology* **3**, 1-19 (2012).

243 Happel, C. M., Thrane, L., Thommes, J., Männer, J. & Yelbuz, T. M. Integration of an optical coherence tomography (OCT) system into an examination incubator to facilitate in vivo imaging of cardiovascular development in higher vertebrate embryos under stable physiological conditions. *Annals of Anatomy - Anatomischer Anzeiger* **193**, 425-435 (2011).

244 Harrison, R. G. The cultivation of tissues in extraneous media as a method of morpho-genetic study. *The Anatomical Record* **6**, 181-193 (1912).

245 Hart, A. Mann-Whitney test is not just a test of medians: differences in spread can be important. *BMJ* **323**, 391-393 (2001).

246 Hartgring, S., Willis, C., Bijlsma, J., Lafeber, F. & van Roon, J. Interleukin-7 aggravated joint inflammation and tissue destruction in collagen-induced arthritis is associated with T-cell and B-cell activation. *Arthritis Research & Therapy* **14**, R137 (2012).

247 Hartigan, J. A. & Hartigan, P. M. The Dip Test of Unimodality. *Annals of Statistics* **13**, 70-84 (1985).

248 Harunaga, J. S. & Yamada, K. M. Cell-matrix adhesions in 3D. *Matrix Biol.* **30**, 363-368 (2011).

249 Haser, H. & Häder, D.-P. Orientation and phototaxis in pseudoplasmodia of an axenic strain of the cellular slime mold, *Dictyostelium discoideum*. *Exp. Mycol.* **16**, 119-131 (1992).

250 Hashimoto, Y., Cohen, M. H. & Robertson, A. Cell density dependence of the aggregation characteristics of the cellular slime mould *Dictyostelium discoideum*. *J. Cell Sci.* **19**, 215-229 (1975).

251 Hasselbring, B. M., Patel, M. K. & Schell, M. A. *Dictyostelium discoideum* as a Model System for Identification of Burkholderia pseudomallei Virulence Factors. *Infect. Immun.* **79**, 2079-2088 (2011).

252 Haugh, J. M., Codazzi, F., Teruel, M. & Meyer, T. Spatial Sensing in Fibroblasts Mediated by 3' Phosphoinositides. *The Journal of Cell Biology* **151**, 1269-1280 (2000).

253 Hecht, E. *Optics (4th Edition)*. (Addison Wesley, 2001).

254 Heid, P. J., Geiger, J., Wessels, D., Voss, E. & Soll, D. R. Computer-assisted analysis of filopod formation and the role of myosin II heavy chain phosphorylation in *Dictyostelium*. *J. Cell Sci.* **118**, 2225-2237 (2005).

255 Heid, P. J. *et al.* The role of myosin heavy chain phosphorylation in *Dictyostelium* motility, chemotaxis and F-actin localization. *J. Cell Sci.* **117**, 4819-4835 (2004).

256 Helmchen, F. & Denk, W. Deep tissue two-photon microscopy. *Nat Meth* **2**, 932-940 (2005).

257 Hereld, D. & Jin, T. *Chemotaxis: Methods and Protocols*. (Springer Berlin Heidelberg, 2009).

258 Hersen, P. & Ladoux, B. Biophysics: Push it, pull it. *Nature* **470**, 340-341 (2011).

259 Hoeller, O. & Kay, R. R. Chemotaxis in the Absence of PIP3 Gradients. *Curr. Biol.* **17**, 813-817 (2007).

260 Hofer, B. *et al.* Artefact reduction for cell migration visualization using spectral domain optical coherence tomography. *Journal of Biophotonics* **4**, 355-367 (2011).

261 Hofer, B. *et al.* Dispersion encoded full range frequency domain optical coherence tomography. *Opt. Express* **17**, 7-24 (2009).

262 Hofer, B. *et al.* Fast dispersion encoded full range optical coherence tomography for retinal imaging at 800 nm and 1060 nm. *Opt. Express* **18**, 4898-4919 (2010).

263 Hongdong, L. & Hartley, R. The 3D-3D Registration Problem Revisited. in *IEEE 11th International Conference on Computer Vision, 2007. ICCV 2007*. 1-8.

264 Howard, I. P. Depth from Perspective in *Perceiving in Depth, Volume 3: Other Mechanisms of Depth Perception* (OUP 2012).

265 Huang, D. *et al.* Optical coherence tomography. *Science* **254**, 1178-1181 (1991).

266 Huang, T. Y., DerMardirossian, C. & Bokoch, G. M. Cofilin phosphatases and regulation of actin dynamics. *Curr. Opin. Cell Biol.* **18**, 26-31 (2006).

267 Huang, X. *et al.* Spiral Waves in Disinhibited Mammalian Neocortex. *The Journal of Neuroscience* **24**, 9897-9902 (2004).

268 Hughes, E. H., Hong, S.-B., Shanks, J. V., San, K.-Y. & Gibson, S. I. Characterization of an Inducible Promoter System in Catharanthus roseus Hairy Roots. *Biotechnol. Prog.* **18**, 1183-1186 (2002).

269 Iglesias, P. A. & Devreotes, P. N. Navigating through models of chemotaxis. *Curr. Opin. Cell Biol.* **20**, 35-40 (2008).

270 Ilina, O. & Friedl, P. Mechanisms of collective cell migration at a glance. *J. Cell Sci.* **122**, 3203-3208 (2009).

271 Insall, R. The *Dictyostelium* genome: the private life of a social model revealed? *Genome Biol.* **6**, 222 (2005).

272 Insall, R. *et al.* Dynamics of the *Dictyostelium* Arp2/3 complex in endocytosis, cytokinesis, and chemotaxis. *Cell Motil. Cytoskeleton* **50**, 115-128 (2001).

273 Insall, R. H. Understanding eukaryotic chemotaxis: a pseudopod-centred view. *Nat Rev Mol Cell Biol* **11**, 453-458 (2010).

274 Insall, R. H., Borleis, J. & Devreotes, P. N. The aimless RasGEF is required for processing of chemotactic signals through G-protein-coupled receptors in *Dictyostelium*. *Current biology : CB* **6**, 719-729 (1996).

275 Insall, R. H. & Machesky, L. M. Actin Dynamics at the Leading Edge: From Simple Machinery to Complex Networks. *Dev. Cell* **17**, 310-322 (2009).

276 Insall, R. H., Soede, R. D., Schaap, P. & Devreotes, P. N. Two cAMP receptors activate common signaling pathways in *Dictyostelium*. *Mol. Biol. Cell* **5**, 703-711 (1994).

277 Ishiwata, H., Itoh, M. & Yatagai, T. A new method of three-dimensional measurement by differential interference contrast microscope. *Opt Commun* **260**, 117-126 (2006).

278 Itoh, G. & Yumura, S. A novel mitosis-specific dynamic actin structure in *Dictyostelium* cells. *J. Cell Sci.* **120**, 4302-4309 (2007).

279 Iwadate, Y. & Yumura, S. Actin-based propulsive forces and myosin-II-based contractile forces in migrating *Dictyostelium* cells. *J. Cell Sci.* **121**, 1314-1324 (2008).

280 Iwadate, Y. & Yumura, S. Cyclic stretch of the substratum using a shape-memory alloy induces directional migration in *Dictyostelium* cells. *Biotechniques* **47**, 757–767 (2009).

281 Izatt, J. A. & Choma, M. A. Theory of Optical Coherence Tomography in *Optical Coherence Tomography: Technology and Applications* (eds Wolfgang Drexler & James G. Fujimoto) Ch. 2, 47-72 (Springer-Verlag, 2008).

282 Jain, R., Yuen, I. S., Taphouse, C. R. & Gomer, R. H. A density-sensing factor controls development in *Dictyostelium*. *Genes & Development* **6**, 390-400 (1992).

283 Jaklenec, A., Stamp, A., Deweerd, E., Sherwin, A. & Langer, R. Progress in the Tissue Engineering and Stem Cell Industry "Are we there yet?". *Tissue Eng Part B Rev* (2012).

284 Janetopoulos, C., Ma, L., Devreotes, P. N. & Iglesias, P. A. Chemoattractant-induced phosphatidylinositol 3,4,5-trisphosphate accumulation is spatially amplified and adapts, independent of the actin cytoskeleton. *Proc. Natl. Acad. Sci. U. S. A.* **101**, 8951-8956 (2004).

285 Janoo, V. Quantification of shape, angularity, and surface texture of base course materials. *Cold Regions Research and Engineering Laboratory, Hanover NH, USA* **No. CRREL-SR-98-1**, 1-22 (1998).

286 Janson, J.-C. & Jönsson, J. Å. Introduction to Chromatography in *Protein Purification* 23-50 (John Wiley & Sons, Inc., 2011).

287 Jay, P. Y., Pham, P. A., Wong, S. A. & Elson, E. L. A mechanical function of myosin II in cell motility. *J. Cell Sci.* **108**, 387-393 (1995).

288 Judex, S. *et al.* Quantification of adiposity in small rodents using micro-CT. *Methods* **50**, 14-19 (2010).

289 Kahle, N. A., Brenner-Weiss, G., Overhage, J., Obst, U. & Hänsch, G. M. Bacterial quorum sensing molecule induces chemotaxis of human neutrophils via induction of p38 and leukocyte specific protein 1 (LSP1). *Immunobiology* **218**, 145-151 (2013).

290 Kajić, V. *et al.* Robust segmentation of intraretinal layers in the normal human fovea using a novel statistical model based on texture and shape analysis. *Opt. Express* **18**, 14730-14744 (2010).

291 Kajiya, J. T. The rendering equation. *SIGGRAPH Comput. Graph.* **20**, 143-150 (1986).

292 Kamimura, Y. & Devreotes, P. N. Phosphoinositide-dependent Protein Kinase (PDK) Activity Regulates Phosphatidylinositol 3,4,5-Trisphosphate-dependent and -independent Protein Kinase B Activation and Chemotaxis. *J. Biol. Chem.* **285**, 7938-7946 (2010).

293 Kamimura, Y. *et al.* PIP3-Independent Activation of TorC2 and PKB at the Cell's Leading Edge Mediates Chemotaxis. *Curr. Biol.* **18**, 1034-1043 (2008).

294 Kawauchi, T. Cell Adhesion and Its Endocytic Regulation in Cell Migration during Neural Development and Cancer Metastasis. *International Journal of Molecular Sciences* **13**, 4564-4590 (2012).

295 Kay, R. R., Langridge, P., Traynor, D. & Hoeller, O. Changing directions in the study of chemotaxis. *Nat Rev Mol Cell Biol* **9**, 455-463 (2008).

296 Kay, R. R. & Thompson, C. R. L. Forming Patterns in Development without Morphogen Gradients: Scattered Differentiation and Sorting Out. *Cold Spring Harbor Perspectives in Biology* **1**, a001503 (2009).

297 Kayman, S. C. & Clarke, M. Relationship between axenic growth of *Dictyostelium discoideum* strains and their track morphology on substrates coated with gold particles. *The Journal of Cell Biology* **97**, 1001-1010 (1983).

298 Keller, T. & Thompson, C. R. L. Cell type specificity of a diffusible inducer is determined by a GATA family transcription factor. *Development* **135**, 1635-1645 (2008).

299 Kessin, R. H. *Dictyostelium: evolution, cell biology, and the development of multicellularity*. (Cambridge University Press, 2001).

300 Keung, A. J., Healy, K. E., Kumar, S. & Schaffer, D. V. Biophysics and dynamics of natural and engineered stem cell microenvironments. *Wiley Interdisciplinary Reviews: Systems Biology and Medicine* **2**, 49-64 (2010).

301 Khaire, N. *et al.* Filamin-regulated F-actin Assembly Is Essential for Morphogenesis and Controls Phototaxis in *Dictyostelium*. *J. Biol. Chem.* **282**, 1948-1955 (2007).

302 Khandoga, A. G. *et al.* In Vivo Imaging and Quantitative Analysis of Leukocyte Directional Migration and Polarization in Inflamed Tissue. *PLoS ONE* **4**, e4693 (2009).

303 Kidoaki, S. & Matsuda, T. Microelastic gradient gelatinous gels to induce cellular mechanotaxis. *J. Biotechnol.* **133**, 225-230 (2008).

304 Killich, T. *et al.* The locomotion, shape and pseudopodial dynamics of unstimulated *Dictyostelium* cells are not random. *J. Cell Sci.* **106**, 1005-1013 (1993).

305 Kim, H.-D. & Peyton, S. R. Bio-inspired materials for parsing matrix physicochemical control of cell migration: A Review. *Integrative Biology* **4**, 37-52 (2012).

306 Kim, K.-H., Gohtani, S., Matsuno, R. & Yamano, Y. Effects of oil droplet and agar concentration on gel strength and microstructure of O/W emulsion gel. *Journal of Texture Studies* **30**, 319-335 (1999).

307 Kim, K. H., Buehler, C. & So, P. T. C. High-Speed, Two-Photon Scanning Microscope. *Appl. Opt.* **38**, 6004-6009 (1999).

308 King, J. *et al.* Genetic Control of Lithium Sensitivity and Regulation of Inositol Biosynthetic Genes. *PLoS ONE* **5**, e11151 (2010).

309 King, J. S. *et al.* The mood stabiliser lithium suppresses PIP3 signalling in *Dictyostelium* and human cells. *Dis Model Mech.* **2**, 306-312 (2009).

310 King, J. S., Veltman, D. M., Georgiou, M., Baum, B. & Insall, R. H. Scar/WAVE is activated at mitosis and drives myosin-independent cytokinesis. *J. Cell Sci.* **123**, 2246-2255 (2010).

311 Kingshott, P., Andersson, G., McArthur, S. L. & Griesser, H. J. Surface modification and chemical surface analysis of biomaterials. *Curr. Opin. Chem. Biol.* **15**, 667-676 (2011).

312 Knecht, D. A., Jung, J. & Matthews, L. Quantification of transformation efficiency using a new method for clonal growth and selection of axenic *Dictyostelium* cells. *Dev. Genet.* **11**, 403-409 (1990).

313 Knecht, D. A. & Loomis, W. F. Developmental consequences of the lack of myosin heavy chain in *Dictyostelium discoideum*. *Dev. Biol.* **128**, 178-184 (1988).

314 Knecht, D. A. & Shelden, E. Three-Dimensional Localization of Wild-Type and Myosin II Mutant Cells during Morphogenesis of *Dictyostelium*. *Dev. Biol.* **170**, 434-444 (1995).

315 Kocaoglu, O. P. *et al.* Imaging cone photoreceptors in three dimensions and in time using ultrahigh resolution optical coherence tomography with adaptive optics. *Biomed. Opt. Express* **2**, 748-763 (2011).

316 Koch, N. *et al.* Abp1 employs the Arp2/3 complex activator Scar/WAVE in bristle development. *J. Cell Sci.* **125**, 3578-3589 (2012).

317 Kölsch, V., Charest, P. G. & Firtel, R. A. The regulation of cell motility and chemotaxis by phospholipid signaling. *J. Cell Sci.* **121**, 551-559 (2008).

318 Konjin, T. M. Microbiological assay of cyclic 3',5'-AMP. *Experientia* **26**, 367-369 (1970).

319 Kopachik, W., Oohata, A., Dhokia, B., Brookman, J. J. & Kay, R. R. *Dictyostelium* mutants lacking DIF, a putative morphogen. *Cell* **33**, 397-403 (1983).

320 Kotula, L. & Steudle, E. Measurements of oxygen permeability coefficients of rice (Oryza sativa L.) roots using a new perfusion technique. *Journal of experimental botany* **60**, 567-580 (2009).

321 Kowal, A. S. & Chisholm, R. L. Uncovering a Role for the Tail of the *Dictyostelium discoideum* SadA Protein in Cell-Substrate Adhesion. *Eukaryot. Cell* **10**, 662-671 (2011).

322 Kreft, M., Stenovec, M. & Zorec, R. Focus-Drift Correction in Time-Lapse Confocal Imaging. *Ann. N. Y. Acad. Sci.* **1048**, 321-330 (2005).

323 Kriebel, P. W., Barr, V. A., Rericha, E. C., Zhang, G. & Parent, C. A. Collective cell migration requires vesicular trafficking for chemoattractant delivery at the trailing edge. *The Journal of Cell Biology* **183**, 949-961 (2008).

324 Kubow, K. E. & Horwitz, A. R. Reducing background fluorescence reveals adhesions in 3D matrices. *Nat Cell Biol* **13**, 3-5 (2011).

325 Kuo, J.-C., Han, X., Hsiao, C.-T., Yates Iii, J. R. & Waterman, C. M. Analysis of the myosin-II-responsive focal adhesion proteome reveals a role for [beta]-Pix in negative regulation of focal adhesion maturation. *Nat Cell Biol* **13**, 383-393 (2011).

326 Kuo, W.-C. *et al.* Polarization-sensitive optical coherence tomography for imaging human atherosclerosis. *Appl. Opt.* **46**, 2520-2527 (2007).

327 Kushiro, K. & Asthagiri, A. R. Modular Design of Micropattern Geometry Achieves Combinatorial Enhancements in Cell Motility. *Langmuir* **28**, 4357-4362 (2012).

328 Laevsky, G. & Knecht, D. A. Cross-linking of actin filaments by myosin II is a major contributor to cortical integrity and cell motility in restrictive environments. *J. Cell Sci.* **116**, 3761-3770 (2003).

329 Laevsky, G. & Knecht, D. A. Under-Agarose Folate Chemotaxis of *Dictyostelium discoideum* Amoebae in Permissive and Mechanically Inhibited Conditions. *Biotechniques* **31**, 1140-1149 (2001).

330 Lahaye, M. & Rochas, C. Chemical structure and physico-chemical properties of agar. *Hydrobiologia* **221**, 137-148 (1991).

331 Lam, T. Y., Pickering, G., Geltosky, J. & Siu, C. H. Differential Cell Cohesiveness Expressed by Prespore and Prestalk Cells of *Dictyostelium discoideum*. *Differentiation* **20**, 22-28 (1981).

332 Lammermann, T. *et al.* Rapid leukocyte migration by integrin-independent flowing and squeezing. *Nature* **453**, 51-55 (2008).

333 Landfear, S. M. & Lodish, H. F. A role for cyclic AMP in expression of developmentally regulated genes in *Dictyostelium discoideum*. *PNAS* **77**, 1044-1048 (1980).

334 Lang, C., Pollithy, A. & Schüler, D. Identification of Promoters for Efficient Gene Expression in Magnetospirillum gryphiswaldense. *Appl. Environ. Microbiol.* **75**, 4206-4210 (2009).

335 Langridge, P. D. & Kay, R. R. Blebbing of *Dictyostelium* cells in response to chemoattractant. *Exp. Cell Res.* **312**, 2009-2017 (2006).

336 Langridge, P. D. & Kay, R. R. Mutants in the *Dictyostelium* Arp2/3 complex and chemoattractant-induced actin polymerization. *Exp. Cell Res.* **313**, 2563-2574 (2007).

337 Larin, K. V., Eledrisi, M. S., Motamedi, M. & Esenaliev, R. O. Noninvasive Blood Glucose Monitoring With Optical Coherence Tomography. *Diabetes Care* **25**, 2263-2267 (2002).

338 Lauffenburger, D. & Aris, R. Measurement of leukocyte motility and chemotaxis parameters using a quantitative analysis of the under-agarose migration assay. *Math. Biosci.* **44**, 121-138 (1979).

339 Lauffenburger, D., Rothman, C. & Zigmond, S. H. Measurement of leukocyte motility and chemotaxis parameters with a linear under-agarose migration assay. *The Journal of Immunology* **131**, 940-947 (1983).

340 Lauffenburger, D. A. & Horwitz, A. F. Cell Migration: A Physically Integrated Molecular Process. *Cell* **84**, 359-369 (1996).

341 Lauffenburger, D. A. & Zigmond, S. H. Chemotactic factor concentration gradients in chemotaxis assay systems. *J. Immunol. Methods* **40**, 45-60 (1981).

342 Lavinskiene, S. *et al.* Peripheral Blood Neutrophil Activity During Dermatophagoides pteronyssinus -Induced Late-Phase Airway Inflammation in Patients with Allergic Rhinitis and Asthma. *Inflammation* **35**, 1600-1609 (2012).

343 Lechleiter, J., Girard, S., Peralta, E. & Clapham, D. Spiral calcium wave propagation and annihilation in Xenopus laevis oocytes. *Science* **252**, 123-126 (1991).

344 Lee, A. *virtualdub.org*, <http://www.virtualdub.org/index.html> (2011).

345 Lee, A. K. & Falkow, S. Constitutive and inducible green fluorescent protein expression in Bartonella henselae. *Infect. Immun.* **66**, 3964-3967 (1998).

346 Lee, E., Seastone, D. J., Harris, E., Cardelli, J. A. & Knecht, D. A. RacB Regulates Cytoskeletal Function in *Dictyostelium* spp. *Eukaryot. Cell* **2**, 474-485 (2003).

347 Lee, N.-S., Veeranki, S., Kim, B. & Kim, L. The function of PP2A/B56 in non-metazoan multicellular development. *Differentiation* **76**, 1104-1110 (2008).

348 Lee, S. *4. Chemotaxis of a population of Dictyostelium cells to cAMP*, <http://biology.ucsd.edu/~firtel/video/ax320x/video.htm> (2012).

349 Lee, S. *et al.* TOR Complex 2 Integrates Cell Movement during Chemotaxis and Signal Relay in *Dictyostelium*. *Mol. Biol. Cell* **16**, 4572-4583 (2005).

350 Lee, S., Shen, Z., Robinson, D. N., Briggs, S. & Firtel, R. A. Involvement of the Cytoskeleton in Controlling Leading-Edge Function during Chemotaxis. *Mol. Biol. Cell* **21**, 1810-1824 (2010).

351 Legant, W. R. *et al.* Measurement of mechanical tractions exerted by cells in three-dimensional matrices. *Nat Meth* **7**, 969-971 (2010).

352 Leitgeb, R. *et al.* Real-time assessment of retinal blood flow with ultrafast acquisition by color Doppler Fourier domain optical coherence tomography. *Opt. Express* **11**, 3116-3121 (2003).

353 Leitgeb, R. A. Optical Coherence Tomography - high resolution imaging of structure and function. *Engineering in Medicine and Biology Society, 2007. EMBS 2007. 29th Annual International Conference of the IEEE*, 530-532 (2007).

354 Levchenko, A. & Iglesias, P. A. Models of Eukaryotic Gradient Sensing: Application to Chemotaxis of Amoebae and Neutrophils. *Biophys. J.* **82**, 50-63 (2002).

355 Levental, I., Georges, P. C. & Janmey, P. A. Soft biological materials and their impact on cell function. *Soft Matter* **3**, 299-306 (2007).

356 Levi, S., Polyakov, M. V. & Egelhoff, T. T. Myosin II dynamics in *Dictyostelium*: Determinants for filament assembly and translocation to the cell cortex during chemoattractant responses. *Cell Motil. Cytoskeleton* **53**, 177-188 (2002).

357 Levine, H., Aranson, I., Tsimring, L. & Truong, T. V. Positive genetic feedback governs cAMP spiral wave formation in *Dictyostelium*. *PNAS* **93**, 6382-6386 (1996).

358 Levine, H., Kessler, D. A. & Rappel, W.-J. Directional sensing in eukaryotic chemotaxis: A balanced inactivation model. *PNAS* **103**, 9761-9766 (2006).

359 Li, J. *et al.* Quantitative measurement of optical parameters of cell lines 5-8F and 6-10B using polarization sensitive optical coherence tomography. *Arch. Biochem. Biophys.* **522**, 125-129 (2012).

360 Li, L. Integrating Intensity and Texture Differences for Robust Change Detection. *IEEE Transactions on Image Processing* **11**, 105-112 (2002).

361 Li, L. *et al.* Binary and Gray-Scale Patterning of Chemical Functionality on Polymer Films. *J. Am. Chem. Soc.* **130**, 13512-13513 (2008).

362 Li, X. & et al. High-speed optical coherence tomography signal processing on GPU. *Journal of Physics: Conference Series* **277**, 012019 (2011).

363 Lidke, D. S., Lidke, K. A., Rieger, B., Jovin, T. M. & Arndt-Jovin, D. J. Reaching out for signals. *The Journal of Cell Biology* **170**, 619-626 (2005).

364 Liebling, M. *PoorMan3DReg*, <http://sybil.ece.ucsb.edu/pages/poorman3dreg/index.html> (2005-2010).

365 Lippok, N., Coen, S., Nielsen, P. & Vanholsbeeck, F. Dispersion compensation in Fourier domain optical coherence tomography using the fractional Fourier transform. *Opt. Express* **20**, 23398-23413 (2012).

366 Lippok, N., Nielsen, P. & Vanholsbeeck, F. in *Advanced Data Processing and Signal Enhancement (ADPSE), European Conference on Biomedical Optics* Vol. 8091 80910Q (SPIE, Munich, Germany, 2011).

367 Liu, G., Zhang, J., Yu, L., Xie, T. & Chen, Z. Real-time polarization-sensitive optical coherence tomography data processing with parallel computing. *Appl. Opt.* **48**, 6365-6370 (2009).

368 Liu, H. & Roy, K. Biomimetic Three-Dimensional Cultures Significantly Increase Hematopoietic Differentiation Efficacy of Embryonic Stem Cells. *Tissue Eng* **11**, 319-330 (2005).

369 Liu, L., Das, S., Losert, W. & Parent, C. A. mTORC2 Regulates Neutrophil Chemotaxis in a cAMP- and RhoA-Dependent Fashion. *Dev. Cell* **19**, 845-857 (2010).

370 Liu, L. & Parent, C. A. TOR kinase complexes and cell migration. *The Journal of Cell Biology* **194**, 815-824 (2011).

371 Liu, M. J. J., Chou, S. M., Chua, C. K., Tay, B. C. M. & Ng, B. K. The development of silk fibroin scaffolds using an indirect rapid prototyping approach: Morphological analysis and cell growth monitoring by spectral-domain optical coherence tomography. *Medical Engineering & Physics* **35**, 253-262 (2013).

372 Lo, C.-M., Wang, H.-B., Dembo, M. & Wang, Y.-l. Cell Movement Is Guided by the Rigidity of the Substrate. *Biophys. J.* **79**, 144-152 (2000).

373 Loesberg, W. A. *et al.* The threshold at which substrate nanogroove dimensions may influence fibroblast alignment and adhesion. *Biomaterials* **28**, 3944-3951 (2007).

374 Lombardi, M. L., Knecht, D. A., Dembo, M. & Lee, J. Traction force microscopy in *Dictyostelium* reveals distinct roles for myosin II motor and actin-crosslinking activity in polarized cell movement. *J. Cell Sci.* **120**, 1624-1634 (2007).

375 Loomis Jr, W. F. Sensitivity of *Dictyostelium discoideum* to nucleic acid analogues. *Exp. Cell Res.* **64**, 484-486 (1971).

376 Loomis, W. F. & Smith, D. W. Molecular phylogeny of *Dictyostelium discoideum* by protein sequence comparison. *PNAS* **87**, 9093-9097 (1990).

377 Lorentzen, A., Bamber, J., Sadok, A., Elson-Schwab, I. & Marshall, C. J. An ezrin-rich, rigid uropod-like structure directs movement of amoeboid blebbing cells. *J. Cell Sci.* **124**, 1256-1267 (2011).

378 Lück-Vielmetter, D., Schleicher, M., Grabatin, B., Wippler, J. & Gerisch, G. Replacement of threonine residues by serine and alanine in a phosphorylatable heavy chain fragment of *Dictyostelium* myosin II. *FEBS Lett.* **269**, 239-243 (1990).

379 Luke, H. D. The origins of the sampling theorem. *Communications Magazine, IEEE* **37**, 106-108 (1999).

380 Luker, G. D. & Luker, K. E. Optical Imaging: Current Applications and Future Directions. *J. Nucl. Med.* **49**, 1-4 (2008).

381 Luo, T. *et al.* Understanding the Cooperative Interaction between Myosin II and Actin Cross-Linkers Mediated by Actin Filaments during Mechanosensation. *Biophys. J.* **102**, 238-247 (2012).

382 Lusche, D. F. *et al.* The IplA Ca2+ channel of *Dictyostelium discoideum* is necessary for chemotaxis mediated through Ca2+, but not through cAMP, and has a fundamental role in natural aggregation. *J. Cell Sci.* **125**, 1770-1783 (2012).

383 Lusche, D. F., Wessels, D. & Soll, D. R. The effects of extracellular calcium on motility, pseudopod and uropod formation, chemotaxis, and the cortical localization of myosin II in *Dictyostelium discoideum*. *Cell Motil. Cytoskeleton* **66**, 567-587 (2009).

384 Machesky, L. M. & Insall, R. H. Scar1 and the related Wiskott Aldrich syndrome protein, WASP, regulate the actin cytoskeleton through the Arp2/3 complex. *Current biology : CB* **8**, 1347-1356 (1998).

385 Maciver, S. & Hussey, P. The ADF/cofilin family: actin-remodeling proteins. *Genome Biol.* **3**, 3007.3001-3007.3012 (2002).

386 MacWilliams, H. K. & Bonner, J. T. The prestalk-prespore pattern in cellular slime molds. *Differentiation* **14**, 1-22 (1979).

387 Maechler, M. *diptest: Hartigan's dip test statistic for unimodality - corrected code*, <http://CRAN.R-project.org/package=diptest> (2012).

388 Mahadeo, D. C. & Parent, C. A. Signal Relay During the Life Cycle of *Dictyostelium* in *Curr. Top. Dev. Biol.* Vol. Volume 73 (ed P. Schatten Gerald) 115-140 (Academic Press, 2006).

389 Mahajan, V. N. *Aberration Theory Made Simple, 2nd Edition*. (SPIE Press, 2011).

390 Manahan, C. L., Iglesias, P. A., Long, Y. & Devreotes, P. N. Chemoattractant signaling in *Dictyostelium discoideum*. *Annu. Rev. Cell Dev. Biol.* **20**, 223-253 (2004).

391 Mann, H. B. & Whitney, D. R. On a test of whether one of two random variables is stochastically larger than the other. *Annals of Mathematical Statistics* **18**, 50-60 (1947).

392 Mann, S. K. & Firtel, R. A. cAMP-dependent protein kinase differentially regulates prestalk and prespore differentiation during *Dictyostelium* development. *Development* **119**, 135-146 (1993).

393 Mann, S. K. O. & Firtel, R. A. A developmentally regulated, putative serine/threonine protein kinase is essential for development in *Dictyostelium*. *Mech. Dev.* **35**, 89-101 (1991).

394 Manstein, D. J., Titus, M. A., De, L. & Spudich, J. A. Gene replacement in *Dictyostelium*: generation of myosin null mutants. **8**, 923-932 (1989).

395 Mantzouranis, L., Bagattini, R. & Souza, G. KeaA, a *Dictyostelium* kelch-domain protein that regulates the response to stress and development. *BMC Dev. Biol.* **10**, 79 (2010).

396 Margolskee, J. P., Froshauer, S., Skrinska, R. & Lodish, H. F. The effects of cell density and starvation on early developmental events in *Dictyostelium discoideum*. *Dev. Biol.* **74**, 409-421 (1980).

397 Maria, O. M., Zeitouni, A., Gologan, O. & Tran, S. D. Matrigel Improves Functional Properties of Primary Human Salivary Gland Cells. *Tissue Engineering Part A* **17**, 1229-1238 (2010).

398 Marks, D., Carney, P. S. & Boppart, S. A. Adaptive spectral apodization for sidelobe reduction in optical coherence tomography images. **9**, 1281-1287 (2004).

399 Marks, D. L., Ralston, T. S. & Boppart, S. A. Data Analysis and Signal Postprocessing for Optical Coherence Tomography in *Optical Coherence Tomography: Technology and Applications* (eds Wolfgang Drexler & James G. Fujimoto) Ch. 13, 405-426 (Springer-Verlag, 2008).

400 Marquardt, D. An algorithm for least-squares estimation of nonlinear parameters. *Journal of the Society for Industrial and Applied Mathematics* **11**, 431-441 (1963).

401 Marshall, R. J. & Marshall, R. W. Quantification of skin surface texture by macrophotography and computer aided scanning densitometry. *J. Vis. Commun. Med.* **6**, 98-103 (1983).

402 Mato, J. M., Losada, A., Nanjundiah, V. & Konijn, T. M. Signal input for a chemotactic response in the cellular slime mold *Dictyostelium discoideum*. *PNAS* **72**, 4991-4993 (1975).

403 Matsuoka, S., Miyanaga, Y., Yanagida, T. & Ueda, M. Single-Molecule Imaging of Stochastic SIgnaling Events in Living Cells in *Single-Molecule Techniques: A Laboratory*

Manual (eds Paul R. Selvin & Taekjip Ha) Ch. 11, 239-251 (Cold Spring Harbor Laboratory Press, New York, USA, 2008).

404 Mattei, S. *et al.* Dd-Alix, a conserved endosome-associated protein, controls *Dictyostelium* development. *Dev. Biol.* **279**, 99-113 (2005).

405 Mattheyses, A. L., Simon, S. M. & Rappoport, J. Z. Imaging with total internal reflection fluorescence microscopy for the cell biologist. *J. Cell Sci.* **123**, 3621-3628 (2010).

406 Mattila, P. K. & Lappalainen, P. Filopodia: molecular architecture and cellular functions. *Nat Rev Mol Cell Biol* **9**, 446-454 (2008).

407 Matz, M. V. *et al.* Fluorescent proteins from nonbioluminescent Anthozoa species. *Nat. Biotechnol.* **17**, 969-973 (1999).

408 Mayer, M. A. *et al.* Wavelet denoising of multiframe optical coherence tomography data. *Biomed. Opt. Express* **3**, 572-589 (2012).

409 McCaffrey, L. M. & Macara, I. G. Widely Conserved Signaling Pathways in the Establishment of Cell Polarity. *Cold Spring Harbor Perspectives in Biology* **1** (2009).

410 McCann, C. P., Kriebel, P. W., Parent, C. A. & Losert, W. Cell speed, persistence and information transmission during signal relay and collective migration. *J. Cell Sci.* **123**, 1724-1731 (2010).

411 Meier, J. K. H. *et al.* Specific differences in migratory function of myofibroblasts isolated from Crohn's disease fistulae and strictures. *Inflamm. Bowel Dis.* **17**, 202-212 (2011).

412 Meijering, E. *TransformJ: A Java Package for Geometrical Image Transformation*, <http://www.imagescience.org/meijering/software/transformj/> (1996-2011).

413 Meijering, E. H., Niessen, W. J. & Viergever, M. A. Quantitative evaluation of convolution-based methods for medical image interpolation. *Med. Image Anal.* **5**, 111-126 (2001).

414 Meili, R., Alonso-Latorre, B., del Álamo, J. C., Firtel, R. A. & Lasheras, J. C. Myosin II Is Essential for the Spatiotemporal Organization of Traction Forces during Cell Motility. *Mol. Biol. Cell* **21**, 405-417 (2010).

415 Meinhardt, H. Orientation of chemotactic cells and growth cones: models and mechanisms. *J. Cell Sci.* **112**, 2867-2874 (1999).

416 Mendoza, M. C. & Firtel, R. A. Assaying Chemotaxis of *Dictyostelium* Cells in *Dictyostelium discoideum Protocols* (eds Ludwig Eichinger & Francisco Rivero) (Humana Press, Inc., 2006).

417 Mertz, J. *Introduction to optical microscopy*. (Roberts, 2010).

418 Metz, C. T. *Digitally Reconstructed Radiographs* Master's thesis, Utrecht University, (2005).

419 Mieszawska, A. & Kaplan, D. Smart biomaterials - regulating cell behavior through signaling molecules. *BMC Biol.* **8**, 59 (2010).

420 Millius, A., Watanabe, N. & Weiner, O. D. Diffusion, capture and recycling of SCAR/WAVE and Arp2/3 complexes observed in cells by single-molecule imaging. *J. Cell Sci.* **125**, 1165-1176 (2012).

421 Min, W., Freudiger, C. W., Lu, S. & Xie, X. S. Coherent Nonlinear Optical Imaging: Beyond Fluorescence Microscopy. *Annu. Rev. Phys. Chem.* **62**, 507-530 (2011).

422 Mitchel, J. A. & Hoffman-Kim, D. Cellular Scale Anisotropic Topography Guides Schwann Cell Motility. *PLoS ONE* **6**, e24316 (2011).

423 Miura, K. & Siegert, F. Light affects cAMP signaling and cell movement activity in *Dictyostelium discoideum*. *PNAS* **97**, 2111-2116 (2000).

424 Miura, S. *et al.* Functional Conservation for Lipid Storage Droplet Association among Perilipin, ADRP, and TIP47 (PAT)-related Proteins in Mammals, Drosophila, and *Dictyostelium*. *J. Biol. Chem.* **277**, 32253-32257 (2002).

425 Mondal, S. *et al.* Regulation of the Actin Cytoskeleton by an Interaction of IQGAP Related Protein GAPA with Filamin and Cortexillin I. *PLoS ONE* **5**, e15440 (2010).

426 Mondia, J. P., Adams, D. S., Orendorff, R. D., Levin, M. & Omenetto, F. G. Patterned femtosecond-laser ablation of Xenopus laevis melanocytes for studies of cell migration, wound repair, and developmental processes. *Biomed. Opt. Express* **2**, 2383-2391 (2011).

427 Moore, D. T. Telecentric Lens. United States patent (1973).

428 Moores, S. L., Sabry, J. H. & Spudich, J. A. Myosin dynamics in live *Dictyostelium* cells. *PNAS* **93**, 443-446 (1996).

429 Moran, C. M. *et al.* A Comparison of the Imaging Performance of High Resolution Ultrasound Scanners for Preclinical Imaging. *Ultrasound in Medicine & Biology* **37**, 493-501 (2011).

430 Mori, Y., Jilkine, A. & Edelstein-Keshet, L. Wave-Pinning and Cell Polarity from a Bistable Reaction-Diffusion System. *Biophys. J.* **94**, 3684-3697 (2008).

431 Morris, H. R., Taylor, G. W., Masento, M. S., Jermyn, K. A. & Kay, R. R. Chemical structure of the morphogen differentiation inducing factor from *Dictyostelium discoideum*. *Nature* **328**, 811-814 (1987).

432 Morton, P. E. & Parsons, M. Dissecting cell adhesion architecture using advanced imaging techniques. *Cell Adhesion & Migration* **5**, 351-359 (2011).

433 Murphy-Ullrich, J. E. The de-adhesive activity of matricellular proteins: is intermediate cell adhesion an adaptive state? *The Journal of Clinical Investigation* **107**, 785-790 (2001).

434 Murphy, D. B. *Fundamentals of light microscopy and electronic imaging*. (Wiley-Liss, 2001).

435 Murphy, M. B. & Egelhoff, T. T. Biochemical characterization of a *Dictyostelium* myosin II heavy-chain phosphatase that promotes filament assembly. *Eur. J. Biochem.* **264**, 582-590 (1999).

436 Muzzey, D. & van Oudenaarden, A. Quantitative Time-Lapse Fluorescence Microscopy in Single Cells. *Annu. Rev. Cell Dev. Biol.* **25**, 301-327 (2009).

437 Myshkin, N. K., Grigoriev, A. Y., Chizhik, S. A., Choi, K. Y. & Petrokovets, M. I. Surface roughness and texture analysis in microscale. *Wear* **254**, 1001-1009 (2003).

438 Nachmias, V. T., Fukui, Y. & Spudich, J. A. Chemoattractant-elicited translocation of myosin in motile *Dictyostelium*. *Cell Motil. Cytoskeleton* **13**, 158-169 (1989).

439 Nagasaki, A., Itoh, G., Yumura, S. & Uyeda, T. Q. P. Novel Myosin Heavy Chain Kinase Involved in Disassembly of Myosin II Filaments and Efficient Cleavage in Mitotic *Dictyostelium* Cells. *Mol. Biol. Cell* **13**, 4333-4342 (2002).

440 Nation, J. L. A new method using hexamethyldisilazane for preparation of soft insect tissues for scanning electron microscopy. *Stain Technol.* **58**, 347-351 (1983).

441 NationalInstruments. *Announcing 64-bit LabVIEW*, <http://zone.ni.com/devzone/cda/tut/p/id/10184> (Jan 13, 2011).

442 NationalInstruments. *How Much Memory can LabVIEW 32-bit or 64-bit Use?*, <http://digital.ni.com/public.nsf/allkb/AC9AD7E5FD3769C086256B41007685FA> (2011).

443 Nayar, V. T., Weiland, J. D., Nelson, C. S. & Hodge, A. M. Elastic and viscoelastic characterization of agar. *Journal of the Mechanical Behavior of Biomedical Materials* **7**, 60-68 (2012).

444 Neilson, M. P. *et al.* Chemotaxis: A Feedback-Based Computational Model Robustly Predicts Multiple Aspects of Real Cell Behaviour. *PLoS Biol.* **9**, e1000618 (2011).

445 Nelson, R. D., Quie, P. G. & Simmons, R. L. Chemotaxis Under Agarose: A New and Simple Method for Measuring Chemotaxis and Spontaneous Migration of Human Polymorphonuclear Leukocytes and Monocytes. *The Journal of Immunology* **115**, 1650-1656 (1975).

446 Neujahr, R. *et al.* Three-dimensional Patterns and Redistribution of Myosin II and Actin in Mitotic *Dictyostelium* Cells. *The Journal of Cell Biology* **139**, 1793-1804 (1997).

447 Nicol, A., Rappel, W., Levine, H. & Loomis, W. F. Cell-sorting in aggregates of *Dictyostelium discoideum*. *J. Cell Sci.* **112**, 3923-3929 (1999).

448 Niewöhner, J., Weber, I., Maniak, M., Müller-Taubenberger, A. & Gerisch, G. Talin-Null Cells of *Dictyostelium* Are Strongly Defective in Adhesion to Particle and Substrate Surfaces and Slightly Impaired in Cytokinesis. *The Journal of Cell Biology* **138**, 349-361 (1997).

449 Nikolaeva, I., Huber, R. & O'Day, D. EGF-like peptide of *Dictyostelium discoideum* is not a chemoattractant but it does restore folate-mediated chemotaxis in the presence of signal transduction inhibitors. *Peptides* **34**, 145-149 (2012).

450 Noegel, A. A. & Schleicher, M. The actin cytoskeleton of *Dictyostelium*: a story told by mutants. *J. Cell Sci.* **113**, 759-766 (2000).

451 Normand, V., Lootens, D. L., Amici, E., Plucknett, K. P. & Aymard, P. New Insight into Agarose Gel Mechanical Properties. *Biomacromolecules* **1**, 730-738 (2000).

452 Ntziachristos, V. Fluorescence Molecular Imaging. *Annu. Rev. Biomed. Eng.* **8**, 1-33 (2006).

453 Okano, T., Yamada, N., Okuhara, M., Sakai, H. & Sakurai, Y. Mechanism of cell detachment from temperature-modulated, hydrophilic-hydrophobic polymer surfaces. *Biomaterials* **16**, 297-303 (1995).

454 Ostrow, B. D., Chen, P. & Chisholm, R. L. Expression of a myosin regulatory light chain phosphorylation site mutant complements the cytokinesis and developmental defects of *Dictyostelium* RMLC null cells. *The Journal of Cell Biology* **127**, 1945-1955 (1994).

455 Otsu, N. A threshold selection method from gray-level histograms. *IEEE Trans. Syst. Man Cybern.* **9**, 62-66 (1979).

456 Ou, L. *et al.* Intracardiac injection of matrigel induces stem cell recruitment and improves cardiac functions in a rat myocardial infarction model. *J. Cell. Mol. Med.* **15**, 1310-1318 (2011).

457 P., M., G., A., J., A. & JA., M. Par-1 controls myosin-II activity through myosin phosphatase to regulate border cell migration. *Current biology : CB* **22**, 363-372 (2012).

458 Padilla-Parra, S. & Tramier, M. FRET microscopy in the living cell: Different approaches, strengths and weaknesses. *Bioessays* **34**, 369-376 (2012).

459 Palsson, E. A 3-D model used to explore how cell adhesion and stiffness affect cell sorting and movement in multicellular systems. *J. Theor. Biol.* **254**, 1-13 (2008).

460 Pálsson, E. *et al.* Selection for spiral waves in the social amoebae *Dictyostelium*. *PNAS* **94**, 13719-13723 (1997).

461 Pampaloni, F., Reynaud, E. G. & Stelzer, E. H. K. The third dimension bridges the gap between cell culture and live tissue. *Nat Rev Mol Cell Biol* **8**, 839-845 (2007).

462 Pankov, R. *et al.* A Rac switch regulates random versus directionally persistent cell migration. *The Journal of Cell Biology* **170**, 793-802 (2005).

463 Parent, C. A. *Dictyostelium* Cell Dynamics in *Current Protocols in Cell Biology* (John Wiley & Sons, Inc., 2001).

464 Parent, C. A., Blacklock, B. J., Froehlich, W. M., Murphy, D. B. & Devreotes, P. N. G Protein Signaling Events Are Activated at the Leading Edge of Chemotactic Cells. *Cell* **95**, 81-91 (1998).

465 Parent, C. A. & Devreotes, P. N. A Cell's Sense of Direction. *Science* **284**, 765-770 (1999).

466 Parent, C. A. & Devreotes, P. N. Molecular Genetics of Signal Transduction in *Dictyostelium*. *Annu. Rev. Biochem.* **65**, 411-440 (1996).

467 Park, J. *et al.* A dual-modality optical coherence tomography and fluorescence lifetime imaging microscopy system for simultaneous morphological and biochemical tissue characterization. *Biomed. Opt. Express* **1**, 186-200 (2010).

468 Park, J., Kim, H. N., Kim, D. H., Levchenko, A. & Suh, K. Y. Quantitative Analysis of the Combined Effect of Substrate Rigidity and Topographic Guidance on Cell Morphology. *NanoBioscience, IEEE Transactions on* **11**, 28-36 (2012).

469 Park, K. C. *et al.* Rac regulation of chemotaxis and morphogenesis in *Dictyostelium*. *EMBO J.* **23**, 4177-4189 (2004).

470 Parkinson, K. *et al.* Regulation of Rap1 activity is required for differential adhesion, cell-type patterning and morphogenesis in *Dictyostelium*. *J. Cell Sci.* **122**, 335-344 (2009).

471 Pattison, D. & Davies, M. Actions of ultraviolet light on cellular structures in *Cancer: Cell Structures, Carcinogens and Genomic Instability* Vol. 96 *Experientia Supplementum* Ch. 6, 131-157 (Birkhäuser Basel, 2006).

472 Paul, A. S. & Pollard, T. D. Energetic Requirements for Processive Elongation of Actin Filaments by FH1FH2-formins. *J. Biol. Chem.* **284**, 12533-12540 (2009).

473 Pawley, J. *Handbook of Biological Confocal Microscopy*. (Springer, 2006).

474 Peracino, B. *et al.* G Protein β Subunit–null Mutants Are Impaired in Phagocytosis and Chemotaxis Due to Inappropriate Regulation of the Actin Cytoskeleton. *The Journal of Cell Biology* **141**, 1529-1537 (1998).

475 PerkinElmer. *4.1. How are angle, bearing and elevation calculated?*, <http://cellularimaging.perkinelmer.com/helpdesk/index.php?pg=kb.page&id=269 > (2011).

476 PerkinElmer. Volocity User Guide. 1-540 (2011).

477 Petersen, O. W., Rønnov-Jessen, L., Howlett, A. R. & Bissell, M. J. Interaction with basement membrane serves to rapidly distinguish growth and differentiation pattern of normal and malignant human breast epithelial cells. *PNAS* **89**, 9064-9068 (1992).

478 Petrie, R. J., Doyle, A. D. & Yamada, K. M. Random versus directionally persistent cell migration. *Nat. Rev. Mol. Cell Biol.* **10**, 538-549 (2009).

479 Petrie, R. J., Gavara, N., Chadwick, R. S. & Yamada, K. M. Nonpolarized signaling reveals two distinct modes of 3D cell migration. *The Journal of Cell Biology* **197**, 439-455 (2012).

480 Petrou, M. & Petrou, C. Image Segmentation and Edge Detection in *Image Processing: The Fundamentals* Ch. 6, 527-668 (John Wiley & Sons, 2010).

481 Petrou, M. & Sevilla, P. G. *Image processing: dealing with texture.* (John Wiley & Sons Inc., 2006).

482 Peyton, S., Ghajar, C., Khatiwala, C. & Putnam, A. The emergence of ECM mechanics and cytoskeletal tension as important regulators of cell function. *Cell Biochemistry and Biophysics* **47**, 300-320 (2007).

483 Peyton, S. R. *et al.* Marrow-Derived stem cell motility in 3D synthetic scaffold is governed by geometry along with adhesivity and stiffness. *Biotechnol. Bioeng.* **108**, 1181-1193 (2011).

484 Pezacki, J. P. *et al.* Chemical contrast for imaging living systems: molecular vibrations drive CARS microscopy. *Nat. Chem. Biol.* **7**, 137-145 (2011).

485 Pharr, M. & Humphreys, G. *Physically Based Rendering: From Theory to Implementation.* (Elsevier Science, 2004).

486 Pollard, T. D. & Borisy, G. G. Cellular Motility Driven by Assembly and Disassembly of Actin Filaments. *Cell* **112**, 453-465 (2003).

487 Pollitt, A. Y. & Insall, R. H. WASP and SCAR/WAVE proteins: the drivers of actin assembly. *J. Cell Sci.* **122**, 2575-2578 (2009).

488 Poloz, Y., Catalano, A. & O'Day, D. H. Bestatin Inhibits Cell Growth, Cell Division, and Spore Cell Differentiation in *Dictyostelium discoideum*. *Eukaryot. Cell* **11**, 545-557 (2012).

489 Poloz, Y. & H. O'Day, D. Colchicine affects cell motility, pattern formation and stalk cell differentiation in *Dictyostelium* by altering calcium signaling. *Differentiation* **83**, 185-199 (2012).

490 Polte, T. R., Eichler, G. S., Wang, N. & Ingber, D. E. Extracellular matrix controls myosin light chain phosphorylation and cell contractility through modulation of cell shape and cytoskeletal prestress. *American Journal of Physiology - Cell Physiology* **286**, C518-C528 (2004).

491 Ponche, A., Bigerelle, M. & Anselme, K. Relative influence of surface topography and surface chemistry on cell response to bone implant materials. Part 1: Physico-chemical effects. *Proceedings of the Institution of Mechanical Engineers, Part H: Journal of Engineering in Medicine* **224**, 1471-1486 (2010).

492 Ponte, E., Bracco, E., Faix, J. & Bozzaro, S. Detection of subtle phenotypes: The case of the cell adhesion molecule csA in *Dictyostelium*. *PNAS* **95**, 9360-9365 (1998).

493 Ponte, E., Rivero, F., Fechheimer, M., Noegel, A. & Bozzaro, S. Severe developmental defects in *Dictyostelium* null mutants for actin-binding proteins. *Mech. Dev.* **91**, 153-161 (2000).

494 Popescu, D. P., Hewko, M. D. & Sowa, M. G. Speckle noise attenuation in optical coherence tomography by compounding images acquired at different positions of the sample. *Opt Commun* **269**, 247-251 (2007).

495 Postma, M., Bosgraaf, L., Loovers, H. M. & Van Haastert, P. J. M. Chemotaxis: signalling modules join hands at front and tail. *EMBO Rep.* **5**, 35-40 (2004).

496 Postma, M. & Haastert, P. J. M. v. Mathematics of Experimentally Generated Chemoattractant Gradients in *Chemotaxis Methods and Protocols* (eds Tian Jin & Dale Hereld) Ch. 31, (Humana Press, 2009).

497 Postma, M. *et al.* Uniform cAMP Stimulation of *Dictyostelium* Cells Induces Localized Patches of Signal Transduction and Pseudopodia. *Mol. Biol. Cell* **14**, 5019-5027 (2003).

498 Potsaid, B. *et al.* Ultrahigh speed 1050nm swept source / Fourier domain OCT retinal and anterior segment imaging at 100,000 to 400,000 axial scans per second. *Opt. Express* **18**, 20029-20048 (2010).

499 Potsaid, B. *et al.* Ultrahigh speed Spectral / Fourierdomain OCT ophthalmic imaging at70,000 to 312,500 axial scans per second. *Opt. Express* **16**, 15149-15169 (2008).

500 Považay, B. *et al.* Three-dimensional optical coherence tomography at 1050nm versus 800nm in retinal pathologies: enhanced performance and choroidal penetration in cataract patients. *J. Biomed. Opt.* **12**, 041211 (2007).

501 Považay, B. *et al.* Impact of enhanced resolution, speed and penetration on three-dimensional retinal optical coherence tomography. *Opt. Express* **17**, 4134-4150 (2009).

502 Preza, C., Snyder, D. L. & Conchello, J.-A. Theoretical development and experimental evaluation of imaging models for differential-interference-contrast microscopy. *J. Opt. Soc. Am. A* **16**, 2185-2199 (1999).

503 Price, H. P., MacLean, L., Marrison, J., O'Toole, P. J. & Smith, D. F. Validation of a new method for immobilising kinetoplastid parasites for live cell imaging. *Mol. Biochem. Parasitol.* **169**, 66-69 (2010).

504 Provenzano, P. P., Eliceiri, K. W. & Keely, P. J. Shining new light on 3D cell motility and the metastatic process. *Trends Cell Biol.* **19**, 638-648 (2009).

505 R_Development_Core_Team. *R: A language and environment for statistical computing*, <http://www.R-project.org/> (2012).

506 Radmacher, M. *Diploma Thesis*, Technische Universitat Munchen, (1991).

507 Ràfols, I., Sawada, Y., Amagai, A., Maeda, Y. & MacWilliams, H. K. Cell type proportioning in *Dictyostelium* slugs: lack of regulation within a 2.5-fold tolerance range. *Differentiation* **67**, 107-116 (2001).

508 Rai, V. & Dey, N. The Basics of Confocal Microscopy in *Laser Scanning, Theory and Applications* (ed Chau-Chang Wang) Ch. 5, 75-96 (InTech, 2011).

509 Rai, V. & Egelhoff, T. T. Role of B Regulatory Subunits of Protein Phosphatase Type 2A in Myosin II Assembly Control in *Dictyostelium discoideum*. *Eukaryot. Cell* **10**, 604-610 (2011).

510 Rajnicek, A. M., Foubister, L. E. & McCaig, C. D. Alignment of corneal and lens epithelial cells by co-operative effects of substratum topography and DC electric fields. *Biomaterials* **29**, 2082-2095 (2008).

511 Ralston, T. S., Marks, D. L., Carney, P. S. & Boppart, S. A. Real-time interferometric synthetic aperture microscopy. *Opt. Express* **16**, 2555-2569 (2008).

512 Ranganathan, A. The Levenberg-Marquardt Algorithm. *Tutorial on LM Algorithm* (2004).

513 Rangarajan, R. & Zaman, M. H. Modeling cell migration in 3D: Status and challenges. *Cell Adhesion & Migration* **2**, 106-109 (2008).

514 Ren, X. D. *et al.* Focal adhesion kinase suppresses Rho activity to promote focal adhesion turnover. *J. Cell Sci.* **113**, 3673-3678 (2000).

515 Renn, D. W. Agar and agarose: indispensable partners in biotechnology. *Industrial & Engineering Chemistry Product Research and Development* **23**, 17-21 (1984).

516 Řezníčková, A., Kolská, Z., Hnatowicz, V., Stopka, P. & Švorčík, V. Comparison of glow argon plasma-induced surface changes of thermoplastic polymers. *Nuclear Instruments and Methods in Physics Research Section B: Beam Interactions with Materials and Atoms* **269**, 83-88 (2011).

517 Rhee, S. Fibroblasts in three dimensional matrices: cell migration and matrix remodeling. *Experimental & Molecular Medicine* **41**, 858–865 (2009).

518 Ribeiro, C., Petit, V. & Affolter, M. Signaling systems, guided cell migration, and organogenesis: insights from genetic studies in Drosophila. *Dev. Biol.* **260**, 1-8 (2003).

519 Rico, M. & Egelhoff, T. T. Myosin heavy chain kinase B participates in the regulation of myosin assembly into the cytoskeleton. *J. Cell. Biochem.* **88**, 521-532 (2003).

520 Ridley, A. Blebbing: motility research moves in a new direction. *Nat Rev Mol Cell Biol* **10**, 164-164 (2009).

521 Rietdorf, J., Siegert, F. & Weijer, C. J. Analysis of Optical Density Wave Propagation and Cell Movement during Mound Formation in *Dictyostelium discoideum*. *Dev. Biol.* **177**, 427-438 (1996).

522 Rietdorf, J., Siegert, F. & Weijer, C. J. Induction of Optical Density Waves and Chemotactic Cell Movement in *Dictyostelium discoideum* by Microinjection of cAMP Pulses. *Dev. Biol.* **204**, 525-536 (1998).

523 Rifkin, J. L. Folate reception by vegetative *Dictyostelium discoideum* amoebae: Distribution of receptors and trafficking of ligand. *Cell Motil. Cytoskeleton* **48**, 121-129 (2001).

524 Rivero, F. *et al.* A comparative sequence analysis reveals a common GBD/FH3-FH1-FH2-DAD architecture in formins from *Dictyostelium*, fungi and metazoa. *BMC Genomics* **6**, 28 (2005).

525 Roelofs, J., Meima, M., Schaap, P. & Van Haastert, P. J. M. The *Dictyostelium* homologue of mammalian soluble adenylyl cyclase encodes a guanylyl cyclase. *EMBO J.* **20**, 4341-4348 (2001).

526 Rørth, P. Collective Cell Migration. *Annu. Rev. Cell Dev. Biol.* **25**, 407-429 (2009).

527 Roussos, E. T., Condeelis, J. S. & Patsialou, A. Chemotaxis in cancer. *Nat. Rev. Cancer* **11**, 573-587 (2011).

528 Rowekamp, W. & Firtel, R. A. Isolation of developmentally regulated genes from *Dictyostelium*. *Dev. Biol.* **79**, 409-418 (1980).

529 Rubart, M. Two-Photon Microscopy of Cells and Tissue. *Circ. Res.* **95**, 1154-1166 (2004).

530 Ruppel, K. M., Uyeda, T. Q. & Spudich, J. A. Role of highly conserved lysine 130 of myosin motor domain. In vivo and in vitro characterization of site specifically mutated myosin. *J. Biol. Chem.* **269**, 18773-18780 (1994).

531 Russ, M., Croft, D., Ali, O., Martinez, R. & Steimle, P. A. Myosin heavy-chain kinase A from *Dictyostelium* possesses a novel actin-binding domain that cross-links actin filaments. *Biochem. J.* **395**, 373-383 (2006).

532 Sadik, C. D. & Luster, A. D. Lipid-cytokine-chemokine cascades orchestrate leukocyte recruitment in inflammation. *J. Leukoc. Biol.* **91**, 207-215 (2012).

533 Sahai, E. & Marshall, C. J. Differing modes of tumour cell invasion have distinct requirements for Rho/ROCK signalling and extracellular proteolysis. *Nat Cell Biol* **5**, 711-719 (2003).

534 Saka, S. & Rizzoli, S. O. Super-resolution imaging prompts re-thinking of cell biology mechanisms. *Bioessays* **34**, 386-395 (2012).

535 Sakata, L. M., DeLeon-Ortega, J., Sakata, V. & Girkin, C. A. Optical coherence tomography of the retina and optic nerve – a review. *Clinical & Experimental Ophthalmology* **37**, 90-99 (2009).

536 San Martín, A. *et al.* Dual Regulation of Cofilin Activity by LIM Kinase and Slingshot-1L Phosphatase Controls Platelet-Derived Growth Factor–Induced Migration of Human Aortic Smooth Muscle Cells. *Circ. Res.* **102**, 432-438 (2008).

537 Sanz-Moreno, V. & Marshall, C. J. The plasticity of cytoskeletal dynamics underlying neoplastic cell migration. *Curr. Opin. Cell Biol.* **22**, 690-696 (2010).

538 Saran, S. *et al.* cAMP signaling in *Dictyostelium*. *J. Muscle Res. Cell Motil.* **23**, 793-802 (2002).

539 Sasaki, A. T., Chun, C., Takeda, K. & Firtel, R. A. Localized Ras signaling at the leading edge regulates PI3K, cell polarity, and directional cell movement. *The Journal of Cell Biology* **167**, 505-518 (2004).

540 Sasaki, A. T. & Firtel, R. A. Spatiotemporal Regulation of Ras-GTPases During Chemotaxis in *Chemotaxis Methods and Protocols* Vol. 571 *Methods in Molecular Biology* (eds Tian Jin & Dale Hereld) 333-348 (Humana Press, 2009).

541 Sasaki, A. T. *et al.* G protein–independent Ras/PI3K/F-actin circuit regulates basic cell motility. *The Journal of Cell Biology* **178**, 185-191 (2007).

542 Sawai, S., Thomason, P. A. & Cox, E. C. An autoregulatory circuit for long-range self-organization in *Dictyostelium* cell populations. *Nature* **433**, 323-326 (2005).

543 Saxer, G., Brock, D., Queller, D. & Strassmann, J. Cheating does not explain selective differences at high and low relatedness in a social amoeba. *BMC Evol. Biol.* **10**, 76 (2010).

544 Schaap, P. Evolutionary crossroads in developmental biology: *Dictyostelium discoideum*. *Development* **138**, 387-396 (2011).

545 Schaloske, R. *et al.* Ca2+ regulation in the absence of the iplA gene product in *Dictyostelium discoideum*. *BMC Cell Biol.* **6**, 13 (2005).

546 Scherer, A. *et al.* Ca2+ chemotaxis in *Dictyostelium discoideum*. *J. Cell Sci.* **123**, 3756-3767 (2010).

547 Schermelleh, L., Heintzmann, R. & Leonhardt, H. A guide to super-resolution fluorescence microscopy. *The Journal of Cell Biology* **190**, 165-175 (2010).

548 Schindl, M. *et al.* Cell-substrate interactions and locomotion of *Dictyostelium* wild-type and mutants defective in three cytoskeletal proteins: a study using quantitative reflection interference contrast microscopy. *Biophys. J.* **68**, 1177-1190 (1995).

549 Schmitt, J. M. Optical coherence tomography (OCT): a review. *Selected Topics in Quantum Electronics, IEEE Journal of* **5**, 1205-1215 (1999).

550 Schmitt, J. M., Xiang, S. H. & Yung, K. M. Speckle in Optical Coherence Tomography. *J. Biomed. Opt.* **4**, 95-105 (1999).

551 Schneider, I. C. & Haugh, J. M. Mechanisms of Gradient Sensing and Chemotaxis: Conserved Pathways, Diverse Regulation. *Cell Cycle* **5**, 1130-1134 (2006).

552 Schroeder, T. Imaging stem-cell-driven regeneration in mammals. *Nature* **453**, 345-351 (2008).

553 Seelamantula, C. S., Villiger, M. L., Leitgeb, R. A. & Unser, M. Exact and efficient signal reconstruction in frequency-domain optical-coherence tomography. *J. Opt. Soc. Am. A* **25**, 1762-1771 (2008).

554 Segers, V. F. M. & Lee, R. T. Biomaterials to Enhance Stem Cell Function in the Heart. *Circ. Res.* **109**, 910-922 (2011).

555 Semino, C. E., Merok, J. R., Crane, G. G., Panagiotakos, G. & Zhang, S. Functional differentiation of hepatocyte-like spheroid structures from putative liver progenitor cells in three-dimensional peptide scaffolds. *Differentiation* **71**, 262-270 (2003).

556 Semmler, W. & Schwaiger, M. *Molecular Imaging*. (Springer, 2008).

557 SeniorTechnicalSupportSpecialist. (ed Sara Rey) (PerkinElmer Coventry, 2011).

558 Sepich, D. S., Calmelet, C., Kiskowski, M. & Solnica-Krezel, L. Initiation of convergence and extension movements of lateral mesoderm during zebrafish gastrulation. *Dev. Dyn.* **234**, 279-292 (2005).

559 Sergeev, A. *et al.* In vivo endoscopic OCT imaging of precancer and cancer states of human mucosa. *Opt. Express* **1**, 432-440 (1997).

560 Servant, G. *et al.* Polarization of Chemoattractant Receptor Signaling During Neutrophil Chemotaxis. *Science* **287**, 1037-1040 (2000).

561 Seth, A., Otomo, C. & Rosen, M. K. Autoinhibition regulates cellular localization and actin assembly activity of the diaphanous-related formins FRLα and mDia1. *The Journal of Cell Biology* **174**, 701-713 (2006).

562 Shannon, K. B. IQGAP Family Members in Yeast, *Dictyostelium*, and Mammalian Cells. *International Journal of Cell Biology* **2012**, Article ID 894817 (2012).

563 Shebanova, O. & Hammer, D. A. Biochemical and mechanical extracellular matrix properties dictate mammary epithelial cell motility and assembly. *Biotechnol. J.* **7**, 397-408 (2012).

564 Shelden, E. & Knecht, D. A. Mutants lacking myosin II cannot resist forces generated during multicellular morphogenesis. *J. Cell Sci.* **108**, 1105-1115 (1995).

565 Sheppard, K. (ed Sara Rey) 1 (Chicago, 2010).

566 Shih, W. & Yamada, S. Myosin IIA Dependent Retrograde Flow Drives 3D Cell Migration. *Biophys. J.* **98**, L29-L31 (2010).

567 Shimada, Y. *et al.* Validation of swept-source optical coherence tomography (SS-OCT) for the diagnosis of occlusal caries. *J. Dent.* **38**, 655-665 (2010).

568 Shu, S., Liu, X. & Korn, E. D. Blebbistatin and blebbistatin-inactivated myosin II inhibit myosin II-independent processes in *Dictyostelium*. *Proc. Natl. Acad. Sci. U. S. A.* **102**, 1472-1477 (2005).

569 Shu, S., Liu, X., Kriebel, P. W., Daniels, M. P. & Korn, E. D. Actin cross-linking proteins cortexillin I and II are required for cAMP signaling during *Dictyostelium* chemotaxis and development. *Mol. Biol. Cell* **23**, 390-400 (2012).

570 Shu, S. *et al.* Expression of Y53A-Actin in *Dictyostelium* Disrupts the Cytoskeleton and Inhibits Intracellular and Intercellular Chemotactic Signaling. *J. Biol. Chem.* **285**, 27713-27725 (2010).

571 Siegert, F. & Weijer, C. Digital image processing of optical density wave propagation in *Dictyostelium discoideum* and analysis of the effects of caffeine and ammonia. *J. Cell Sci.* **93**, 325-335 (1989).

572 Siegert, F. & Weijer, C. J. Spiral and concentric waves organize multicellular *Dictyostelium* mounds. *Current biology : CB* **5**, 937-943 (1995).

573 Signal, S. In Brief. *The Journal of Cell Biology* **142**, 0-2 (1998).

574 Sillo, A. *et al.* Genome-wide transcriptional changes induced by phagocytosis or growth on bacteria in *Dictyostelium*. *BMC Genomics* **9**, 291 (2008).

575 Silveira, L. A., Smith, J. L., Tan, J. L. & Spudich, J. A. MLCK-A, an unconventional myosin light chain kinase from *Dictyostelium*, is activated by a cGMP-dependent pathway. *PNAS* **95**, 13000-13005 (1998).

576 Smal, I., Draegestein, K., Galjart, N., Niessen, W. & Meijering, E. Particle Filtering for Multiple Object Tracking in Dynamic Fluorescence Microscopy Images: Application to Microtubule Growth Analysis. *Medical Imaging, IEEE Transactions on* **27**, 789-804 (2008).

577 Smith, A.-S. & Sackmann, E. Progress in Mimetic Studies of Cell Adhesion and the Mechanosensing. *ChemPhysChem* **10**, 66-78 (2009).

578 Smith, E., Fisher, P. R., Grant, W. N. & Williams, K. L. Sensory Behaviour in *Dictyostelium discoideum* Slugs: Phototaxis and Thermotaxis are not Mediated by a Change in Slug Speed. *J. Cell Sci.* **54**, 329-339 (1982).

579 Soares, C. P. *et al.* 2D and 3D-Organized Cardiac Cells Shows Differences in Cellular Morphology, Adhesion Junctions, Presence of Myofibrils and Protein Expression. *PLoS ONE* **7**, e38147 (2012).

580 Soede, R. D., Insall, R. H., Devreotes, P. N. & Schaap, P. Extracellular cAMP can restore development in *Dictyostelium* cells lacking one, but not two subtypes of early cAMP receptors (cARs). Evidence for involvement of cAR1 in aggregative gene expression. *Development* **120**, 1997-2002 (1994).

581 Soll, D. R., Wessels, D., Heid, P. J. & Voss, E. Computer-Assisted Reconstruction and Motion Analysis of the Three-Dimensional Cell. *The Scientific World Journal* **3**, 827-841 (2003).

582 Soll, D. R., Wessels, D., Kuhl, S. & Lusche, D. F. How a Cell Crawls and the Role of Cortical Myosin II. *Eukaryot. Cell* **8**, 1381-1396 (2009).

583 Song, L. *et al. Dictyostelium discoideum* chemotaxis: Threshold for directed motion. *Eur. J. Cell Biol.* **85**, 981-989 (2006).

584 Spanhoff, R. *Dictyostelium Cells and Agarose Films: Atomic Force Microscopy Techniques in Physics and Biology* MPhys thesis, Universiteit Leiden, (2004).

585 Sriskanthadevan, S., Zhu, Y., Manoharan, K., Yang, C. & Siu, C.-H. The cell adhesion molecule DdCAD-1 regulates morphogenesis through differential spatiotemporal expression in *Dictyostelium discoideum*. *Development* **138**, 2487-2497 (2011).

586 Sroka, J., von Gunten, M., Dunn, G. A. & Keller, H. U. Phenotype modulation in non-adherent and adherent sublines of Walker carcinosarcoma cells: the role of cell-substratum contacts and microtubules in controlling cell shape, locomotion and cytoskeletal structure. *The International Journal of Biochemistry & Cell Biology* **34**, 882-899 (2002).

587 Steffen, A. *et al.* Filopodia Formation in the Absence of Functional WAVE- and Arp2/3-Complexes. *Mol. Biol. Cell* **17**, 2581-2591 (2006).

588 Steimle, P. A., Licate, L., Côté, G. P. & Egelhoff, T. T. Lamellipodial localization of *Dictyostelium* myosin heavy chain kinase A is mediated via F-actin binding by the coiled-coil domain. *FEBS Lett.* **516**, 58-62 (2002).

589 Stellwagen, J. & Stellwagen, N. C. Internal Structure of the Agarose Gel Matrix. *The Journal of Physical Chemistry* **99**, 4247-4251 (1995).

590 Stellwagen, N. C. Electrophoresis of DNA in agarose gels, polyacrylamide gels and in free solution. *Electrophoresis* **30**, S188-S195 (2009).

591 Stephens, M. A. EDF Statistics for Goodness of Fit and Some Comparisons. *Journal of the American Statistical Association* **69**, 730-737 (1974).

592 Sternfeld, J. & David, C. N. Oxygen Gradients Cause Pattern Orientation in *Dictyostelium* Cell Clumps. *J. Cell Sci.* **50**, 9-17 (1981).

593 Stites, J. *et al.* Phosphorylation of the *Dictyostelium* myosin II heavy chain is necessary for maintaining cellular polarity and suppressing turning during chemotaxis. *Cell Motil. Cytoskeleton* **39**, 31-51 (1998).

594 Süel, G. M., Garcia-Ojalvo, J., Liberman, L. M. & Elowitz, M. B. An excitable gene regulatory circuit induces transient cellular differentiation. *Nature* **440**, 545-550 (2006).

595 Sultana, H. *et al.* Ectopic expression of cyclase associated protein CAP restores the streaming and aggregation defects of adenylyl cyclase a deficient *Dictyostelium discoideum* cells. *BMC Dev. Biol.* **12**, 3 (2012).

596 Sun, B., Ma, H. & Firtel, R. A. *Dictyostelium* Stress-activated Protein Kinase α, a Novel Stress-activated Mitogen-activated Protein Kinase Kinase Kinase-like Kinase, Is

Important for the Proper Regulation of the Cytoskeleton. *Mol. Biol. Cell* **14**, 4526-4540 (2003).

597 Sun, C., Standish, B. & Yang, V. X. D. Optical coherence elastography: current status and future applications. *J. Biomed. Opt.* **16**, 043001 (2011).

598 Sung, Y. & Sheppard, C. J. R. Three-dimensional imaging by partially coherent light under nonparaxial condition. *J. Opt. Soc. Am. A* **28**, 554-559 (2011).

599 Swaney, K. F., Huang, C.-H. & Devreotes, P. N. Eukaryotic Chemotaxis: A Network of Signaling Pathways Controls Motility, Directional Sensing, and Polarity. *Annual Review of Biophysics* **39**, 265-289 (2010).

600 Swanson, E. A. *et al.* In vivo retinal imaging by optical coherence tomography. *Opt. Lett.* **18**, 1864-1866 (1993).

601 Swanson, J. A. & Lansing Taylor, D. Local and spatially coordinated movements in *Dictyostelium discoideum* amoebae during chemotaxis. *Cell* **28**, 225-232 (1982).

602 Syed, S. H., Larin, K. V., Dickinson, M. E. & Larina, I. V. Optical coherence tomography for high-resolution imaging of mouse development in utero. *J. Biomed. Opt.* **16**, 046004 (2011).

603 Takahashi, C., Shirai, T. & Fuji, M. Electron Microscopic Observation of Fine Morphology of Wet Agar Gel Using a Typical Hydrophilic Ionic Liquid, 1-Butyl-3-Methylimidazolium Tetrafluorob. *Advances in Technology of Materials and Materials Processing* **13**, 39-47 (2011).

604 Tako, M. & Nakamura, S. Gelation mechanism of agarose. *Carbohydr. Res.* **180**, 277-284 (1988).

605 Tan, J. L. & Spudich, J. A. Characterization and bacterial expression of the *Dictyostelium* myosin light chain kinase cDNA. Identification of an autoinhibitory domain. *J. Biol. Chem.* **266**, 16044-16049 (1991).

606 Tan, W., Vinegoni, C., Norman, J. J., Desai, T. A. & Boppart, S. A. Imaging cellular responses to mechanical stimuli within three-dimensional tissue constructs. *Microsc. Res. Tech.* **70**, 361-371 (2007).

607 Tanaka, H. *et al.* Chondrogenic differentiation of murine embryonic stem cells: Effects of culture conditions and dexamethasone. *J. Cell. Biochem.* **93**, 454-462 (2004).

608 Tang, S., Zhou, Y. & Ju, M. J. Multimodal optical imaging with multiphoton microscopy and optical coherence tomography. *Journal of Biophotonics* **5**, 396-403 (2012).

609 Tearney, G. J. *et al.* Three-Dimensional Coronary Artery Microscopy by Intracoronary Optical Frequency Domain Imaging. *JACC: Cardiovascular Imaging* **1**, 752-761 (2008).

610 Teixeira, A. I., Nealey, P. F. & Murphy, C. J. Responses of human keratocytes to micro- and nanostructured substrates. *Journal of Biomedical Materials Research Part A* **71A**, 369-376 (2004).

611 Teo, R. *et al.* Glycogen Synthase Kinase-3 Is Required for Efficient *Dictyostelium* Chemotaxis. *Mol. Biol. Cell* **21**, 2788-2796 (2010).

612 Thévenaz, P. *Turbo Reg: An ImageJ plugin for the automatic alignment of a source image or a stack to a target image.*, <http://bigwww.epfl.ch/thevenaz/turboreg/> (2011).

613 Thévenaz, P., Ruttimann, U. E. & Unser, M. A pyramid approach to subpixel registration based on intensity. *Image Processing, IEEE Transactions on* **7**, 27-41 (1998).

614 Thevenot, P., Nair, A., Dey, J., Yang, J. & Tang, L. Method to Analyze Three-Dimensional Cell Distribution and Infiltration in Degradable Scaffolds. *Tissue Eng Part C Methods* **14**, 319-331 (2008).

615 Thorlabs. *Scan Lenses for OCT System*, <http://www.thorlabs.de/NewGroupPage9.cfm?ObjectGroup_ID=2910> (1999 - 2011).

616 Tibbitt, M. W. & Anseth, K. S. Hydrogels as extracellular matrix mimics for 3D cell culture. *Biotechnol. Bioeng.* **103**, 655-663 (2009).

617 Tillinghast, H. S. & Newell, P. C. Chemotaxis towards pteridines during development of *Dictyostelium*. *J. Cell Sci.* **87**, 45-53 (1987).

618 Titus, M. A. A class VII unconventional myosin is required for phagocytosis. *Curr. Biol.* **9**, 1297-1303 (1999).

619 Tomchik, K. & Devreotes, P. Adenosine 3',5'-monophosphate waves in *Dictyostelium discoideum*: a demonstration by isotope dilution--fluorography. *Science* **212**, 443-446 (1981).

620 Torti, C. *et al.* Adaptive optics optical coherence tomography at 120,000 depth scans/s for non-invasive cellular phenotyping of the living human retina. *Opt. Express* **17**, 19382-19400 (2009).

621 Traynor, D., Tasaka, M., Takeuchi, T. & Williams, J. Aberrant pattern formation in myosin heavy chain mutants of *Dictyostelium*. *Development* **120**, 591-601 (1994).

622 Tsujioka, M., Yoshida, K. & Inouye, K. Talin B is required for force transmission in morphogenesis of *Dictyostelium*. *EMBO J.* **23**, 2216-2225 (2004).

623 Tsujioka, M. *et al.* Overlapping Functions of the Two Talin Homologues in *Dictyostelium*. *Eukaryot. Cell* **7**, 906-916 (2008).

624 Tumlinson, A. R. *et al.* Inherent homogenous media dispersion compensation in frequency domain optical coherence tomography by accurate k-sampling. *Appl. Opt.* **47**, 687-693 (2008).

625 Tyson, J. J. & Murray, J. D. Cyclic AMP waves during aggregation of *Dictyostelium* amoebae. *Development* **106**, 421-426 (1989).

626 Tzvetkova-Chevolleau, T. *et al.* The motility of normal and cancer cells in response to the combined influence of the substrate rigidity and anisotropic microstructure. *Biomaterials* **29**, 1541-1551 (2008).

627 Uchida, K. S. K. & Yumura, S. Dynamics of novel feet of *Dictyostelium* cells during migration. *J. Cell Sci.* **117**, 1443-1455 (2004).

628 Underwood, J., Greene, J. & Steimle, P. Identification of a new mechanism for targeting myosin II heavy chain phosphorylation by *Dictyostelium* myosin heavy chain kinase B. *BMC Research Notes* **3**, 56 (2010).

629 Unser, M., Aldroubi, A. & Eden, M. The L2-Polynomial Spline Pyramid. *IEEE Transactions on Pattern Analysis and Machine Intelligence* **15**, 364-379 (1993).

630 Unterhuber, A. *et al.* Broad Bandwidth Laser and Nonlinear Optical Light Sources in *Optical Coherence Tomography: Technology and Applications* (eds Wolfgang Drexler & James G. Fujimoto) 300-358 (Springer-Verlag, 2008).

631 Ura, S. *et al.* Pseudopod Growth and Evolution during Cell Movement Is Controlled through SCAR/WAVE Dephosphorylation. *Current biology : CB* **22**, 553-561 (2012).

632 Uyeda, T. Q. P., Iwadate, Y., Umeki, N., Nagasaki, A. & Yumura, S. Stretching Actin Filaments within Cells Enhances their Affinity for the Myosin II Motor Domain. *PLoS ONE* **6**, e26200 (2011).

633 Vaillant, F., Lindeman, G. & Visvader, J. Jekyll or Hyde: does Matrigel provide a more or less physiological environment in mammary repopulating assays? *Breast Cancer Res.* **13**, 108 (2011).

634 Valluru, M., Staton, C. A., Reed, M. W. R. & Brown, N. J. Transforming growth factor-beta and endoglin signalling orchestrates wound healing. *Frontiers in Physiology* **2**, 1-12 (2011).

635 van de Linde, S., Heilemann, M. & Sauer, M. Live-Cell Super-Resolution Imaging with Synthetic Fluorophores. *Annu. Rev. Phys. Chem.* **63**, 519-540 (2012).

636 Van der Meer, F. *et al.* Apoptosis- and necrosis-induced changes in light attenuation measured by optical coherence tomography. *Lasers in Medical Science* **25**, 259-267 (2010).

637 Van Egmond, W. N. *et al.* Intramolecular Activation Mechanism of the *Dictyostelium* LRRK2 Homolog Roco Protein GbpC. *J. Biol. Chem.* **283**, 30412-30420 (2008).

638 Van Haastert, P. J., Bishop, J. D. & Gomer, R. H. The cell density factor CMF regulates the chemoattractant receptor cAR1 in *Dictyostelium*. *The Journal of Cell Biology* **134**, 1543-1549 (1996).

639 Van Haastert, P. J., Wang, M., Bominaar, A. A., Devreotes, P. N. & Schaap, P. cAMP-induced desensitization of surface cAMP receptors in *Dictyostelium*: different second messengers mediate receptor phosphorylation, loss of ligand binding, degradation of receptor, and reduction of receptor mRNA levels. *Mol. Biol. Cell* **3**, 603-612 (1992).

640 Van Haastert, P. J. M. Amoeboid Cells Use Protrusions for Walking, Gliding and Swimming. *PLoS ONE* **6**, e27532 (2011).

641 Van Haastert, P. J. M. A Model for a Correlated Random Walk Based on the Ordered Extension of Pseudopodia. *PLoS Comput. Biol.* **6**, e1000874 (2010).

642 Van Haastert, P. J. M. & Devreotes, P. N. Chemotaxis: signalling the way forward. *Nat Rev Mol Cell Biol* **5**, 626-634 (2004).

643 Van Haastert, P. J. M., Keizer-Gunnink, I. & Kortholt, A. Essential role of PI3-kinase and phospholipase A2 in *Dictyostelium discoideum* chemotaxis. *The Journal of Cell Biology* **177**, 809-816 (2007).

644 Van Haastert, P. J. M. & Veltman, D. M. Chemotaxis: Navigating by Multiple Signaling Pathways. *Sci. STKE* **2007**, pe40- (2007).

645 Varnum-Finney, B. J., Voss, E. & Soll, D. R. Frequency and orientation of pseudopod formation of *Dictyostelium discoideum* amebae chemotaxing in a spatial gradient: Further evidence for a temporal mechanism. *Cell Motil. Cytoskeleton* **8**, 18-26 (1987).

646 Veltman, D. M., Keizer-Gunnik, I. & Van Haastert, P. J. M. Four key signaling pathways mediating chemotaxis in *Dictyostelium discoideum*. *The Journal of Cell Biology* **180**, 747-753 (2008).

647 VisageImaging. in *Amira 5 User's Guide* (2010).

648 Vithalani, K. K. *et al.* Identification of Darlin, a *Dictyostelium* Protein with Armadillo-like Repeats that Binds to Small GTPases and Is Important for the Proper Aggregation of Developing Cells. *Mol. Biol. Cell* **9**, 3095-3106 (1998).

649 Wallis, J. W., Miller, T. R., Lerner, C. A. & Kleerup, E. C. Three-dimensional display in nuclear medicine. *Medical Imaging, IEEE Transactions on* **8**, 297-230 (1989).

650 Walther, P., Hentschel, J., Herter, P., Müller, T. & Zierold, K. Imaging of intramembranous particles in frozen-hydrated cells (Saccharomyces cerevisiae) by high resolution cryo SEM. *Scanning* **12**, 300-307 (1990).

651 Wang, Y., Chen, C.-L. & Iijima, M. Signaling mechanisms for chemotaxis. *Development, Growth & Differentiation* **53**, 495-502 (2011).

652 Wang, Y., Liang, Y. & Xu, K. Signal processing for sidelobe suppression in optical coherence tomography images. *J. Opt. Soc. Am. A* **27**, 415-421 (2010).

653 Wang, Y. *et al. Dictyostelium* huntingtin controls chemotaxis and cytokinesis through the regulation of myosin II phosphorylation. *Mol. Biol. Cell* **22**, 2270-2281 (2011).

654 Wang, Y. & Wang, R. K. High-resolution computed tomography of refractive index distribution by transillumination low-coherence interferometry. *Opt. Lett.* **35**, 91-93 (2010).

655 Watanabe, Y. & Itagaki, T. Real-time display on Fourier domain optical coherence tomography system using a graphics processing unit. *J. Biomed. Opt.* **14**, 060506 (2009).

656 Watts, D. J. & Ashworth, J. M. Growth of myxamoebae of the cellular slime mould *Dictyostelium discoideum* in axenic culture. *Biochem. J.* **119**, 171-174 (1970).

657 Weber, I. Is there a pilot in a pseudopod? *Eur. J. Cell Biol.* **85**, 915-924 (2006).

658 Weijer, C. J. Collective cell migration in development. *J. Cell Sci.* **122**, 3215-3223 (2009).

659 Weijer, C. J. & Williams, J. G. *Dictyostelium*: Cell Sorting and Patterning in *Encyclopedia of Life Sciences* (John Wiley & Sons, Ltd, 2001).

660 Weiss, P. Experiments on cell and axon orientation in vitro: The role of colloidal exudates in tissue organization. *J. Exp. Zool.* **100**, 353-386 (1945).

661 Welch, D. R. *et al.* Transfection of Constitutively Active Mitogen-activated Protein/Extracellular Signal-regulated Kinase Kinase Confers Tumorigenic and Metastatic Potentials to NIH3T3 Cells. *Cancer Res.* **60**, 1552-1556 (2000).

662 Wells, R. G. The role of matrix stiffness in regulating cell behavior. *Hepatology* **47**, 1394-1400 (2008).

663 Wen-Chi, C. *et al.* The migration of cancer and normal cells in response to the surface topography and rigidity. in *2011 IEEE International Conference on Nano/Micro Engineered and Molecular Systems (NEMS).* 483-486.

664 Wessels, D. *et al.* RasC Plays a Role in Transduction of Temporal Gradient Information in the Cyclic-AMP Wave of *Dictyostelium discoideum*. *Eukaryot. Cell* **3**, 646-662 (2004).

665 Wessels, D., Kuhl, S. & Soll, D. R. Application of 2D and 3D DIAS to Motion Analysis of Live Cells in Transmission and Confocal Microscopy Imaging in *Dictyostelium discoideum Protocols* (eds Ludwig Eichinger & Francisco Rivero) 261-279 (Humana Press, 2006).

666 Wessels, D., Murray, J., Jung, G., Hammer, J. A. & Soll, D. R. Myosin IB null mutants of *Dictyostelium* exhibit abnormalities in motility. *Cell Motil. Cytoskeleton* **20**, 301-315 (1991).

667 Wessels, D., Murray, J. & Soll, D. R. Behavior of *Dictyostelium* amoebae is regulated primarily by the temporal dynamic of the natural cAMP wave. *Cell Motil. Cytoskeleton* **23**, 145-156 (1992).

668 Wessels, D. *et al.* Cell motility and chemotaxis in *Dictyostelium* amebae lacking myosin heavy chain. *Dev. Biol.* **128**, 164-177 (1988).

669 Wessels, D. J., Kuhl, S. & Soll, D. R. Light Microscopy to Image and Quantify Cell Movement in *Chemotaxis Methods and Protocols* Vol. 571 455-471 (2009).

670 Wetterauer, B. *et al.* Wild-Type Strains of *Dictyostelium discoideum* Can Be Transformed Using a Novel Selection Cassette Driven by the Promoter of the Ribosomal V18 Gene. *Plasmid* **36**, 169-181 (1996).

671 White, G. E. & Greaves, D. R. Fractalkine: A Survivor's Guide. *Arterioscler. Thromb. Vasc. Biol.* **32**, 589-594 (2012).

672 Wieser, W., Biedermann, B. R., Klein, T., Eigenwillig, C. M. & Huber, R. Multi-Megahertz OCT: High quality 3D imaging at 20 million A-scans and 4.5 GVoxels per second. *Opt. Express* **18**, 14685-14704 (2010).

673 Wilkins, A. & Insall, R. H. Small GTPases in *Dictyostelium*: lessons from a social amoeba. *Trends Genet.* **17**, 41-48 (2001).

674 Wilkins, A. *et al.* *Dictyostelium* RasD is required for normal phototaxis, but not differentiation. *Genes & Development* **14**, 1407-1413 (2000).

675 Wilkins, M. R. & Williams, K. L. The extracellular matrix of the *Dictyostelium discoideum* slug. *Cell. Mol. Life Sci.* **51**, 1189-1196 (1995).

676 Williams, J. G. Transcriptional regulation of *Dictyostelium* pattern formation. *EMBO Rep.* **7**, 694-698 (2006).

677 Wirtz, D., Konstantopoulos, K. & Searson, P. C. The physics of cancer: the role of physical interactions and mechanical forces in metastasis. *Nat. Rev. Cancer* **11**, 512-522 (2011).

678 Wójciak-Stothard, B., Curtis, A., Monaghan, W., Macdonald, K. & Wilkinson, C. Guidance and Activation of Murine Macrophages by Nanometric Scale Topography. *Exp. Cell Res.* **223**, 426-435 (1996).

679 Wolf, K. *et al.* Compensation mechanism in tumor cell migration. *The Journal of Cell Biology* **160**, 267-277 (2003).

680 Wolf, K., Müller, R., Borgmann, S., Bröcker, E.-B. & Friedl, P. Amoeboid shape change and contact guidance: T-lymphocyte crawling through fibrillar collagen is independent of matrix remodeling by MMPs and other proteases. *Blood* **102**, 3262-3269 (2003).

681 Wozniak, M. A., Modzelewska, K., Kwong, L. & Keely, P. J. Focal adhesion regulation of cell behavior. *Biochimica et Biophysica Acta (BBA) - Molecular Cell Research* **1692**, 103-119 (2004).

682 Woznica, D. & Knecht, D. A. Under-Agarose Chemotaxis of *Dictyostelium discoideum* in *Dictyostelium discoideum Protocols* Vol. 346 (eds Ludwig Eichinger & Francisco Rivero) Ch. 19, 311-325 (Humana Press Inc, 2006).

683 Wu, J. *et al.* Gradient biomaterials and their influences on cell migration. *Interface Focus* **2**, 337-355 (2012).

684 Wu, M.-H., Urban, J. P. G., Cui, Z. F., Cui, Z. & Xu, X. Effect of Extracellular pH on Matrix Synthesis by Chondrocytes in 3D Agarose Gel. *Biotechnol. Prog.* **23**, 430-434 (2007).

685 Xiong, Y. *et al.* Automated characterization of cell shape changes during amoeboid motility by skeletonization. *BMC Syst. Biol.* **4**, 33 (2010).

686 Xu, X. S. *et al.* During Multicellular Migration, Myosin II Serves a Structural Role Independent of its Motor Function. *Dev. Biol.* **232**, 255-264 (2001).

687 Yang, Y. *et al.* Investigation of optical coherence tomography as an imaging modality in tissue engineering. *Phys. Med. Biol.*, 1649-1659 (2006).

688 Yang, Y. & Leong, K. W. Nanoscale surfacing for regenerative medicine. *Wiley Interdisciplinary Reviews: Nanomedicine and Nanobiotechnology* **2**, 478-495 (2010).

689 Yang, Y. *et al.* Optical scattering coefficient estimated by optical coherence tomography correlates with collagen content in ovarian tissue. *J. Biomed. Opt.* **16**, 090504 (2011).

690 Yin, Z., Kanade, T. & Chen, M. Understanding the phase contrast optics to restore artifact-free microscopy images for segmentation. *Med. Image Anal.* **16**, 1047-1062 (2012).

691 Yoo, T. *et al.* Visualizing Cells and Humans in 3D; Biomedical Image Analysis at Nanometer and Meter Scales. *IEEE Computer Graphics and Applications* **32**, 39-49 (2012).

692 Yoshida, K. & Inouye, K. Myosin II-dependent cylindrical protrusions induced by quinine in *Dictyostelium*: antagonizing effects of actin polymerization at the leading edge. *J. Cell Sci.* **114**, 2155-2165 (2001).

693 Yoshida, K. & Soldati, T. Dissection of amoeboid movement into two mechanically distinct modes. *J. Cell Sci.* **119**, 3833-3844 (2006).

694 Yu, H. & Wilamowski, B. Levenberg-Marquardt Training. *The Industrial Electronics Handbook* **5**, 1-16 (2010).

695 Yuen, I. S. *et al.* A density-sensing factor regulates signal transduction in *Dictyostelium*. *The Journal of Cell Biology* **129**, 1251-1262 (1995).

696 Yumura, S. *et al.* Multiple Myosin II Heavy Chain Kinases: Roles in Filament Assembly Control and Proper Cytokinesis in *Dictyostelium*. *Mol. Biol. Cell* **16**, 4256-4266 (2005).

697 Yuste, R. Fluorescence microscopy today. *Nat Meth* **2**, 902-904 (2005).

698 Zaman, M. H. *et al.* Migration of tumor cells in 3D matrices is governed by matrix stiffness along with cell-matrix adhesion and proteolysis. *PNAS* **103**, 10889-10894 (2006).

699 Zegers, M. M. P., O'Brien, L. E., Yu, W., Datta, A. & Mostov, K. E. Epithelial polarity and tubulogenesis in vitro. *Trends Cell Biol.* **13**, 169-176 (2003).

700 Zhang, E. Z. *et al.* Multimodal photoacoustic and optical coherence tomography scanner using an all optical detection scheme for 3D morphological skin imaging. *Biomed. Opt. Express* **2**, 2202-2215 (2011).

701 Zhang, H. *et al.* Constitutively Active Protein Kinase A Disrupts Motility and Chemotaxis in *Dictyostelium discoideum*. *Eukaryot. Cell* **2**, 62-75 (2003).

702 Zhang, H. *et al.* Phosphorylation of the myosin regulatory light chain plays a role in motility and polarity during *Dictyostelium* chemotaxis. *J. Cell Sci.* **115**, 1733-1747 (2002).

703 Zhang, K. & Kang, J. U. Real-time 4D signal processing and visualization using graphics processing unit on a regular nonlinear-k Fourier-domain OCT system. *Opt. Express* **18**, 11772-11784 (2010).

704 Zhang, P., Wang, Y., Sesaki, H. & Iijima, M. Proteomic identification of phosphatidylinositol (3,4,5) triphosphate-binding proteins in *Dictyostelium discoideum*. *PNAS* **107**, 11829-11834 (2010).

705 Zhao, Y. *et al.* Integrated multimodal optical microscopy for structural and functional imaging of engineered and natural skin. *Journal of Biophotonics* **5**, 437-448 (2012).

706 Zhu, X. *et al.* Enhancement of the mechanical and biological properties of a biomembrane for tissue engineering the ocular surface. *Annual Academy of Medicine of Singapore* **35**, 210-214 (2006).

707 Zhu, X. *et al.* Cellular Reactions of Osteoblasts to Micron- and Submicron-Scale Porous Structures of Titanium Surfaces. *Cells Tissues Organs* **178**, 13-22 (2004).

708 Zicha, D., Dunn, G. A. & Brown, A. F. A new direct-viewing chemotaxis chamber. *J. Cell Sci.* **99**, 769-775 (1991).

709 Zigmond, S. H. [6] Orientation chamber in chemotaxis in *Methods Enzymol.* Vol. Volume 162 (ed Sabato Giovanni Di) 65-72 (Academic Press, 1988).

710 Zigmond, S. H. Ability of polymorphonuclear leukocytes to orient in gradients of chemotactic factors. *The Journal of Cell Biology* **75**, 606-616 (1977).

Appendices

Publications and Conference Presentations

Publications as first author:

Sara M Rey, Boris Považay, Bernd Hofer, Angelika Unterhuber, Boris Hermann, Adrian Harwood, Wolfgang Drexler, Three- and four-dimensional visualization of cell migration using optical coherence tomography, Journal of Biophotonics, 6-7, p370-379 (2009). (Attached at end of Appendices).

Oral Presentations:

Sara M. Rey, Adrian Harwood, Boris Považay, Bernd Hofer, Angelika Unterhuber, Boris Hermann, Wolfgang Drexler, Visualization of 3D cell migration using high speed ultrahigh resolution optical coherence tomography *(Invited Paper)*, OCT in Tissue Engineering and Regenrative Medicine III, SPIE Photonics West 2009

Sara M. Rey, Adrian Harwood, Boris Považay, Bernd Hofer, Boris Hermann, Angelika Unterhuber, Wolfgang Drexler, Visualization of 3-D and 4-D Cell Migration Using Three-Dimensional Ultrahigh Resolution Optical Coherence Tomography, Optical Coherence Tomography and Coherence Techniques, European Conferences on Biomedical Optics (ECBO), 2009

Rey, Sara M., Považay, Boris, Hofer, Bernd, Unterhuber, Angelika, Harwood, Adrian John and Drexler, Wolfgang, Mutant and wild type cell chemotaxis in 3D and 4D with ultrahigh-resolution optical coherence tomography in Optical Coherence Tomography and Coherence Domain Optical Methods in Biomedicine XIV, SPIE Photonics West 2010.

Sara M. Rey, Boris Považay, Bernd Hofer, Adrian Harwood, Wolfgang Drexler, Chemotaxis and migration of mutant and wild-type cells in 3D and 4D using ultra-high-resolution optical coherence tomography, Optical Interactions with Tissue and Cells XXII, SPIE Photonics West, 2011.

Poster Presentations:

Sara Rey, Boris Považay, Bernd Hofer, Wolfgang Drexler and Adrian Harwood, Four-dimensional chemotaxis of *Dictyostelium* cells using optical coherence tomography in Dicty 2010, Annual International Dictyostelium Meeting, 2010.

Appendix 1: HL-5 medium with maltose

HL-5 Medium for Dictyostelium
For 1 liter

Bactopeptone [Oxoid L37]	14.3 g
Yeast extract [Sigma Y-1625 or Difco 0127-17-9]	7.15 g
Maltose monohydrate [Sigma M-5895]	18 g
Na2HPO4 . 2H2O [Merck 6580] (3.6mM)	0.641 g
KH2PO4 (3.6mM) [Fluka 60220]	0.490 g

Complete to desired volume with autoclaved ddH2O.
Dissolve by stirring.
Check the pH : approx. 6.65
Autoclave and keep at 4°C.

Appendix 2: ImageJ macro to find the substrate, crop and area around it and produce summed enface images

```
//Macro selects the ROI round the interface,crops it, reslices it and saves it

cropped=18;     //Enter number of slices want to sum round the interface over

//Opens a ready deskewed, denoised, cropped .tif file
base = "filepath\\filename-"; //Filepath and first part of the filename
startNum = 1;    //Enter first volume number
numVol = 61;    //Enter final volume number

fileloc= "filepath"; //Enter filepath for saving

for (i=startNum; i<=numVol; i+=1) {
open(base + toString(i)+" affined.tif"); //Opens the files one by one

//Duplicates the image and rotates it
t = getTitle();
width=getWidth();
height=getHeight();
sliceno=getSliceNumber();
slices=nSlices;

run("Duplicate...", "title=["+t+"-profile.tif] duplicate range=1-+sliceno+"); //duplicates the image and
names it title-profile.tif
selectWindow(""+t+"-profile.tif");
run("Rotate 90 Degrees Right");
```

```
s = getTitle();

run("Z Project...", "start=1 stop=slices projection=[Average Intensity]");
run("Select All");
selectWindow(""+s+"");
close();

//Outputs the profile as an array
selectWindow("AVG_"+t+"-profile.tif");
profile = getProfile();

//Closes the average of the stack
selectWindow("AVG_"+t+"-profile.tif");
close();

//Outputs the differences between two stacks into an array
number=0;
diff=newArray(height);
len=lengthOf(profile)-1;
	for (number=0; number<len; number++) {

	diff[number]= (profile[number] - profile[number+1]); //= ArrDiff
	}

//Returns the maximum of the profile array
		min=0;
	for (number=0; number<lengthOf(diff); number++) {
			min=minOf(diff[number], min);
		}
		max=min;
	for (number=0; number<lengthOf(diff); number++) {
			max=maxOf(diff[number], max);
		}



//Returns the pixel number at which the maximum is found
		for (a=0; a<lengthOf(diff); a++) {
			if (diff[a]==max) {
				b=a+1;
```

```
                    }
                }


//Applies the above to the stack
selectWindow(""+t+"");

rec=(height-b);
part=cropped*(3/4);
rectangle=(rec-part); //Starts the ROI a little bit offset from the interface (downwards)
makeRectangle(0, rectangle, width, cropped);

run("Crop");
ID =  getImageID();
run("Reslice [/]...", "output=1.000 start=Top");
selectImage(ID);
close();
ID =  getImageID();
run("Z Project...", "start=1 stop=18 projection=[Sum Slices]");
selectImage(ID);
close();

ID =  getImageID();
t = getTitle();

saveAs("Tiff", fileloc + ""+t+".tif"); //Saving z projection

selectImage(ID);
close();
}
```

Appendix 3: Sequential stack registration using ImageJ plugins

```
//This macro counts through the stacks backwards from startNum and ends at the final set stack (numVolfirst)
- the beginning in this case- opening two stacks for a comparison and then the next set stack etc...

base = "base = "filepath\\filename-"; //Filepath and first part of the filename
numVol = 66;
numVolfirst= 1;
sliceStart = 1;
```

```
numSlice = 800;
sumOver= 20; //Set variable to number of slices to sum over
count=1;
i=1;

//Finds the central stack or if an odd number rounds up
if ((numVol%2)==0) {
startNum= (numVol-(numVolfirst-1))/2 +(numVolfirst-1);
}
else{
startNum=((numVol-(numVolfirst-1) +1)/2) +(numVolfirst-1);
}
numVolsub=startNum-1;
numVolsub2=startNum+1;

//Enter the savefile location
fileloc= "filepath"; //Enter filepath for saving
filelocb= ""+filepath+"\\Bscan\\";

//Opens the files sequentially in descending order
for (i=startNum; i>=numVolfirst&&i<numVol; i-=1) {
  fList = getFileList(base + toString(i));
        open(base + toString(i)+" affined-1.tif"); //Opens the files one by one
        run("8-bit");
        slicesNum=nSlices;
        midslice=nSlices/2;
        doubleSlice=2*slicesNum;
        newStackslicesNum= slicesNum+1;
        w= getWidth();
        h= getHeight();
        ww= (w+50);
        hh= (h+50);
        numSlice = nSlices;
sliceHalf = numSlice/2;
startHalf= sumOver+1;
stopHalf= numSlice-sliceHalf;

setSlice(midslice);

//Rename file to remove bits on the end and duplicate tif
```

```
            s=getTitle();
  short = substring(s,0,indexOf(s,'-')+1);
  title= ""+short+i;
  rename(title);

//Opens a second stack on the first iteration
if (count==1) {

for (j=i-1; j>=numVolsub; j-=1) {
fList = getFileList(base + toString(j));
ID = getImageID();
t = getTitle();    //First iteration so name the just opened file as the first one i.e. t
open(base + toString(j)+" affined-1.tif");
i-=1;

run("8-bit");

//Rename file to remove bits on the end and duplicate tif
s=getTitle();
short = substring(s,0,indexOf(s,'-')+1);
title= ""+short+i;
rename(title);
t2 = getTitle();

setSlice(midslice);

//Concatenates the stacks and use the PoorMan3DReg plugin to align the two opened stacks

run("Concatenator ", "stack_1=["+t+"] stack_2=["+t2+"] title=["+i+"]");
run("PoorMan3DReg ", "transformation=Translation number="+slicesNum+" projection=[Max Intensity]");
ID =  getImageID();
run("Substack Maker", "slices="+sliceStart+"-"+slicesNum+"");    //Takes out the first loaded stack from the concatenated stacks


//Saves the first loaded stack from the concatenated stacks
saveAs("Tiff", fileloc + ""+t+".tif"); //Saving first loaded stack from concatenated stacks
run("Slice Remover", " first="+sliceStart+" last="+sliceHalf+" increment=1");
run("Slice Remover", "first="+startHalf+" last="+stopHalf+" increment=1");
```

```
ID =  getImageID();
run("Z Project...", " start=1 stop="+sumOver+" projection=[Sum Slices]");
saveAs("Tiff", filelocb + ""+t+".tif");
close();

selectImage(ID);
close();

wait(5);
ID =  getImageID();
run("Substack Maker", "slices="+newStackslicesNum+"-"+doubleSlice+"");          //Takes     out     the
second loaded stack from the concatenated stacks
selectImage(ID); //Selects the concatenated stacks
close();

//Saves the second loaded stack from the concatenated stacks
saveAs("Tiff", fileloc + ""+t2+".tif"); //Saving second stack
run("Duplicate...", "title=tempsubstack duplicate range=+sliceStart+-+slicesNum+");
run("Slice Remover", "first=1 last=142 increment=1");
run("Slice Remover", "first=21 last=658 increment=1");
ID =  getImageID();  //Small stack with slices removed
run("Z Project...", "start=1 stop=20 projection=[Sum Slices]");
saveAs("Tiff", filelocb + ""+t2+".tif");
close();

selectImage(ID); //Selects the Small stack with slices removed
close();

t = getTitle(); //Reassigns the second stack to be the new first stack
count++;
                        }
            }

//If it is not the first iteration
else{

//Rename file to remove bits on the end and duplicate tif
s=getTitle();
short = substring(s,0,indexOf(s,'-')+1);
title= ""+short+i;
```

```
rename(title);
t2 = getTitle();

setSlice(midslice);
run("Concatenator ", "stack_1=["+t+"] stack_2=["+t2+"] title=["+i+"]");
run("PoorMan3DReg ", "transformation=Translation number="+slicesNum+" projection=[Max
Intensity]");
ID =  getImageID();
run("Substack Maker", "slices="+newStackslicesNum+"-"+doubleSlice+"");
selectImage(ID); //Selects the concatenated stacks
close();

//Saving the next stack in the series
//selectImage(ID);
saveAs("Tiff", fileloc + ""+t2+".tif"); //Saving Stack-24
run("Duplicate...", "title=tempsubstack duplicate range=+sliceStart+-+slicesNum+");
run("Slice Remover", "first=1 last=142 increment=1");
run("Slice Remover", "first=21 last=658 increment=1");
ID =  getImageID();  //Small stack with slices removed
run("Z Project...", "start=1 stop=20 projection=[Sum Slices]");
saveAs("Tiff", filelocb + ""+t2+".tif");
close();

selectImage(ID); //Selects the Small stack with slices removed
close();

t = getTitle(); //Reassigns the second stack to be the new first stack
ID =  getImageID(); //Just for in the case of the final stack in the series (1 prob)
count++;

if (i==numVolfirst) { //Close the final stack loaded (first one)
close();
                    }
}

//New part for starting again from middle stack
if (i==numVolfirst) {

count=1;          //Reset count to 1
```

```
//Opens files sequentially in ascending order
	for (i=startNum; i<=numVol; i+=1) {
	fList = getFileList(base + toString(i));
	open(base + toString(i)+" affined-1.tif");
	run("8-bit");
		slicesNum=nSlices;
		midslice=nSlices/2;
		doubleSlice=2*slicesNum;
		newStackslicesNum= slicesNum+1;

		newStackslicesNum= slicesNum+1;
		w= getWidth();
		h= getHeight();
		ww= (w+50);
		hh= (h+50);


		count++;



//Rename file to remove bits on the end and duplicate tif
s=getTitle();
short = substring(s,0,indexOf(s,'-')+1);
title= ""+short+i;
rename(title);

t2=getTitle(); //Necessary for the second iteration- in the 'else' case. Otherwise it is overwritten anyway

if (count==2) {		//Opens a second stack on the first iteration ascending

for (j=i+1; j<=numVolsub2; j+=1) {
fList = getFileList(base + toString(j));
ID = getImageID();
t = getTitle(); //Assigns t to already opened stack
open(base + toString(j)+" affined-1.tif");
i+=1;

run("8-bit");
```

```
//Rename file to remove bits on the end and duplicate tif
s=getTitle();
short = substring(s,0,indexOf(s,'-')+1);
title= ""+short+i;
rename(title);
t2 = getTitle();

setSlice(midslice);

//Concatenates the stacks and use the PoorMan3DReg plugin to align the two opened stacks
run("Concatenator ", "stack_1=["+t+"] stack_2=["+t2+"] title=["+i+"]");
run("PoorMan3DReg ", "transformation=Translation number="+slicesNum+" projection=[Max Intensity]");
ID =  getImageID();
run("Substack Maker", "slices="+sliceStart+"-"+slicesNum+"");    //Takes out the first loaded stack from the concatenated stacks


//Saves the first loaded stack from the concatenated stacks
                saveAs("Tiff", fileloc + ""+t+".tif"); //Saving first loaded stack from concatenated stacks
                run("Slice Remover", "first=1 last=142 increment=1");
                run("Slice Remover", "first=21 last=658 increment=1");
                ID =  getImageID();
                run("Z Project...", "start=1 stop=20 projection=[Sum Slices]");
                saveAs("Tiff", filelocb + ""+t+".tif");
                close();

                selectImage(ID);
                close();

                wait(5);
                ID =  getImageID();
                t = getTitle();
                run("Substack Maker", "slices="+newStackslicesNum+"-"+doubleSlice+"");
        //Takes out the second loaded stack from the concatenated stacks
                selectImage(ID); //Selects the concatenated stacks
                close();
```

```
//Saves the second loaded stack from the concatenated stacks
                    saveAs("Tiff", fileloc + ""+t2+".tif"); //Saving second stack
                    run("Duplicate...",  "title=tempsubstack  duplicate  range=+sliceStart+-+slicesNum+");

                    run("Slice Remover", "first=1 last=142 increment=1");
                    run("Slice Remover", "first=21 last=658 increment=1");
                    ID =  getImageID();  //Small stack with slices removed
                    run("Z Project...", "start=1 stop=20 projection=[Sum Slices]");
                    saveAs("Tiff", filelocb + ""+t2+".tif");
                    close();

                    selectImage(ID); //Selects the Small stack with slices removed
                    close();

//Rename file to remove bits on the end and duplicate tif
s=getTitle();
short = substring(s,0,indexOf(s,'-')+1);
title= ""+short+i;
rename(title);
t = getTitle(); //Reassigns the second stack to be the new first stack
count++;
                    }
          }

else{
//Concatenates the stacks and use the PoorMan3DReg plugin to align the two opened stacks
run("Concatenator ", "stack_1=["+t+"] stack_2=["+t2+"] title=["+i+"]");
run("PoorMan3DReg ", "transformation=Translation number="+slicesNum+" projection=[Max
Intensity]");
ID =  getImageID();
run("Substack Maker", "slices="+newStackslicesNum+"-"+doubleSlice+"");
selectImage(ID); //Selects the concatenated stacks
close();

//Saving the next stack in the series
saveAs("Tiff", fileloc + ""+t2+".tif"); //Saving Stack-24
                    run("Duplicate...",  "title=tempsubstack  duplicate  range=+sliceStart+-+slicesNum+");

                    run("Slice Remover", "first=1 last=142 increment=1");
                    run("Slice Remover", "first=21 last=658 increment=1");
```

```
ID =  getImageID();  //Small stack with slices removed
run("Z Project...", "start=1 stop=20 projection=[Sum Slices]");
saveAs("Tiff", filelocb + ""+t2+".tif");
close();

selectImage(ID); //Selects the Small stack with slices removed
close();

//Rename file to remove bits on the end and duplicate tif
s=getTitle();
short = substring(s,0,indexOf(s,'-')+1);
title= ""+short+i;
rename(title);
t = getTitle(); //Reassigns the second stack to be the new first stack
ID =  getImageID(); //Just for in the case of the final stack in the series (1 prob)
count++;
}

if (i==numVol) { //Closes the final stack
close();
                        }

        }
}
}
```

Appendix 4: Alignment of all stacks to the central stack using ImageJ plugins

```
//This macro counts through the stacks backwards from startNum and ends at the final set stack (numVolfirst)-
the beginning in this case- opening two stacks for a comparison and then the next set stack etc...

base = "base = "filepath\\filename-"; //Filepath and first part of the filename
startNum = 1;
numVol = 66;
numVolfirst= 1;
sliceStart = 1;
numSlice = 800;
sumOver= 20; //Set variable to number of slices to sum over
count=1;
i=1;
```

```
//Finds the central stack or if an odd number rounds up
if ((numVol%2)==0) {
j= (numVol-(numVolfirst-1))/2 +(numVolfirst-1);
}
else{
j=((numVol-(numVolfirst-1) +1)/2) +(numVolfirst-1);
}
numVolsub=startNum-1;
numVolsub2=startNum+1;

//Enter the savefile location
fileloc= "filepath"; //Enter filepath for saving
filelocb= ""+filepath+"\\Bscan\\";


for (i=startNum; i<=numVol; i+=1) {
open(base + toString(j)+" affined-1.tif"); //Open the middle stack
run("8-bit");

numSlice = nSlices;
sliceHalf = numSlice/2;
startHalf= sumOver+1;
stopHalf= numSlice-sliceHalf;
w=getWidth();
h=getHeight();
ww=(w+50);
hh=(h+50);

//Rename file to remove bits on the end and duplicate tif
s=getTitle();
short = substring(s,0,indexOf(s,'-')+1);
title= ""+short+j;
rename(title);
t = getTitle();

fList = getFileList(base + toString(i));
open(base + toString(i)+" affined-1.tif"); //Opens the files one by one
run("8-bit");
slicesNum=nSlices;
```

```
midslice=nSlices/2;
doubleSlice=2*slicesNum;
newStackslicesNum= slicesNum+1;

//Rename file to remove bits on the end and duplicate tif
s=getTitle();
short = substring(s,0,indexOf(s,'-')+1);
title= ""+short+i;
rename(title);
t2 = getTitle();

//If the second file opened is the same as the first- save
if(i==j){
close();
saveAs("Tiff", fileloc + ""+t2+".tif"); //Saving reference stack
                run("Slice Remover", "first="+sliceStart+" last="+sliceHalf+" increment=1");
run("Slice Remover", "first="+startHalf+" last="+stopHalf+" increment=1");
ID =  getImageID();  //Small stack with slices removed
run("Z Project...", "start=1 stop="+sumOver+" projection=[Sum Slices]");          saveAs("Tiff",
filelocb + ""+t2+".tif");
                close();

                selectImage(ID); //Selects the Small stack with slices removed
                close();
}

//In all other cases concatenate and register the stacks
else{
//Register the stacks
run("Concatenator ", "stack_1="+t+" stack_2="+t2+" title="+i+"");
run("PoorMan3DReg ", "transformation=Translation number="+slicesNum+" projection=[Max
Intensity]");
run("Substack Maker", "slices="+newStackslicesNum+"-"+doubleSlice+"");                //Takes out
the second loaded stack from the concatenated stacks

//Save the second lot from the concatenated stacks
saveAs("Tiff", fileloc + ""+t2+""); //Saving second stack
wait(10);
run("Slice Remover", "first="+sliceStart+" last="+sliceHalf+" increment=1");
run("Slice Remover", "first="+startHalf+" last="+stopHalf+" increment=1");
```

```
ID =  getImageID();  //Small stack with slices removed
run("Z Project...", "start=1 stop="+sumOver+" projection=[Sum Slices]");  saveAs("Tiff",  filelocb  +
""+t2+"");
wait(10);
close();

selectImage(ID); //Selects the Small stack with slices removed
close();

selectWindow(""+i+""); //Selects the concatenated stacks
close();

}
}
```

Appendix 5: ImageJ macro to align stacks by finding the interface between agarose and agar

```
//Macro selects the ROI round the interface,crops it, reslices it and saves it

//Opens a ready cropped .tif file
base = "base = "filepath\\filename-"; //Filepath and first part of the filename
startNum = 1;
numVol = 61;

sliceStart = 1;//First slice of the stack. Nearly always 1.
offset= -5;//Set to give some offset form the exact interface at the camp agar. NOTE Must be less
than smallest index of maximum
offset2= -30;//Gives leeway at top of the stack to compensate for differences in height. NOTE Larger
size makes shorter (height) stack
sumOver= 20; //Set variable to number of slices to sum over

//Enter the savefile location
fileloc= "filepath"; //Enter filepath for saving
filelocb= ""+filepath+"\\Bscan\\";

for (i=startNum; i<=numVol; i+=1) {
open(base + toString(i)+".tif"); //Opens the files one by one

//Rename file to remove bits on the end and duplicate tif
s=getTitle();
```

```
short = substring(s,0,indexOf(s,'-')+1);
title= ""+short+i;
rename(title);

//Duplicates the image and rotates it
t = getTitle();
width=getWidth();
height=getHeight();
sliceno=getSliceNumber();
slices=nSlices;

heightcrop=(height/2);
fullheight=(height-heightcrop);

run("Duplicate...", "title=["+t+"-profile.tif] duplicate range=1-+sliceno+"); //duplicates the image and names it title-profile.tif
selectWindow(""+t+"-profile.tif");
run("Rotate 90 Degrees Right");
s = getTitle();
run("Z Project...", "start=1 stop="+slices+" projection=[Average Intensity]");
run("Select All");
selectWindow(""+s+"");
close();

//Outputs the profile as an array
selectWindow("AVG_"+t+"-profile.tif");
makeRectangle(0, 0, heightcrop, width);
run("Crop");
selectWindow("AVG_"+t+"-profile.tif");
run("Select All");
profile = getProfile();

//Closes the average of the stack
selectWindow("AVG_"+t+"-profile.tif");
close();

//Finds the difference between numbers in the array
number=0;
diff=newArray(height);
len=lengthOf(profile)-1;
```

```
for (number=0; number<len; number++) {

	diff[number]= (profile[number] - profile[number+1]); //= ArrDiff
	}

//Returns the maximum of the profile array
min=0;
	for (number=0; number<lengthOf(diff); number++) {
			min=minOf(diff[number], min);
		}
		max=min;
	for (number=0; number<lengthOf(diff); number++) {
			max=maxOf(diff[number], max);
		}

//Returns the pixel number at which the maximum is found
		for (a=0; a<lengthOf(diff); a++) {
			if (diff[a]==max) {
				b=a+1;
				}
			}
selectWindow(""+t+"");

//Having found the interface- crop the image a set point around it to encompass the entire ROI
rec=(height-b);		//Point at which the interface lies
rectangle= rec+20;	//Want to add in a bit off the camp agar- have added about 20px here
bot= (b-20);		//20 gives a little leeway

//Runs for the first iteration
if (i==startNum){
top= (height-b); //top sets the number of pixels to remain constant

run("Flip Vertically", "stack");
makeRectangle(0, bot, width, top);
run("Crop");
run("Flip Vertically", "stack");

ID =  getImageID();

//Saves the registered file
```

```
saveAs("Tiff", fileloc + ""+t+""); //Saving cropped tif
run("Slice Remover", "first="+sliceStart+" last="+sliceHalf+" increment=1");
run("Slice Remover", "first="+startHalf+" last="+stopHalf+" increment=1");
ID =  getImageID();  //Small stack with slices removed
run("Z Project...", "start=1 stop="+sumOver+" projection=[Sum Slices]");
saveAs("Tiff", filelocb + ""+t+"");

close();

selectImage(ID); //Selects the Small stack with slices removed
close();
}

//Runs in all other cases than the first iteration
else{

run("Flip Vertically", "stack");
makeRectangle(0, bot, width, top);
run("Crop");
run("Flip Vertically", "stack");

ID =  getImageID();

//Saves the registered stack
saveAs("Tiff", fileloc + ""+t+""); //Saving cropped tif
run("Slice Remover", "first=1 last=10 increment=1");
run("Slice Remover", "first=21 last=49 increment=1");
ID =  getImageID();  //Small stack with slices removed
run("Z Project...", "start=1 stop=20 projection=[Sum Slices]");
saveAs("Tiff", filelocb + ""+t+"");

close();

selectImage(ID); //Selects the Small stack with slices removed
close();
}
}
```

Appendix 6: ImageJ macro to align stacks by inputting shift manually

```
//Macro to shift every slice by entered amount (negative numbers for the opposite direction)
//Additions required to attempt to automate detection of differences between stacks and auto load them
//Load stack to be shifted
waitForUser("Open stack to be shifted");

fileloc= "N:\\3D STACKREGED\\DEVELOPED\\20100617 Ax2 agarose - StackReg2 - Copy - Copy\\";
//Make this variable set the filesave location so don't keep having to change it
filelocb= ""+fileloc+"\\Bscan\\";
t = getTitle();
w = getWidth();
h = getHeight();
sliceno=getSliceNumber();
numSlice=nSlices();
sumOver= 20; //Set variable to number of slices to sum over

w=getWidth();
h=getHeight();
ww=(w+50);
hh=(h+50);
numSlice = nSlices;
sliceHalf = numSlice/2;
startHalf= sumOver+1;
stopHalf= numSlice-sliceHalf;

xshift=0
yshift=0

//Enter the shifts x
Dialog.create("Enter x shift")
Dialog.addNumber("by # to the right", xshift)
Dialog.show();
xshift = Dialog.getNumber();

//Enter the shifts y
Dialog.create("Enter y shift")
Dialog.addNumber("by # down", yshift)
Dialog.show();
yshift = Dialog.getNumber();
```

```
for (i=0; i<numSlice; i++){
setSlice(i+1);
run("Translate...", "x="+xshift+" y="+yshift+" interpolation=Bicubic slice");
}

//Optional save- comment out if don't want

//Tick a box if you don't want to save and want the macro to exit instead
//(useful if you are not happy with the result)

leave=false;
if(leave==false){

Dialog.create("Save?")
Dialog.addCheckbox("Tick to not save", false)
Dialog.show();
	xshift = Dialog.getNumber();
	leave = Dialog.getCheckbox();

if(leave==false){

waitForUser("Pressing ok will save file"); //Double checks that the file should be saved

saveAs("Tiff", fileloc + ""+t+""); //Saving stack
wait(10);
run("Slice Remover", "first="+sliceStart+" last="+sliceHalf+" increment=1");
run("Slice Remover", "first="+startHalf+" last="+stopHalf+" increment=1");
ID =  getImageID();  //Small stack with slices removed
run("Z Project...", "start=1 stop="+sumOver+" projection=[Sum Slices]");
saveAs("Tiff", filelocb + ""+t+"");
wait(10);
close();

selectImage(ID); //Selects the Small stack with slices removed
close();
}
else{
close();
}
```